Computational Studies of the Structures and Properties of Microporous Materials

A thesis submitted to Cardiff University for the degree of

Doctor of Philosophy (PhD) in the Faculty of Chemistry

2024

Edward William Stacey *

Supervisor: Professor Sir Richard Catlow

Cardiff School of Chemistry

Acknowledgements

I would like to offer my sincerest gratitude to the incredible contributions to my studies from both my supervisors Professor Sir Richard Catlow and Dr Matthew Quesne. Both of whom have provided invaluable guidance and insight throughout my studies during my time at Cardiff University, particularly during the unprecedented challenges presented by the disruption caused by the Coronavirus pandemic. I also would like to thank the rest of the University faculty and support staff for their assistance. I also wish to thank Cardiff University's School of Chemistry for the funding for this studentship.

I also thank all the funding and research bodies involved including the EPSRC, UKRI and the Catalysis Hub for all the opportunities presented during my studies, as well as all the high-performance computing facilities: The EPSRC, Materials Chemistry Consortium (MCC), and Supercomputing Wales.

SUPERCOMPUTING WALES
UWCHGYFRIFIADURA CYMRU

HEC MCC UK

EPSRC
Pioneering research
and skills

CatalysisHub

UKRI
Engineering and
Physical Sciences
Research Council

Table of Contents

Declaration

None of the work contained within this thesis has been submitted in support of an application pertaining to another degree or qualification of Cardiff University or another University or academic institute.

Thesis Abstract

This thesis applies a range of computational modelling methodologies to different problems in the science of microporous materials.

We present an assessment of different interatomic potential methodologies for the modelling of pure silica zeolites and consider the extent charge transfer plays in accurate determination of lattice energies. The assessment of these parameters enabled the selection of a model that is compatible with Quantum Mechanical methods to provide a suitably accurate methodology for modelling the molecular mechanical (MM) region in hybrid quantum mechanical molecular mechanical (QM/MM) calculations. These same silica structures are also modelled using quantum mechanical methods based on Density Functional Theory to calculate zeolite cohesive energies. The results of both the lattice and cohesive energies are compared with published thermochemical data. Zeolite energies were produced with a high level of accuracy using DFT when compared to experimental values, with energy values from interatomic potential methods reproducing the same trends across a large variety of microporous structures. The formal charge shell model is determined to be superior to the partial charge rigid ion model due to the inherent modelling of polarisability which prevents the erroneous calculation of linear bond angels sometimes present in the rigid ion model. Furthermore, the same approach is then applied to study microporous alumino-phosphates (AlPOs) to assess the ability of the different methodologies to reproduce energies in comparison to experimental data. The calculation of these AlPOs was shown to be more reliable with the shell model approach than with DFT.

We then focus on the zeolite ZSM-5 where we use hybrid Quantum Mechanical Molecular Mechanical (QM/MM) methods, to model the properties of cation exchanged systems in the context of their use in oxidation catalysis. Molecular oxygen is introduced to determine whether these cations form either an activated oxo species or an activated super-oxo species. We demonstrate that Fe(II), Mn(II), Mn(III), Cu(I), Zn(I), Ti(II), Ti(III), Mo(I) and Mo(II) systems could activate molecular oxygen and form a super-oxide species upon coordination to the metal cation as indicated by the oxygen bond length extending to 1.3 Å.

Furthermore, both Au(I), Cu(I) structural types yield positive binding energies along with b-type Na(I) and Zn(II) structures, indicating oxygen is unable to bind to these cationic centres.

The abstraction of a hydrogen atom by these oxo/super-oxo species is subsequently modelled in order to predict a viable catalyst for the activation of methane via a novel reaction pathway. Mo(I) cations are shown to break the oxygen-oxygen bond of the coordinating molecule to form a hydroxyl and thus is unlikely to act as a catalyst. Using a valence bond approach we demonstrate that the [Zn(I)-ZSM-5]-super-oxo complex has a sufficiently low $\mathbf{\Delta_{acid}}$ suggesting it would be a viable alternative for the catalytic activation of methane, with a low bond dissociation energy that is comparable to the currently used μ-nitrido-bridged diiron-oxo porphyrin. Whilst Cu(I) and Na(I) form super-oxo species with similar basicities to the natural porphyrin alternative, they cannot bind molecular oxygen as demonstrated by their positive binding energies.

The final part of this thesis aims to model comprehensively the behaviour of water within the pores of two different ZSM-5 structures at different temperatures. Both H-ZSM-5 and Na-ZSM-5 systems are simulated with loadings of 1-3 water molecules at two temperatures (298 K and 400 K) for a simulated timeframe of 10 ps using *Ab-Initio* Molecular Dynamics (AIMD) techniques. Water clusters of significance from the AIMD are modelled using hybrid Quantum Mechanical Molecular Mechanical (QM/MM) methods and their corresponding vibrational spectra are calculated using the Generalised Vibrational Perturbation Theory (GVPT2).

Water clustering behaviour is analysed and compared between the H-ZSM-5 and Na-ZSM-5 systems to elucidate the effect the cation has on the anharmonicity of water clusters, and how the two temperatures influence the dynamics of the water clusters. The general trends from the resultant spectra show similar dynamics with a loading of one water molecule with it coordinating to either cation at both temperatures illustrating no anharmonic cross-coupling behaviour. At a loading of two water molecules, we reveal a difference in clustering dynamics between the two cationic systems, with hydrogen bonding present in the H-ZSM-5 system resulting in significant shifts of the asymmetric vibrations. Hydrogen bonding was not present in Na-ZSM-5 system between the water molecules, but a coordinating water's hydrogens can potentially interact with oxygens in the zeolite's pore wall causing a slight shift to the observed vibrational frequencies. Finally at loadings of three water

molecules we demonstrate a propensity for the H-ZSM-5 system to form hydroxonium ions, with a greater frequency of formation at the higher temperatures with significant shifting behaviour of the anharmonic vibrations. Na-ZSM-5 is able to form hydrogen bonds between water molecules but do not form hydroxonium ions, instead forming weak clusters involving only two of the waters as the large cation size prevents formation of larger stabilising water clusters. The large Na cation exerts a minor influence over the cluster that can shift the frequencies down-field. The key results are highlighted which will form the foundation of future work analysing experimental 2D-IR spectra.

The thesis highlights the role of a range of computational techniques in probing different aspects of the properties of microporous materials, and provides new insights into our understanding of structure, stability, adsorption, and reactivity in these widely investigated materials.

CHAPTER 1

Introduction

1.0 Catalysis

Catalysis is an extensive field of science that encompasses multiple disciplines, including chemical engineering and materials chemistry, in addition to several other branches of the chemical sciences. Catalysis is commonly categorised using three distinct types of process: heterogeneous catalysis, whereby the catalytic process involves more than one phase; homogeneous, where the catalysis takes place in one phase and bio-catalysis, where the reaction is catalysed by enzymes. Catalytic processes employ a reagent, termed a "catalyst", that enhances the rate of a chemical reaction by providing an alternative reaction pathway with a lower activation energy and is not itself consumed in the reaction, allowing it to be recovered at the end of the reaction and reused. Catalysts can be applied to batch processes where the desired product is removed in groups at the end of the reaction period, or flow processes which allow for the continual removal of the product as the reaction proceeds.

There are many different types of catalysts with each having different advantages and disadvantages; often a comparison is made of the differences between the two main types: homogeneous and heterogeneous. Homogeneous catalysts can be particularly advantageous as they are in the same phase as the reaction mixture, which allows for a high degree of interaction between the catalyst and reactant mixture. Secondly, they can be very selective towards the formation of the product. Unfortunately, there are significant disadvantages to homogeneous catalysts; whilst occupying the same phase as the reactant mixture is a desirable property, leading to a high degree of interaction, it also means it is very difficult, and sometimes impossible to recover the catalyst at the end of the reaction. Additionally, by occupying the same phase as the reaction mixture, they can often be limited by the solubility of the reactants and the products in the solvent.

Alternatively, heterogeneous catalysts occupy a different phase to the reaction, thus allowing for the easy separation from the products and can easily be adapted to a continuous flow process instead of batch processes. Furthermore, heterogeneous catalysts often prove to be more stable and therefore more resistant to deactivation than homogeneous catalysts. However, there are drawbacks as heterogeneous catalysts can be limited by the surface area of the catalyst and the rate of diffusion of reactants and products both to and from the surface of the catalyst.

Even within these groups there are further differentiations such as inorganic and organic catalysts. This thesis concentrates on inorganic catalysts, of which the two most common types are nano-particulate and microporous catalysts. Nano-particle catalysts comprise of small particles, commonly consisting of precious metals, with a diameter, typically 2-5 nm and deposited upon a support medium such as carbon, metal-oxides, or even microporous materials; although we note that nanoclusters and even single metal atom catalysts are increasingly topical. Microporous materials also consist of various types: aluminosilicates more commonly referred to as zeolites; alumino-phosphates (AlPOs) and Metal Organic Frameworks (MOFs). The focus of this dissertation is primarily on the first two; AlPOs and zeolites; however, several zeolites may be obtained as pure silica systems, and much of our work will focus on these systems.

1.0.1 Microporous Materials

Microporous materials are framework structured crystalline solids with pores of molecular dimensions (usually in the range 2 – 12 Å). Zeolites can be defined as microporous crystalline frameworks, comprising corner shared aluminosilicate tetrahedra (AlO_4 and SiO_4). Pure silica frameworks are charge neutral; however the inclusion of AlO_4 tetrahedra introduces a charge deficit in the framework resulting from the Al(III) cation. Extra-framework cations compensate the charge deficit and are therefore introduced to restore electroneutrality to the system. Protons are often used to achieve this charge compensation by bonding to the bridging oxygen atoms between tetrahedra and forming a Brønsted Acid Site (BAS) and can play a key role in the catalytic behaviour of zeolites within a multitude of reactions. Alternatively, different metal ions can be introduced to the system as extra-framework cations to achieve electroneutrality.

Microporous crystalline materials can also be formed from AlO_4 and PO_4 tetrahedra forming a class of materials denoted AlPOs, which maintains the same general formula of TO_2. In a perfect lattice the Al(III) and P(V) T-sites alternate, however defects can form whereby this strict alternation is broken upon the introduction of a cation of a different element or terminate with the formation of P-OH or P=O groups.[1] Like zeolites, AlPOs exist in a diverse range of structures and compositions with pore sizes equal to molecular dimensions.

Zeolites occur in nature but can also be synthesised using hydrothermal techniques.[2] There are a wide range of framework topologies comprising of pores with various dimensions. Some typical structures are shown in ***Fig. 1.1.***, including zeolite ZSM-5 (MFI), Zeolite-A (LTA) and Zeolite-Y/Faujasite (FAU), and we note that a three-letter code is used to denote zeolite structural types (e.g. that of ZSM-5 is MFI). We pay particular attention to ZSM-5, which contains two sets of perpendicular and intersecting channels. These channels are formed by 10-membered and 8-membered rings, as shown below in ***Fig. 1.1***.

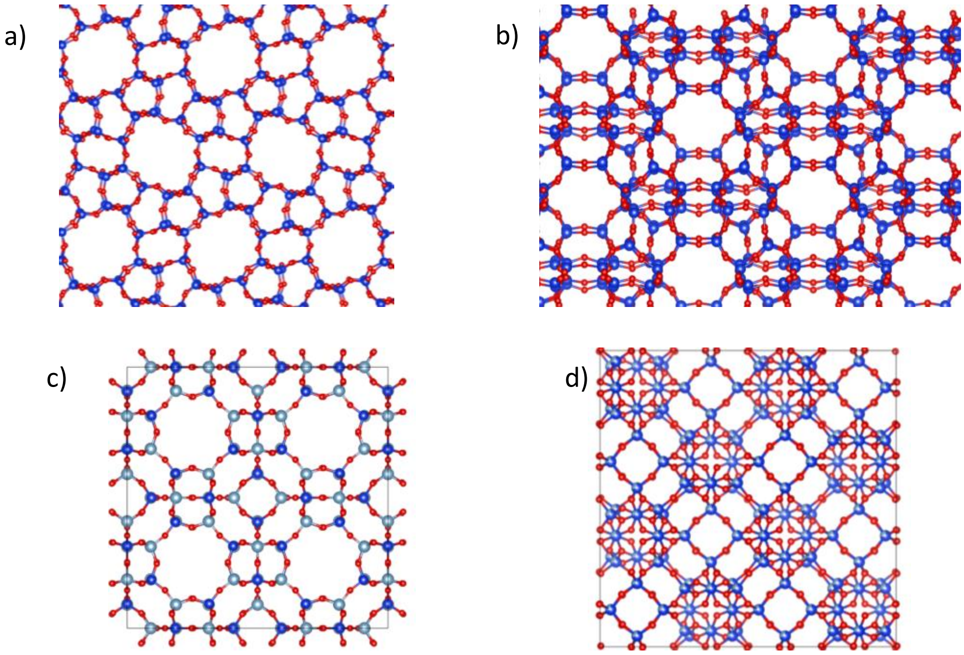

Fig. 1.1. ZSM-5 structure with 10-membered rings (a) and 8-membered ring (b) channels. Bottom: (c) LTA zeolite and (d) Zeolite-Y/FAU, both contain aluminium within the framework. Atom colours are: Si: dark blue, Al: light blue and O: red.

1.0.2 Brønsted Acidity

Brønsted acidity is a key property for many microporous catalysts and arises from the inclusion of a proton as the extra-framework compensating cation in a microporous material, as mentioned in the previous section 1.0.1. In zeolites, a Si(IV) cation, with a formal charge of +4, is often substituted by an Al(III) cation, with the formal charge +3, resulting in a charge deficit of -1. The formal +1 charge of the extra-framework proton compensates this deficit when binding to one of the oxygens surrounding the aluminium, which is, however, more difficult to achieve in AlPO systems due to the inherent nature of the alternating tetrahedral units, with 3 and 5 valence. The typical solution is the isomorphous substitution of the P atom by a Si(IV) atom forming a SAPO structure, or by substituting the Al(III) by a divalent cation (M(II)) such as Mg(II), Mn(II), Zn(II), Co(II) to form a MAPO structure. MAPO structures hence exhibit improved catalytic activity as a direct result of these negative charges, stemming from the charge deficit, allowing the introduction of Brønsted acid sites (BAS).[3–5] A general scheme for the generation of Brønsted acid site structures for these different materials is illustrated in **Fig. 1.2** below.

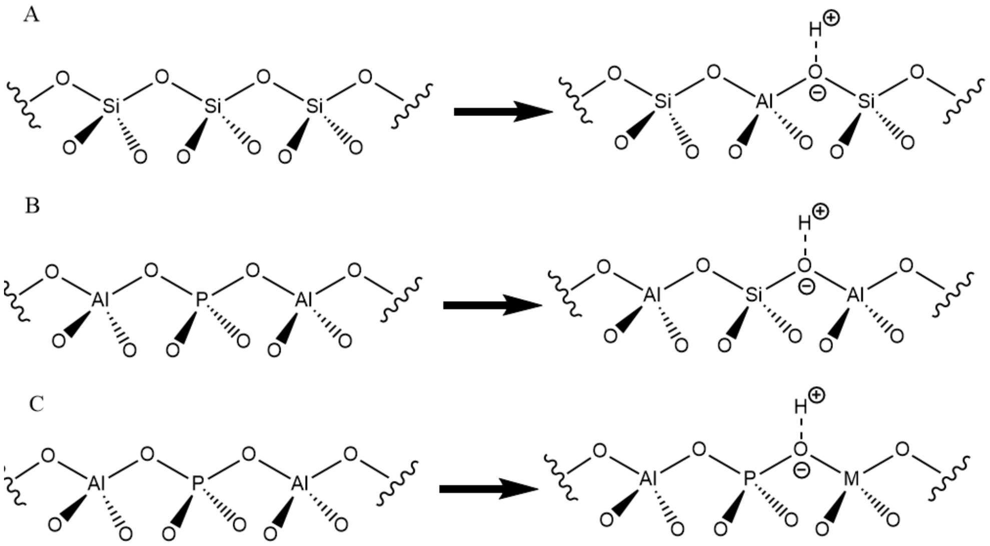

Fig. 1.2. Diagrams representing how framework substitutions lead to a negatively charged framework, which can be compensated by introducing a Brønsted acid proton in a zeolite (A), AlPO (B) and a MAPO (C).

Alternatively, aluminophosphates can generate a BAS by creating an anionic open framework that is then compensated by a proton. These materials are formed by a one-dimensional chain of alternating AlO_4 and PO_4 tetrahedra with two-dimensional layers that extend the networks, and a three-dimensional open framework with an Al/P ratio below 1 due to the existence of terminal P-OH or P=O functional groups.[6] The negative charge on the resulting frameworks can be compensated by a proton transferred from a protonated amine molecule which is used as a template. Unfortunately, once these templates are removed through calcination, the structure becomes unstable. However, Yan *et al* were able to synthesise AlPO-CJB1 which was able to retain its Brønsted acidity once the template was removed.[7]

Zeolites have been utilised for an extensive range of industrial processes, with arguably the largest application being the catalytic cracking of long chain hydrocarbons to shorter chain hydrocarbons used for fuel. Commonly zeolite-Y/Faujasite (FAU) is used for this purpose as it contains a Brønsted acid site which forms the active site for the catalytic cracking process.[8] Zeolites can also be used for isomerisation reactions, specifically the ZSM-5 zeolite, which is used for hydrocarbon isomerisation reactions[9–11] and the conversion of methanol to gasoline and diesel.[12,13] The TS-1 catalyst has been routinely involved in redox reactions by incorporating Ti into the framework so that its variable oxidation states can facilitate redox reactions where Si and Al otherwise could not.[14,15] Other catalytic uses of microporous materials include hydrocarbon synthesis from CO_2,[16] and a variety of other oxidation reactions such as the oxidation of Volatile Organic Compounds (VOCs).[17]

A key feature of microporous materials is their intrinsic ability to control the size and shape of product distributions via shape selectivity caused by the steric constraints they place upon molecules in a reaction.[18,19] Finally, we note that there are other major applications of zeolites including gas separation[20–22] and ion exchange.[23–25]

This thesis explores several aspects of the structure, stability and chemistry of microporous materials using a range of computer modelling methods. We examine first the framework energetics, where we can make a comparison with experimental calorimetric data; second, the stability and reactivity of extra-framework transition metal cations and thirdly, the structures, dynamics, and spectroscopic signatures of sorbed water molecules in proton and cation exchanged systems. The computational techniques employed will be introduced in the next section.

1.2 Computational Techniques

The advent of computational technology created an opportunity to assist with the modelling and understanding of chemical systems. In the earlier days computational power was very limited compared to modern hardware and software capabilities, and as such approximations to models had to be made to perform calculations in reasonable time frames at the cost of accuracy. This led to the development of interatomic potential methods based on classical Newtonian mechanics for solid state systems. Due to the ordered nature of zeolites, as well as alumino-phosphates, this approach provided a prime opportunity for developing computational models as both a modelling and predictive tool for molecular design. The fields of both computational modelling and zeolite theory have since greatly benefited from the development of High-Performance Computing (HPC) technologies, allowing for the utilisation of quantum chemical techniques employing large scale parallel processing. Indeed, computational methods have hence become a standardised practice in most areas of scientific research.

The practice of computational modelling has been incorporated into many areas of chemistry, but possibly none greater than catalysis. With these models it is now possible to provide predictions of a plethora of different aspects within the field such as active site structures, transition state energies, lattice energies and system entropy and dynamics among many others. One area that attracted a lot of interest in catalysis is the study of highly ordered porous materials, of which the most intensively studied are zeolites. It is of no coincidence that the history and development of computational techniques has evolved in parallel with the study of these highly functionalised materials.

1.2.1 Computational Techniques Applied to Modelling Zeolites

1.2.2 Interatomic potential based methods

In the early development of computational techniques there was a strong incentive to develop reliable potential based methods for modelling silicates, which would allow for reasonable predictions for structural defects and the cohesive energies of silicates and how they are influenced by temperature and pressure. A classical Born model with formal ionic charges and including a pair potential description was initially developed to successfully model pyroxenoids.[26] This model provided a crucial starting point which was then developed for the predictive modelling of other solid-state materials via energy minimisation calculations.[27,28]

As a result, ordered crystalline materials offered the appropriate system from which to develop computational techniques, and indeed many early studies have involved highly ordered silica in the form of α-quartz. One of the earliest developed techniques was to model silica using interatomic force-field potentials which subsequently became common practice, owing to its effectiveness and low computational cost. Interatomic potentials were derived in various forms, but arguably the most common form were “Buckingham potentials”.[29] These potentials, which are discussed in more detail in Chapter 2, are a means to describe both the Pauli repulsive and the van der Waals attractive energy of an interaction between two atoms that are not directly bonded to each other as a function of interatomic distance, referred to as an empirical two-body model and provided the parameters are fixed by reference to experimental data.

Limitations to this empirical two-body model later became apparent as it encountered problems when it was discovered it could not accurately model the elastic, dielectric and dynamical properties of certain structures including α-quartz.[30] In due course Sanders *et al*[31] set out to elaborate on this potential based model by including a three-body and bond-bending terms that would accommodate torsion between bonding tetrahedral units. This proved to be very successful and acted as a crucial step to modelling α-quartz and various other silica polymorphs. These were assessed against the energetics of other silica structures, namely coesite and α-cristobalite to validate their accuracy.[31]

In a paper by van Beest *et al,*[32] bulk force-fields were developed initially based off *ab-initio* calculations on small clusters that were representative of the finite system; they omitted the bond-bending terms that had been employed by Sanders *et al,*[31] and also used partial rather than formal charges. These cluster calculations were shown to provide a logical starting point for the development of bulk force-fields that would ensure near-neighbour interactions would be accurately described. However, the range of these interatomic potentials extends beyond the range of these nearest neighbours, and so it becomes crucial to include information of the finite system into the derivation of these force-fields. However, the accuracy of a force-field that is derived from cluster information may be uncertain when applied to bulk silica. When modelling larger clusters such as $H_6Si_2O_7$, the effects of short-range interactions could only properly be accounted for across inter-tetrahedral distances when modelling the bulk system. When using potentials derived in this manner, using empirical data, to model other silica polymorphs such as α-cristobalite, coesite, stishovite and molecular sieve silicalite, they were found to be more accurate than earlier partial charge potentials derived by Tsuneyuki[33] by a factor of two, thus, proving that the incorporation of α-quartz data when fitting the potential (using empirical data) enhances the potentials' ability to model extended structures. This type of potential and approach for parameterisation was also found to transfer relatively well to $AlPO_4$ systems with similar discrepancies between theory and experiment for both structural and elastic properties.[32]

The application of interatomic potentials continued to prove useful, yielding accurate energetic and structural data with available computational power and over time became more widely adopted into regular practice. The potentials derived by Sanders *et al*[31] have also continued to prove popular due to their relative accessibility and transferability to other, larger, zeolitic silica structures, which resulted in a broad range of studies on various silica and aluminosilicate zeolites, such as the work by Jackson *et al*[34] who investigated framework structures and stabilities, as well as the position of extra framework cations. Using these interatomic potentials, the minimum energy configurations for Faujasite, Zeolite A (LTA), and Silicalite (ZSM-5/MFI) were investigated, and the observed structures were accurately reproduced.

1.2.3 Quantum Mechanical Techniques

As computational power evolved, so too did the field of computational chemistry, resulting in more advanced models operating under higher levels of theory, making quantum mechanical modelling feasible on larger systems. The most common method which utilises these highly intensive calculations is Density Functional Theory (DFT). DFT involves the calculation of the electron charge density with self-consistency from the iterative derivation of molecular orbitals.

The one-electron states used to construct the electron density for these calculations are derived from a potential that includes coulomb and electron exchange correlation terms dependent on all electrons in the system. Any change to the one-electron wave function that lowers the energy of a particular electron will subsequently change the potential for all the electrons in the system. To account for this the wave function and potentials are calculated in an iterative manor until no significant changes are found, therefore becoming self-consistent and satisfies the Kohn-Sham equations. Importantly, for this thesis, DFT has been shown to reproduce the properties of microporous zeolites with a high degree of accuracy.

DFT has proven to be a reliable and widely used method for modelling zeolitic structures and has led to accurate predictions of structural stabilities and mechanical properties.[35-36] A large selection of studies has been very comprehensively covered in review articles over the years, including those by Van Speybroek *et al.*[37,38] These literature reviews cover numerous studies involving the use of DFT to effectively model different structures such as: SOD, LTA, CHA, MOR and MFI and benchmarking against α-/β-quartz, α-/β-Cristobalite and β-Tridymite, yielding results with excellent agreement to experimental data. Calculations were performed using DFT-LTA plane-wave pseudopotential techniques to determine the equilibrium geometries, elastic properties, and cohesive energies. The latter of these three appeared almost independent of the structure used, despite large variations of Si – O – Si angle distributions among the zeolites. Large elastic anisotropy was observed along with a strong dependence on network constraints and space group for the bulk moduli, which determines whether Si – O – Si angles can relax cooperatively to mitigate stress, crudely modelled in the potentials method as covered earlier. Questions posed over whether the polarisation of the Si – O bond varies per T-site, or whether they can be structure dependent, were relegated to future work. The paper also concludes that for empirical potentials to be transferable, the cohesive energy differences should be small whilst bulk moduli are large.

A common practice is the use of DFT in the characterisation of acid sites. In a study by Lo and Trout,[39] DFT was utilised to investigate four distinct areas in order to characterise the acid sites in the commonly used zeolite: chabazite (CHA). These calculations aimed to determine the deprotonation energies, adsorption energies of bases both weak (methanol and acetonitrile) and strong (ammonia and pyridine), OH vibrations and the topological visualisation of electron localisation functions. Whilst utilising geometry optimisations and Electron Localisation Functions (ELF), Lo and Trout were able to distinguish two proton positions which yielded an energy-minimum on the oxygen atoms located at the acid sites.

The deprotonation energies were revealed to be approximately the same for the four acidic oxygens at the aluminium T-site, which would be expected due to their similar chemical environment but did not correlate to OH bond length or stretching frequency. The adsorption energies of the various bases and these acid site oxygens were again similarly universal and based more upon the proton affinity of the particular base used.

A study conducted in 2001 by Soscún *et al,*[40] attempted to define an acidity scale based on the 'intrinsic acidity' of O-H groups, defined by the ratio between O-H distance and the frequency of the corresponding vibrational mode. A linear correlation between this 'intrinsic acidity' and the total charge was observed for zeolite cluster models. Unfortunately, this 'intrinsic acidity' did not correlate to the adsorption energies for the periodic models in the Lo and Trout study.[39] Small differences in the calculated intrinsic acidities indicated the four acid sites were approximately the same. Thus, ultimately leading to the conclusion of the problematic validity and usefulness of the intrinsic acidity factor as a quantification of zeolitic acidity. Upon the inclusion of Al atoms into the framework, neither deprotonation energies nor base adsorption energies significantly change, a result that was replicated with implementing defects near the acid site. This study clearly demonstrates DFT's applicability and versatility for a diverse range of studies, as four different areas were analysed, and a large amount of accurate information was determined from this singular calculation method.

Another example in which the structure and Brønsted acidity of a zeolite were studied using DFT is in the work of Wang *et al.*[41] This study investigated these properties in a similar manner as previously discussed, but in relation to one specific zeolite, optimised T-MCM-22 (where T is a dopant B, Fe, Ga or Al), and how the proton affinity, vibrational frequencies and the charge on the acidic proton changes. The order of acidity was derived to be B < Fe < Ga < Al which was subsequently corroborated with experimental data. OH stretching frequencies transpired to be less dependent on the basis set used than the structural optimisations and proton affinities, but Al and B doped structures both gave a reasonable agreement with experimental data. Additionally, the equilibrium structure of B-MCM-22 was examined to elucidate the energetic effect that B has in the synthesis of Ti-MCM-22. Wang *et al*'s study reveals a significantly large stabilisation effect for the substitution energies of approximately 71 kJ mol^{-1} linked to the presence of the B. Once again this demonstrates

DFT's ability not only to provide accurate structural data for zeolites, but also to aid experimentalists in other areas such as zeolite synthesis.

To conclude this section, it can clearly be seen how computational techniques have developed over time, gradually becoming more complex as computational power has increased, making higher levels of theory more accessible. In turn the modelling of microporous materials has developed in parallel, which is in some cases now approaching chemical accuracy. Techniques have evolved significantly from the less taxing and simpler interatomic potential based methods, applicable to both dense and less dense metastable phases, to the more complex approaches like DFT that account for the electronic structure of the system. The huge leap in computational capability observed over recent decades provides an exciting outlook for future developments with the advent of powerful new tools such as quantum computing, machine learning and artificial intelligence entering the fray of computational materials modelling.

More details of the techniques employed in this thesis are given in Chapter 2.

1.3.0 Protons, Metals and Metal Centres in Zeolites

There are multiple ways of enhancing, or even introducing activity into heterogeneous catalysts which is often achieved by altering the structural and topological properties. With zeolites, catalytic activity is largely tied to both the structural properties (as zeolites are shape dependent catalysts) and electronic properties of the system. As such there are different approaches to altering the system including modifying the framework and introducing extra-framework species in the zeolite structure. The following section aims to highlight different scenarios where this approach has been investigated for various systems and reactions to achieve a better catalytic outcome or deeper understanding of the underlying properties of a catalyst.

Zeolite activity can stem from Brønsted acidity as previously discussed, or from Lewis acidity. Whilst Brønsted acidity is a clearly defined feature that arises from an extra-framework proton forming a hydroxyl group bridging the silicon and aluminium tetrahedra, Lewis acidity is not as clearly defined. Lewis acid sites in zeolites can be created in a similar way, by the introduction of heteroatoms such as Ti, Sn or Zr into the framework, and have subsequently been used to catalyse reactions such as aldol condensation and propylene epoxidation;[42,43] however, their synthesis procedures are complex and are often limited to certain topologies. By comparison Lewis acidic aluminium centres within zeolites are far easier to generate and are not limited by their topologies. Additionally, Lewis acid sites in zeolites are not necessarily defined by one particular structural feature as is the case for Brønsted acidity, and as such the total Lewis acidity can comprise of contributions from multiple species. As such, the determination of Lewis acid strength and structure is an area of ongoing research and debate.[44–47]

Much of the uncertainty surrounding Lewis acidity arises from the plethora of possible Lewis acid sites within a structure that occur as a result of the structural versatility of aluminium resulting in many different aluminium species within the framework. However, aluminium sites with Lewis acidic character can be generated intentionally using post-synthesis techniques including steaming, calcination at high temperatures, acid, or base leaching.[48–51] These techniques typically result in hydrolysing the framework Si-O-Al bonds, thus effectively removing the aluminium from the initial framework.[52] Alternatively, the Lewis acidity derived from the aluminium cation can be a property that is inherent to the zeolite framework without requiring any post-synthesis treatments.[44,46,47]

Furthermore, the introduction of two aluminium (IV) sites, formed with hydroxyl groups in acidic zeolite catalysts, in both dehydrated and catalytically active states can also play a role in altering the catalytic properties of zeolites, as was displayed in the work of Chen *et al.*[53] Using ultra-high field $^{27}Al\{^{1}H\}$ 2D correlation NMR, the authors were able to characterise two Al bridging sites with corresponding hydroxyl groups within the H-ZSM-5 zeolite, in both the catalytically active and dehydrated states. The resulting new Brønsted acid site is created by a second tetrahedral Al atom and the protons in the zeolite were resolved at 35.2 T. NMR studies were coupled with computational DFT models to determine that the second tetrahedrally coordinated aluminium site has an increased chemical shift combined with unique quadrupolar parameters relative to the BAS in dehydrated and hydrated states. The second aluminium site arises from a partially bonded framework $(SiO)_{4-n}Al(OH)_n$ species, and is responsible for a significant increase in the catalytic activity of benzene hydride transfer along with n-hexane catalytic cracking reactions. These $(SiO)_{4-n}Al(OH)_n$ species can be created via defects in the crystallisation or from incomplete post-synthetic hydrolysis of a framework aluminium before it forms an extra-framework species. The number of these second acidic sites was shown to be dependent on the treatment of the catalyst post-synthesis and could be transferred to other zeolite structures for enhancing other reactions.

The first example of improving catalytic performance covered in this thesis involves the utilisation of metal cations to increase the catalytic properties of a zeolite. In the study of Yu *et al*[54] the zeolite is utilised as a support medium for nano-particle based catalysts, whereby Rh_2O_2 nanoparticles are supported upon the ZSM-5 zeolite. This work provided some interesting results: supported nanoparticles with a diameter of around 2.4 nm were shown to increase the direct oxidation of methane to various oxygenates using molecular oxygen at low temperatures in the presence of CO. In addition to the catalyst's own properties, CO was also shown to play a critical and complimentary role in the promotion of CH_4 activation over the Rh-ZSM-5 catalyst, highlighting the interplay between catalyst and reaction.

The properties of Brønsted acid centres are crucially important in many areas of catalysis. An example is detailed in the works of Gonzales *et al*[55] where the addition of a charge compensating proton to an extra-framework Al in ZSM-5, can cause geometrical changes to the Brønsted acid site as well as altering the positive charge density of the aluminium atom, which leads to a reduction of the proton affinity of the acid site proton, potentially increasing the acid strength. Different aspects of the local structure and composition were also shown to influence proton affinity and the binding energies of the proton to weak bases.

Metal exchanged zeolites*,* which will be one of the themes of this thesis, are very commonly studied in catalytic applications, including the conversion of methane to methanol or methanol to BTX chemicals/hydrocarbons (MTH process). The latter is demonstrated in the works of Pinilla-Herrero *et al,*[56] where different Zn-ZSM-5 catalysts were prepared with different loadings to determine the effect on dehydrogenation vs hydrogen transfer reactions in the conversion of methanol to aromatics. This is an important area of study as light aromatic hydrocarbons, specifically benzene, toluene, and xylenes (often referred to as BTX chemicals) are intermediates commonly utilised as solvents in the petrochemical industry. Using a variety of spectroscopic techniques it was determined that catalytic activity was linked to a $[Zn(H_2O)_n(OH)]^+$ species in the system with little to no contribution from either ZnO or metallic zinc. Higher zinc content resulted in greater yields of aromatic compounds whilst keeping alkane production relatively low. Hydrogen transfer and alkane formation was favourable in systems with similar zinc content but with a higher number of aluminium sites. Thus overall, it was concluded that higher Zn/Al ratios in the zeolite tended to favour hydrogen releasing dehydrogenation reactions.

Alternatively, in the work of Yoshio Ono and Kunihiko Kanae,[57] Zn and Ga were incorporated into H-ZSM-5 to enhance the selectivity in the conversion of butane to aromatic hydrocarbons. The focus of this publication was the activation of butanes at 773K, where Zn and Ga served as the catalytic centres for the dehydrogenation of the starting alkanes, resulting in an 80-85 % conversion, whilst the remainder underwent cracking reactions on the acidic sites. This conversion understandably fell to 70 % when dehydrogenating isobutane owing to the higher stability of isoalkanes compared to straight chain or even branched alkanes. It was subsequently determined that the activation of alkanes relies heavily upon the ease at which the carbenium ion is formed and the strength of the acid site in the zeolite. The Ga-ZSM-5 system had a higher acidity which resulted in hydrogen transfer from intermediate alkenes resulting in the formation of alkanes, hence a lower yield of aromatics was observed in the Ga-ZSM-5 system than in the Zn-ZSM-5 system.

A similar study was carried out by Kowalska-Kuś *et al*[58] using iron substituted ZSM-5 for the oxy-dehydrogenation of ethane and propane in the presence of N_2O. Oxidants are strongly influenced by the strength and nature of Brønsted acid sites, due to their propensity for oxidation reactions to form light paraffins. This study demonstrated that in the presence of strong protonic sites, oxydehydrogenation reactions occur simultaneously. Alternatively, if these acid sites are removed then the route of reaction is altered and shifts to the promotion of consecutive cracking reactions and even the total oxidation of reactants.

The key influence of metal centres in zeolite catalysed reactions can be illustrated in a study by Lubango and Scurrell,[59] whereby the aromatisation of alkanes to BTX was improved from 75-80 % to over 91 %. This sizeable improvement was primarily achieved by the introduction of a second transition metal centre in an already metal doped Zn-ZSM-5. Iron and other transition metals were introduced by solid state ion exchange (SSIE), but these improvements were not seen for all compositions. The ideal zinc and iron contents were 0.5 % and 1.0 % by mass and the introduction of the iron was accompanied by restoration of substantial Brønsted acidity. This acidity is originally found in the H-ZSM-5 structure but is lost upon introduction of the Zn as was determined by temperature programmed desorption (TPD). It was hence hypothesised that selectivities towards BTX chemicals results from competition for ion-exchange sites. The evidence suggested that at higher Zn contents this competition is more likely to occur, and this competition could explain the reduction in BTX selectivity for systems with higher Zn contents. Only a few ion-exchange sites are favourable for the Iron/cations that improve the selectivity and as such the zinc also competes for these sites. High zinc content reduces the formation of the second metal centre via mutual displacement, however, attempts at introduction of iron first, followed by zinc, to circumvent this problem were unsuccessful. This led to the conclusion that iron exchange dominates and the beneficial effects of Zn are hard to obtain once iron is introduced.

1.3.1 Zeolites in Catalysis and Gas Adsorption

One area of particular interest in the realm of zeolite catalysis is their intrinsic ability to adsorb gases. Of significant importance is the adsorbance of two gases, CO_2 and methane, owing to the relative ease at which they can be converted into fuels. CO_2 is of increased interest due to the increase of CO_2 levels in the atmosphere as a direct result of fossil fuel use over the last 200 years.[60,61] CO_2 is a major greenhouse gas that significantly contributes to global warming and as such there is a strong focus on developing technology for CO_2 adsorption/desorption using natural and synthetic zeolites.

The article by Bonenfant *et al*[62] highlights some key aspects concerning CO_2 adsorption and shows that it is heavily reliant and largely controlled by the inclusion of cations; as discussed previously, these introduce basicity by bonding to the bridging oxygens in turn and modifying the electronic properties of the material and introducing Lewis base sites on the oxygen anions. These two factors can vary greatly depending on the nature, number, and distribution of cations within the framework. The basicity and electronic properties are also inherently determined by the zeolite framework itself and vary with the Si/Al ratio. Adsorption of CO_2 can be limited by the pore dimensions and the subsequent carbonates that are formed during adsorption. Furthermore, the polarity of an adsorbing molecule can also play a crucial role on the Lewis basicity of a material. Molecules that contain a significant quadrupole moment, such as CO_2, can interact strongly with zeolites depending on the zeolite's electronic properties creating favourable conditions for adsorption. External factors such as temperature and pressure in experimental conditions will, of course, influence the extent of CO_2 adsorption, with, as expected an increase observed with gas phase pressure and decrease with temperature. In relation to later chapters in this thesis, we note that the presence of water can significantly decrease the ability of cationic zeolites to adsorb gases as the water molecules can shield the cations and also promote the formation of bicarbonates.

Several industrial processes require the separation of CO_2 from N_2, and zeolites are commonly used for this purpose. The high tunability of zeolites allows the alteration of adsorption properties, particularly by introducing extra framework cations as discussed previously. As such a study by Hudson *et al*[63] investigated the propensity of Chabazite (SSZ-13) in both an acidic form and a copper-exchanged form, to separate CO_2 from N_2 based on the adsorption properties of these structures. Ideally the adsorption selectivity should exceed 70 % to mark an improvement to the adsorption properties from the unmodified zeolite. This study found that the heat released when adsorbing CO_2 (isosteric heat of adsorption) was 33.1 kJ mol^{-1} for Cu-SSZ-13 and 34.0 kJ mol^{-1} for H-SSZ-13. Utilising *in situ* neutron powder diffraction the propensity towards CO_2 over N_2 was attributed to the differences in the binding sites for the two gases. The binding site for the CO_2 was elucidated and found to be in the centre of the 8-membered pore ring, leading to important implications for gas separation using zeolites, as the binding mode had not previously been observed and is responsible for the high selectivity of CO_2 over N_2.

The pore size has also been found to be an important factor for CO_2 adsorption in other studies. The crucial role of porosity was further highlighted in a study by Chen and Ahn,[64] who used X-ray powder diffraction, N_2 adsorption-desorption isotherms and scanning electron microscopy (SEM) coupled with energy dispersive X-ray spectroscopy to assess the effect of mesoporosity in CO_2 adsorption in LTA zeolites. The LTA zeolite was prepared using dimethyloctadecyl[3-(trimethoxysilyl)propyl] ammonium chloride, which is used as a structure directing agent to obtain the mesoporous structure, resulting in LTA structures containing mesopores of around 9 nm diameter. This study found that rapid gas transport occurred within the zeolite, with faster CO_2 adsorption kinetics than that of the microporous LTA at 298 K under 1 bar. It was also shown that the CO_2 uptake of the mesoporous structure surpassed the microporous structure under higher pressures, more than 10 bar, which was attributed to a combination of both the effect of the mesopores and the larger pore volume.

The adsorption of methane is also of particular interest. Unlike CO_2, methane does not benefit from a quadrupole that can assist with adsorption but does have hydrogen atoms which can form weak hydrogen bonds to the oxygen atoms in the wall of the pore. However, when studying the adsorption of different gases such as methane, CO_2 can often provide a useful reference point as is the case of the work of Choudhary and Mayadevi.[65] This study investigated the thermodynamics of adsorption for methane, ethane, ethylene and CO_2 on silicalite-I using a gravimetric adsorption apparatus. The overall heat of adsorption was determined to be in the order $CH_4 < CO_2 < C_2H_4 \leq C_2H_6$. Methane and ethane adsorption isotherms at 305 K and 453 K respectively were found to fit the Dubinin-Polanyi equation, which considers a pore-filling mechanism instead of a layered surface coverage,[66] whilst isotherms for methane and CO_2 at 353 K, and ethane at 453 K were found to fit the Freundlich equation that relates solute concentration to the adsorption onto a surface.[67] The Langmuir isothermal model, which relates adsorbate concentration in solution with surface coverage of the adsorbent, whilst also assuming the reversable adsorption of an ideal gas,[68] was found to represent ethylene at temperatures of 305 K and 353 K and CO_2 at 305 K. The isosteric heat of adsorption for all gases was determined to be between 18 and 32 kJ mol^{-1} with ethane yielding the highest value. It was also determined that the heat of adsorption is not significantly influenced by the surface coverage of the gases, except for methane which exhibited a notable decrease in the heat of adsorption with a concomitant increase in loading. Furthermore, the mobility of adsorbed methane increased with increasing loading whilst it decreases for the other adsorbates.

Further to these studies, adsorption properties can be modelled using molecular simulations to provide accurate predictions for experiments. One example which assesses the ability to model adsorption against experimental data, is the study by Macedonia *et al*[69] which specifically modelled the adsorption of methane, ethane, and argon in sodium mordenite (Na-MOR). The adsorption properties were investigated under ambient and cryogenic conditions (87.3 K) experimentally and using Grand Canonical Monte Carlo (GCMC) simulations using different Na-MOR samples with Si/Al ratios of ~5 and ~9, with an additional purely siliceous structure and varying the crystal symmetry from Cmcm to Pbcn. The GCMC modelling yields a good agreement with experiment at ambient temperatures with minor differences between computed isotherms resulting from the different crystal symmetries.

Despite these slight differences, the adsorption properties of argon exhibit different behaviours at 87.3 K, with the Pbcn structure giving a better agreement with experimental results. It was hence determined that the cryogenic adsorption can be sensitive to the slight structural differences of the zeolite lattice. Additionally, the inclusion of cations and framework aluminium species with realistic charge distributions was a prerequisite for the simulations to accurately match the experimental results.

Further computational studies including the work of García-Pérez *et al*[70] sought to model the adsorption of CO_2, N_2 and CH_4 within all-silica zeolites. Adsorption isotherms were modelled using GCMC methods and measured for single molecule sorbates within MFI, which resulted in a good agreement with experimental adsorption isotherms. Additional simulations were carried out over a wide range of temperatures and pressures for single sorbates, binary and ternary mixtures of different compositions. The selectivity towards adsorption was carried out for 50:50 compositions of CO_2/CH_4 and CO_2/N_2, a 10:90 ratio of CO_2/N_2, and a 5:90:5 mixture of $CO_2/N_2/CH_4$ for a selection of six systems (MFI, MOR, ISV, ITE, CHA and DDR). Selectivity was shown to be very high towards the adsorption of CO_2 over N_2 and even CH_4 in both binary and ternary mixtures, but the extent of the selectivity can vary depending on the type of crystal and the bulk composition. This study proved the powerful and versatile nature of computational models for predicting adsorption behaviour of multicomponent mixtures for varying temperatures, pressures, and bulk chemical compositions.

1.3.1 Computational Modelling of Acid and Metal Centres in Zeolites

With such a complex interplay between various effects in catalytic processes, the use of computational methods can play a pivotal role in understanding how these various effects influence a catalytic system. The work of O'Malley *et al*[71] utilised hybrid quantum mechanical molecular mechanical (QM/MM) techniques as an embedded cluster model for H-ZSM-5 and H-Y (Faujasite). This study involved modelling the energetics of deprotonation, methanol adsorption and methoxylation in the two zeolites with acid sites in three main sections of the structure: the straight channel, sinusoidal channel, and intersection region of H-ZSM-5. Faujasite was shown to have the lowest deprotonation energy followed by the straight channel site in H-ZSM-5. However, in the case of methanol adsorption the reverse result was observed, as can be explained by the adsorbed system geometry which allows two of the methyl hydrogens to form hydrogen-bonds to the framework oxygens. Thus, it was proposed that this behaviour could be a dominant factor influencing adsorption energy. Faujasite was again shown to give one of the lowest methoxylation energies, however the intersection site in H-ZSM-5 was lowest overall. The combination of these factors suggested that the total exothermicity of methoxylation is not dependent on the methanol adsorption energy, but rather that the framework coordination was a considerable factor as the increased hydrogen bonding resulted in the lowest energy configurations.

Additional computational studies by Nastase *et al*[72] sought to gain more insight into the mechanism of methylation by H-ZSM-5 with *ab-initio* molecular dynamics. Nastase *et al* investigated the influence of higher methanol loading and acid site density during the initial stages of the MTH process. The results showed the formation of methanol clusters around the active site and allowed for the deprotonation of the Brønsted acid site, resulting in charged methanol clusters that had been stabilised around the site, indicating that the number of methanol molecules within the cluster can influence their distance from the active site. This stability is hence impacted by the introduction of a second acid site within close proximity to the first, resulting in favourable methylation of the framework. Combining the effects of higher methanol loadings and acid site density can also lead to more favourable pre-organisation patterns for methylation pathways. Conversely for low methanol loadings, it was observed that the reaction barriers varied with acid site density but can be significantly lowered at high acid site density, due to the concerted interactions between the acid sites. It was deduced that the confinement effects of the pore coupled with the number of additional methanol molecules plays a smaller role in cluster stabilisation than was previously anticipated from the experimental data. It was suggested that there is a different type of acid site at play resulting from additional framework defects or aluminium content, or from a higher acid density influencing the methoxylation process, but elucidation of this effect would require further research.

In the same year as the earlier work of O’Malley *et al*, another computational study was published by Mahyuddin *et al*[73] who modelled the direct conversion of methane to methanol via ZSM-5 exchanged with four different metal centres: Fe, Co, Ni and Cu. This study utilised the plane wave VASP Density Functional Theory (DFT) code,[74–78] which will be discussed further in Chapter 3. The results of these calculations indicated that the reactivity towards the C-H bond dissociation increases from Co to Ni to Fe to Cu, however the trend in selectivity followed the order of Fe < Co < Ni < Cu. This study also indicated that ZSM-5 exerts a confinement effect that causes the adsorption of methane to destabilise and thus lowers the activation energy for the dissociation of the C-H bond. Furthermore, it demonstrated that the direct conversion of ethane to ethanol has a higher product selectivity and lower C-H bond activation when using FeO^+ZSM-5. The role of ZSM-5 on the catalytic activity of MO^+ species was compared to the results of the gas phase calculations carried out by Shiota and Yoshizawa,[79] which are outlined below.

The Shiota and Yoshizawa study[79] utilised DFT to study methane to methanol conversion using first-row transition-metals. The conversion of methane to methanol by MO^+ complexes occur via two transition steps as outlined below:

$$MO^+ + CH_4 \longrightarrow OM^+(CH_4) \longrightarrow \left[TS\right]^{\dagger} \longrightarrow HO\text{-}M^+\text{-}CH_3$$

$$HO\text{-}M^+\text{-}CH_3 \longrightarrow \left[TS\right]^{\ddagger} \longrightarrow M^+(CH_3OH) \longrightarrow M^+ + CH_3OH$$

This study modelled the potential energy surfaces (PES) for both low-spin and high-spin scenarios. From these calculations it was determined that some spin inversion can occur where potential energy surfaces cross and thus can play a crucial role in reducing the energy barrier for transition states. The MO^+ complexes of the early transition metals (Sc, Ti & V) exhibited a large energy barrier for conversion of methane to methanol and as such would not act as effective catalysts, whilst the later transition metals such as Fe, Ni and Cu suggested a much more viable reaction pathway for efficient conversion. In the case of the CuO^+ complex, the conversion pathway was downhill in terms of energy profile, and it was concluded that it would make for a good mediator for methane hydroxylation due to this large exothermic character. Therefore, the non-adiabatic process, in which electrons cross from low to high spin and vice versa, were shown to play a pivotal role in lowering the activation energies of the transition states.

A more recent application is the use of charge compensating metal cations to influence the coordination and subsequent activation of molecular oxygen. The activation of molecular oxygen is a topic of interest for the direct conversion of methane to methanol, to later be used in the conversion of methanol to hydrocarbons (MTH). Many different transition metal ions (TMIs) have been incorporated into zeolites to achieve this, such as copper, iron and manganese. Oxygen activation can be achieved using different oxidants such as N_2O, O_2 or even H_2O_2 and have been summarised in the 2009 review by Smeets *et al.*[80]

The difficulty of using TMIs for oxygen activation lies in trying to prevent the over-oxidation of methane to carbon dioxide, as carbon dioxide formation results in a lower methanol yield. To circumvent this problem, the process could be treated as stepwise, comprising of three separate steps: catalyst activation, the reaction of the methane and the extraction of the methanol using either steam or a solvent. This way methane can be selectively oxidised by a catalysed reaction whilst preventing the over-oxidation of the chemisorbed intermediate, resulting in highly selective methanol yields.[81,82]

This stepwise approach has been investigated for Cu exchanged zeolites and involves the pre-activation of a catalyst by an oxidant at fairly high temperatures. Reducing these high temperatures is crucial for achieving a more green and sustainable chemical reaction. DFT has been employed by Mahyuddin *et al*[83] to model the activation of oxygen over copper doped Mordenite (MOR). Specifically, they modelled multi-copper centres which had been previously observed experimentally using Raman spectroscopy; the two active site motifs were the $[Cu_2(\mu\text{-}O)]^{2+}$ and $[Cu_3(\mu\text{-}O)]^{2+}$ (bimetallic and trimetallic sites),[84] with the bimetallic site at twice the concentration, $2[Cu_2]^{2+}$, of the trimetallic site. These calculations yielded interesting results in which two possible reaction routes were discovered: the first involves the cleavage of the oxygen-oxygen bond, leading to an activated $[Cu_2(\mu\text{-}O)]^{2+}$ species and a trans-μ-1,2-peroxo-Si_2 species; the second involves the simultaneous formation of two adjacent $[Cu_2(\mu\text{-}O)]^{2+}$ active species. Whilst both routes were exothermic the oxygen-oxygen bond activation energies were different, which subsequently led to the proposal of a peroxo-Cu_3O intermediate species with two transition states: The first arises from the rearrangement of the tri-copper species and the second involves the cleavage of the peroxo bond. The former transition state was found to have the highest energy barrier, thus providing the rate-determining step and specifically the tri-copper reaction was found to be more endothermic than the bi-copper reaction pathway.

A novel discovery was made in 2020 in the work of Bunting *et al*[85] whilst investigating mechanisms for the selective oxidation of methane to methanol over a single Rhodium atom supported on ZSM-5. One of the mechanisms investigated was the metal oxo route involving the addition of methane across a Rh=O species forming an Rh(CH_3)OH species. DFT calculations were performed on an oxidative addition pathway, metal oxo pathway (Rh=O) and the Hydrogen 'X' Reductive Elimination (HXRE) pathway using [Rh(O_2)] for a system 'X'. All the oxygen promoted pathways encounter large activation energy barriers; however, those from the metal oxo species were notably lower in energy than expected at 1.24 eV. Contrasting the Cu and Rh zeolite system it was determined that the Rhodium metal oxo-species was 1.65 eV more favourable than the Copper oxo formation, indicating a relatively low likelihood of formation of the latter system. This discovery is a very promising step for research into an alternative partial oxidation pathway and metal exchanged zeolite catalysts.

In 2022, another study explored a similar topic for the selective oxidation of methane to methanol with diatomic oxygen using Au-ZSM-5. The works of Qi *et al*[86] utilised DFT calculations with a PBE functional[87] and a D3 dispersion correction[88] to model both stepped surfaces using periodic slabs, but also an extra-framework Au(I) cation in the pore of ZSM-5. A common aspect that was shared across these different structures is that the adsorption of diatomic oxygen is concomitant by the donation of an electron from the metal cation to produce an activated O_2^{-}* radical, that forms a surface bound super-oxo species. However, for the purposes of this introduction the focus is directed towards the extra-framework cationic Au(II)O_2-ZSM-5 system. Whilst this species was capable of readily activating O_2, it was found to lack a redox centre in close enough proximity to bind to the distal oxygen. As such Au(III)O-ZSM-5 formation could only occur by the abstraction of hydrogen from the methane molecule, which was unfortunately found to be obstructed by a large energy barrier of approximately 140 kJ mol^{-1}, and as such was probably not a viable pathway for methane to methanol conversion.

Around the same time as the Bunting *et al*[85] study, a paper was published by Tabor *et al*[89] in which the dissociation of dioxygen was investigated over a catalytic system designed to mimic the functionality observed in enzymes. This study applied DFT to model two Fe(II) cations (binuclear) in two adjacent ß sites of Ferrierite forming two Fe(IV)=O^{2+} species. A gaseous triplet state O_2 molecule was shown to adsorb to one of the cations forming a monodentate complex, whilst the O_2 molecule remained in the same spin state.

This coordinated O_2 can then follow one of two pathways: the first involves a spin crossover resulting in a $[FeOO_{mono}…Fe]$ monodentate complex with the O_2 now in a singlet state, or it could rearrange its geometry to form a $[FeOO_{bi}…Fe]$ bidentate complex. With the formation of the latter, a change in spin state is observed, whereby the coordinated O_2 again occupies a singlet state. Oxidation typically occurs from the bidentate complex that is most stable, subsequently rearranging to the monodentate complex, which then places the coordinated oxygen into a more favourable position, allowing it to interact with the second Fe(II) site. This process leads to cleavage of the oxygen-oxygen bond via an [Fe-O-O-Fe] transition state at 104.5 kJ mol^{-1} to form two Fe=O sites. The key point is that this oxidation reaction is easy to achieve but would be slower than with N_2O, owing to the energy barrier to dioxygen cleavage at the Fe-O-O-Fe transition state being 43.5 kJ mol^{-1} lower than is observed with molecular oxygen. Whilst this system is reminiscent of the active site found in methane mono-oxygenases, the mechanism and oxidised structures are significantly different, owing to the separation of the two oxygen atoms formed from the oxygen bond cleavage, facilitated by the distance between the iron cations and the rigidity of the zeolite's framework.

As previously mentioned, enzymes have a propensity to hydroxylate the relatively inert C-H bonds of ethane at room temperatures, however, iron active sites in other zeolites have also shown considerable promise. In the work of Snyder *et al*[90] the influence of steric effects of constricted pore aperture sizes, acting as cages, were investigated for the methane hydroxylation mechanism for the two zeolites: Chabazite (CHA), and the partially disordered intergrowth zeolite Beta (*BEA). Snyder proposes that both zeolites can accommodate the extra-framework Fe cation in a six-membered ring which forms the iron-oxo, Fe(IV)=O, species thought to take part in the oxidation reaction. Both zeolites contained similar Si:Al ratios, iron loadings and cage diameters. Despite this similarity the two zeolites exhibited a significant difference in terms of the accessibility of their active sites. The Fe containing zeolite *BEA has an Fe(IV)=O site that can be accessed through its large 12-membered ring channels, whereas in CHA this Fe(IV)=O site is located within a cage, despite which, the cage in CHA has the dimensions of 11 Å and *BEA's channel size is 10.6 Å and is therefore a similar size; the difference comes in the form of the aperture to the pore with CHA's diameter being 3.7 Å whilst *BEA's is 5.9 Å as illustrated in **Fig. 1.3** below.

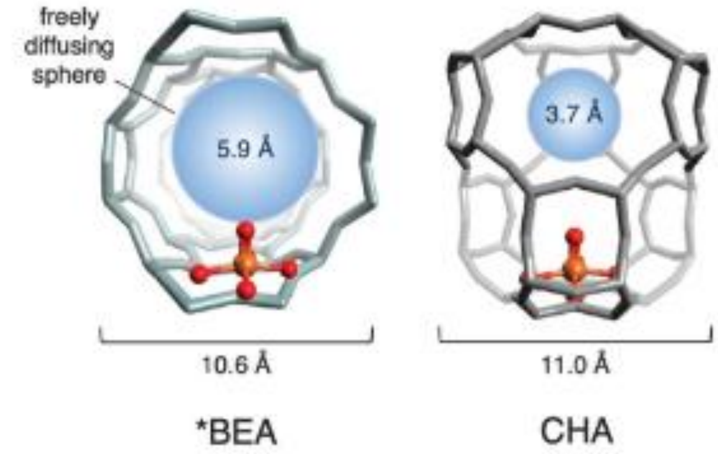

Fig. 1.3 Comparison of pore aperture dimensions between the intergrowth *BEA and CHA.[90]

These two zeolites were studied using a series of stoichiometric reactions involving the activation of reduced Fe(II) sites by N_2O which inserts α-oxygen atoms. Subsequently, one of the activated Fe(IV)O sites then abstracts a hydrogen from the methane molecule, creating both a hydroxyl group on the iron site and a methyl radical species. The Fe(II) site is regenerated if the methyl radical rebinds to the Fe(III)OH site, thus the overall catalyst is also regenerated. However should the methyl radicals diffuse away from the site, they can become trapped by neighbouring sites forming inert Fe(III)OCH_3 sites. This radical trapping is particularly inconvenient since the Fe(III) sites cannot be re-oxidised by the N_2O under the reactions mild conditions and in the case of *BEA the ratio of radical escape is large compared to radical rebinding. This radical diffusion is somewhat restricted in CHA due to the smaller 8-unit window, which translates into a single-turnover of approximately 40 %, whereas *BEA is negligible. CHA allows the methanol product to migrate from the Fe(II) site to the BAS almost immediately which allows for a subsequent reaction cycle to occur.

This selection of works highlights a couple of major issues; first, that the activation of a C-H bond is very similar for both methane and methanol and as such this would reduce the selectivity of a catalyst. The diffusion of methanol away from the active site prevents over-oxidation and regenerates the Fe(II) sites by confining methyl radicals near the active sites. The second issue is replacing the N_2O oxidant with a cheaper oxidant like molecular O_2 as discussed in some of the previous studies.

To conclude this section; we can see that valuable insight has been given to a vast array of chemistry resulting from a simple concept. Inclusion of protons or metal cations can control catalytic processes in a zeolite. Furthermore, the crucial role of this concept has been highlighted regarding the methanol to hydrocarbon and BTX reactions. Additionally, there have been some interesting recent developments into a newer reaction pathway involving the activation of molecular oxygen by an extra-framework metal cation, which then abstracts a hydrogen from a methane molecule. Whilst there has been limited success with this new mechanism, there is considerable potential to develop a new pathway of methane activation with a lower activation energy and cheaper oxidant, which, however, comes with a new set of challenges including product selectivity and catalyst regeneration. Whilst we have seen experimental techniques provide valuable comprehension of topological, morphological, and mechanistic properties, it is now clear that computational chemistry has become an indispensable tool within this complex field of study. The modelling of metal centres within zeolites is therefore one of the major themes of this thesis.

1.4 The Influence of Water Within the Pores of Zeolites

Water can play a vital role in the adsorptive and catalytic properties of zeolites and there has also been some debate over the role of water in the structural stabilities of zeolites.[91] Water partial pressures, temperatures, along with chemical composition and modifications of zeolite structures post-synthesis can significantly affect their stability and catalytic performance. At low temperatures water vapour is purely limited to adsorption whilst higher temperatures can lead to structural and compositional changes. Liquid water, however, can cause chemical changes at lower temperatures and at higher temperatures can lead to significantly destabilising structural changes, causing a collapse in the supramolecular structure. The influence of water within zeolitic systems is complex, and the next section of this Introduction aims to emphasise the importance of these effects. Additionally, this section also seeks to highlight the elegance of computational methods in assistance to experimental work in the characteristic determination of these features.

Water is a common solvent for a plethora of reactions throughout the field of chemistry, thus it is a reasonable assumption that understanding the influence of water within the pores of zeolites can be an important aspect to enhancing our knowledge of a catalytic system. As a result, there have been extensive literature reviews covering this topic over the years such as those by Khulbe *et al*[92] and Resasco *et al.*[93] As previously shown, it is agreed that this behaviour can deviate substantially from system to system, especially when altering the heteroatoms included within the zeolitic framework. It is widely reported that a protonated ZSM-5 framework (H-ZSM-5) has two forms of adsorbing water to the Brønsted Acid site: a hydrogen bonded form[94] and a protonated ion-pair form[95] as shown in ***Fig. 1.4.*** below:

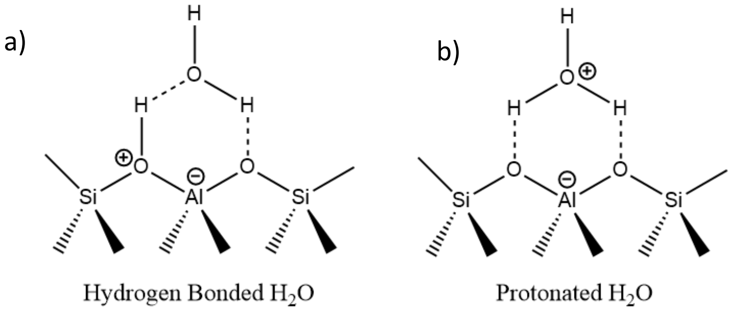

Fig. 1.4. Coordination of a water molecule to the BAS (a) and formation of a hydroxonium ion at the BAS (b).

However there has been extensive debate over the existence of the hydroxonium species in experimental situations, as evidence for their existence appears in some techniques, while not in others.

There have been several applications of modelling techniques to study water in zeolites. For example, in the work of Zhou *et al*[96] classical molecular dynamics was employed to model interactions of liquid water with purely siliceous FAU and MFI/ZSM-5. Two distinct microstructures of water were observed within these systems compared to the properties of bulk water. This methodology was used to sample the shortest unbroken chains of hydrogen bonded water (termed geodesic paths) from a reference water molecule.[93] Bulk water exhibits a Gaussian distribution of shapes with a maximum of approximately 10-11 hydrogen bonds and falling to a path length limit of 15 hydrogen bonds between molecules. In the pore of ZSM-5, constraints are placed on the chain due to the channels and so a more one-dimensional chain forms with shorter lived hydrogen bonds. This geometry yields a greater frequency of fluctuation in hydrogen bond formation and breaking for both FAU and ZSM-5 compared to the bulk, which results from the reorientation of water molecules causing hydrogen bonds to switch from one neighbour to the other.

As Zhou's study demonstrated, the dynamics of water in zeolites can be particularly sensitive to even the slightest change and as such would be significantly influenced by the structural features, including cations and protons covered in the second section of this introduction. These features can act as nucleation centres for water clusters and can be difficult to determine experimentally. In the works of Bukowski *et al*[97] computational *ab-initio* molecular dynamics (AIMD) was employed to simulate different sizes of water cluster within beta-zeolite. Sn was introduced as a tetravalent framework species and as a trivalent framework SnOH (with a charge compensating proton). It was shown that both Sn and SnOH localise water clusters via hydrogen bonds reducing the entropy of the water cluster. With densities of around 23 water molecules (the approximate density of a bulk liquid and fully occupying the pore's volume) within the unit cell, water behaves more like a liquid and forms extensive hydrogen bond networks, but localised clusters can still be preserved. The defects arising from $Si(OH)_4$ vacancies do not however result in nucleation of water at lower densities but tend to stabilise more delocalised networks. The nucleation of water was analysed experimentally by infrared spectroscopy with various water pressures in both high and low defect Si-beta. The OH stretching frequencies indicated that in high-defect zeolite beta, hydrogen bonding networks formed whilst very little water was adsorbed in the low-defect sample.

Fast proton exchange between water molecules, hydroxonium ions and OH groups has been observed in ^{1}H MAS (Magic Angle Spinning) NMR by Hunger *et al*,[98] a phenomenon which makes experimental determination of hydroxonium ions difficult, especially when trying to determine such behaviour at low loadings. Hydroxonium ions were reported at low pressures in the IR analysis by Jentys *et al.*[99] However, these results were somewhat contested by the works of Parker *et al,*[100] whose IR analysis suggested that partial proton transfer occurred but not hydroxonium ion formation. Further attempts at elucidating the behaviour of an adsorbed water species were reported in the work of Kondo *et al.*[101]

Fourier-Transformed Infrared (FT-IR) spectroscopy demonstrated that there was an equilibrium between gaseous, hydrogen bonded, dimeric and even polymeric water species above 373 K, allowing for the assignment of the adsorbed water molecule and the OH of the Brønsted acid site. This study thus concluded that only the neutral water molecules were present in the system.

Ab-Initio calculations carried out in the works of Krossner and Sauer,[102] as well as the works of Zygmunt *et al,*[103] showed that the hydrogen bonded system occupied the minimum on the potential energy surface. However, the hydroxonium species formed a transition state, with a low energy difference, for the transfer of the proton from the Brønsted acid site to the water and vice versa. Hydroxonium species were attributed to a dimeric water species of $H_5O_2^+$ in the *ab-initio* dynamics calculations, thus illustrating the importance of computational models in assisting experimental determinations. Whilst this transition state barrier is small, the earlier study at the start of this section and a study by Shah *et al*[104] illustrated that the physical properties of a zeolite, such as the size of the pore channels and cages, can influence the energy required for this proton transfer.

As an alternative to IR studies there have been several applications of Inelastic Neutron Scattering (INS) to model the adsorption of water. This technique is very sensitive to vibrational modes that involve hydrogen, owing to the large incoherent cross section and low mass of the proton.[105] INS intensities can be directly related to atomic displacements which are routinely modelled with techniques such as *ab-initio* molecular dynamics and empirical force field methods. In the work of Jobic *et al,*[106] INS was employed to model water's interactions with H-Mordenite at low loadings and some vibrational features were assigned to hydrogen bonded water, free hydroxyl groups and hydroxonium ions, in accordance with the earlier IR work, mentioned previously, by Jentys *et al*.[93] In subsequent work by Jobic *et al*[107] similar adsorption bands were observed to those in the work on H-Mordenite with the INS spectrum of H-ZSM-5 at low loadings. The hydrogen-bonded model provided a better fit to both experimental data and calculated spectra than the hydroxonium model and found that a large proportion of bridging OH groups are not accessible to water molecules. They conclude that for their small Si/Al ratio (21.5) system, no protonated species are observed.

Ab-initio methods are now routine in modelling water-containing zeolite systems. The work of Sauer *et al*[108] used this technique with a DZP basis set to show the water complex hydrogen bonding with the bridging OH group nearest the aluminium acting as a proton donor, and the oxygen of the water acting as a proton acceptor, with the other OH group being free. This work also found that under the DZP approximation the hydrogen bonding form was 18 kJ mol^{-1} more stable than the ion-pair structure; however, comparisons using the electron-correlation contributions in the MP2 method yielded similar energies. The MP2 method contained some inherent uncertainties and as such no conclusions were reached over the nature of the adsorbed complex.

Alternatively, the study by Pelmenschikov and Santen *et al*[94] utilised a different basis set, 6-31G*, for their *ab-initio* frequency calculations using the GAUSSIAN-90 package on the water molecule complex hydrogen bonding to the acid proton. Contrasting the results from their simulation against experimental IR frequencies, they concluded that five OH bands can be attributed to the water molecule complex with the bridging hydrogen. Two bands indicate that there are two hydrogen bonds between the bridging OH group and nearest AlOSi and the oxygen of the water and the other OH group on the water molecule. Whilst we have seen some contention, the findings of these studies and many others have led to the generally accepted conclusion that low doses of water, such as a single water molecule per acid site, leads to the neutral hydrogen bonded form being favoured over the protonated form.

Next, we consider the modelling of additional water molecules in the pores of zeolites. Such is the work of Jungsuttiwong *et al*,[109] who endeavoured to study further the modes of adsorption of the water dimers previously mentioned in both ZSM-5 and Faujasite systems. This work utilised an embedded cluster model for 7 of the tetrahedral units in the wall of zeolite pores, applying the hybrid B3LYP functional[110,111] to model the modes of water dimer adsorption with DFT. The results indicated that there were two adsorption pathways: one in which the water molecule binds strongly to one of the oxygens attached to the aluminium, whilst the other water weakly binds to the zeolite framework; the other adsorption mode is where both molecules form a hydrogen bonded network with the proton from the Brønsted acid site and oxygen of a water molecule, and the hydrogen of the second water molecule forms another hydrogen bond to the oxygen within the zeolite pore wall. With the inclusion of the Madelung potential, both the neutral and ion-pair complexes were found to be stable for H-ZSM-5 with adsorption energies of -63.3 and -61.7 kJ mol^{-1}, whereas in H-FAU only the ion-pair complex was stable with a lower adsorption energy of -61.3 kJ mol^{-1}. The results of this study concluded that the adsorption properties do not entirely depend on the acidity of the acid site but also on features derived from the topology such as spatial confinement effects.

Another study by Vener *et al,*[112] focussed on the protonation of water clusters, was carried out by modelling protonated chabazite (H-SSZ-13) with loadings of 1 to 4 water molecules per acid site. Once again using DFT calculations and coupled with Car-Parrinello MD simulations, the proton affinity was shown to increase with increasing cluster size. When modelled using the PBE functional,[87] the protonated water dimer was the most stable equilibrium structure but not upon raising the temperature. However, when using the BLYP functional instead the neutral complex is favoured. Clusters that involve four water molecules transferred the proton from the acid site to the cluster to form the most stable clusters; however, this phenomenon was much shorter lived with loadings of three water molecules.

Water loadings have subsequently been hypothesised in acidic forms of zeolites, to break the Löwenstein rule, which states that aluminium pairs (Al-O-Al) are forbidden in zeolites.[113] However, the works of Heard *et al*[114] utilised AIMD simulations on H-CHA under anhydrous conditions (no water molecules), water loadings of 1 molecule, and 15 water molecules (corresponding to 5 molecules per zeolite cage). This simulation demonstrated that under high water solvation, the rule is obeyed for the acid form of chabazite (H-CHA) but disobeyed under anhydrous conditions. The variation of water loading in the pore results in dramatic effects on active site structure and solvation dynamics. The solvation of Brønsted protons provided the energetic driving force for the Löwenstein Al distribution. In the case of non-Lowenstein moieties, this energetic driving force is absent and so this preference for solvated protons would lead to the assumption that the protonated water cluster is the catalytically active species in zeolites, rather than the framework Brønsted acid site. This study clearly illustrates the need for accurate modelling of solvent conditions for simulations to reflect experiments more precisely.

Introduction of extra-framework cations and structural defects such as silanol groups into zeolite pores can alter the clustering dynamics of water molecules. Experiments carried out by Zhang *et al*[115] highlighted that defect-free silicalite maintains structural integrity due to its hydrophobic nature, whilst hydrophilic silicalites containing internal silanol defects lose their crystallinity. Furthermore, the introduction of these silanol defects lead to the formation of water clusters from the vapor phase at nucleation sites. Silanols containing monovalent cations such as Na(I) exhibit stronger hydrophilic character than isolated Silanols, leading to the formation of water hexamers in NaX and NaY Faujasite structures.[116,117] Importantly the distance between defect sites controls water nucleation as the interior of a defect-free silicalite is mostly hydrophobic. If a sample is free of these internal silanol groups, then the ratio of Si:Al may determine the nucleation centre for water molecules.[118] Olson proposed that acidic protons are likely more attractive to water molecules than silanol groups, by varying Si:Al ratios at low pressures water adsorption was shown to be directly dependent on this ratio. Strong adsorption of water therefore corresponded to acidic protons caused by framework Al atoms.[119] When using low loadings of water, each proton in a high-silica ZSM-5 structure was solvated by a maximum of four water molecules.

Charge compensating cations can also affect water adsorption as demonstrated by Tahraoui *et al*[120] using experimental XRD and NMR, combined with water uptake measurements. Cation type and charge were shown to be significant factors influencing the amount of water that could be adsorbed, addition of Na(I), Li(I) and Mg(II) result in increasing water adsorption in LTA and FAU structures with the volume of the pores assisting in water uptake.

Cations can significantly influence solvent molecules such as water and perturb the dynamics of the bulk solvent. Suresh *et al*[121] report that the water molecules within the first solvation shell of the Na(I) cation largely retain their structure with the average number of hydrogen bonds and average dipolar alignments only deviating slightly from that of bulk water. The lack of deviation of the Na(I) cation from bulk water stems from a ‘caging’ effect by the water molecules. However, water molecules surrounding small ions with a high charge density such as Al(III), strongly align their dipoles in the direction of the field reducing the number of hydrogen bonds per molecule. Alternatively, water molecules surrounding large ions with low charge densities such as Cs(I) are oriented so that their hydrogen bond axes involving a lone pair of electrons faces the ion to maximise hydrogen bond interactions at other bonding sites. Beyond the first solvation shell the degree of hydrogen bonding becomes similar to that of bulk water, although changes in molecular orientation and non-linear polarisation effects have been shown to persist up to 3-4 hydration shells away.[121]

Concluding this section, we have seen how the dynamics of water evolves within the pores of zeolites with a diverse range of cluster behaviours. The relationship of water within zeolites cannot be confined to two distinct separate entities of water and zeolite structure, but in-turn water configurations and dynamics can influence zeolite structure and vice versa. This complex relationship has led to debate stemming from experimental studies over fundamentals like hydroxonium ion formation as covered previously. This issue largely arises from the limitations of analytical techniques which sample many different structures at once and provide an averaged snapshot of the whole system. Computational techniques have proved to be an invaluable resource in this respect, as they can model specific systems without having interfering background contributions and can provide energetic predictions of water clusters. This allows extrapolation to experimental work, as shown throughout this section, to assist with a more comprehensive explanation for the observed results.

1.5 Summary of Dissertation Objectives

Catalytic science poses challenging problems, many of which derive from the dynamic nature of catalytic systems through synthesis, activation, and deactivation. The limitations of experiments in defining subtle yet quintessential structure-activity relationships of catalytic systems, leaves a gap in our understanding that provides a prime justification for the use of computational models.

The primary aim of this dissertation is to utilise computational techniques to improve our understanding of a range of zeolite structures and behaviours through the lens of catalysis. This Introduction has sought to highlight the importance and indispensable nature of microporous materials as catalysts for industrial processes, and this thesis will have a strong emphasis on ZSM-5, as it has proved to be active for the conversion of methane to methanol in cation exchanged systems, as well as the conversion of methanol into hydrocarbons.

With this in mind, our initial work seeks to benchmark various different methodologies including two interatomic potential methods and Density Functional Theory to assess their suitability for modelling the energetics and thermodynamics of microporous materials. These methodologies will be assessed by comparison with experimental data. The information garnered from these studies, gives insight into the role and effectiveness of these methodologies in modelling zeolites including ZSM-5.

The second part of this thesis will apply these methodologies to model different metal centres within the ZSM-5 zeolite. The main aim here is to utilise these metal centres to enhance ZSM-5's catalytic properties for the conversion of methane to methanol. As highlighted within section 1.3.0 of this introduction, the activation of a methane C-H bond forms the basis of a potential new pathway in the conversion of methane to methanol but is limited by the formation of the oxo species. As such we endeavour to determine whether there are more energetically favourable systems that can enable this catalytic pathway to become viable. The chapter also gives more general insights into the activity of metal cations within zeolites.

The final project focusses on modelling the behaviour of low concentrations of water within the pore of two ZSM-5 structures, employing the benchmarked methodologies and two of the ZSM-5 systems modelled in the previous chapter. As has been discussed within this Introduction, water can play a major role in zeolites on the structure, energetics and crucially the activity of the zeolite. Therefore, we seek to understand the differences between the dynamics of water in H-ZSM-5 and Na-ZSM-5 and characterise these distinct behaviours through simulated IR spectra. The variations observed within these spectra can form a foundation that can help elucidate some of the unexplained cross-coupling observed in novel experimental 2D-IR studies currently being performed at the UK Central Laser Facility (CLF). More details of the aims and contents of each study are given below.

1.5.1 Chapter 3

The work in these chapters aims to provide an overview of different computational methods, utilising both quantum mechanical and molecular mechanical techniques. These techniques will be benchmarked on their ability to model the energetics of microporous frameworks, and so will model over a hundred microporous materials (both zeolites and AlPOs respectively). Interatomic potential based methods will benchmark two distinct models: a formal charge shell model approach and a partial charge rigid ion model. These models are contrasted with each other and their accuracy to experimental data. A Density Functional Theory (DFT) model is then applied to the same selection of structures; these energies are compared to experimental data from the literature which can illustrate the relative strengths and weaknesses of each computational method. Additionally, this body of work will aid in the determination of a suitable molecular mechanical methodology that can be applied in the subsequent studies when applying hybrid quantum mechanical molecular mechanical (QM/MM) methods.

1.5.2 Chapter 4

Next, we present a study that combines the previous approaches of quantum mechanical methods and molecular mechanical methods into a hybrid QM/MM approach to model different metal centres in different oxidation states within the pore of the ZSM-5 zeolite. This work will focus on each system's ability to activate molecular oxygen, leading to an assessment on each systems catalytic feasibility for the new reaction pathway for the conversion of methane to methanol. We therefore model the hydrogen abstraction energies (**BDE_{OH}**), which is one of the required steps for the direct conversion of the methane to methanol. This work will address whether this pathway could be a viable alternative using different extra-framework cations to the previously modelled Au(I) and Rh(III) cations, and when compared to the natural porphyrin alternative catalyst. It also provides more general insights into the activation of molecular oxygen by extra-framework cations in zeolites.

1.5.3 Chapter 5

Following the hybrid QM/MM calculations, we used the same methodology to model both H-ZSM-5 and Na-ZSM-5 with a low concentration of water molecules within the pore. Water plays a crucial role in the energies and activities of zeolite structures and improved knowledge of these systems can assist with experimental understanding and the design of future catalysts. The objective of this project is therefore to build upon the ground covered in the previous two projects and utilise some of the same methodologies to determine the structures and differences in the dynamics of sorbed water in the two systems. This work can subsequently be combined with experimental studies at the STFC Central Laser Facility (CLF) to assist with the interpretation of experimental 2D-IR spectra. By employing a variety of computational techniques, including *Ab-Initio* Molecular Dynamics (AIMD), we can model the behaviour of water in the pore of ZSM-5 frameworks. Configurations generated by the AIMD are then fed into hybrid QM/MM methods for optimisation. Generalised Vibrational Perturbation Theory (GVPT) calculations are then run on these structures to generate IR spectra.

The next chapter will explore in greater detail the methodologies employed in the thesis.

CHAPTER 2

Methodology:

Computational Methods Overview and Theory

2.0 Overview

With the advent of computers there has been a concomitant exponential increase in computing power. This increase in computing power is popularly characterised by Moore's Law from 1965 that states the number of transistors on a silicon chip would double every year,[122] but which was subsequently revised to a more pessimistic 18 months. Nevertheless, with such a versatile new technology it was quickly harnessed for a range of scientific applications, but most pertinently to this thesis is the use of computational technology as a tool for modelling materials. This allows an opportunity to determine information about systems and reactions that would otherwise be impossible or extremely difficult to determine through experimentation, such as binding energies, transition states, reaction pathways and thermochemical data amongst many others.

Early computational hardware was limited in comparison to modern day hardware, thus more approximate methods were devised that struck a reasonable balance between approximations and accuracy. This then formed the genesis for the first family of modelling techniques that will be discussed in this section: Molecular Mechanical (MM) methodologies often referred to as force field techniques. These techniques focussed on different ways of modelling the electrostatic properties of a system through a more classical Newtonian lens, often using experimental data as a basis for their parameters. Atoms are considered as point-charges connected to other atoms through springs, described using force constants, whilst ignoring the contribution of electron distribution. Importantly, a drawback of this methodology means that it cannot be used to model bond formation or dissociation pathways. Whilst computational power may have increased, molecular mechanical methods still play an important role as a relatively simple and resource-light way of modelling a system to a respectable degree of accuracy.

Whilst these force fields were successful, they had many drawbacks, namely their intrinsic inability to model electronic structure, which requires Quantum Mechanical (QM) methods, which form the second of the two main branches of computational methodologies that will be discussed in this section. Quantum mechanical methods are naturally more resource intensive as they solve the Schrödinger equation ($\hat{\mathrm{H}}\boldsymbol{\varphi} = \boldsymbol{E}\boldsymbol{\varphi}$) at some level of approximation for other than one electron atoms.[123] This higher computational cost therefore imposes a limit on the size of the system which can be modelled. However, as advances in computer hardware continue, this limit is reduced making the modelling of more complex systems such as zeolites and enzymes more accessible.

Whilst these two different approaches broadly encompass the main types of atomic level computational methodologies, there have been variations upon these that have expanded their versatility, increasing the types of system they can be used to model. Notably, a compromise can be made between these two methodologies in the form of hybrid quantum mechanical molecular mechanical techniques (QM/MM), which allows for the highly accurate determination of properties for large chemical systems, whilst reducing the large computational cost incurred by high-level methods.

All these methodologies have been extended over the years, leading to the ability not just to model energies of a system but also their properties. This section of thesis aims to provide an overview of the methodologies outlined above, in addition to some more specialised calculations that will be employed in some of the projects covered in this thesis.

2.1 Interatomic Potential Methods

The internal energy, **U**, of a system is a many-body quantity that is dependent upon both the positions and momentum of all nuclei and electrons. Interatomic potential methods assume that the energy of the system can be written as an analytical function of the nuclear coordinates:

$$\boldsymbol{U = \sum_{i=1}^{N} U_i + \frac{1}{2}\sum_{i=1}^{N}\sum_{j=1\neq i}^{N} U_{ij} + \frac{1}{6}\sum_{i=1}^{N}\sum_{j=1\neq i}^{N}\sum_{k=1}^{N} U_{ijk} + \cdots} \qquad (2.1)$$

The first term in this equation represents the contribution from the energy of each atom, $\mathbf{U_i}$, which is simply summed over the number of atoms, **N**, in the system. The second term is a summation over all pairs of atoms, **i,j** to obtain the pairwise interaction terms, $\mathbf{U_{ij}}$, and the third term, $\mathbf{U_{ijk}}$, picks up the three-body terms. It can reasonably be assumed that higher order terms decrease in magnitude and the further apart two atoms are, the weaker their interaction, hence a cut-off for the potentials is introduced to reduce the scale of the computational calculation.[124]

The type of interaction is typically chosen based on the nature of the forces between the particles in the system. The Morse potential would be employed when modelling covalent systems as it is harmonic when at a minimum but leads to dissociation at large bond lengths.[125] Alternatively, the Buckingham potential models Pauli repulsion and van der Waals interaction for two atoms that are not directly bonded to each other and is commonly employed in the modelling of ionic systems.[126] These potentials are discussed in greater detail below.

Coulombic Interaction

The coulombic interaction can account for approximately 90 % of the total energy for ionic systems and is simply given by Coulomb's Law:

$$\boldsymbol{U_{ij}}^{\boldsymbol{Coul}} = \frac{\boldsymbol{q_i q_j}}{\boldsymbol{4\pi\varepsilon_0 r_{ij}}} \qquad (\mathbf{2.2})$$

Where $\mathbf{U_{ij}}^{\mathbf{coul}}$ is the coulombic contribution of the two-body energy between the two point-charges: $\mathbf{q_i}$ and $\mathbf{q_j}$, whilst $\mathbf{r_{ij}}$ is the distance between the two point-charges (**i** and **j**) and $\boldsymbol{\varepsilon_0}$ is the electric constant. For periodic systems it is a more complex scenario as the coulombic energy is a conditionally convergent series. The most adopted solution to this problem is Ewald's method for 3D materials, whereby a convergence criteria of charge neutrality and a zero-dipole moment is implemented to generate a series with a well-defined limit.[127] The coulombic term is subsequently subject to a Laplace transformation and split into two components: the first is rapidly convergent in real space, and the second decays rapidly in reciprocal space.

Polarisation

The *shell model* provides a description of the polarisability of atoms by comprising of a core representing the nucleus and inner electrons, whilst a shell represents the outer electrons. This shell and core are connected by a harmonic spring with a specified spring constant.[128] It has been shown that the modelling of polarisability using the shell model can be crucial as the lack of a polarisability term can lead to non-physical linear bond angles.[129]

In contrast to this model, van Beest *et al*[32] derived bulk force fields from *ab-initio* calculations of small clusters to represent the infinite system and ensured the nearest-neighbour interactions were described properly. Since the interatomic potentials ranged beyond the nearest neighbour, empirical data on α-quartz (the infinite system) was incorporated into the derivation of the potentials. Notably in this method the three-body term is not included, and there is no explicit description of polarisability which, it is hoped, is partially incorporated into the potentials.

Buckingham Potentials

Buckingham potentials like the Lennard-Jones potential[130] are used to describe the Pauli repulsion and van der Waals contributions of an interaction between two atoms that are not directly bonded to each other, as a function of interatomic distance (**r**),[131] and takes the form:

$$\boldsymbol{U_{ij}{}^{rep-dis}(r_{ij}) = A_{ij}\exp\left(\frac{-r_{ij}}{\rho_{ij}}\right) - \frac{C_{ij}}{r_{ij}{}^{6}} + \frac{q_1 q_2}{4\pi\varepsilon_0 r_{ij}}} \qquad (\mathbf{2.3})$$

Where $\mathbf{U_{ij}^{rep\text{-}disp}}$ is the repulsion-dispersion contribution of $\mathbf{U_{ij}}$, **A**, **C** and $\frac{1}{\rho}$ (often denoted as **B**) are constants, with the two terms, excluding the coulomb term, representing a repulsion and attraction as indicated by the negative and positive terms in the equation. Although the potential works well for most interatomic distances, it can become problematic at very short distances as the $\mathbf{Cr_{ij}^{-6}}$ term tends to infinity as **r** tends to zero.

There have been variations in models that utilise Buckingham potentials, notably those discussed in the introductory chapter of this thesis derived by Sanders *et al*[31] and van Beest *et al.*[32] The potential model derived by Sanders *et al* uses formal charges, a three-body term, and a shell model. Formal charges were used as it was the most convenient method of accurately describing the cohesive properties of a system. The three-body term describes the bond-bending that occurs for O-Si-O bonds, which is described by the quadratic energy term:

$$\boldsymbol{U_{ijk} = K_B\,(\theta_{ijk} - \theta_{0,ijk})} \qquad (\mathbf{2.4})$$

in which the $(\boldsymbol{\theta_{ijk}\text{-}\theta_{0,ijk}})$ term describes the deviation of the bond angle from the ideal tetrahedral bond angle of 109.45°, and $\mathbf{K_B}$ is a harmonic force constant for the bond-bending component. As such the three-body term models the rigidity of the SiO_4 tetrahedron stemming from the sp^3 hybridisation in the bonding between the silicon and oxygen atoms.[32,120,121]

Geometry Optimisations

Changes in the geometry of a system can result in substantial changes to the overall energy of that same system, even if the geometric changes are relatively small. Quantum mechanical software such as the VASP code used in this thesis,[74–78] employ several algorithms to optimise a structure from its initial geometry to find this energy minimum. This is achieved for all computational methods by calculating the first derivative of energy to all three degrees of freedom for each atom in the system which translates to nuclear distances, angles, and dihedral angles. At a local minimum on the PES the first derivative against each coordinate is equal to zero:

$$\frac{\partial \boldsymbol{U}}{\partial \boldsymbol{x}_{ik}\boldsymbol{x}_{jl}} = \mathbf{0} \tag{2.5}$$

Whilst previously, $\mathbf{r}_{ij}$ or $\mathbf{r}_{ik}$, were used to represent the length of the vector (distance) between atoms **i** and **j**, here $\mathbf{x}_{ik}$ and $\mathbf{x}_{jl}$ are used to represent the **k** and **l** component of the position vector for each atom. However, the second derivatives have real (greater than zero) values:

$$\frac{\partial^2 \boldsymbol{U}}{\partial \boldsymbol{x}_{ik}{}^2 \boldsymbol{x}_{jl}{}^2} > \mathbf{0} \tag{2.6}$$

Optimisation methods evaluate the functional of the initial geometry as a single point calculation, and then moves the atoms and alters the geometry in such a way that the energy values move down the potential energy gradient. This step is repeated multiple times, lowering the energy of the system iteratively, and checking for local minima until an optimised geometry is found to be consistent within the acceptable tolerances set up in the calculation's input. There are a number of optimisation algorithms, many of which use second derivatives in addition to first derivatives. In this thesis different computational codes are employed with different algorithms.

2.2 Quantum Mechanical Methods

2.2.1 The Potential Energy Surface

Quantum mechanical methods which are more computationally expensive can fall into one of three main classes. All three of these classes attempt to solve the Schrödinger equation, shown below:[123]

$$\hat{\mathrm{H}}\boldsymbol{\varphi} = \boldsymbol{E\varphi} \qquad (\mathbf{2.7})$$

The Schrödinger equation is a partial differential equation derived in 1924, where the Hamiltonian Operator (**Ĥ**) is a set of operators which act on a system's three-dimensional wave function (**φ**) which is a key variable in Hartree-Fock and post-Hartree-Fock era calculations. Born subsequently interpreted this value as probabilistic by demonstrating that the square of the absolute value of a wave function's amplitude gives the probability of a quantum event.[132]

Three years later in 1927, another significant development in quantum theory was proposed by Max Born and J. Robert Oppenheimer, which was later popularly termed the Born-Oppenheimer approximation.[133] This approximation defines a separation of the electronic and nuclear motion within molecules, based on the assumption that the electronic motion is significantly faster than the nuclear motion, hereby inferring that the electronic wave function can be calculated using a fixed nuclear configuration. This defines the energy as a function of nuclear coordinates, forming what is known as the Potential Energy Surface (PES) depicted below in ***Fig. 2.1.*** for both 1D and 3D. These diagrams depict how the energy changes between nuclei as the distance increases. This PES has the same dimensionality as the number of geometric degrees of freedom for a molecule described by **3N-6**, where **N** is the number of atoms, and which has to be greater than 2. At very close distances there is a repulsive force from the nuclei and the electronic Pauli repulsion, thus resulting in a large increase in energy as the bond lengths decrease. As the bond lengths increase, the energy eventually becomes negative; a negative energy equates to an attractive force, thus chemical bonds can form. As the distance increases between each atom the force of attraction weakens, until the nuclei are far enough apart to cause bond dissociation. We now discuss the main classes of quantum mechanical technique.

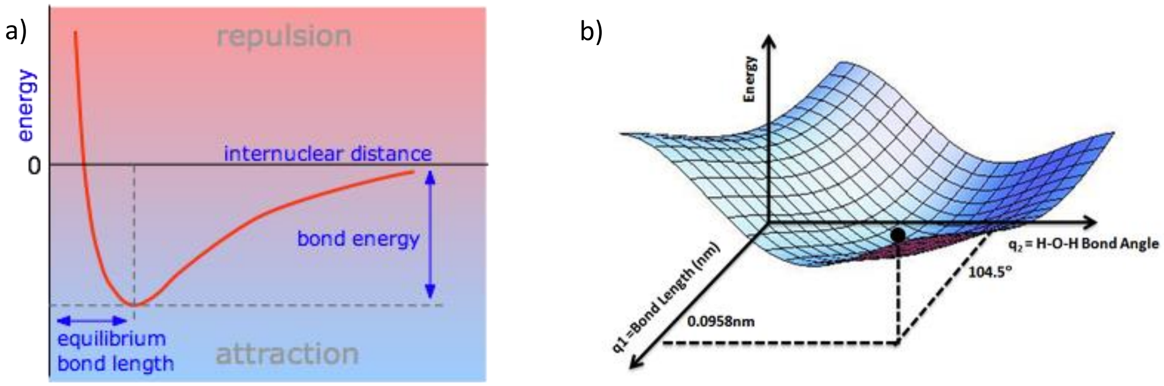

Fig. 2.1. Diagrams depicting the Potential Energy Surface (PES) in one dimension (a) and three dimensions (b) taken from LibreTexts Chemistry.[134]

2.2.2 Ab-Initio Methods

2.2.2.i Hartree-Fock

The Hartree-Fock method, builds upon the PES, and has been very widely used in computational chemistry; it focuses on finding the solution to the Schrödinger's equation using the molecular wave function. The approach has the merit of providing a detailed evaluation of exchange energies but the weakness in its basic form of not including electron correlation energies. This deficiency can be remedied by various "post Hartree Fock" methods including perturbation and coupled cluster methods, but at the expense of much greater computational requirements.

The Hartree-Fock method initially stemmed from Bohr's independent-particle-model (IPM) whereby particles move under the influence of an outer potential and the average potential of all particles within the system. This model was implemented, and the corresponding one-electron Schrödinger equation was solved with an iterative procedure implemented by Hartree.[135] This iterative process was designed to continue iterations until no significant changes in the electric field figures were observed, which is when the process is deemed to be "self-consistent" and as such is termed the Self-Consistent-Field (SCF) method.

2.2.2.ii Density Functional Theory

Density Functional Theory (DFT) also builds upon the PES model set out in the work of Born and Oppenheimer[133] with contributions to the theory coming later in 1927 and again in 1928, with the works of Fermi and Thomas, who demonstrated that electron density could be used instead of the wave function, based on the assumption that the total electronic energy of a system is a function of the electron density, which is experimentally observable.[136,137]

This original model included terms for the kinetic energy of the electrons (**E_T**), potential energy arising from nuclear attraction (**E_V**) and the potential energy from the electron-electron repulsion resulting from the electron density (**E_J**). This model however gives poor predictions for real atoms and molecules, as it is only exact when in the limit of an infinite nuclear charge. The model also fails to compute shell structures of atoms which results in molecular orbitals at higher energies than their constituent atomic orbitals.[138] Despite these issues, it can be considered that this early method is in essence a precursor to the modern DFT methodologies.

Over time this model was developed with numerous contributions by multiple people: An energy exchange term for electrons was added by Dirac,[139] Weizsäcker added a correction term for the kinetic energy of electrons[140] and Slater elaborated upon Dirac's exchange functional by including a constant.[141] Most notably however were the works of both Kohn and Sham.

Kohn devised a function for the total electronic energy, **$E_{tot}[n(r)]$**, and is defined as the electron density, **n(r)**, and demonstrates the total electronic energy, along with other observable properties, are a functional of **n(r)**. Subsequently, the global minimum value of the energy functional results from the ground state electron density being implemented into this functional.[142] This work proved the concept of a universal density functional, but it does not define the functions form or give a description for electron density. Building upon this theory; Kohn and Sham derived an equation which pushed DFT into the realm of computational feasibility. This equation is essentially a version of the Schrödinger equation, but applied to a system of non-interacting electrons with the same density of the system being studied[143] and describes the total electronic energy in a system as shown in the equation below:

$$E_{tot}[n] = E_T[n] + E_V[n] + E_J[n] + E_X[n] + E_C[n] \qquad (2.8)$$

Here the total electronic energy, $\mathbf{E_{tot}[n]}$, is equal to the sum of the kinetic energy of the electrons, $\mathbf{E_T[n]}$, the total potential energy of electrons due to their coulombic attraction to a nuclear centre, $\mathbf{E_V[n]}$, the total potential energy due to the average coulombic repulsion between pairs of electrons, $\mathbf{E_J[n]}$, the total quantum mechanical exchange energy of the electrons, $\mathbf{E_X[n]}$, and the total correlation energy of the electrons, $\mathbf{E_C[n]}$. Both of the last two terms, $\mathbf{E_X[n]}$ and $\mathbf{E_C[n]}$, are used to correct for the $\mathbf{E_J[n]}$ term which does not account for the correlated motion of electrons, in other words the movement of each electron as a result of the influence generated by the positions of neighbouring electrons. The $\mathbf{E_X}$ term tends to be the larger of the two terms and corrects for strongly correlated motion between electrons with the same spin by removing non-physical self-repulsion terms. The smaller $\mathbf{E_C}$ term corrects for the weakly correlated motion of electrons with the opposite spin.

This approximation allows for the accurate computation of the kinetic energy in terms of Kohn-Sham orbitals to a similar level as that of Hartree-Fock. Original DFT calculations used planewave functions as basis sets. Planewave functions describe electrons in a periodic system which have been proven to be highly accurate at modelling extended structures such as crystalline solids and surfaces, and as such are widely used within this thesis.

As the number of electrons in a system increases the computational cost scales up dramatically to compute the higher level of complexity, increasing the CPU time required. *Ab-Initio* methods (discussed later in this section) typically tend to be the costliest but are widely regarded as the most accurate of the quantum mechanical methods.

2.2.2.iii Semi-Empirical Methods

Semi-Empirical methods are specifically designed to be as computationally light as possible and are the least expensive type of quantum mechanical calculation. To reduce the computational cost of these calculations, many of the terms in the *ab-initio* calculations have been either removed or parameterised using empirical data.[144] As these methods are not employed in the thesis, they are not discussed further.

2.2.3 Basis Sets

Basis sets are a set of functions that are used to construct the wave function. Basis sets are usually constructed from atomic orbitals with molecular orbitals built from the Linear Combination of Atomic Orbitals (LCAO). The LCAO for the case of diatomic oxygen is outlined in the paragraph below as it is a simple and pertinent example to this thesis (Chapter 4) which models the coordination of diatomic oxygen to metal centres.

In the relatively simple case of molecular oxygen, each oxygen atom contributes two electrons in both the 1s and 2s orbitals and four electrons in the 2p orbitals, as detailed in ***Fig. 2.2***. The usual representation would have each atom's electrons in their assigned orbitals with energy levels represented in the vertical direction, and the bonded atoms on either side. The orbital mixing is then represented in the middle, between the two atoms with a low energy bonding orbital and higher energy anti-bonding orbital, represented by a σ and σ* notation respectively for each orbital.

In the case of molecular oxygen, electrons are donated from the 1s and 2s orbitals from each atom into the bonding and anti-bonding orbitals completely filling them. Considering each oxygen atom contains three 2p orbitals, one each in the x, y and z planes, they form a total of six p-type molecular orbitals: now there is one 2p σ bonding and two 2p π bonding orbitals with corresponding anti-bonding orbitals as well. With four electrons from each oxygen atom (eight total) they fill up the 2p σ and the two 2p π bonding orbitals. In accordance with Hund's rule of maximum multiplicity, the two 2p π* anti-bonding orbitals fill up separately, giving the system an overall multiplicity of three (triplet) following the 2S+1 rule, whilst the remaining 2p σ* orbital is unoccupied. It is worth noting that the shape of the molecular orbitals in the 2s look different to the 1s orbitals, this phenomenon arises from the 2s orbitals being more diffuse than the 1s, so the spheres become more distorted when forming the node when the phases cancel in the bond's centre. We present the case of molecular oxygen diagrammatically in **Fig. 2.2.** below, with atomic centred s and p orbitals used to construct the molecular orbitals.

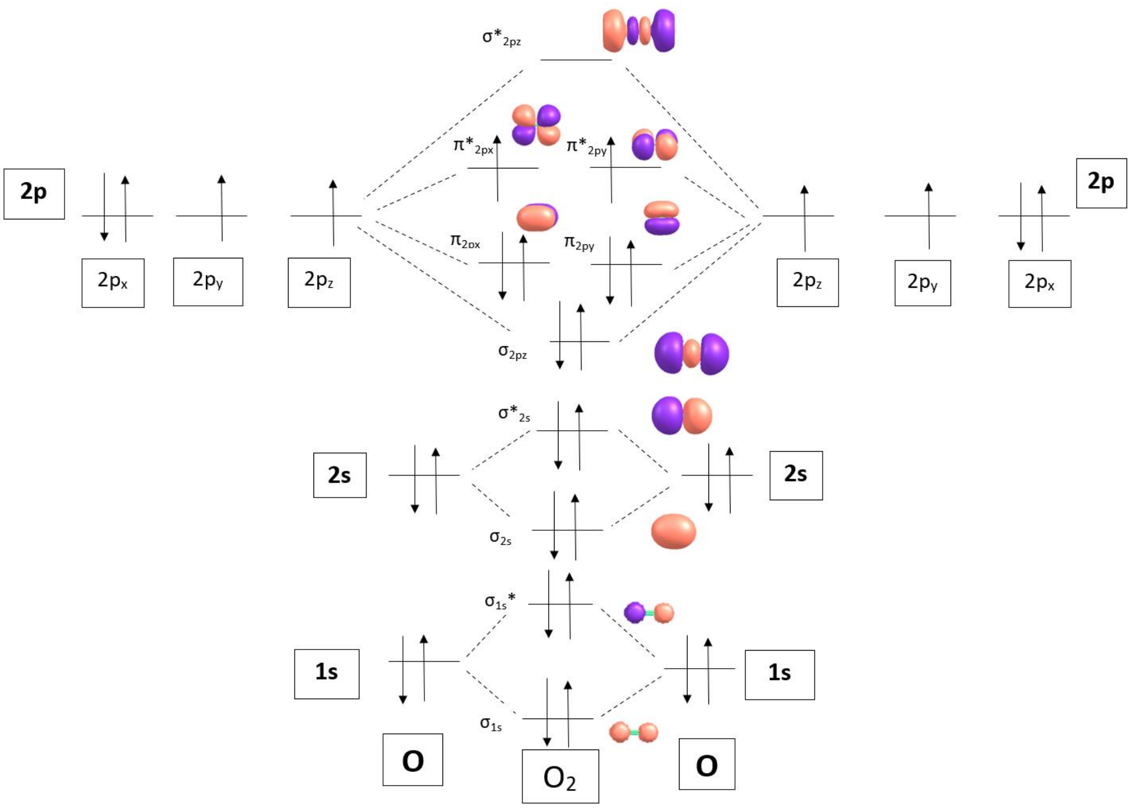

Fig. 2.2. Molecular orbital diagram for diatomic oxygen with the corresponding molecular orbital shapes.

In multi-body systems the situation becomes even more complex. Apropos Chapter 4, the coordination of molecular oxygen to a metal exchanged zeolite structure is investigated, it is therefore also prudent to understand the theory behind the molecular orbitals involved. Thus, in this study an activated oxygen molecule abstracts a hydrogen atom and will therefore accept an electron into either of the two π* orbitals, as such it is worth considering this phenomenon when selecting an appropriate basis set for the calculations.

The Linear Combination of Atomic Orbitals (LCAO) was first proposed by Hückel *et al* in 1931,[145] but whilst the LCAO approach is often favoured for solids as well as molecules, there are alternative ways to form a basis set which use plane waves and are fairly common when modelling solid state materials. There are also several ways to model atomic orbitals in the LCAO which include Gaussian-type orbitals (used within this thesis), Slater-type or numerical orbitals.

Wave functions for the electronic states are constructed using molecular orbitals as described above and are approximate solutions to the Schrödinger equation. A linear combination of functions for atomic orbitals with the same angular function (for s, p, d etc orbital types) but with different radial function exponents, which allows the introduction of flexibility in the functional's form and forms a function for the molecular orbital. This function is called a basis function as they form the basis of the representation of the molecular orbital.[146,147] Additional polarisation functions can be introduced in which functions have a higher angular momentum than would normally be expected, such as p orbitals on hydrogen atoms or d orbitals on first row elements, which provides a description of the distortion atomic orbitals can face when forming a molecular orbital.

Furthermore, a variational theory means values can be changed for parameters in the basis functions and constant coefficients in the linear combination. Additionally, more basis functions can be introduced to make the ground state energy of the molecule (SCF energy) as low as possible and therefore more accurate, and overall improving the accuracy of the basis set.[146–148] The result of which means that as the basis increases the total energy of the structure decreases. However, there is a trade off in computational feasibility as an infinite number of functions cannot be used, thus a basis set limit is introduced so that as a basis set increases in quality (i.e. the number of functions increases) the energy would converge to the energy appropriate to the functional that had been used.

2.2.4 Single Point Calculations

A single point calculation is used to provide an accurate description of a system at a single, fixed geometry that is provided in the structural input file. Often a single point calculation forms the initial step in the optimisation of a structures geometry, as it provides the energies and forces of the initial system, which are then subsequently minimised.

2.3 Hybrid Quantum Mechanical and Molecular Mechanical (QM/MM) Methods

Quantum mechanical methodologies provide detailed information on the electronic structure, which is reflected in the computational power required. Larger systems therefore require an ever-increasing amount of processing power, to the point it no longer becomes viable even with the advances made by modern hardware. Additionally, these larger systems can still require the modelling of electronic processes which molecular mechanical force fields do not describe adequately. To overcome this combination of issues a solution was proposed by Warshel and Levitt,[149] which would treat a relatively small part of the system with the high-level quantum mechanical (QM) description, whilst applying the force field approach (MM) for the larger part of the system. This concept is based on the assumption that the processes involved have a ‘reaction centre’ region and a ‘spectator’ region whose atoms do not directly impact the reaction. Essentially most reactions in solution do not tend to involve reactants outside of the first few solvation shells, and as such the bulk of the solvent has a very limited effect on the reaction.[150] This is to say that whilst the bulk solvent isn’t directly involved, it can however generate long-range interactions that can have a slight influence over the reaction. Similar considerations may apply to reactions on surfaces and within solids. As such hybrid QM/MM calculations have three main types of interactions: the first are between atoms in the QM region, the second are between atoms in the MM region and the third occur between the QM and MM atoms, with the regions highlighted in ***Fig. 2.2.*** below.

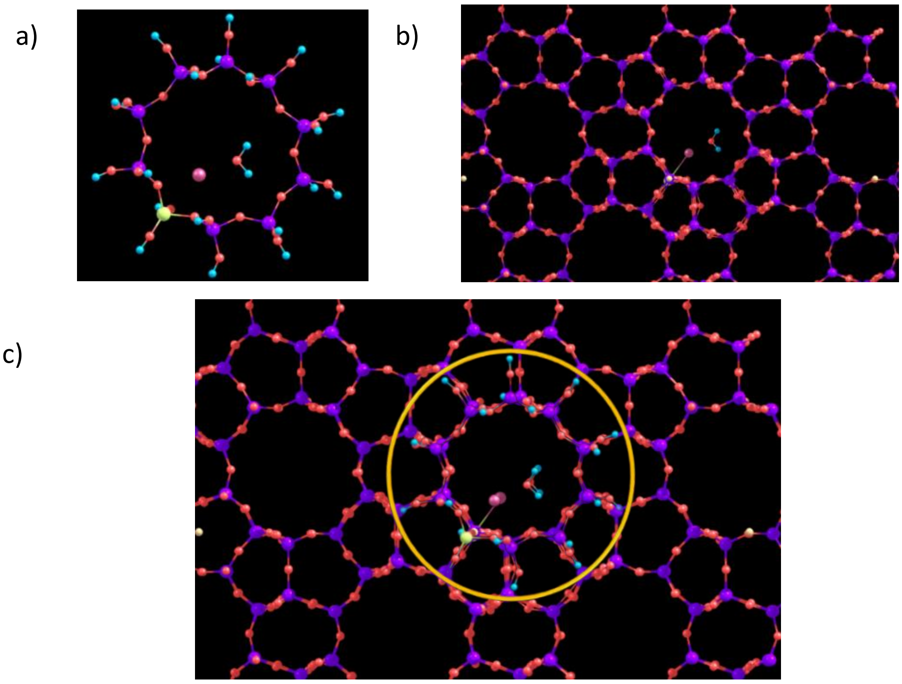

Fig. 2.2. a) QM region with hydrogen linker atoms, b) extended structure, c) QM/MM structure with the QM region in the circle with the yellow ring indicating the boundary region. Atom colours: Si: purple, Al: yellow, O: red, H: light blue and Na: light purple.

The third type of interaction is more difficult to describe and so two approaches have been developed: Subtractive QM/MM coupling and Additive QM/MM coupling, both of which will be outlined in the sections below.

Subtractive coupling is outlined in the equation below and consists of three steps: the first calculates the entire system using the molecular mechanical approach **V_{MM}(QM+MM)**, then the quantum mechanical region is computed with the higher level of theory, **V_{QM}(QM)**. Finally, the QM region is calculated with the molecular mechanical method, **V_{MM}(QM)**, and subtracted which corrects for the inclusion of QM region interactions being effectively included twice.

$$\boldsymbol{V_{QM/MM} = V_{MM}(QM + MM) + V_{QM}(QM) - V_{MM}(QM)} \qquad (2.9)$$

This subtractive method is advantageous as the implementation is straight forward since there is no requirement for both codes to interact with each other. However, a force field is needed for the QM region which may not always be available or flexible enough to accurately reflect the changes that occur during a reaction. The MM region is also unable to perturb the electronic properties of the QM region and as such polarisation from the MM region cannot be modelled, which can lead to inaccuracies when modelling a system with inherent charge transfer events. Often the charges for the QM region are set to zero, simplifying the calculation by allowing the subtraction of the MM calculated QM region. As such there is no complicated boundary region calculation that can significantly alter the overall energy of the system.

The alternative method is Additive QM/MM Coupling (used within this thesis) in which the QM region(s) is embedded in the larger MM region and so the potential energy is the sum of MM terms, QM terms and QM/MM coupling terms described by this equation:

$$\boldsymbol{V_{QM/MM} = V_{QM}(QM) + V_{MM}(MM) - V_{QM-MM}(QM + MM)} \qquad (2.10)$$

Whereby **V_{MM}(MM)** describes the interactions in the MM region at the force field level, and the interactions between the two regions are treated by **$V_{QM\text{-}MM}$(QM+MM)**. These interactions can be treated by different methods with various degrees of accuracy and largely form three main types: Mechanical Embedding, Electrostatic Embedding and Polarisation Embedding.

Mechanical Embedding is considered the more simplistic methodology as it treats the interactions between both regions using force fields, which keeps the QM region in place by MM interactions. Here chemical bonds between the two regions are modelled using harmonic potentials, $\mathbf{V}^{\mathbf{bond}}$, and another harmonic potential describing the angles between a single QM atom and two MM atoms, $\mathbf{V}^{\mathbf{angles}}$. A periodic potential function, $\mathbf{V}^{\mathbf{torsion}}$, is also then used to model torsions between up to two QM atoms. Interactions between atoms that are more than three atoms apart are termed non-bonded interactions and are modelled by force field terms. These interactions comprise a van der Waals term which is modelled by a short-range potential, $\mathbf{V}^{\mathbf{LJ}}$, and an electrostatics term described by the coulomb potential, $\mathbf{V}^{\mathbf{Coul}}$. Like the subtractive method, an additive method using mechanical embedding cannot model polarisability as the electronic wave function is evaluated for the QM system in isolation. This means that the MM region cannot influence the polarisation of electron density in the QM region. The electrostatic interactions can be calculated by either using a fixed set of charges given by a force field, or by recomputing partial charges on the QM atoms at every step of the calculation. The latter method however requires a fitting approach to derive the atomic charges in a way that reduces the electrostatic potential at the surface of the QM region, as outlined in the works of Bayley *et al*[151] and Besler *et al.*[152] Typically, the short-range parameters are not updated during the calculation, which can result in errors should the character of atoms, such as hybridisation, in the QM region change; however, since this function is short-ranged the risk of errors remains minimal.

Expanding upon mechanical embedding is the second method which is electrostatic embedding (the methodology used within this thesis) which seeks to address the issue of modelling polarisability that is neglected in mechanical embedding and subtractive methods. The additive QM/MM scheme is particularly advantageous for the present case, as it makes it much easier to calculate the electrostatic embedding energy contributions. This time the electrostatic interactions between the two regions are addressed when computing the electronic wave function. Charged atoms in the MM region are included in the Hamiltonian as single electron operators, as described in the following equation:

$$\boldsymbol{h_i}^{\boldsymbol{QM-MM}} = \boldsymbol{h_i}^{\boldsymbol{QM}} - \sum_{\boldsymbol{J}}^{\boldsymbol{M}} \frac{\boldsymbol{e^2 Q_J}}{\boldsymbol{4\pi\varepsilon_0 |r_i - R_J|}} \qquad (\mathbf{2.11})$$

With $\mathbf{r}_i$ and $\mathbf{R}_J$ representing the positions of electron **i** and MM atom **J**. The one-electron operator for the kinetic and nuclear attraction energy of electron **i** is described by the $\mathbf{h}_i^{\mathbf{QM}}$ term. The M term in the summation is the number of atoms that have the partial charge $\mathbf{Q}_J$ in the MM region. These MM atoms are hence treated as nuclei with either non-integer or potentially negative charges.

In this approach the atoms in the MM region can now polarise the electron distribution in the QM region. Moreover, the atomic charges for the MM region provide a realistic description of the system. The interactions between the two regions are not solely down to electrostatics between atoms but other effects including polarisation, charge transfer, exchange, and Pauli repulsion. Force fields combine the effects of atomic charges and short-range parameters to give an overall realistic representation of the system; however additional effects are already partially represented in the short-range potential. Consequently, the electrostatic embedding method would require re-parameterisation for the charges of atoms in the MM region, as well as the short-range potential, realistically this is rarely practiced instead opting for use of the default force field parameters. The use of these standard atomic charges for the MM region runs the risk of over polarising the system at the boundary region, as the charges from the MM region can either attract or even repel electrons too strongly, resulting in the electron density overflowing into the MM region. This can lead to rather significant errors when using plane waves or large flexible basis sets. This issue can be accounted for by using a Gaussian distribution to 'smear' the charges as detailed in the works of Amra and Field.[153]

Unlike in the point-charge model, the Coulombic interaction between electrons in the QM region and this Gaussian distribution does not diverge if electrons approach atoms in the MM region, which circumvents the unphysical attraction of electrons to the charged atoms in the boundary region. When applying electrostatic embedding, charged systems can be calculated, however this must occur within a reasonable range and as such the total system charge should be close to neutral.

The final method is Polarisation Embedding which is arguably the most accurate method as this method now accounts for polarisability on the atoms in the MM region. This means that both the QM region and the MM region can now polarise each other. As seen when discussing interatomic potentials earlier in this chapter, one of the methods for modelling polarisation in MM methods is the shell model;[154] however, there are two other methods: the induced dipole method[155] and the fluctuating charge model.[156] Whilst using any of these methods the MM polarisations are calculated at each SCF cycle step of the QM wave function, as well as the polarisation requiring its own SCF approach, which results in a much more computationally demanding calculation. A compromise was proposed by Zhang *et al*[157] in which only a small shell of the MM region surrounding the QM region modelled polarisability; this way the main effects of polarisability between the two regions are accounted for, whilst also reducing the intensiveness of the calculation.

Finally, regardless of which embedding method is utilised, both the QM and MM regions are often joined across a chemical bond which needs to be accounted for. When cutting a bond in half this leaves an unpaired electron in the QM region which would otherwise be paired in a bonding orbital shared with the other atom from the MM region, as such some workarounds have been proposed to circumvent the issues of valences.

The most common method used, and the method used throughout this thesis, is to use what are known as 'Link Atoms'. These are monovalent atoms such as hydrogen (most common) but even methyl groups can be placed along the bond between the QM and MM regions and are only applied in the case of the QM calculation. These linkers introduce three additional degrees of freedom, however since it is placed at a fixed position along the bond in each step, these degrees of freedom are effectively removed and don't need to be accounted for. The forces acting upon the linker atoms are distributed over both the QM and MM atoms of the bond in accordance with the Lever rule, which is based on a simple balancing principle to weight effects to one side or another. Effectively the strength of a force and the distance that force acts along the bond between the two ends of the bond are assumed to be in a global equilibrium at the system temperature.

The alternative is the localised orbital method, which replaces the bridging bond by a doubly occupied orbital and assumes the electronic structure of the bond is unaffected by changes in the QM region. This method is beyond the scope of this thesis and subsequent studies carried out by Rodríguez *et al*[158] and Nicoll *et al*[159] compared the accuracy of both methods and demonstrated that there is little advantage to using this method over the linker atom method.

Depending on whether a covalent system or ionic system is being modelled, the boundary conditions between the QM region and MM region can be treated differently. In particular, when modelling ionic materials such as oxides, pseudopotentials are often employed,[160] however this is not usually the case when modelling covalent materials. These pseudopotentials are implemented to replace the core electrons of atoms within the boundary region with effective potentials, reducing the computational cost of the quantum mechanical calculation. The later chapters of this thesis employ an additive QM/MM scheme with electrostatic embedding protocols and connect the QM and MM regions via the hydrogen linker atom methodology.

2.4 Classical Molecular Dynamics (MD)

Molecular Dynamics is a computational method that utilises classical Newtonian descriptions of motion and applies them to a system with a specified starting state and specified boundary conditions. The effectiveness of the MD calculation is largely dependent on the applied force fields and the type of system they have been applied to including solids, liquids and biomolecules. Depending on the force field specified, as discussed earlier in the interatomic potential section, some effects such as the polarisability of atoms in the system may not be modelled. Leaving significant effects unaccounted for diminishes the effective ability to model the chemical reactivity of the system, and as such may require more intensive calculations such as *Ab-Initio* Molecular Dynamics (AIMD) covered in the next section.[161]

The development of molecular dynamics began in 1957 with Alder and Wainright's work on the compression of hard sphere systems.[162] The hard sphere model is a simplistic model in which a fluid comprises of particles that are treated as hard spheres and is used to study the behaviour of fluids in the absence of attractive forces between the particles. Using a hard sphere model, they were able to simulate the conversion process between a gas and a liquid. This work was later expanded upon in 1972 by Lees *et al*[163] by extending the non-equilibrium system with a velocity gradient to model time-dependent properties under extreme conditions. Anderson[164] later expanded upon this in 1980 by simulating fluid at a constant pressure and temperature, thus giving rise to the constant pressure molecular dynamics method. Three years later, Gillan and Dixon[165] expanded the theory to cover a greater range of systems by developing the molecular dynamics method for non-equilibrium systems. This was then followed in 1984 by Nose's[166] isothermal molecular dynamics method and Car and Parinello's[167] first principles molecular dynamics method in 1985, which allowed for the simulation of covalent bonding and metal systems by unifying electron theory and the molecular dynamics method. Finally, in 1991, Çagin and Pettitt[168] proposed the molecular dynamics method of a giant canonical ensemble to address the problems associated with modelling adsorption.

Molecular Dynamics simulations comprise of multiple steps; the first step involves the geometric, physical, and chemical modelling of the system from the calculation input geometry. For example, in this thesis a pure silica crystallographic structure is taken from the International Zeolite Association (IZA) database,[169] then one of the Si atoms is exchanged for an Al to create the desired chemical composition, with a charge compensating cation bound to the bridging oxygen atoms. The second step applies the initial conditions which includes the boundary conditions for the simulated system, the initial positions and velocities of the particles ensuring the initial step has the system at the correct temperature, and the selection of a potential function that is appropriate for the simulation. The three most commonly used functions are: the Lennard-Jones (L-J)[170] potential, Born-Mayer-Huggins (BMH)[171] potential and the Embedded Atom Method (EAM)[172] potential.

These potentials all address different aspects, with the Lennard-Jones potential arguably being the most simplistic, which models soft repulsive and attractive forces, specifically van der Waals interactions. However, the BMH potential is often used to describe the interactions between ions within an ionic crystal, and as such it is widely used when modelling silicate and aluminate systems such as zeolites. Finally, the EAM potential function is used to separate complex energy functions and so is frequently utilised to predict and simulate properties, structures, and mechanical behaviours of a large array of materials including various metals, non-metals along with composite materials.

The third step is the calculation of the forces of interaction and potential energy between particles, along with their positions and velocities. The calculation therefore requires consideration of static, dynamic, and quasi-static scenarios.[173,174] Finally, the fourth step involves obtaining the radial distribution function (RDF), pairwise distribution function (PDF), other correlation functions and coordination numbers (CN) from the obtained quantities such as temperature, pressure, and volume, thus detailing any changes in bond lengths, angles, and the degree of polymerisation.[164,175]

Molecular dynamics makes use of different algorithms for their simulations which are based on the finite difference method. The finite difference method is used as a way of integrating Newtonian equations of motion and detailing the propagation of time. Whilst there are many different algorithms, only the Verlet algorithm shall be covered within this section as it is the one used within this thesis. The Verlet algorithm[176] is very widely used because it has a relatively simple calculation process and the integration of the central points of a diffuse molecule's motion is very stable. The calculation process comprises of two main properties: position, **r**, and acceleration at time, **t**, thus represented by **r(t)** terms.

$$\boldsymbol{r_i}(\boldsymbol{t} + \delta\mathbf{t}) = -\boldsymbol{r_i}(\boldsymbol{t} - \delta\mathbf{t}) + \mathbf{2}\boldsymbol{r_i}(\boldsymbol{t}) + \sum_{j \neq i} \boldsymbol{f}\left(\boldsymbol{r_{ij}}(\boldsymbol{t})\delta\mathbf{t}^{\mathbf{2}}\right) \qquad (\mathbf{2.12})$$

These represent the position and acceleration of the atom at time increment, **t**, and the position, **r**, to calculate the position of the atom, **r(t+δt)**, with the time increment, **t+δt**. The downside to the Verlet algorithm is that it is not "self-starting", which means another algorithm is required to obtain the first few terms, and as such can lead to inaccuracies.[176]

Due to hardware limitations, the modelling of a system is limited and so Molecular Dynamics typically is not used to model very extensive systems containing millions of ions, and so the number of particles must be fixed at a certain value. Currently, Periodic Boundary Conditions[177] (PBC) are used to achieve this, which essentially means that when atoms or particles run outside the boundary of the model, the same number of particles are added back into the model from the opposite side, resulting in the fixed number of particles remaining constant.

2.5 *Ab-Initio* Molecular Dynamics (AIMDs)

Ab-Initio Molecular Dynamics is similar in many respects to Molecular Dynamics, but with one particular difference that significantly increases computational cost. The difference in *Ab-Initio* Molecular Dynamics, is that finite temperature dynamical trajectories are created using forces generated from the electronic structure calculations rather than interatomic potentials, *i.e.* the key distinction between AIMD and Classical MD methods is that the interatomic forces described by:

$$\frac{\partial \boldsymbol{U}}{\partial \boldsymbol{x}_{ik}\boldsymbol{x}_{jl}} = \mathbf{0} \qquad (2.5)$$

are calculated at each step using electronic structure methods.[178] As a result, this circumvents the key disadvantage of the Classical Molecular Dynamics method, by allowing for the modelling of bond breaking and formation, which cannot be modelled accurately using interatomic potentials. These are fundamentally important features when modelling reactions and the dynamical features of solvents, such as a sampling of different hydrogen bonding patterns, as there are many local minima separated by low barriers. The introduction of thermal energy in MD can overcome these barriers, coupled with bond breaking and formation capabilities, is a large part of the reason this thesis utilises AIMD in the final project instead of Classical MD. The larger computational cost previously alluded to, is intrinsic to the computational complexity arising from the need to perform large numbers of electronic structure calculations, which is required for sufficient sampling.

Ab-Initio Molecular Dynamics typically calculates the potential energy function with DFT or another *ab-initio* method at each step, but broadly come in two distinct varieties: The first is Born-Oppenheimer Molecular Dynamics (BOMD) in which the potential energy is minimised at each step. BOMD assumes that the system in question is comprised of ***N*** numbers of nuclei and ***N_e*** electrons and their wave functions can be treated separately, thus following the Born-Oppenheimer Approximation. This separation of wave functions allows for two levels of theory for each: the nuclei of the system can be treated classically on the ground-state electronic surface. The resulting Hamiltonian is of the following form:

$$\hat{\mathrm{H}} = \boldsymbol{T}_e + \boldsymbol{V}_{ee} + \boldsymbol{V}_{eN} + \boldsymbol{T}_N + \boldsymbol{V}_{NN} \equiv \hat{\mathrm{H}}_{elec} + \boldsymbol{T}_N + \boldsymbol{V}_{NN} \qquad (2.13)$$

Where the terms are defined as: Electronic Kinetic Energy, $\mathbf{T_e}$, Electron-Electron Coulomb repulsion, $\mathbf{V_{ee}}$, Electron–Nuclear Coulomb Attraction, $\mathbf{V_{eN}}$, Nuclear Kinetic Energy, $\mathbf{T_N}$, and Nuclear–Nuclear Coulomb Repulsion, $\mathbf{V_{NN}}$. Using $\mathbf{R_1}$, to $\mathbf{R_N \equiv R}$ to denote the nuclei positions then the classical dynamics of the nuclei can be described using the equation of motion:

$$\boldsymbol{M}_1\boldsymbol{R}_1 = -\nabla[\boldsymbol{\varepsilon}_0(\boldsymbol{R}) + \boldsymbol{V}_{NN}(\boldsymbol{R})] \qquad (2.14)$$

Whereby $\boldsymbol{\varepsilon}_0(\boldsymbol{R})$ represents the ground state eigen value at $\mathbf{R}$. However, as the ground state electronic wave function cannot be determined exactly through the Schrödinger equation, an approximation needs to be made. Normally the electronic structure used in AIMD is the Kohn-Sham formula that relates orbitals to electronic density. The most widely adopted approximations include local density, generalised gradient, and meta generalised gradient approximations (MGGAs), however these fail to treat dispersion accurately and so non-local functionals tend to be adopted. The above equation is integrated numerically at each step in basic AIMD equations and followed up by computing the forces via minimising the Kohn-Sham energy functional and the structural configuration at that part of the calculation. Care must be taken to perform this minimisation at a high level of accuracy to conserve the classical nuclear Hamiltonian.

Alternatively, there is the Car-Parrinello Molecular Dynamics method (CPMD)[167] in which the Kohn-Sham orbitals are given a fictitious time dependence described as $\boldsymbol{\psi_r(r)} \rightarrow \boldsymbol{\psi_r(r,t)}$. Dynamics are introduced for the orbitals that generates a minimised set of orbitals to subsequent minima related to the new nuclear configurations. This maintains the dynamics of an orbital at a designated temperature, $\mathbf{T_e}$, that is lower than the nuclear temperature, $\mathbf{T}$; however, the orbitals remain able to quickly relax in response to nuclear motion. As such $\mathbf{T_e}$ is primarily dictated by the choice of the initial orbital velocities, $\boldsymbol{\{\psi_i\}}$. The total motion of a system can be described by the Car-Parrinello Lagrangian, where coupled electron-ion dynamics are computed, and the electronic degrees of freedom are added as classical degrees of freedom, meaning the electronic degrees of freedom have an intrinsic inertia component, referred to as fictitious mass, $\boldsymbol{\mu}$, which is a function of energy multiplied by a squared time term. The orbital dynamics are hence described by a fictitious kinetic energy term that incorporates this fictitious mass term. The choice of fictitious mass term allows for the decoupling of the nuclear dynamics and by decreasing its value makes the calculation more computationally feasible. Larger values of $\boldsymbol{\mu}$ can be used if thermostatting techniques are applied to the orbitals, however this can lead to additional problems outside the scope of this section.[179]

By comparison to the BOMD method, the computational cost of each step is significantly lower, as there is not a required SCF cycle to make sure that the energies are consistent and force electrons to follow the nuclei in an adiabatic manner. The adiabatic energy scale separation of nuclear and electronic degrees of freedom is ensured by having the highest ionic phonon frequency be much smaller than the lowest electronic frequency.

This results in the fictitious mass, **μ**, acting as a scaling factor that trades accuracy for computational efficiency in contrast to the Born-Oppenheimer surface. This translates to an almost constant shift and so does not affect the nuclear forces present.

Using either method of *ab-initio* molecular dynamics provides an animated snapshot of the dynamics of a system. Analytical methodologies will be applied to AIMD trajectories within this thesis to contextualise the results of these simulations in a more quantitative way. This is achieved by calculating the Root Mean Squared Deviation (RMSD) of a system for each individual step of the simulation by applying the equation below:

$$\boldsymbol{RMSD} = \sqrt{\frac{\mathbf{1}}{\boldsymbol{N}}\sum_{\boldsymbol{i}=\mathbf{1}}^{\boldsymbol{N}} \boldsymbol{\delta_i}^{\mathbf{2}}} \qquad (\mathbf{2.15})$$

Here $\boldsymbol{\delta_i}$ is the distance between atom **i** and the optimised reference atom **N**. This means that each step of a simulation can be defined by the squared sum of deviation/displacement of all atoms within the system from the initial starting structure of the simulation. This principle does not have to be applied to all atoms in a system but can instead be applied selectively to only specific atoms in a larger system, forming a component analysis that details the overall changes in bond lengths throughout the duration of the simulation.

2.6 Anharmonic Simulations (GVPT2)

Computational modelling of spectra using quantum mechanical methods has been developed over the years to achieve a high level of accuracy and effectiveness. The computation of IR and Raman intensities requires the evaluation of the transition matrix for the dipole moment and polarisability between the calculated initial and final states. Using the Born-Oppenheimer approximation, vibrational calculations can be defined by the potential energy surface term. Currently calculations typically rely on a double harmonic approximation in which the potential energy surface calculation only reaches a second order calculation.[180] To improve upon the accuracy of these calculations the use of scaling methods is often commonly applied to the harmonic wave numbers, which allows for the correction of band positions for vibrational modes.

Harmonic spectra can be calculated in different ways depending on the code used, VASP[74–78] for example calculates the harmonic modes using a Finite Difference Time Domain (FDTD) approach. FDTD is a numerical technique developed by Yee and Chen,[181] that uses Maxwell's coupled partial differential equations to solve electromagnetic contributions in frequency domains to produce harmonic spectra. Alternatively, in other codes like ORCA[182] the harmonic modes are calculated using a numerical frequency approach, whereby numerical methods solve differential equations that describe the behaviour of a wave form. This is then used to determine the harmonic frequencies. Both of these approaches use internal dipole characterisations to produce accurate intensity values, and the data can then be scaled to produce accurate frequency values. The drawback to using these scaling methods is that the intensities of vibrations are calculated relatively, rather than calculating specific intensity values. As such there remains a need to distinguish between the low-intensity features attributed to non-fundamental vibrations from the most common species in a system and the fundamental contributions of less common species. To obtain reliable vibrational wave numbers for larger systems, a dynamical or time dependent approach could be applied, which presents a challenge in terms of both accuracy and hardware capabilities.[183]

To circumvent hardware limitations multiple time-independent methodologies have been devised, with one of the most effective methods being based on second-order vibrational perturbation theory (VPT2), which is a very popular method for the treatment of medium to large semi-rigid systems when applied to a 4th order normal mode representation of the anharmonic force field. An adjusted VPT2 model with reduced dimensionality can also be applied to overcome issues encountered when modelling the electronic structure for multidimensional anharmonic potential energy surfaces.

A system has **N** internal degrees of freedom, and vibrational energies are calculated by a series of equations:

Fundamentals:

$$\boldsymbol{v_{1i} = \omega_i + 2\chi_{ii} + \frac{1}{2}\sum_{\substack{j=1 \\ j\neq i}}^{N} \chi_{ij}} \qquad \mathbf{(2.16)}$$

Overtones:

$$\boldsymbol{v_{2i} = 2\omega_i + 6\chi_{ii} + \frac{1}{2}\sum_{\substack{j=1 \\ j\neq i}}^{N} \chi_{ij}} \qquad (\mathbf{2.17})$$

Combinations:

$$\boldsymbol{v_{1i1j} = \omega_i + \omega_j + 2\chi_{ii} + 2\chi_{jj} + 2\chi_{ij} + \frac{1}{2}\sum_{\substack{k=1 \\ k\neq i,j}}^{N} \left[\chi_{ik} + \chi_{jk}\right] = v_{1i} + v_{1j} + \chi_{ij}} \qquad (\mathbf{2.18})$$

Here the **ω** term represents the harmonic wave number associated with vibrational mode **i** or **j**. The third and fourth derivatives (cubic and quartic force constants) for the normalised potential energy, **V**, to dimensionless coordinates, **q**, are described by terms $\mathbf{k_{ijk}}$ and $\mathbf{k_{ijkl}}$. Unfortunately, vibrational energies are negatively affected by Fermi resonances which occur when the wave number is either equal to a sum of two modes or twice the value of a single mode ($\boldsymbol{\omega_i=2\omega_j}$ or $\boldsymbol{\omega_i=\omega_j+\omega_k}$). This results in errors in the anharmonic correction, as such a few methods exist to mitigate this factor, but arguably the most popular is that developed by Martin *et al,*[184] who devised a method of determining the resonant terms which could then be removed via a method called DVPT2 (Deperturbed-VPT2). These terms can be reintroduced in a second step through a variational treatment referred to as Generalised VPT2 (GVPT2). Specifically with this method it is possible to redefine these resonance terms, which can allow for a direct comparison to experimental results by removing these resonant terms and treating them variationally.

Vibrational frequencies are calculated in most quantum mechanical packages as part of the harmonic approximation. To account for anharmonicities within the electronic potential, harmonic frequencies are scaled down by a corrective factor, with values optimised based on whether it is dependent on the method or the basis set. Different scaling factors for specific vibrational modes may be utilised to achieve better parity with experimental values. Various methods exist to reduce the computational cost of modelling anharmonicity: VSCF, VSCF-PT2, cc-VSCF, VCI-P, VT2 and the previously discussed GVPT2. The work carried out within this thesis makes use of the last option, the generalised second-order perturbation theory (GVPT2).[185] This method combines perturbative developments to deal with weakly coupled terms, and tightly coupled ones are treated variationally.

In each of the previously mentioned methods of calculating vibrational frequencies, the calculation of the Potential Energy Surface (PES) is required as a prerequisite. This energy surface is approximated by a quartic force field potential using the second, cubic and quartic derivatives of the PES at the equilibrium geometry. The first, second and third derivatives of the dipole moments must also be calculated to generate the infrared intensities. To achieve a good agreement with experimental data high level *ab-initio* methods are required. Large systems can be treated by hybrid QM/MM approaches, where the geometry and harmonic modes included in the QM region can be modelled at a high level of theory, such as CCSD(T) or B2PLYP and the anharmonic corrections can be calculated at a lower level of theory with DFT or even semi-empirical methods.

The methodology utilised in this thesis makes use of the B3LYP functional[110,111] which limits the size of the system that can be modelled. Hence the anharmonic calculations run in this work utilise hybrid quantum mechanical molecular mechanical methodology to minimise the system size modelling the frequencies. To reduce the computational cost and compensate for a lack of restart functionality in the anharmonic calculations, the geometry optimisations (in relation to energy) are calculated separately beforehand.

CHAPTER 3

Computational Investigation into Zeolite & AlPO Lattice Energies

3.0 Abstract

This chapter presents a comprehensive study of calculated lattice and cohesive energies for pure silica zeolites and aluminophosphates. Computational techniques have proven a useful tool in the realm of catalysis; however, it is important to understand the strengths and limitations of these particular models. This chapter seeks to benchmark interatomic potential and high-level quantum mechanical techniques in the modelling of microporous materials against experimental energies for their use in future modelling work carried out within this thesis. Molecular mechanical and quantum mechanical methodologies based on Density Functional Theory (DFT) are employed to calculate respectively lattice and cohesive energies of purely siliceous microporous structures, whose values are reported relative to that of α-quartz. α-quartz was used as a reference instead of Stishovite, as it is the highest density phase of silica that comprises of purely tetrahedral silica units. Stishovite is a metastable high-density phase resulting from high pressures and comprises of octahedrally coordinated silica and as such a direct comparison would not be valid. These calculated lattice and cohesive energies were subsequently compared to experimental values from the literature. The results confirm that zeolites are metastable in relation to α-quartz, with cohesive energies from DFT methods yielding results closer to experimental calorimetric values than the calculated lattice energies based on interatomic potential methods.

The shell model approach was proven to calculate lattice energy values closer to experimental values than the partial charge rigid ion model. Interatomic potential shell methods are shown to reproduce trends observed in DFT reliably for a greatly reduced computational cost, despite overestimating lattice energies; but potential based models could also have problems modelling partially disordered systems, which can become less prominent when calculated with DFT methods as shown with ITQ-39. Additionally, it is noted that the lack of modelling polarisability can lead to un-physical bond angles in the minimised system, as seen in the works of Salvador *et al*[129] and as such the shell model is superior for modelling these metastable structures. Calculated lattice and cohesive energies for pure alumino-phosphate structures using these methods also produce very similar trends of averaged energy per T-site against density, with a linear trend of increasing energy with decreasing density in agreement with existing literature.[186] Interestingly, the interatomic potential model yielded energies in closer agreement to experimental data than the

higher-level theory of DFT, the reason for which is unclear but may be attributable to the stronger deviation of the idealised structures used within the calculations from the real systems used in experiments, which may contain additional framework cations and defects.

3.1 Introduction

It has been well established that microporous materials are metastable with respect to dense polymorphs,[187,188] with important correlations between the silicious zeolite energies with respect to α-quartz and framework density.[189,190] Computational methods now allow us to both predict new zeolitic structures and extensively model the structures and energies of microporous frameworks.

There have been various studies assessing the extent to which different computational methodologies can quantitatively predict experimental thermodynamic data on microporous materials. The development of computationally inexpensive interatomic potentials was one of the first methods that achieved reliable results and subsequently received wide adoption. Initial potentials took the form of a two-body Buckingham potential that would describe the Pauli exclusion principle and van der Waals energy of an interaction between two atoms that are not directly bonded to each other.[26]

Kramer *et al*[32,191] initially modelled α-quartz by deriving potentials for individual silica tetrahedra using a partial charge model, based off *ab-initio* calculations, which initially led to inaccurate energies of the bulk system. Subsequently, Kramer *et al*[191] derived potentials that were also fitted to macroscopic experimental data, and these were found to scale well to other microporous silica structures.

This method was expanded on by Sanders *et al*[31] due to the limitations of the two-body potential model to model elastic, dielectric and dynamical properties with sufficient accuracy. Sanders *et al*[31] included several new features to enhance the accuracy of their potentials including a three-body term. This bond-bending term was introduced to account for the torsion between tetrahedral units. Arguably the most defining feature of this new potential was the shell model approach, whereby the rigid ion now formed the core of an atom with a shell surrounding it, which allowed for the modelling of polarisability in the system which proved a significant step in modelling molecular systems.[31] The success of this methodology has hence led to widespread adoption across multiple studies.

The other side of the computational modelling spectrum is high level quantum mechanical methods such as Density Functional Theory (DFT), as detailed in this thesis' Methodology section. As was also illustrated in the Introduction of this thesis, DFT has proven popular for modelling zeolitic structures used in catalysis, aiding in the understanding of catalytic reaction pathways, structural stabilities, and mechanical properties.[35,36,192,193] This study seeks to benchmark interatomic potential and high-level quantum mechanical techniques in the modelling of microporous materials against experimental energies for their use in the later chapters of this thesis. It seeks to provide a comparison of different interatomic potential methods, the previously outlined partial charge rigid ion model and the formal charge core-shell model, then assess their ability to reproduce lattice energies in comparison with experimental data. Furthermore, we seek to utilise Density Functional Theory (DFT) methods to model the same structures. These results will be contextualised by a comparison with both the results from the interatomic potential methods and by a broader comparison to experimental data.

Additionally, we note that this study is similar to that conducted by Zwijnenburg *et al*[186] in which a similar approach is applied utilising the Sanders and van Beest potentials for a small selection of 15 siliceous structures and dense phases. These structures were selected as they contained three-membered rings, focussing primarily on the stability of the larger structures as a result the inclusion of these features and their frequency within the larger structure. Zwijnenburg *et al*[186] then proceed to compare the data to DFT calculations using the hybrid B3LYP functional to yield energies closer to experimental results than with the interatomic potential methods. However, where our study differs from this is the inclusion of structures that do not contain these strained 3-membered rings producing a much broader trend with a significantly greater sample size. Furthermore, we use the PBE generalised gradient approximation functional, which is less accurate but reduces the computational cost of the calculations which allows for the application of a finer K-point mesh to more accurately incorporate long range order effects.

Alumino-phosphates (AlPOs) have likewise attracted a large amount of interest over the years and also have an extensive history in the realm of computational modelling.[129,192,194–199] Energies are averaged to each tetrahedral site, despite the tetrahedral units alternating between AlO_2 and PO_2, which could potentially be energetically different from each other but are treated equally for the purpose of this study. Additionally, these averaged energies of metastable phases are contrasted to the averaged tetrahedral energies of the lowest energy and most dense phase tetrahedrally coordinated alumino-phosphate structure Berlinite. The trends derived from the results of these calculations are contrasted with the energies from experimental results in published work.

3.2 Methods

For the first part of this project, interatomic potential based methods are employed to perform both lattice energy minimisations and free energy minimisations on pure-silica microporous materials. To perform these calculations, we used the General Utility Lattice Program (GULP)[200–205] which required only modest computational resources and so were run on a local computer. The second part of this study employs the semi-empirical quantum mechanical method of Density Functional Theory (DFT) which was run on a high-performance supercomputer.

The GULP program sums the electrostatic interactions and short-range potentials between different atomic species and has proved to be a valuable tool when modelling microporous systems.[195–197,206] Most of this study employs the shell model approach where the silicon atoms act as a single formal point-charge which interacts via a specified force field, whilst the oxygen atoms comprise of a core and a shell component. This allows for the modelling of polarisability by allowing forces to act on the shell, which in turn cause displacements which translates into the formation of a dipole. Additional calculations utilised the simpler rigid ion model, where all atoms in the system are treated as point-charges and there is no modelling of polarisability.

It should be noted that both these potential based methods utilise potentials of the Buckingham form below:

$$\phi_{12}(\boldsymbol{r}) = \boldsymbol{A}\boldsymbol{exp}\left(\frac{-\boldsymbol{r}}{\boldsymbol{\rho}}\right) - \frac{\boldsymbol{C}}{\boldsymbol{r}^{6}} \qquad (\mathbf{3.1})$$

Here we take A, ρ and C to be constants, whilst the coulombic term is still present it is not included, as it is not classified as a short-range term. The shell model approach utilised potentials derived by Sanders *et al*[31] and are given in ***Table 3.1.*** using a cut-off of 12 Å. A three-body term is applied to the shell model via a quadratic energy term defined by $\mathbf{U_{ijk}=\frac{1}{2}K_B(\theta_{ijk}-\theta_{0,ijk})^2}$ whereby $\mathbf{(\theta_{ijk}-\theta_{0,ijk})}$ is the deviation from the idealised tetrahedral angle for O-Si-O of 109.47 ° and K_B is a harmonic force constant for the bond bending component of the potential, so the directionality of the Si-O bonding is represented.

Buckingham Potential	**A (eV)**		**ρ (Å)**	**C (eV· Å^6)**
Si^{4+}- O^{2-}	1283.9073		0.32052	10.66158
O^{2-} - O^{2-}	22764.3		0.149	27.88
Core – Shell Potential			**k (eV·Å^{-2})**	
O^{2-}			74.92	
Coulombic Charges (e)		**Si^{4+}**	**O^{2-}core**	**O^{2-}shell**
		+4	+0.86902	-2.86902
Three-Body Term		**Si core O shell O shell**		
K (eV rad^{-2})	**Θ_{0ij} (°)**	**Cut-offs (Å)**		
		i-j	j-k	i-k
2.09724	109.47	1.8	1.8	3.2

Table 3.1. Zeolite Core-Shell Interatomic Potentials as derived for silica structures by Sanders *et al*.[31]

In the case of rigid ion calculations, a partial charge model was adopted, using the parameters derived by Van Beest *et al,*[32] given in ***Table 3.2.*** These potentials employed a cut-off of 4 Å, close to that used in the original parameterisation, as confirmed through benchmarking shown in ***Table S3.1.*** (See Appendix) and yields energies in closer agreement with the experimental data. We noted earlier that there is no consideration of polarisability, and it should be noted that this model does not include bond-bending terms.

Buckingham Potential		**A (eV)**	**ρ (Å)**	**C (eV·Å^6)**
$Si^{2.4+}$- $O^{1.2-}$		18003.7572	0.2052	133.5381
$O^{1.2-}$ - $O^{1.2-}$		1388.773	0.3623	175.0
Coulombic Charges (e)		**$Si^{2.4+}$core**	**$O^{-1.2}$core**	
		+2.4	-1.2	
Three-Body Term			**Si core O shell O shell**	
K (eV rad^{-2})	**$\theta_{0,ij}$ (°)**		**Cut-Offs (Å)**	
		i-j	j-k	i-k
2.09724	109.47	1.8	1.8	3.2

Table 3.2. Zeolite Partial Charge Rigid Ion Potential Parameters derived by Beest *et al*.[32]

Full geometry optimisations of both cell dimensions and atomic coordinates were carried out using these parameters, resulting in a minimal volumetric increase in the unit cell size of around 2 % as the structure relaxes. This expansion can reach as much as 10 % for a structure like CIT-5, most probably as a result of CIT-5's large pore size consisting of a 14 T-site ring, which creates very large pores that allows for significant volumetric change upon compression. For those systems with larger deviations after optimisation, the experimental composition typically differs appreciably from the purely siliceous model used here.

To contextualise the results of these internal energy values, additional free energy minimisation calculations were also run using GULP.[201–205,207] This methodology calculated bulk geometrical lattice properties under a constant pressure and a temperature of 298 K, allowing for the calculation of vibrational entropies of the system. However, these generated very small differences between the lattice energies and free energies (less than 1 % difference in averaged T-site energy values) as such the entropic contributions can be omitted from this study.

Buckingham potentials were also applied for interatomic potential calculations on AlPOs with a shell model approach, as derived by Gale and Henson.[207] These potentials were fitted to Berlinite, the alumino-phosphate equivalent to α-quartz, as it is the densest and lowest energy tetrahedrally coordinated phase polymorph alumino-phosphate and are reported in ***Table 3.3***. As such the averaged tetrahedral site energy of Berlinite serves as the reference energy for the AlPO study. The structural data for the Berlinite reference energy was taken from the work of Sowa *et al.*[208]

Buckingham Potential	***A*** **(eV)**		***ρ*** **(Å)**	***C*** **(eV·Å^6)**
Al^{3+}- O^{2-}	1460.30		0.29912	0.00
P^{5+}- O^{2+}	877.34		0.35940	0.00
O^{2-} - O^{2-}	22764.3		0.149	27.88
Core – Shell Potential			**k (eV·Å^{-2})**	
O^{2-}			74.92	
Coulombic Charges (e)	**P^{5+}**	**Al^{3+}**	**O^{2-}_{core}**	**O^{2-}_{shell}**
	+5	+3	+0.86902	-2.86902
Three-Body Term			**Td core O shell O shell**	
K (eV rad^{-2})	**θ_0 (°)**	**Cutt-offs (Å)**		
		i-j	j-k	i-k
2.09724	109.47	1.8	1.8	3.2

Table 3.3. AlPO core-shell potentials as derived by Gale and Henson.[207]

The higher-level density functional theory (DFT) calculations were carried out using VASP.[74–78] Previous studies have assessed the ability of various PBE functionals[87] to model neutral-framework zeotypes.[209] In this study we implemented the Perdew Burke-Ernzehoff (PBE)[87] generalised-gradient-approximation (GGA) tag[87] for treatment of valence electrons which were generated with conventional LDA reference configurations,[210] whilst core electrons are treated by PAW potentials.[78] A K-point mesh of 5 x 5 x 5 was implemented to account for long range order effects, and the use of an odd number of K-points negates the need to tailor the mesh to the unit cell's dimensions and as such places the unit cell in the middle of a large reciprocal space. A Gaussian smear was applied which is typically applied to metals and ensures more of the K-points are on the Fermi surface. Long range dispersion forces have been shown to play a significant role when modelling porous materials as displayed in the work of Román-Román and Zicovich-Wilson,[211] and as such the Grimme-D3 dispersion correction[88] was applied to our calculations, as this has been shown to drastically improve the modelling of microporous structures.[212] A 520 eV planewave cut-off was used as it gave a reliable convergence criterion, along with a force convergence of -0.01 and an SCF cut-off of 0.00001 eV.

Both interatomic potential and DFT calculations used initial structural data files provided by the Structure Commission of the International Zeolite Association (IZA-SC)[169] with the dense phase α-quartz structural data taken from the work of Ogata *et al*.[213]

3.3 Results and Discussion

Lattice energies are normalised with respect to the number of tetrahedral units (T-sites) and their difference in energy from the densest, low energy stable polymorph for the respective material type and reported in kJ mol^{-1}. For zeolite calculations, α-quartz is used as a reference as it is the lowest energy tetrahedrally coordinated silica polymorph as a function of density, disregarding any higher-pressure phases. α-quartz was benchmarked and gave a close agreement to values found in the literature -1,2418 kJ mol^{-1} compared to -1,2414 kJ mol^{-1} from the work of de Leeuw *et al,*[206] an error below 0.05 %, and so was well within acceptable margins of error. Whilst using the same methodology there was a minor difference, which could arise from converging to a slightly different minimum or as a result of compiling a more modern version of the code (GULP 5.1), with small differences in some of the computational settings. However, the results are well within the expected margin of error and as such confirm the reliability of the code.

Free-Energy Minimisation calculations were performed on a selection of 13 structures with up to 24 T-sites; to determine how large the entropic effects are for ambient temperatures. Admittedly, this slightly biases the sampling away from lower density phases, however we found the percentage difference to be below 1 % of the absolute lattice energies, hence the vibrational entropic contributions are below the intrinsic error from the theory used or the inherent experimental error and can be deemed negligible.

Using the shell model; all calculated structures transpire to be metastable in relation to α-quartz, with a strong correlation to density reported as atomic mass (u) per cubic angstrom (Å^{-3}) using the volumes from the IZA database and not from the result of optimisation to allow for direct comparisons later in the study. A mostly linear trend is reported in line with expectations and displayed in ***Fig. 3.1,*** with a full table of modelled structures provided in the supporting information of this chapter. Some substantial deviations from this trend are observed in several frameworks (FWs) most notably JOZ, WEI, EDI, LOV and NAB. A potential reason for these deviations is the composition of the 'real' experimental structure compared to the pure silica structure that was modelled. For instance, in the case of the WEI framework, the real structure is not a pure aluminosilicate as the lattice contains P, Be and Ca atoms which could contribute to the energetic discrepancy. The same caveat can be applied to the other structures as they also could be influenced by contributions from other metal ions: JOZ contains Be, LOV has Na and Be within its framework, NAB contains Be and Na, whilst EDI contains Ba. Additional outliers such as AHT, AFY and JNT are synthesised as AlPO structures and not aluminosilicates, with JNT also containing Mg atoms within the crystal structure, whilst we calculated these systems as pure silica. ITQ-39 is a partially disordered material (intergrowth) which could be a significant factor that could affect its overall lattice energy. These results from the interatomic potentials are in line with the earlier findings of Henson *et al.*[214]

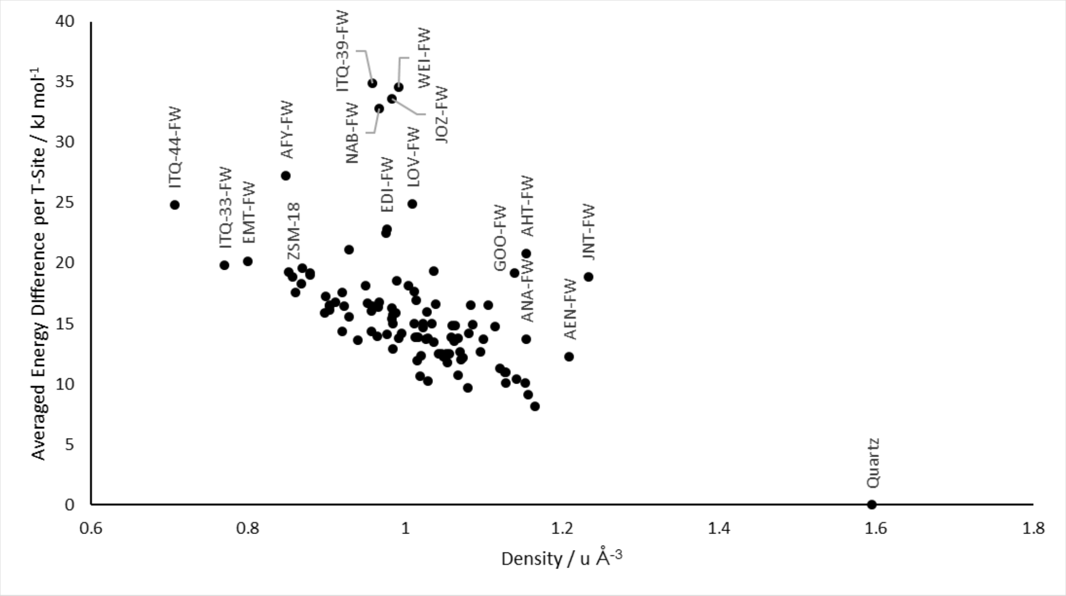

Fig. 3.1. Interatomic Potential Zeolite Lattice Energies Relative to α-quartz against density of the unit cell as a function of atomic mass (u) of all the atoms in the unit against volume (Å^{-3}) of the unit cell.

In the case of the rigid ion model, partial charges are utilised to determine the extent and effect of ionic charge on the relative energies of microporous and dense phases of silica by effectively modelling a lower level of charge transfer. The Buckingham potentials applied were derived by Van Beest *et al,*[32] and a selection of structures were calculated based on the availability of experimental data, a 4 Å cut-off was applied with these potentials which was determined through benchmarking as shown in ***Table S3.1****.* A 3 Å cut-off can result in energies much closer to experimental values but can also yield negative energies on other structures, by contrast any cut-off above 4 Å gives energy values that are too high when compared to the reported experimental values. A comparison between the shell model and rigid ion model can be seen in ***Table 3.4***., where it is evident that generally the rigid ion model exaggerates the lattice energies relative to α-quartz compared to the shell model, most probably due to the lack of modelled polarisability resulting in un-physical linear bond angles as shall be discussed in the next paragraph. There are two structures that defy this general trend; BEA and EMT give lower energies than the shell model approach. The reason for this is unclear, but the BEA structure is a partially disordered material (intergrowth) which may be relevant, as previously ITQ-39 also had comparatively trend defying behaviour from the general trend observed for the shell model.

Structure	Van Beest / kJ mol^{-1}	Sanders / kJ mol^{-1}	ΔB-S / kJ mol^{-1}
EMT	19.02	20.14	-1.12
BEA	13.50	14.39	-0.89
ITE/ITQ-3	14.41	14.12	0.20
IFR/ITQ-4	15.71	14.99	0.72
AST	19.23	18.15	1.08
ISV/ITQ-7	17.92	16.44	1.48
CHA	17.74	16.14	1.60
STT/SSZ-23	16.53	14.70	1.83
FER	13.68	11.78	1.90
MEL/ZSM-11	13.02	10.76	2.26
MFI/ZSM-5	12.48	9.68	2.80
MWW/ITQ-1	17.39	14.37	3.02
MTQ/ZSM-12	11.48	8.16	3.32
CFI/CIT-5	16.65	12.65	4.00
MEI/ZSM-18	23.39	18.85	4.54
AFI	16.76	11.93	4.83

Table 3.4. Van Beest vs Sanders Potentials: Energy differences of siliceous zeolites with respect to α-quartz, averaged to the number of tetrahedral sites in the unit cell. Where ΔB-S is the difference between Van Beest and Sanders averaged T-site energies.

The partial charge rigid ion model lacks a three-body term, which is included in the Sanders potentials; therefore, there is no description of bond bending energies for the O-Si-O bond angles. Additionally, there is no explicit description of polarisability, unlike the core-shell description in the Sanders potential model. As a result of the omission of these terms, systems have shown structures can minimise with bond angles of 180° (linear). The work of Ruiz-Salvador *et al*[129] concluded that it was necessary to include a representation of the polarisability of oxygen to remove these linear bond angles between Al-O-P in the simulated structures, and we demonstrate the same phenomenon here with pure silica structures. We note here that linear bond angles of 180° are observed in the minimisation of the pure silica

CIT-5, FER and ITQ-1 structures with the van Beest potentials, and 178.3° in ZSM-5 across Si-O-Si bonds, which could be related to the higher energies of these structures; however other structures that do not contain linear bond angles are also higher in energy than their shell model counterparts, such as ZSM-18 which has one of the largest energy differences from the shell model. For this reason, a shell model would be more suitable than the rigid ion model for modelling the molecular mechanical environments during hybrid QM/MM calculations.

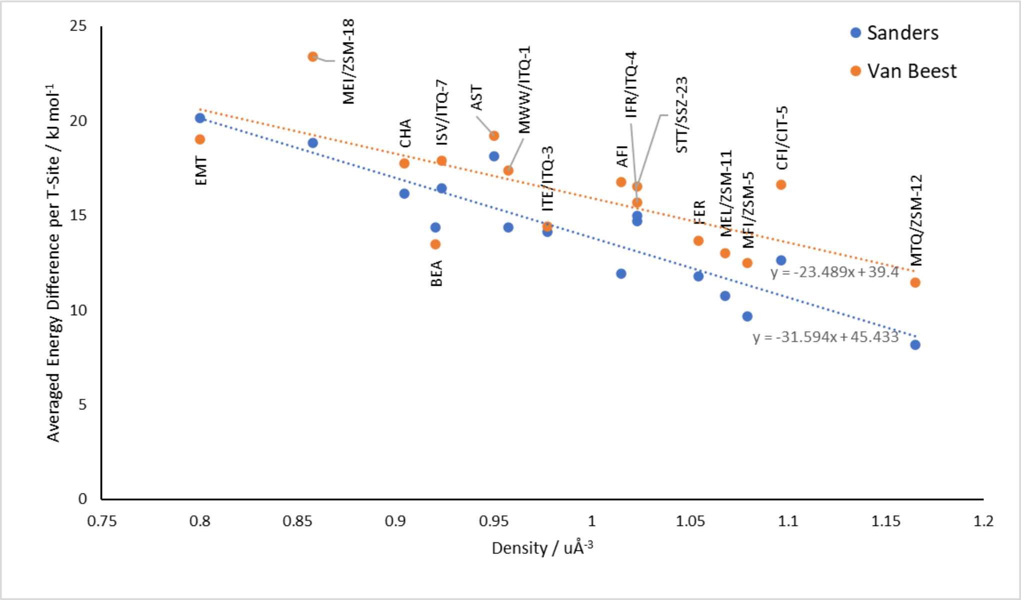

Fig 3.2 Comparison of averaged T-site zeolite energies for both the shell model and rigid ion model plotted against density. Line colours: Sander's potentials: blue, Van Beest potentials: orange.

A comparison between the two models is plotted in **Fig 3.2** against density (u Å^{-3}) in atomic mass (u) per cubic volume of the unit cell (Å^{-3}) taken from the IZA database. The reported volumes were used instead of post optimisation volumes to allow for an easier comparison of the structure's energy from the two methods. Here the Sanders potentials have a steeper gradient of -31.6 kJ mol^{-1} u^{-1} Å^{-3} compared to the van Beest structures with a gradient of -23.5 kJ mol^{-1} u^{-1} Å^{-3}. As a result, the energies provided by the van Beest potentials deviate significantly from those of the Sanders potentials at higher densities, but these differences reduce when modelling less dense metastable structures. Despite this the Sanders potentials are generally lower in energy and also closer to the experimental energies as shown below in **Table 3.5** and shall be discussed later.

The shell model approach was again employed to model a selection of alumino-phosphates (AlPOs) where both the aluminium and phosphorus cations act as rigid ions, whilst the oxygen atoms again have a core and a shell that models polarisability. The potentials used for the AlPOs were taken from Gale and Henson[207] and were fitted to Berlinite, which as noted is the lowest energy most dense tetrahedrally coordinated alumino-phosphate, and as such was used as a reference for the averaged T-site energies. All of the AlPO systems and their calculated energies are provided in the supporting information that accompanies this chapter. A similar trend to the siliceous zeolites is displayed with Berlinite as the lowest energy and densest phase, whilst all other AlPOs scale linearly with energies relative to density, as can be seen in ***Fig. 3.3.*** with all the energies reported in ***Table S3.3***.

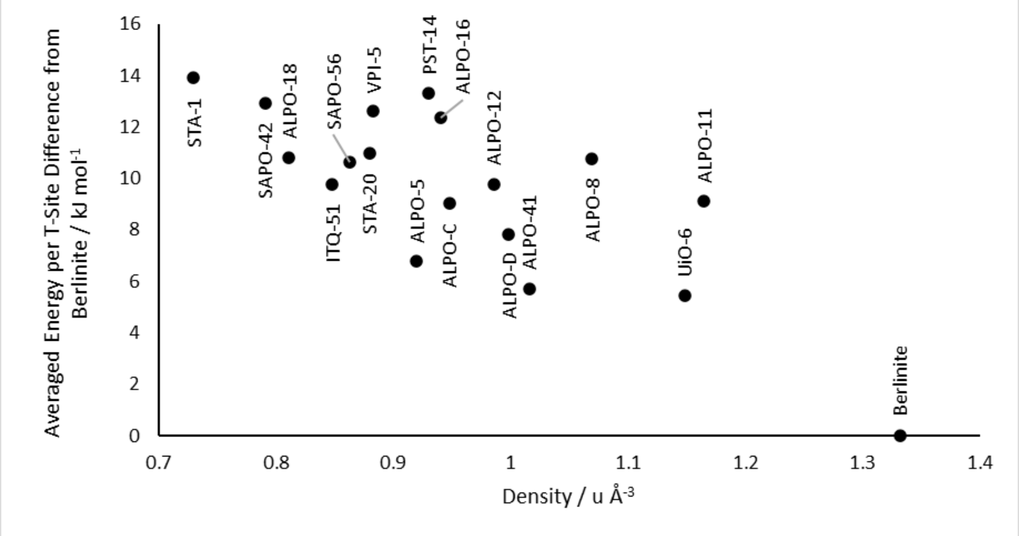

Fig. 3.3. Interatomic Potential AlPO Lattice Energies Averaged per T-site Relative to Berlinite vs Density.

As with the previous section of this work the DFT cohesive energies were averaged to the number of tetrahedral sites and the energies reported with respect to those of α-quartz. The energy values are reported in ***Table S3.4.*** and when plotting the energy difference against density, a linear trend is observed and is displayed in ***Fig. 3.4.,*** which reaffirms the established relationship between density and cohesive energy. A similar distribution of zeolite energies to the interatomic potentials is observed, with most structures occupying a similar relative position on the graph as they did in the interatomic potential study.

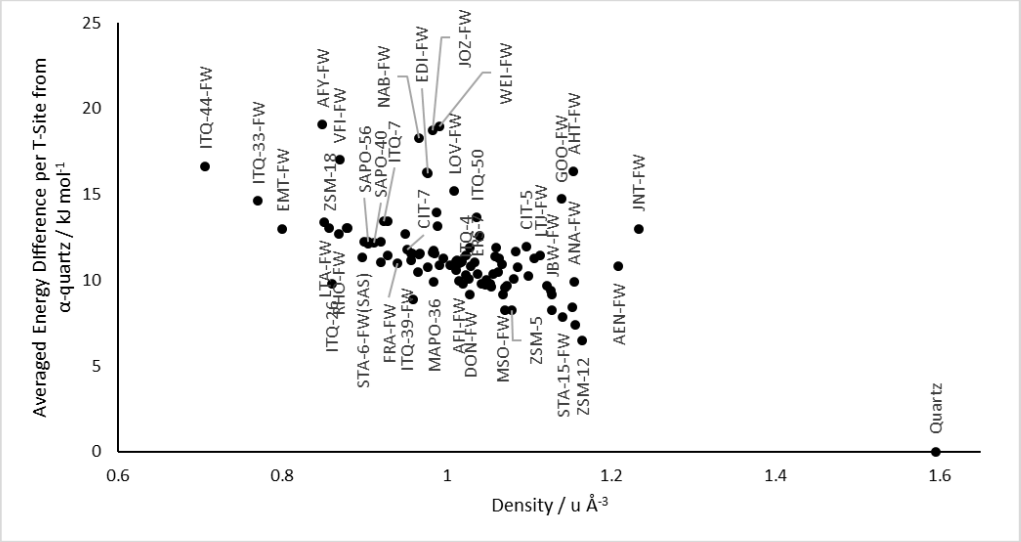

Fig. 3.4. DFT Zeolite Energies averaged per T-site with respect to α-quartz vs density.

All calculated zeolite structures and their cohesive energies from DFT are detailed in the supporting information that accompanies this chapter. The linear trend observed in both zeolite studies highlights the correlation between an increase in lattice energies (interatomic potentials) or cohesive energies (DFT) as zeolite porosity increases. As previously mentioned, these results fall in line with expectations with the generally accepted idea that these zeolites are metastable structures with respect to the dense structures. The calculated energies plotted against densities follow a similar trend to the interatomic potential based method, which is more explicitly shown in **Fig. 3.6**. Many of the structures deviating from the general trend in both studies are the same, such as NAB, WEI, EDI, LOV and JOZ, which suggests that the previous reasoning regarding the influence of framework cations of different species over the energies of these outlier structures is sound.

These higher-than-expected energies transfer across the different methods and are most likely attributable to inherent structural characteristics. The largest discrepancy between the two methods is that of ITQ-39; with DFT this zeolite's energy is much lower than with the interatomic potential method, as well as more closely following the established trend as is observed in **Fig 3.5**. This could imply that the modelling of electronic contributions, as achieved with DFT, can have a rather significant effect when it comes to modelling partially disordered materials. ITQ-26 is also reported to have a lower energy, this time lower than the general trend, however the 'real' lattice once again contains different elements such as Germanium, which results in an inaccuracy when modelling the structure as a pure silica framework.

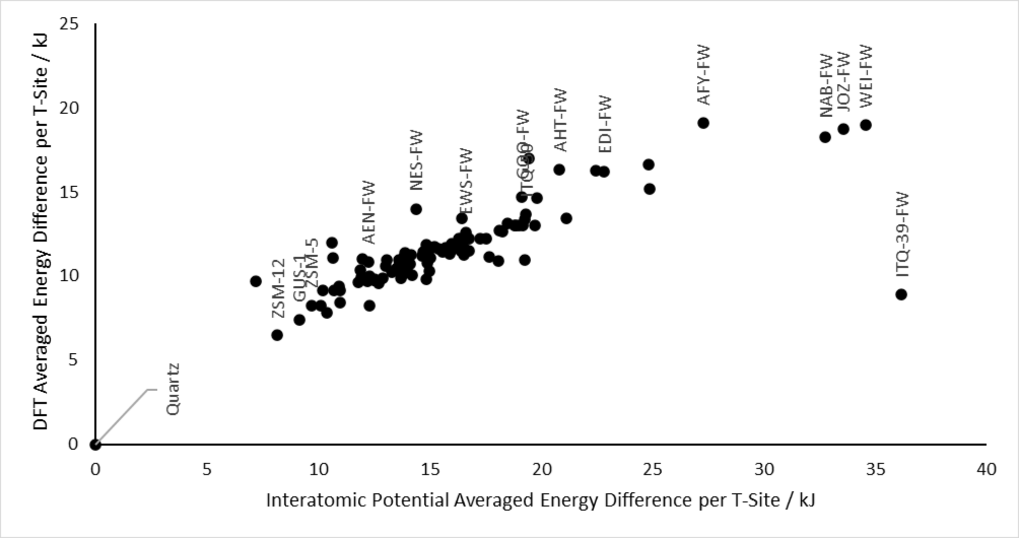

Fig. 3.5. Correlation between DFT and Sanders' Interatomic Potentials averaged energy per T-site difference from α-quartz.

When comparing the trends of both interatomic potential and DFT averaged T-site energy differences against unit cell density as displayed below in **Fig. 3.6** we can see the same general trend. However, it becomes apparent that the outlier structures from the interatomic potential study have a much larger difference in energy from the general trend than is observed in the DFT study. When factoring in these outliers, the trend line for interatomic potentials is skewed to a steeper gradient, although a steeper gradient would be observed for the potentials even if these were omitted. The result is that there is a greater energy difference between the two methods as systems being modelled become less dense. An interesting observation is that the trend lines end up intersecting at an average T-site energy of 5.44 kJ mol^{-1} and a density of 1.4 uÅ^{-3}; however, there are no structures with a density around this region as the polymorphs transform from stable to metastable structures.

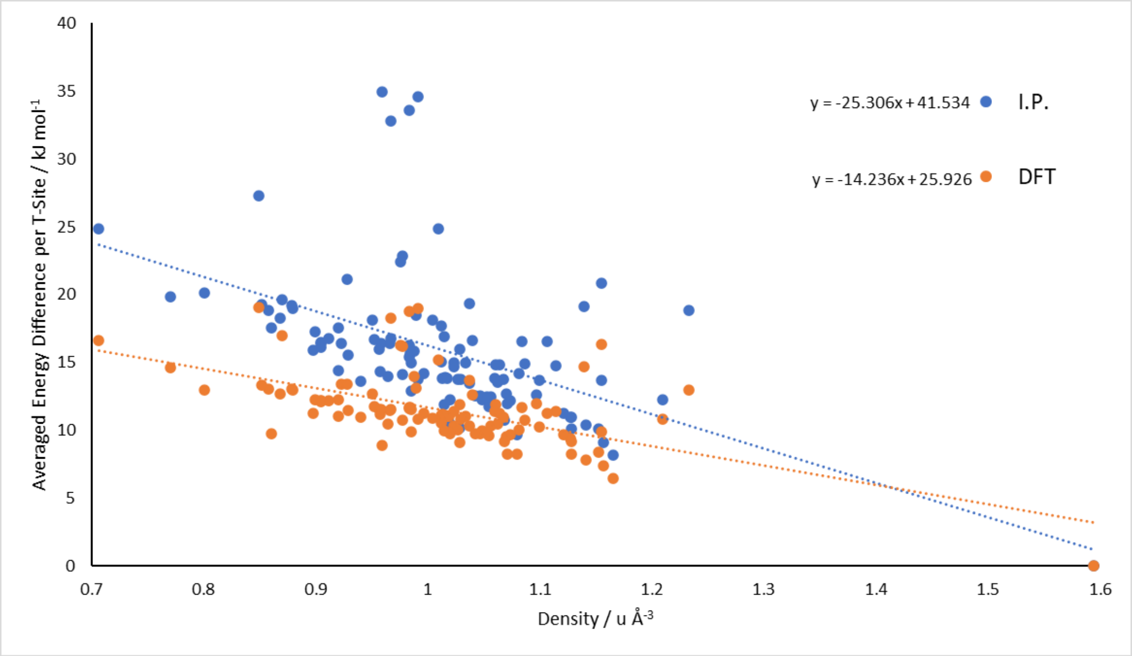

Fig 3.6. Averaged T-site energy difference from both interatomic potential methods (I.P.) and DFT against unit cell density. Line colours: Sander's Interatomic Potentials: blue, DFT: orange.

The same DFT methodological procedure was implemented for the optimization of AlPO structures. Again, the full comprehensive list of modelled AlPO structures is given in the supporting information at the end of this chapter. As with the interatomic potential study of AlPOs, the energy difference per tetrahedral site was reported in relation to Berlinite. Relative energies are reported in the ***Table S3.5.***, a similar linear trend to the potentials study is observed in ***Fig. 3.4.***; however, there are some subtle differences in this trend. A large difference in reported energies can be seen for AlPO-11, which in relative terms is much closer to the energy of UiO-6. When calculated with DFT, there is a decrease in the energy difference between the two structures from 3.7 kJ mol^{-1} to 2.6 kJ mol^{-1}. AlPO-18 and SAPO-42 are now 1.5 kJ mol^{-1} closer in energy with DFT (0.6 kJ mol^{-1}) than with interatomic potentials (2.1 kJ mol^{-1}).

When comparing these calculations with experimental calorimetric data provided by Navrotsky and co-workers,[188,215] we understand that the three values we compare in ***Table 3.5.*** are not exactly the same. Notably, the experimental values contain heat capacity contributions, but as we reported earlier entropic and temperature contributions were benchmarked and shown to be below the experimental margin of error, as such a comparison can be drawn between the three different energies. As expected, and highlighted above, results from the lattice energy methods are larger than the cohesive energies from DFT, whilst the cohesive values are relatively close to the experimental values, with small discrepancies of around 1-2 kJ mol^{-1}, and only CIT-5 displays an appreciable difference between calculated and experimental energies.

An additional caveat worth noting in comparison to experiment, is that all calculations assume an ideal and non-defective pure silica framework. An element to consider is that experimental samples may have appreciable differences arising from additional defects and extra-framework species. As is noted in the experimental thermochemistry study performed by Piccione *et al*,[215] internal silanol groups arising as a result of defects can result in the destabilisation of zeolites. Specifically, when comparing the calorimetric data for MFI and BEA, as synthesised in hydroxide or fluoride media, these silanol defects result in a $\leq$2.4 kJ mol^{-1} destabilisation of the calcined system, which could therefore contribute to the discrepancies observed between the experimental and calculated systems. Since this is a destabilisation energy, it would therefore lead to a slightly larger energy value than the calculated system and as such would apply to: ITQ-7, ZSM-18 and ZSM-12.

Structure	I.P. / kJ mol^{-1}	DFT / kJ mol^{-1}	EXP / kJ mol^{-1}	EXP Error / %
FER	11.8	9.6	6.6	NA
MFI/ZSM-5	9.7	8.3	6.8	± 0.8
AFI	11.9	10.0	7.2	NA
MEL/ZSM-11	10.8	9.2	8.2	± 1.3
MTQ/ZSM-12	8.2	6.5	8.7	NA
CFI/CIT-5	12.7	12.0	8.8	± 0.8
STT/SSZ-23	14.7	11.4	9.2	± 1.2
BEA	14.4	11.0	9.3	± 0.8
IFR/ITQ-4	15.0	10.3	10	± 1.2
ITE/ITQ-3	14.1	10.7	10.1	± 1.2
MWW/ITQ-1	14.4	11.2	10.4	± 1.5
EMT	20.1	13.0	10.5	± 0.9
AST	18.1	12.7	10.9	± 1.2
CHA	16.1	12.2	11.4	± 1.5
MEI/ZSM-18	18.9	13.0	13.9	± 0.4
ISV/ITQ-7	16.4	13.4	14.4	± 1.1

Table 3.5. Comparison of calculated lattice energies using the Interatomic Potential model (I.P.), Shell model (with the Sanders potentials) and DFT compared to experimental values (EXP) with the reported experimental errors (EXP Error).[188,215]

In **Fig. 3.7** below these energies are plotted against the density of the unit cell as a function of atomic mass (u) of the unit cell and the volume (Å^{-3}) taken from the crystallographic data provided by the IZA database.

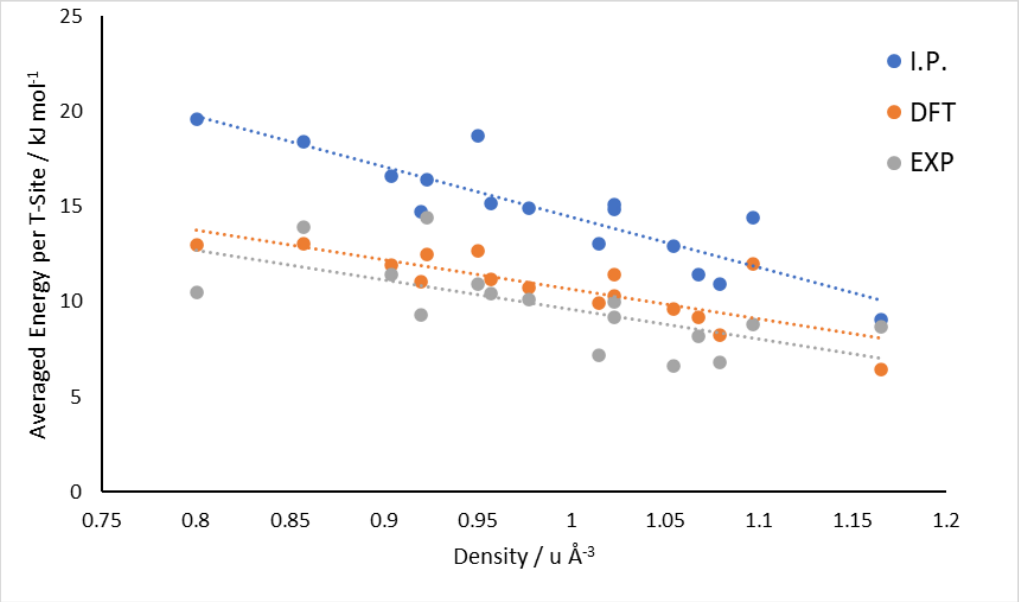

Fig 3.7. Comparison of averaged zeolite energies per T-Site from Interatomic Potentials (I.P.), DFT and Experimental methods plotted against density. Line colours: Sander's Interatomic Potentials: blue, DFT: orange, Experimental data: grey.

As can be seen from **Fig. 3.7.** the interatomic potential energies are substantially higher than both DFT and experimental energies. α-quartz has been omitted from this plot to prevent the skew of the trend line that arises from the different nature of the dense phase when compared to the metastable phase. These results agree qualitatively with the work reported by Zwijnenburg *et al*[186] with the DFT yielding energies closer to experimental values than the interatomic potential method, despite the use of the lower accuracy functional and the inclusion of siliceous structures without the strained three-membered ring sub-structures. Interestingly, the gradients of the trend lines for the experimental and DFT energies are -15.7 and -15.5 6 kJ mol^{-1} u^{-1} Å^{-3} respectively, which is remarkably similar with a discrepancy of 1.3 %. The consistency of the deviation of the trend indicates there is a systematic discrepancy that is not accounted for by the DFT calculations. The gradient generated by the interatomic potential data is noticeably steeper with a gradient of -26.545 kJ mol^{-1} u^{-1} Å^{-3}, a difference of 10.889 (70 %) from the experimental trend. This translates to an increased energetic discrepancy for more porous, less dense metastable structures.

When comparing the calculated zeolite lattice energies and the DFT cohesive energies, a clear linear trend is observed. The works of Navrotsky *et al*[188,216] also reports data from high temperature drop calorimetry with $2PbO \bullet B_2O_3$ for a selection of AlPOs, and in the comparison to these data we see a different result from that observed in the zeolite study. In this case the interatomic potential lattice energies give values closer to experimental values than the DFT cohesive energies as displayed in ***Table 3.6***.

It is unclear why there is a poorer agreement between the higher-level theory calculations and experiment, but errors could arise from differences from the idealised pure alumino-phosphates used in the calculations compared to the real experimental systems. It should be noted, however, that this discrepancy would apply to both sets of calculations as they both used the same initial structural data. The indeterminate nature of this result could warrant further study to elucidate the reason behind the discrepancy.

Structure	**I.P. / kJ mol^{-1}**	**DFT / kJ mol^{-1}**	**EXP / kJ mol^{-1}**	**EXP Error / %**
Berlinite	0	0	0	0.54
AlPO-8	10.76	10.35	5.56	1.42
AlPO-11	9.10	10.90	6.18	1.17
AFI / AlPO-5	6.77	10.83	7.0	2.15
AlPO-42 (SAPO-42)	12.90	13.87	7.82	1.94
VPI-5	12.60	14.48	8.38	2.26
AST / AlPO-16	12.37	14.15	10.9	1.18

Table 3.6. Calculated and Experimental AlPO Energies Averaged per T-site with respect to Berlinite. Experimental values from the work of Navrotsky *et al.*[188,216,217]

The averaged energy difference per T-site from Berlinite for interatomic potential, DFT and experimental methods have been plotted against their density as a function of atomic mass per unit cell volume as reported by the IZA database in **Fig. 3.8.** below. The inclusion of Berlinite skews the trend lines as it is a dense phase instead of a microporous metastable phase structure and as such has been omitted.

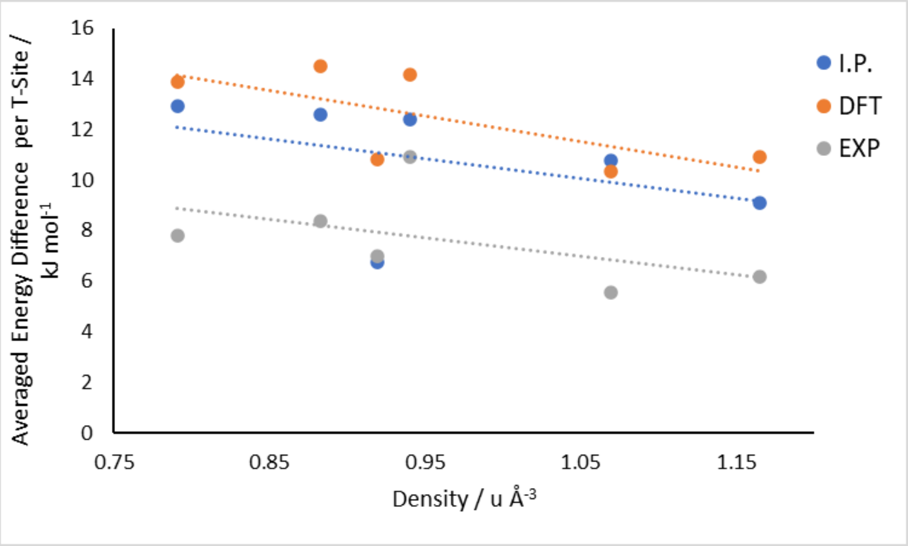

Fig. 3.8. Comparison of interatomic potential, DFT and experimental energies against density. Line colours: Interatomic Potentials: blue, DFT: orange, Experimental data: grey.

The trend lines presented in **Fig. 3.8.** have similar gradients to the experimental trendline and interatomic potential gradients being -7.20 and -7.90 kJ mol^{-1} u^{-1} Å^{-3} respectively, which is a difference of 0.69 kJ mol^{-1} u^{-1} Å^{-3} (9.6 %) which, whilst a more significant deviation than was observed between the experimental and DFT gradients for zeolites, is still within a very reasonable margin of error. However, in this case, the gradient for the DFT energies is noticeably steeper at -10.07 kJ mol^{-1} u^{-1} Å^{-3}, deviating from the experimental gradient by 2.87 kJ mol^{-1} u^{-1} Å^{-3} (40 %), which is significantly higher than for the DFT calculations on the zeolite structures, but significantly lower than when modelling zeolites with interatomic potentials. It should be noted that the low energy resulting from the AlPO-5 calculation with interatomic potentials probably has a significant effect on lowering the gradient of the trendline for interatomic potentials, despite which the AlPO-5 energy is much closer to the reported experimental energy. Overall, the trend lines appear to show that the discrepancies in modelling AlPOs are systematic as the trendlines run mostly parallel to the experimental trend lines, with the interatomic potentials fitting better to the experimental line than DFT.

3.4 Conclusions

We performed an extensive benchmarking exercise to assess the ability of different interatomic potential based methods and quantum mechanical methods. A large number of zeolite energies have been calculated with interatomic potential and quantum mechanical based techniques, with all structures and their energies detailed in the supporting information of this chapter. For the potential based methods, we conclude that the formal charge shell model approach results in energies closer to experimental values than the partial charge rigid ion model approach. However, there are a couple of instances where the rigid ion model performed better, notably in the case of the BEA framework which is a partially disordered material which may be relevant. Additionally, the lack of polarisability in the rigid ion model produced un-physical linear bond angles for several structures, therefore a shell model that explicitly models the polarisation of the atoms is recommended for the modelling of molecular mechanical environments in hybrid QM/MM work.

The results from the DFT section of this study illustrates a similar trend and distribution to the interatomic potential result, however they are generally a little lower in energy than the potential based method and tend to be closer to the experimental values. Both computational methods have a propensity to exaggerate lattice energies when compared to the experimental values, with the potential based method doing so by a more significant margin. The modelling of ITQ-39 has a significant difference in energy between the two methods, with DFT yielding a much lower energy, this brings it in line with other structures following the energy vs density trend. Again, this could be alluding to the inability of potentials to model partially disordered materials, which was probably an issue also observed in the rigid ion model, however it is overall very good at reproducing the trends observed in DFT for a significantly reduced cost. It should also be noted that DFT was able to reproduce energy values close enough to experimental data that, when factoring in experimental error, were within chemical accuracy.

A comprehensive study of calculated lattice and cohesive energies for pure alumino-phosphate structures using different computational methodologies was also carried out. Both molecular mechanical and quantum mechanical methodologies (DFT) were employed and contrasted with experimental values. Energies were calculated and reported in relation to each tetrahedral unit, and their difference from that of Berlinite's averaged

T-site energy was reported. Both methods produce an almost identical linear trend, scaling the increasing energy with decreasing AlPO density as expected. However, when interatomic potential lattice energies are contrasted with DFT cohesive energies, the interatomic potentials tend to give lower energies except for AlPO-8. When comparing calculated energies to the experimental values, the interatomic potential lattice energies are closer than the cohesive energies despite being a lower level of theory, the reason for which is not clear although there may be some deviation with the real experimental systems from the idealised structures used in the calculations; there may be more defects or even additional framework cations which could influence the electronics and overall energy of the system. Hence, we now elect to use a shell model approach for the modelling of the molecular mechanical region when performing hybrid QM/MM calculations in the next couple of chapters of research in this thesis.

A summary of the work presented in this chapter has been published in the open literature.[218]

3.5 Supporting Information

	2 Å	**3 Å**	**4 Å**	**5 Å**	**6 Å**	**7 Å**	**8 Å**	**9 Å**	
α-Quartz Energy for Reference	-17453.42	-16498.63	-16620.56	-16756.95	-16818.48	-16848.92	-16871.17	-16882.45	
Energy Difference from α-Quartz for Different Cut-offs / kJ mol^{-1}									
Structure	**2 Å**	**3 Å**	**4 Å**	**5 Å**	**6 Å**	**7 Å**	**8 Å**	**9 Å**	**EXP / kJ mol^{-1}**
AST-FW	1.58	1.38	19.07	37.99	42.59	46.77	50.15	51.55	10.9
BEA-FW	3.74	5.48	13.73	30.03	37.44	41.56	46.12	47.93	9.3
CIT-5	-1.43	-3.37	16.85	25.47	30.32	32.69	36.90	38.58	8.8
CHA	5.66	8.48	19.53	37.98	49.04	53.33	57.61	59.52	11.4
ITQ-4	4.95	8.32	15.51	31.49	37.48	41.64	45.35	46.96	10
ITQ-7	4.80	8.14	17.59	34.46	41.37	45.76	50.31	52.20	14.4
ITQ-3	3.09	3.89	14.98	32.53	40.61	44.21	48.46	50.25	10.1
ZSM-11	-0.09	-1.51	13.56	22.51	29.87	32.70	36.68	37.92	8.2
ZSM-5	-0.96	-3.02	12.79	22.20	28.50	31.38	35.26	36.46	6.8
ITQ-1	3.49	4.88	17.52	27.65	36.65	39.78	43.74	45.27	10.4
SSZ-23	2.66	3.91	16.28	30.59	38.91	42.63	46.68	48.29	9.2
AFI-FW	-0.61	-1.93	23.85	28.97	29.38	32.02	36.78	38.05	7.2
EMT-FW	8.34	13.34	18.32	43.40	53.06	57.17	61.38	63.63	10.5
FER-FW	0.19	-0.79	15.38	21.56	30.08	32.59	36.46	37.20	6.6
ZSM-18	8.40	13.57	22.19	40.46	49.27	54.24	58.74	60.82	13.9
ZSM-12	-2.06	-4.89	11.96	21.99	26.00	28.58	32.24	33.45	8.7

Table S3.1. Van Beest lattice energies averaged per T-site cut-off parameter benchmarks with total α-quartz lattice energies as a reference for each cut-off. Whilst this table shows that using a cut-off below 4 Å often results in common negative energy values for a lot of structures, all calculations were able to converge on an energetic minimum. The energy values generated above this cut-off parameter are substantially larger than the experimentally reported value, hence the cut-off of 4 Å was determined to be the best option for these calculations.

Structure	Averaged T-Site Energy / kJ mol^{-1}	Averaged T-Site Energy ΔE α-Quartz / kJ mol^{-1}	Structure	Averaged T-Site Energy / kJ mol^{-1}	Averaged T-Site Energy ΔE α-Quartz / kJ mol^{-1}	Structure	Averaged T-Site Energy / kJ mol^{-1}	Averaged T-Site Energy ΔE α-Quartz / kJ mol^{-1}	Structure	Averaged T-Site Energy / kJ mol^{-1}	Averaged T-Site Energy ΔE α-Quartz / kJ mol^{-1}
α-Quartz	-12418.0	0	JSW-FW	-12401.5	16.5	GME-FW	-12401.5	16.5	LTJ-FW	-12403.3	14.8
ITQ-33	-12398.2	19.8	ABW-FW	-12405.5	11.9	LOS-FW	-12404.1	13.9	LTL-FW	-12399.9	18.1
CIT-5	-12405.4	12.7	ANA-FW	-12404.3	13.7	FRA-FW	-12404.4	13.6	MAR-FW	-12404.2	13.1
CIT-7	-12401.3	15.2	DON-FW	-12407.8	10.2	LTF-FW	-12401.1	19.3	MEP-FW	-12405.8	12.2
EDI-FW	-12395.2	22.8	BIK-FW	-12406.7	7.2	MAPO-39-FW	-12405.3	12.7	MER-FW	-12401.8	16.3
ITQ-12	-12403.1	14.9	LOV-FW	-12393.1	24.9	STA-6-FW	-12402.1	15.9	MON-FW	-12403.2	14.9
AEN-FW	-12405.8	12.2	MOZ-FW	-12400.3	17.7	STA-15-FW	-12407.6	10.4	MOR-FW	-12405.7	12.3
SAPO-40-FW	-12401.2	16.8	MWW-FW	-12403.6	14.4	SIZ-7-FW	-12402.6	15.4	MSO-FW	-12406.0	12.0
ACO-FW	-12399.5	18.5	SAPO-31-FW	-12407.9	10.1	DAC-FW	-12405.7	12.3	BEA-FW	-12403.6	14.4
ITQ-13-FW	-12405.5	12.5	SAPO-56-FW	-12401.6	16.4	EPI-FW	-12404.5	13.5	BRE-FW	-12404.3	13.3
ITQ-22	-12404.1	13.9	VFI-FW	-12398.4	19.5	DOH-FW	-12407.4	10.6	CAN-FW	-12404.1	13.9
ITQ-24-FW	-12402.4	15.6	ZSM-12	-12409.8	8.2	EAB-FW	-12401.6	16.4	CAS-FW	-12407.1	11.0
ITQ-3	-12403.9	14.1	AEL-FW	-12407.9	11.0	EMT-FW	-12397.9	20.1	NAT-FW	-12395.6	22.4
ITQ-34-FW	-12405.5	12.5	AHT-FW	-12397.2	20.8	EON-FW	-12403.0	13.0	NES-FW	-12402.2	15.9

ITQ-38-FW	-12403.8	14.2	ITQ-33-FW	-12398.2	19.8	ERI-FW	-12401.6	16.4	OFF	-12401.2	16.8
ITQ-4	-12403.0	15.0	ITQ-39-FW	-12383.1	36.2	ERS-7	-12404.5	13.5	PHI-FW	-12402.3	15.7
ITQ-49-FW	-12400.5	17.6	ITQ-44-FW	-12393.2	24.8	ETR-FW	-12396.9	21.1	PST-21	-12402.0	16.0
ITQ-50	-12398.7	19.3	GOO-FW	-12398.9	19.1	FAR-FW	-12404.3	13.7	PST-22	-12403.0	15.0
ITQ-52	-12404.2	13.8	GUS-1	-12406.2	9.1	HEU-FW	-12405.5	12.5	RHO-FW	-12399.7	18.3
ITQ-7	-12401.6	16.4	FER-FW	-12404.1	11.8	JBW-FW	-12407.0	11.0	ITQ-26-FW	-12400.5	15.2
ZSM-5	-12408.3	9.7	AFG-FW	-12399.0	13.9	JOZ-FW	-12384.4	33.6	AFY-FW	-12390.7	27.3
ZON-FW	-12401.5	16.6	AFS-FW	-12404.0	19.0	KFI-FW	-12400.8	17.3	ZSM-18	-12399.2	18.9
MAPO-36	-12405.1	12.9	BOG-FW	-12398.8	14.0	LAU-FW	-12403.8	14.2	ZSM-11	-12407.3	10.8
WEI-FW	-12383.4	34.6	BPH-FW	-12403.0	19.2	LEV-FW	-12402.0	16.0	EWS-FW	-12401.4	16.6
JNT-FW	-12399.2	18.8	GIS-FW	-12404.2	15.0	LIO-FW	-12404.1	13.9	NAB-FW	-12385.2	32.8
DFT-FW	-12403.2	14.8	GIU-FW	-12398.9	13.8	LTA-FW	-12398.7	19.3	LTJ-FW	-12403.3	14.8
AST-FW	-12399.9	18.1	CHA	-12401.9	16.1	SSZ-23	-12403.3	14.7	AFI-FW	-12406.1	11.9

Table S3.2. Averaged lattice energies per T-site calculated with the Buckingham potentials derived by Sanders and implemented via the shell model. Energies reported per tetrahedral silica unit, and their deviation from α-quartz, the densest and lowest energy phase of silica.

Framework	Averaged T-Site Energy Energy / kJ mol^{-1}	Averaged T-Site Energy ΔE Berlinite / kJ mol^{-1}
Berlinite	-12938.8	0
UiO-6	-12933.4	5.4
AlPO-41	-12933.1	5.7
AlPO-5	-12932.1	6.8
AlPO-D	-12931.0	7.8
AlPO-C	-12929.8	9.0
AlPO-11	-12929.7	9.1
AlPO-12	-12929.1	9.8
ITQ-51	-12929.1	9.8
SAPO-56	-12928.2	10.6
AlPO-18	-12928.0	10.8
AlPO-8	-12928.1	10.8
STA-20	-12927.9	11.0
AlPO-16	-12926.5	12.4
VPI-5	-12926.2	12.6
SAPO-42	-12925.9	12.9
PST-14	-12925.5	13.3
STA-1	-12924.9	13.9

Table S3.3. Interatomic potential AlPO energies as both an average per tetrahedral unit, and these averaged energy differences from the densest phase low energy polymorph alumino-phosphate; Berlinite.

Structure	**Averaged T-Site Cohesive Energy / kJ mol^{-1}**	**Averaged T-Site ΔE α-Quartz / kJ mol^{-1}**	**Structure**	**Averaged T-Site Cohesive Energy / kJ mol^{-1}**	**Averaged T-Site ΔE α-Quartz / kJ mol^{-1}**	**Structure**	**Averaged T-Site Cohesive Energy / kJ mol^{-1}**	**Averaged T-Site ΔE α-Quartz / kJ mol^{-1}**	**Structure**	**Averaged T-Site Cohesive Energy / kJ mol^{-1}**	**Averaged T-Site ΔE α-Quartz / kJ mol^{-1}**
α-Quartz	-2314.9	0	JSW-FW	-2303.7	11.2	GME-FW	-2302.7	10.9	LTJ-FW	-2303.5	11.4
ITQ-33	-2300.3	14.5	ABW-FW	-2304.6	10.3	LOS-FW	-2303.8	10.9	LTL-FW	-2304.0	10.8
CIT-5	-2303.0	11.9	ANA-FW	-2305.0	9.9	FRA-FW	-2304.0	9.6	MAR-FW	-2304.0	10.9
CIT-7	-2303.2	11.7	DON-FW	-2305.8	9.1	LTF-FW	-2303.9	11.0	MEP-FW	-2305.2	9.6
EDI-FW	-2298.7	16.1	BIK-FW	-2305.2	9.6	MAPO-39-FW	-2305.3	9.5	MER-FW	-2303.2	11.6
ITQ-12	-2304.1	10.7	LOV-FW	-2299.7	15.1	STA-6-FW	-2303.6	11.2	MON-FW	-2305.1	9.7
AEN-FW	-2304.1	10.8	MOZ-FW	-2303.9	11.0	STA-15-FW	-2307.1	7.8	MOR-FW	-2305.1	8.2
SAPO-40-FW	-2302.7	12.1	MWW-FW	-2303.7	11.1	SIZ-7-FW	-2303.3	11.5	MSO-FW	-2306.7	11.0
ACO-FW	-2301.8	13.1	SAPO-31-FW	-2306.7	8.2	DAC-FW	-2304.9	10.0	BEA-FW	-2303.9	10.8
ITQ-13-FW	-2305.2	9.7	SAPO-56-FW	-2302.7	12.2	EPI-FW	-2304.5	10.4	BRE-FW	-2304.7	10.2
ITQ-22	-2304.0	10.8	VFI-FW	-2297.9	16.9	DOH-FW	-2303.9	11.1	CAN-FW	-2303.8	11.0
ITQ-24-FW	-2303.5	11.4	ZSM-12	-12409.8	8.2	EAB-FW	-2303.4	11.0	CAS-FW	-2305.5	9.4
ITQ-3	-2304.2	10.7	AEL-FW	-2306.5	8.4	EMT-FW	-2301.9	11.5	NAT-FW	-2298.7	16.2

ITQ-34-FW	-2305.2	9.7	AHT-FW	-2298.6	16.3	EON-FW	-2304.4	12.9	NES-FW	-2301.0	13.9
ITQ-38-FW	-2303.6	11.2	ITQ-33-FW	-2303.6	14.5	ERI-FW	-2303.4	10.5	OFF	-2303.4	11.5
ITQ-4	-2304.6	10.3	ITQ-39-FW	-2304.6	8.8	ERS-7	-2304.6	10.3	PHI-FW	-2303.3	11.6
ITQ-49-FW	-2302.7	12.2	ITQ-44-FW	-2302.7	16.6	ETR-FW	-2301.5	13.3	PST-21	-2303.0	11.8
ITQ-50	-2301.3	13.6	GOO-FW	-2300.2	14.6	FAR-FW	-2304.9	10.0	PST-22	-2303.9	11.0
ITQ-52	-2304.1	10.8	GUS-1	-2307.5	7.4	HEU-FW	-2305.1	9.8	RHO-FW	-2302.3	12.6
ITQ-7	-2301.5	11.7	FER-FW	-2305.3	9.6	JBW-FW	-2305.8	9.1	ITQ-26-FW	-2301.6	13.3
ZSM-5	-2306.7	8.2	AFG-FW	-2303.9	11.0	JOZ-FW	-2296.2	18.6	AFY-FW	-2295.8	19.0
ZON-FW	-2303.2	11.6	AFS-FW	-2302.1	12.9	KFI-FW	-2302.7	12.2	ZSM-18	-2301.9	13.0
MAPO-36	-2305.0	9.8	BOG-FW	-2304.5	10.40	LAU-FW	-2304.9	10.0	ZSM-11	-2305.7	9.1
WEI-FW	-2295.9	18.9	BPH-FW	-2301.9	13.0	LEV-FW	-2303.4	11.5	EWS-FW	-2302.3	12.5
JNT-FW	-2301.9	12.9	GIS-FW	-2303.4	11.5	LIO-FW	-2303.5	11.3	NAB-FW	-2296.6	18.2
DFT-FW	-2303.7	11.2	GIU-FW	-2304.1	10.8	LTA-FW	-2301.6	13.3	LTJ-FW	-2303.5	11.4
AST-FW	-2302.2	12.7	CHA	-2302.7	12.2	SSZ-23	-2303.5	11.4	AFI-FW	-2305.0	10.0

Table S3.4. DFT cohesive energies of different zeolites as both an averaged energy per tetrahedral silica unit, and as this energy's difference from the densest and lowest energy phase of silica: α-quartz.

Framework	Averaged T-Site Energy / kJ mol^{-1}	Averaged T-Site Energy ΔE Berlinite / kJ mol^{-1}
Berlinite	-2192.5	0
UiO-6	-2184.1	8.3
AlPO-D	-2183.0	9.5
AlPO-41	-2183.0	9.5
ITQ-51	-2182.2	10.3
AlPO-8	-2182.1	10.4
AlPO-5	-2181.6	10.8
AlPO-11	-2181.6	10.9
AlPO-C	-2181.2	11.3
AlPO-12	-2180.1	12.4
STA-20	-2180.1	12.4
SAPO-56	-2179.3	13.1
AlPO-18	-2179.1	13.3
SAPO-42	-2178.6	13.9
PST-14	-2178.5	14.0
AlPO-16	-2178.3	14.2
VPI-5	-2178.0	14.5
STA-1	-2177.9	14.6

Table S3.5. DFT AlPO Cohesive Energies as an averaged energy per T-site and their difference from the Berlinite, different ΔE values arise from the same Averaged Energy values as a result of rounding to 1 decimal place.

CHAPTER 4

Hybrid QM/MM Modelling of Different Metal Centres in ZSM-5

4.1 Introduction

As discussed in Chapter 1, the properties of a zeolite can be altered in two main ways: the introduction of defects in the structure’s framework, or by the introduction of different cations into the structure. This high tunability offers an extensive range of prospects for catalyst design.

As described in detail in Chapter 1, a framework charge is often introduced in silicate frameworks by replacing a framework silicon with an aluminium, where this defect is compensated by either a mono- or polyvalent cation. The local geometry of the extra-framework cation site was found to be substantially influenced by these cations, leading to a significant alteration of the proton affinity of that site. When a proton (H^+) was used as the counter ion for an aluminium atom at the adjacent BAS, a number of geometrical changes were observed, which resulted in a change to the positive charge density of the aluminium atom. This culminates in the lowering of the proton affinity of the acid site proton and increasing the strength of acidity. Clearly these are substantial changes to the overall properties of the catalyst that result from the introduction of a minor defect. As a result of this high tunability, this concept has been broadly applied to a variety of industrial processes, but most keenly in the realm of optimising the catalytic conversion of methanol to hydrocarbons to enhance catalyst selectivity.[219]

In the pursuit of enhancing catalyst properties, it is common practice to look to the natural world for inspiration. Natural catalysts exist in the form of enzymes that have evolved over millions of years to be highly specific for their corresponding reactions. In heme-based P-450, peroxide enzymes and non-heme iron dioxygenases there is often a highly oxidised iron site (Fe=O, ferryl), which is capable of abstracting a hydrogen atom from organic molecules to form an organic radical. The oxygen atom bound to the iron site then forms a hydroxyl (Fe-OH), but also needs to capture the newly formed radical species by forming a new stable C-O bond before the radical diffuses away.[220] The ion exchanged metal sites in zeolites, can resemble some of the key structural features of active sites within enzyme macromolecules.

This theory was applied by Bunting *et al*[221] who used DFT to investigate the mechanism and ligand effects of a single rhodium atom supported on the ZSM-5 zeolite, in the catalytic selective conversion of methane to methanol. This study demonstrated that the most favourable mechanism for methane activation was via oxidative addition and not a metal-oxo intermediate, with the C-OH bond formation being the rate determining step. The coordination of CO to the rhodium was seen to strongly promote this bond formation, whilst water prevents the CO from poisoning the catalyst by forming an RhOOH intermediate species. Despite the metal-oxo pathway being less favourable, it was shown to have an energy barrier of 119.6 kJ mol^{-1} for C-H activation, which is 115.8 kJ mol^{-1} less than the rate limiting part of the oxidative addition pathway. This reactive metal-oxo species activates methane more readily than the alternative species, where oxygen had already adsorbed to the rhodium with energy barriers of 119.6 kJ mol^{-1} and 115.8 kJ mol^{-1}respectively. Despite being a less favourable pathway for methane activation, the energy barrier for the metal-oxo species shows promise, indicating there could be potential to developing catalysts for this alternative pathway.

A very similar observation was discovered in the works of Qi *et al*[86] when modelling the selective oxidation of methane to methanol and ethanoic acid using molecular oxygen via an Au-ZSM-5 catalyst. Whilst the main focus of this study was on gold nanoparticles supported on ZSM-5, an extra-framework cationic gold system was also investigated. Computational studies were carried out on this system using DFT with a PBE functional[87] and D3 dispersion correction, which modelled the adsorption of the oxygen, followed by the electron donation from the metal, producing an activated O_2^-* bound super-oxo species. The extra-framework cationic gold system: Au(II)O_2^-ZSM-5, was able to activate oxygen very strongly, but it was shown that there was an absence of an adjacent redox centre that could bind the distal oxygen, which therefore meant that the formation of an Au(III)O^-ZSM-5 species could only proceed via a route where hydrogen is abstracted from a methane. Unfortunately, this reaction pathway was impeded by a high energy barrier of ~140 kJ mol^{-1}.

This chapter seeks to explore further the potential for methane activation on metal exchanged ZSM-5, as discussed above, and approaches it from a theoretical and computational perspective. Having previously benchmarked both interatomic potential and DFT methods, we combine the two levels of theory in hybrid quantum mechanical molecular mechanical (QM/MM) techniques to model the ZSM-5 zeolite. We seek to identify an alternative catalyst for the more favourable conversion of methane to methanol via the oxo formation pathway. By combining these two levels of theory we can calculate systems that are not charge neutral, which allows for the modelling of metal cations in higher oxidation states than would realistically be the case. Computation of large macrostructures at a high level of theory can incur a very high computational cost, as such this cost can be mitigated using this hybrid approach. From these optimised metal cation structures, molecular oxygen is subsequently introduced to the system and modelled using the same methodology, to determine the metal ion system’s propensity to activate the oxygen and form a super-oxo species, which will be the active oxidant for the rate limiting hydrogen abstraction step. Subsequently, hydrogen atoms are added axially to the optimised oxygen systems to model the hydrogen abstraction step in the MTH process, which allows for the calculation of the energies for the hydrogen affinities and subsequent acidities.

4.2 Methods

The hybrid additive QM/MM approach was implemented by the TCL-Chemshell code,[222–224] where the quantum mechanical (QM) region of the system was treated by ORCA[182] and the molecular mechanical (MM) region of the system is treated by DL_POLY.[225] The hybrid methodology is advantageous over semi-empirical methods as it allows for the modelling of systems that are not charge neutral, and hence allows for the modelling of metal cations in higher oxidation states.

The QM region used for this series of calculations was selected from previous work in the literature by Nastase[226] and O’Malley[71] and is shown in ***Fig. 5.1.*** The QM region used from these two studies was modified, whereby a single aluminium atom replaces a silicon atom creating a charge defect which is then compensated by the metal cation. This region was selected as these studies had assessed that deprotonation of ZSM-5 with an aluminium site, at the intersection of the zeolite channels, provides a deprotonation energy that matches extremely well to experimental values, which allows us to model a more realistic system that would probably exist in experimental conditions. It has also been reported that transition metal ions (TMIs) in MFI tend to be located in the 10-membered ring channels or intersections, coordinating to a 6-membered ring with one or two aluminium tetrahedra,[227] further enforcing our choice for the aluminium site location.

The QM region terminates with only oxygen atoms, allowing the Chemshell[228] program to attach hydrogen linker atoms to maintain the correct valences and electrostatic embedding protocols between the QM and the MM regions. The QM treatment of the calculation implemented the def2-TZVP basis set,[229] with a Grimme-D3 dispersion correction[88] and B3LYP functional,[110,111] with a tight SCF convergence criterion of 1.0 x10^8 au, a methodology which was selected due to its high accuracy in previous work by O'Malley *et al* who modelled a similar system.[71] We previously investigated the interatomic potentials as derived by Sanders *et al*[31] which introduced polarisability by way of the shell model approach. The ability to model polarisability in both our study (Chapter 3) and the works of Ruiz-Salvador *et al*[129] was shown to be crucial for retaining non-linear, physical bond angles and reproducing energetic trends. As such a shell model was again implemented, however, using the more recent potentials derived by Hill and Sauer.[230] These potentials were used in place of the Sanders potentials from the previous chapter, as they were derived specifically for hybrid QM/MM calculations. Specifically, the Sander's potentials were optimised to model the structures and properties of microporous alumino-silicates, whilst the potentials derived by Sauer are optimised for embedding which is critical to the hybrid calculations performed in this chapter. As such the use of Sanders potentials for this purpose would cause issues when trying to link both the QM and MM regions together, hence the Sauer potentials were also applied for the MM treatment in O'Malley *et al's*[71] study. Thus, this offers a convenient way for us to benchmark our calculations and make a direct comparison for this body of work, whilst retaining the use of the shell model approach.[121]

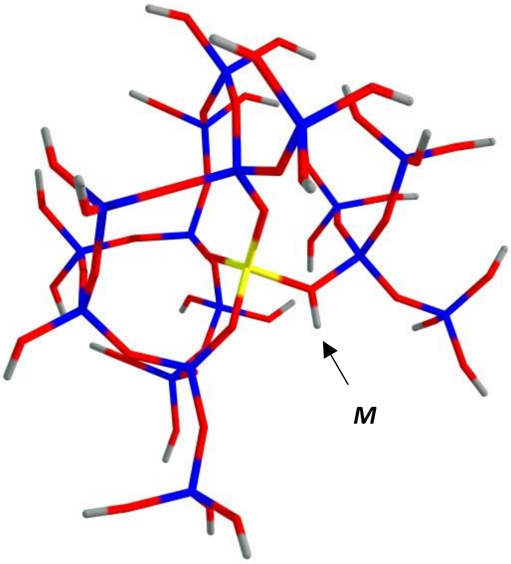

Fig. 4.1. Quantum Mechanical Region Used for Protonated ZSM-5 Calculation with Terminal Hydrogens with Atom M representing the Substituted Cation Location. The colour scheme is as follows: Si (dark blue), O (red), Al (yellow) and H (grey).

Initial calculations were run on ZSM-5 with an aluminium substitution and an overall formal charge of -1, which would provide the initial structural file into which each cation could be inserted. Charge compensating cations were then added to the region highlighted '**M**' in ***Fig. 4.1.*** to the previously optimised structure as this would likely reduce the computational cost of the subsequent calculations.

Isolated metal cations were calculated exclusively with DFT using ORCA[182] and implementing the same def2-TZVP basis set,[229] B3LYP functional[110,111] but with a Very Tight SCF convergence criterion of 1.0 x10^{-9} au, which is a tighter criterion than the main calculations, but it is only treating a single gaseous cation so allows for a smaller margin of error. All cations are calculated as gaseous ions with the designated charge and corresponding electron spin multiplicities as given by the formula **2S+1**.

4.3 Results and Discussion

The results of the hybrid QM/MM metal cation binding energy calculations are displayed below in ***Table 4.1.***, which shows the overall system energy, the energy of the metal cation and its corresponding binding energy to the acid site. The binding energy of each cation was calculated using the following equation:

$$E_{Binding} = E_{Total} - E_{Ion} - E_{Deprotonated} \qquad (4.1)$$

Where the binding energy, $\mathbf{E_{Binding}}$, is equal to the total energy, $\mathbf{E_{Total}}$, minus the energy of the cation, $\mathbf{E_{Ion}}$, and the energy of the deprotonated zeolite, $\mathbf{E_{Deprotonated}}$. The calculation of the metal ions alone in the gaseous state ensures there are no additional forces acting on the ion and so gives a more accurate binding energy.

	Energy / kJ mol^{-1}	**Ion Energy / kJ mol^{-1}**	**Binding Energy / kJ mol^{-1}**
Deprotonated	-22795905	0	-
Protonated/H$^+$	-22797004	0	-1099
Cu(I)	-27060787	-4264336	-545
Mo(I)$^+$	-22972560	-176115	-539
Au(I)$^+$	-23148323	-351890	-527
Zn(I)$^+$	-27421787	-4625362	-520
Na(I)$^+$	-23217671	-421326	-439
Co(II)	-26389794	-3591887	-2002
Cu(II)	-27059882	-4262358	-1619
Fe(II)	-26080110	-3282638	-1567
Mg(II)	-23315153	-517729	-1519
Ti(II)	-25003371	-2205966	-1500
Zn(II)	-27421008	-4623615	-1488
Mn(II)	-25787153	-2989836	-1412
Au(III)	-23146188	-346538	-3745
Fe(III)	-26079042	-3279658	-3478
Mn(III)	-25785782	-2986482	-3395
Ti(III)	-25002267	-2203484	-2878
Fe(IV)	-26077413	-3274279	-7229
Ti(IV)	-25000740	-2199283	-5551

Table 4.1. ZSM-5 System Energies and Respective Binding Energies of Metal Ions.

Initially we benchmarked the protonation of the Brønsted acid site against a similar methodology implemented by O'Malley *et al.*[71] We report the proton binding energy to the Brønsted acid site as 1,098.7 kJ mol^{-1}, whereby O'Malley reports the deprotonation of the same acid site (referred to as I2 due to its location at the intersection of ZSM-5's channels) to be 1,100.4 kJ mol^{-1} using the same B3LYP functional.[110,111] Additionally, Eichler *et al* report a deprotonation energy for H-ZSM-5 of 1,205 kJ mol^{-1} when calculated with Hartree-Fock methods using a Double-Zeta Plus polarisation (DZP) basis set for hydrogen, silicon and aluminium atoms in conjunction with a Triple-Zeta Plus (TZP) polarisation basis set for treatment of the oxygen atoms.[231] Whilst there is less than a 10 % difference between these values, it can be ascribed to the different methodologies level of accuracy, our value is still within a reasonable margin of error by comparison, confirming our methodology gives results in good agreement with earlier work. Additionally, this site had previously been identified as one of the most stable locations for the substituted aluminium and charge compensating proton in the work of Schröder *et al.*[232] Whilst in a real-life scenario, cations with charges above +1 would reduce to form a neutral system, this theoretical model allows for the determination of energies for systems with cations in these oxidation states. In contrast to the protonated ZSM-5 system, when a metal cation coordinates to the framework's aluminium site it tends to coordinate between the two oxygen atoms rather than to the single bridging oxygen to which the proton binds. The difference in the coordination geometry could reasonably arise from the charge deficit created by the aluminium being spread across the surrounding oxygens rather than being localised on a single oxygen atom. Thus, the negative charge is spread over a larger area and is then compensated by the positive charge experienced over a larger area in the form of the larger cation. It should be noted that since these cations are not part of the framework they can potentially be exchanged by other cations. Previous *ab-initio* calculations and experimental work on Co(II) and Cu(II) in six-ring sites within FAU highlighted that the cations are not symmetrically coordinated, and as such can lead to a strong distortion in the acid site arising from the propensity of cations to maximise their coordination number.[233–237] The optimised structures from our calculations also reflect this asymmetric binding at the aluminium centre.

The data displayed in ***Table 4.1.***, generally indicate that ions that have been more oxidised, such as Fe(IV), are more likely to be unstable in the gaseous phase, therefore the binding energies produced will be substantially more exothermic when factoring in the energies of the whole system. As such it is more relevant to form comparisons between different elements in the same oxidation state as each other. The higher charge density could also mean a sizeable increase in the acidity of the zeolite which could increase the rates of reaction. Whilst a protonated system is a commonly studied system for its acidity and relatively easy proton transfer from the framework, the Fe(IV) cation is almost seven times more energetically favourable in terms of binding energy than this proton. This contrasts with the Zn(I) system having the lowest overall energy and the Zn(II) gaseous cation having the lowest energy for a cation. Notably there tends to be an increase in the binding energy for all cations tested as their oxidation level increases, which may be largely due to electrostatic factors.

It is interesting to note that, we would expect the binding energy of a proton to be relatively high as this is a very favourable interaction, however, what the data suggests is that there are cations with a greater binding energy: Au(III), Zn(II), Mg(II), Ti(II-IV), Cu(II), Fe(II-IV), Co(II) and Mn(II-III) due to electrostatic effects . Thus, it is more relevant to compare ions in the same oxidation state to each other, and in the case of the (I) oxidation state, a comparison can be made to the proton binding energy. If the binding energy of a cation in the same oxidation state is greater than the binding energy of the proton, then it will exchange with the proton at the acid site. As such it can be seen from ***Table 4.1.***, that all (I) cations are less energetically favourable than a proton, with an energetic order of H(I) > Cu(I) > Au(I) > Zn(I) > Na(I). The energy range is narrow between the metal cations with only 106.1 kJ mol^{-1} (9.7 % of the lowest binding energy) between them, at around the low -500 kJ mol^{-1} region, with the exception of Na(I), despite which they are all almost half as favourable at binding to the acid site as a proton, which interacts very strongly with the framework oxygen lone pair, and so no displacement would occur.

When contrasting the energetics of the cations in the (II) oxidation state, we observed an energetic order of: Co > Cu > Ti > Zn > Mn. There is a decrease in the binding energy across this group of 590.7 kJ mol^{-1}. A noticeable gap in energies is observed between the Co(II) and Cu(II) cation binding energies of 383.5 kJ mol^{-1}, which illustrates how favourable the Co(II) ion binding is, whilst the Cu(II) remains favourable, although only 119.3 kJ mol^{-1} more favourable than the next cation Ti(II). The range of energies is much smaller for the last three cations as they all have binding energies between -1,400 and -1,500 kJ mol^{-1}.

Additionally, the order of binding energies can be compared to the orders found experimentally in different zeolites, notably FAU, LTA and MOR. The works of Wu and Navrotsky report the synthesis and thermodynamics of metal exchanged LTA and FAU using a selection of M(II) counter ions (Mn(II), Co(II), Cu(II) and Zn(II)).[217] The reported formation enthalpies for LTA range from -1,233.2 kJ mol^{-1} to -1,363.3 kJ mol^{-1} and exhibit the following selectivity preference: Mn > Cu > Co > Zn, with Mn being the most thermodynamically favourable cation. Energetically, our calculated values for M(II) cations are in a similar range of -1,411.7 kJ mol^{-1} to -2,002.5 kJ mol^{-1}, however we note that they are noticeably lower in energy which could be attributed to the nature of the zeolite structure. It should be noted that comparison to experimental values can be difficult as there are large contributions resulting from energies of hydration, thus a more detailed comparison is not possible, however relativistic trends can provide valuable insight. Wu and Navrotsky report in the same study the enthalpies for the same cations in the FAU zeolite, with an energy range of -1,130.9 kJ mol^{-1} to -1,176.5 kJ mol^{-1}, and a selectivity preference of Mn > Co ~ Cu > Zn.

Again, these values are more exothermic than what we report for ZSM-5, but approximately 100 kJ mol^{-1} more exothermic than the values reported for LTA, once again indicating the difference is due to the zeolite topology and contributions from hydration energies. We report an order of selectivity as follows: Co > Cu > Ti > Zn > Mn. Some similarities are apparent with the order of selectivities reported for FAU, with Co being more endothermic than Cu, which is more endothermic than Zn. The key discrepancy here lies with the more exothermic nature of Mn in ZSM-5, it is however unclear how significant the contributions from hydration energies vary for each coordinated cationic species. In conjunction with these findings, we also note the nature of coordinating protons in zeolites allows them to move around in the charge deficit region of the zeolite, and so larger less strongly bound cations can also move, which can impact the reported binding energies if bound at a different site.[238–241]

In addition, a study by Barrer and Townsend[242] performed a series of ion exchange experiments with ammonium mordenite. The ion exchange of Mn(II), Co(II), Ni(II), Cu(II) and Zn(II) was studied in aqueous solution over a pH range of 4-7 at 25 °C, and the thermodynamic affinities were deduced as Mn(II) > Cu(II) > Co(II) ~ Zn(II) > Ni(II). Once again this is very similar to the affinity series presented by Wu and Navrotsky for the LTA zeolite, thus we can remain confident that our results follow the same trend for Cu, Co and Zn. However, there is still the discrepancy resulting from Mn(II). It is therefore hard to determine whether the placement of Mn(II) in the series is due to the nature of ZSM-5, or the modelling of the cation and the high stability nature of its 3d^5 electron configuration.

However, it should be noted that there are some contrasting results reported in the work of Maes and Cremers.[243] This study investigated the ion exchange of the bivalent metal cations: Co, Ni, Cu and Zn on synthetic zeolite NaX and NaY (variations on the FAU zeolite with Si:Al <2 and >2 respectively). Ion exchange isotherms were measured for the eight systems in a temperature range of 5-45 °C, and the selectivity in small cages was found to be dependent on the occupancy and type of ion present in the larger cavities. The overall selectivity for both zeolites was found to be Ni < Co < Zn < Cu, which appears to be different from that discussed in the previous studies. Therefore, it could be reasonable to assume our selectivity is influenced by the occupancy and ion type present in the larger cavity of ZSM-5.

In the case of the (III) oxidation state cations, there is a concomitant jump in binding energy as observed previously and a resultant energetic order of Au > Fe > Mn > Ti. As a result, the substantial increase of binding energy for the (III) ions is accompanied by an increase in the energy range to 866.4 kJ mol^{-1}, which equates to 23.1 % of the lowest binding energy. The energy gap between the most favourable and next favourable cations (Au and Fe) also increases to 266.3 kJ mol^{-1}, which indicates that at the higher oxidation states the gap in energetic favourability can also increase. Energetically, this trend continues with the two systems modelling cations in the (IV) oxidation state, with Fe(IV) and Ti(IV) yielding substantially lower binding energies of -7,228.5 and -5,551.3 kJ mol^{-1} respectively. The energetic gap between these two cations also widens to 1,677.3 kJ mol^{-1} which forms 23.2 % of the lowest binding energy resulting from the Fe(IV) cation. This is a minor increase in percentage compared to previous systems, whilst the data could be skewed by only having two (IV) cations, it could also suggest that the percentage increase plateaus at around 23 %.

4.3.2 Oxygen Affinity to Metal Exchanged ZSM-5

The next set of calculations focussed on the addition of molecular diatomic oxygen into the pore of ZSM-5 next to the metal cation site, to model the coordination of the molecule to the aluminium site cation. These calculations utilised the previously optimised selection of metal cation structures, and a diatomic oxygen molecule was placed so that both oxygen atoms are an equal distance from the cation, however two different minima were reported as shown below in **Fig 4.2**. Molecular oxygen was initially calculated separately using only the QM methodology in ORCA,[182] as the QM/MM calculations would treat the coordinating oxygen at the QM level of theory. The diatomic oxygen subsequently optimised to an absolute bond length of 1.20458 Å with an energy of -389,655 kJ mol^{-1} under this methodology. We note that this oxygen-oxygen bond length is slightly shorter than is typically reported from experimental data, which reports the bond length of O_2 as approximately 1.207 Å,[244] however the absolute bond length that results from the optimisation is dependent on the methodology used. Therefore, it is more appropriate to measure the change in oxygen-oxygen bond length from this calculated initial length. The energy of the diatomic oxygen molecule was then subtracted from the overall system energy and the previous energy of the metal cation system to obtain the binding energy of oxygen, $\mathbf{E_{Binding}}$, to the metal cation as shown below:

$$E_{Binding} = E_{Total} - E_{Oxygen} - E_{M+ZSM-5} \qquad (4.2)$$

Where $\mathbf{E_{Total}}$ is the total energy of the system, $\mathbf{E_{Oxygen}}$ is the calculated energy of a diatomic oxygen molecule in the triplet ground state and $\mathbf{E_{M+ZSM-5}}$ is the energy of the cationic ZSM-5 structure. To determine whether the molecular oxygen forms an activated oxo or an activated super-oxo group, the oxygen-oxygen bond length is measured.

The initial molecular oxygen bond length was calculated to be 1.2 Å (specifically 1.20458 Å), if the oxygen-oxygen bond length extends beyond this value upon coordination but remains below 1.3 Å it can be assumed it forms a simple activated oxo group. Provided the bond length extends to 1.3 Å or longer, then it can be assumed an activated super-oxo group is formed. Whilst this can be considered short for a super-oxo bond length, which are often reported with bond lengths around 1.4-1.5 Å, there have been in depth studies that report super-oxo formation at these bond lengths when bonding side-on to metal centres such as Fe(III) similar to the results of our study.[245,246] Two initial starting structures were used, with one more likely to optimise to a super-oxide structure, labelled type-a, whilst the other started from a structure that was more likely to obtain a molecular oxygen structure, referred to here as a type-b structure, as shown below in ***Fig. 4.2.***

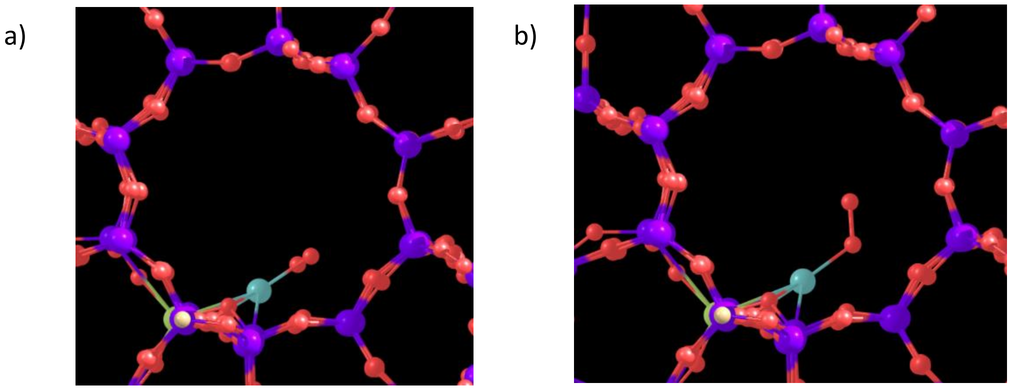

Fig. 4.2. Optimised structures with a) **type-a** structure and b) **type-b** starting structures. The Cu(I) cation shown is replaced at the start of each calculation by the corresponding atom type, whilst everything else remains the same. Atom colours: Si: purple, Al: yellow, O: red and Cu: light blue.

The results are displayed below in ***Table 4.2.***, where multiple systems are shown to be capable of activating molecular oxygen to form different oxo and super-oxo species. Here, the **a** and **b** notation refer to the structural type that was produced at the end of the optimisation step, either an oxo species or super-oxo species respectively. The notation given corresponds to the initial oxidation step of the metal centre before oxygen binding, the resulting (**type-a**) super-oxo structures will correlate to a one electron oxidation of these centres.

System	E / kJ mol^{-1}	Bond Lengths / Å	O_2 Binding E / kJ mol^{-1}
Mo(I) a	-23291927	1.44873	-402
Mo(I) b	-23291794	1.27017	-268
Zn(I) a	-27727161	1.36251	-94
Au(I) a	-23466741	1.35097	11
Cu(I) a	-27367167	1.31849	12
Au(I) b	-23466703	1.22697	50
Cu(I) b	-27367127	1.23233	52
Na(I) a	-23535756	1.20521	132
Mo(II) a	-23291238	1.36228	-424
Mo(II) b	-23291062	1.24781	-246
Ti(II) a	-25316306	1.31022	-216
Mn(II) b	-26097610	1.20691	-149
Co(II) b	-26698397	1.20225	-149
Co(II) a	-26698375	1.23556	-127
Mn(II) a	-26097585	1.29771	-124
Fe(II) a	-26389631	1.29724	-113
Ti(II) b	-25316205	1.2509	-113
Fe(II) b	-26389584	1.21876	-65
Mg(II) a	-23633132	1.20126	-64
Cu(II) a	-27366326	1.21656	-50
Zn(II) a	-27726328	1.21958	-38
Cu(II) b	-27366304	1.20094	-28
Zn(II) b	-27726240	1.20057	51
Fe(III) b	-26388638	1.20222	-187
Ti(III) a	-25315164	1.2997	-174
Ti(III) b	-25315096	1.2144	-106
Au(III) a	-23464704	1.25001	-81
Mn(III) b	-26096165	1.19484	-69
Au(III) b	-23464685	1.20076	-62
Mn(III) a	-26096157	1.29952	-61
Fe(IV) b	-26387208	1.20102	-383
Ti(IV) b	-25313682	1.20706	-216

Table 4.2. Binding energies of diatomic oxygen in cationic ZSM-5 systems, with oxygen-oxygen bond lengths.

Despite a large range in energy differences for cation binding energy of 6,789.4 kJ mol^{-1}, the range for oxygen coordination energies is smaller at 556.4 kJ mol^{-1}. From the bond length values in ***Table 4.2.***, the following metal cations: Au(I), Fe(II), Mn(II), Mn(III), Cu(I), Zn(I), Ti(II), Ti(III), Mo(I) and Mo(II) all display a propensity to activate molecular oxygen and form a super-oxo species, which is demonstrated by the characteristic lengthening of the oxygen-oxygen bond length from 1.2 Å for a coordinated oxo species to approximately 1.3 Å for a coordinated super-oxo species. It can be noted that the Mo(I) system has an uncharacteristically long oxygen-oxygen bond length which is accompanied by a comparatively very low binding energy of -424.1 kJ mol^{-1}, with similar binding energies to Fe(IV) and Mo(II). Although it should be noted that Fe(IV) does not form an activated super-oxo species with a bond length longer than 1.3 Å. Additionally, we note that both types of Au(I), Cu(I) structures along with the Na(I) and Zn(II) **b** systems yielded positive binding energies indicating that oxygen would not realistically bind to these cationic centres.

As well as this trend, there is a case that the **type-a** structures are predominantly lower in energy upon the coordination of oxygen, which does not, however, apply to all metal cations. In the case of Mn(II) and Mn(III), the **type-b** structures are lower in energy than the **type-a** counterpart, but unlike its counterpart the **type-b** structure does not form a super-oxo species. These are the only two cations that exhibit this behaviour and demonstrate that just because a system can form a super-oxo species, it does not necessarily mean that it is more energetically favourable to do so. Additionally, six cations converge to a single structure type which are Fe(III), Fe(IV), Mg(II), Na(I), Zn(I) and Ti(IV) suggesting that only the indicated configuration forms a stable minimum.

4.3.4 Hydrogen affinity to activated oxygen on metal exchanged ZSM-5

The next set of calculations builds upon these metal-oxo systems by attaching a hydrogen, which is bound axially to the coordinated oxygen system, on the oxygen atom furthest away from the cation and pointing into the pore, as shown in ***Fig. 4.3.***

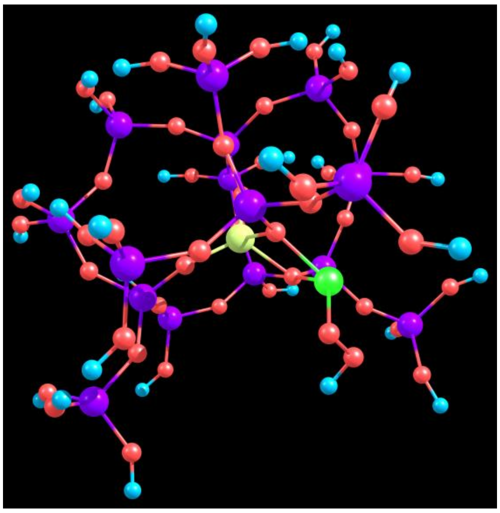

Fig. 4.3. Optimised Mn(II)-ZSM-5 with bound oxygen with a hydrogen atom attached to the axial oxygen pointing into the pore. Atom colours: Si: purple, Al: yellow, O: red, H: light blue and Mn(II): light green.

The energy for the hydrogen atom was calculated, where the atom exists as a single gaseous hydrogen atom and not a proton, or half of a diatomic hydrogen value, and has a with a value of -1,283.28 kJ mol^{-1}. The hydrogen affinity, **BDE$_{OH}$**, was calculated in the same way to the oxygen binding energy, just with the subtraction of the hydrogen atom value. The energy values from these calculations are reported below in ***Table 4.3.***, which reports the entire system energy, the difference in energy from the bound oxygen systems, the oxygen-oxygen bond lengths and the change in oxygen-oxygen bond length that arises from the addition of the hydrogen.

System	E / kJ mol^{-1}	ΔE Oxide / kJ mol^{-1}	BDE_{OH} / kJ mol^{-1}	O_2 Bond Lengths/ Å	Bond Length Change / Å
Mo(I)	-23293951	-2157	-873	Dissociated O2	-
Na(I)	-23537469	-1713	-430	1.32764	0.12270
Cu(I)	-27368809	-1682	-399	1.35311	0.12078
Au(I)	-23468385	-1682	-399	1.33161	0.10464
Zn(I)	-27728812	-1653	-369	1.48876	0.12625
Mg(II)	-23634756	-1763	-480	1.31316	0.11013
Fe(II)	-26391339	-1755	-472	1.35605	0.13729
Mo(II)	-23292797	-1735	-452	1.45796	0.21015
Ti(II)	-25317930	-1726	-442	1.40164	0.15074
Zn(II)	-27727959	-1719	-436	1.30591	0.10534
Cu(II)	-27367918	-1592	-308	1.38379	0.16723
Co(II)	-26699923	-1548	-265	1.41081	0.17525
Mn(II)	-26099120	-1535	-251	1.43038	0.13267
Mn(III)	-26098046	-1889	-606	1.43391	0.13439
Ti(III)	-25316916	-1752	-468	1.46131	0.16161
Au(III)	-23466320	-1617	-334	1.40175	0.15174
Fe(III)	-26390229	-1592	-309	1.29552	0.09369
Fe(IV) *	-26388746	-1854	-571	1.31414	0.1038
Ti(IV)	-25315404	-1721	-438	1.36753	0.16047

Table 4.3. Table of hydrogen affinity energies and the respective change in oxygen-oxygen bond distances, *indicates a lower convergence criterion was used to obtain this value.

From these data, it is observed that the range in hydrogen affinity energies, **BDE_{OH}**, is once again substantial at 622.0 kJ mol^{-1} and is comparable to the oxygen coordination energy range; thus, the largest influence on the overall system energy is the metal cation as is expected. We can see that the addition of hydrogen to the molecular oxygen results in an elongation of the oxygen-oxygen bond length of between 0.10 Å to 0.16 Å.

We note that the Fe(IV) system required a lower convergence criterion of 3.0 $\times10^{-7}$ au compared to the usual 1.0 $\times10^{-8}$ au. Whilst this is 30 times less precise than the conventional criterion it is higher than the recommended criterion for a single point calculation (1.0 $\times10^{-6}$ au) so is within a reasonable level of accuracy. The failure to converge at the higher level of precision illustrates that the system is probably unstable in this higher oxidation state despite the lower energy.

From a qualitative perspective the Mo(I) system optimises to a structure whereby the oxygen-oxygen bonds completely dissociate as shown below in ***Fig. 4.4.***, forming a hydroxyl group and a single bond from the Mo(I) cation and oxygen. This behaviour can be further understood when looking at the affinity towards the abstraction of hydrogen as it has the lowest **BDE$_{OH}$** energies out of all the modelled systems at -873.4 kJ mol^{-1}. The energetics imply that the oxygen would abstract the hydrogen and dissociate forming the hydroxyl and oxygen incredibly quickly, regardless of the starting geometry of the bound oxygen. We note that the hydrogen affinity value also includes the cleavage of the oxygen-oxygen bond, and so it is somewhat difficult to determine the value of each separate contribution.

When also considering the Zn(II)-super-oxo system, which is probably formed from the Zn(I) cation precursor, the bond length is shown to elongate more than in the other structures by 0.13 Å to 1.49 Å. As a result, it forms the longest oxygen-oxygen bond length, which could suggest that the oxygen-oxygen bond is significantly weaker than the other cation systems upon the abstraction of a hydrogen. This weakened oxygen bond could subsequently help facilitate the oxygen-oxygen bond cleavage in a following step by lowering the energetic barrier. The largest change in oxygen bond length occurs with the Mn(III)-super-oxo complex, formed from the Mn(II) precursor, which extends by 0.21 Å to 1.46 Å, making it the third longest oxygen-oxygen bond of all systems, leading to a substantial weakening of the bond which makes its cleavage more energetically favourable.

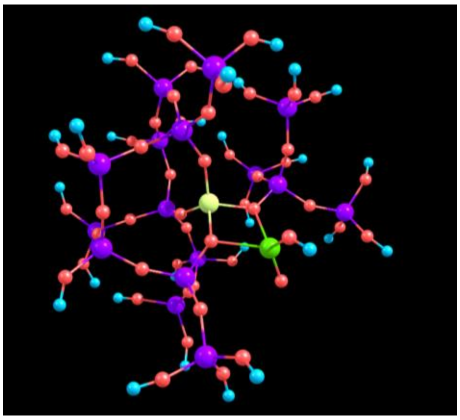

Fig. 4.4. Optimised structure of both Mo(I) structures when modelling the hydrogen affinity of a bound oxygen complex. Atom colours: Si: purple, Al: yellow, O: red, H: light blue and Mo(I): light green.

The super-oxo formed from the Mn(III) precursor has the second highest hydrogen affinity after Mo(I) but oxygen-oxygen bond cleavage is not observed. Interestingly, after oxygen and hydrogen binding, the Mo(I) precursor forms a Mo(IV)(O_2^-) (OH^-) species, whilst the Mn(III) precursor retains its starting oxidation state. The **BDE_{OH}** energy of the complex is significantly higher than that of Mo(I) (267.5 kJ mol^{-1}) and results in elongating the oxygen-oxygen bond to a length of 1.43 Å upon hydrogen abstraction. This elongation will weaken the strength of the oxygen-oxygen bond; thus, a further step could lead to a similar result to the Mo(I) systems without requiring a significant energetic contribution.

In general, the addition of the hydrogen atom results in all oxygen-oxygen bond lengths elongating to around the 1.3 Å length, which suggests that even if the coordinated oxygens only formed an activated oxo species, the addition of the hydrogen forces the oxygen complex to lose its double bond and adopt a super-oxo type structure, in line with expectations. For complexes where the oxygen-oxygen bond length extends to over 1.4 Å, there does not appear to be a correlated energetic increase or decrease linked to the additional increase in bond length.

The Mn(II) calculation gave the highest energy structure at -251.4 kJ mol^{-1}, and thus is the most unstable, extending the oxygen-oxygen bond by 0.13 Å to 1.43 Å. Despite this high value, it still forms one of the longer oxygen-oxygen bond lengths, thus a subsequent step that cleaves the bond in two could have a lower energy barrier, which could potentially facilitate the oxygen-oxygen bond cleavage. Considering the coordination of the oxygen molecule is more favourable at -149.3 kJ mol^{-1} than -123.8 kJ mol^{-1} and the binding energy of the cation is very low at -1,411.7 kJ mol^{-1}; the -251.4 kJ mol^{-1} hydrogen affinity energy (**BDE_{OH}**) is still the highest across both oxygen coordination and hydrogen abstraction steps. Thus it can be assumed that Mn(II) would be least efficient for the conversion of methane to methanol.

4.4 Thermochemical Properties of Metal Exchanged ZSM-5 Toward Methane Activation.

In nature, the enzyme methane monooxygenase (MMO) uses high valence di-iron co-factors to abstract hydrogen from methane at low turnover frequencies.[247,248] Additionally, the P450 super-family of oxygenases offer an important target for directed evolution and can efficiently convert the oxygenation of un-activated C−H bonds. However, currently methane is the only short chain alkane that such bioengineered enzymes cannot oxidise efficiently.[249–251] This μ-nitrido-bridged diiron-oxo porphyrin catalyst is the exemplar homogeneous catalyst for methane conversion and is based on a dimer of two of the heme co-enzymes found in P450s.[252–255] A previous DFT study comparing the single porphyrin to the diiron catalyst showed a reduction in the rate-limiting hydrogen atom abstraction step of 56.9 kJ mol^{-1}, which would imply a rate enhancement of ~1,010 with an increase in the basicity of the active oxidant which is key to this improved activity.[256–259] The same valence bond approach to rationalising the oxidative power of metal dependant oxidants has been extensively validated for both homogeneous catalysts[260] and biological[261,262] catalytic systems. Such an approach will also be used in the remainder of this chapter to screen metal cations for efficient catalysation of methane conversion.

From periodic DFT calculations on Au(I) cation exchanged ZSM-5, it was determined that both the radical super-oxo (Au(II)−OO*) and the gold oxo (Au(III)=O^{2-}) catalysed a methane conversion reaction pathway with a single dominant hydrogen atom abstraction (HAT) barrier; the oxo species proceeded via an accessible HAT barrier of ~47 kJ mol^{-1}, whilst a high barrier of ~125 kJ mol^{-1} was observed for the super-oxo alternative.[86] One way of improving the oxidation activity of metal exchanged zeolites is to engineer the framework for higher metal loadings to activate molecular oxygen in a similar way to that observed in MMO,[86] however, our study takes a different approach and screens sustainable cations to determine the oxidative potential of each candidate using a valence bond approach.

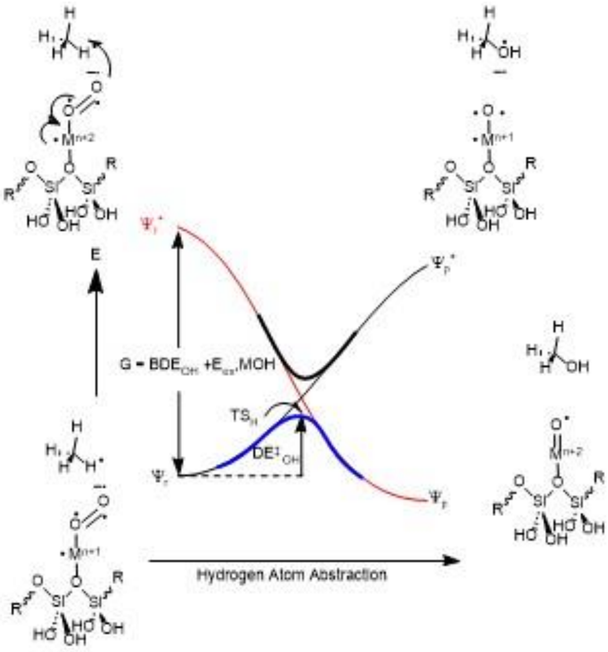

Fig. 4.5. Valence bond curve crossing diagram for the methane hydroxylation by metal exchanged zeolites. Dots represent valence electrons and lines (curved or straight) implicate chemical bonds.

Fig. 4.5. rationalises the contributions to the rate-limiting HAT barrier by connecting the ground state reactant, **Ψr**, to an excited species with the geometry of the product and the reactants wave function, **Ψp***; when the ground state product, **Ψp**, is also connected to a species with the geometry of the reactant and the wave function of the product, **Ψr***, an avoidance crossing is created at the transition point, **TS_{HA}**. The analysis determines that the energy of **TS_{HA}** (**$DE^{‡}_{OH}$**) comprises: a bond formation energy for the metal-hydroperoxo, **BDE_{OH}**, a bond breaking energy for the formation of the methyl radical, **BDE_{CH}**, and a molecular orbital change, **$E_{ex}MO$**, correlated to electron-transfer energies and rehybridization. Since the energy of the C−H bond in methane will be constant for all calculations (432.4 kJ mol^{-1})[263] the HAT barrier will be determined by the formation energy for the metal-hydroperoxide, **BDE_{OH}**. The **BDE_{OH}** energy can be further divided into electron affinity, **EA**, and acidity, **Δ_{acid}**, of each metal super-oxo, as illustrated via the Hess cycle in ***Fig. 4.6.*** The ionisation energy of a hydrogen atom[233] was calculated to be -1,283.28 kJ mol^{-1}.

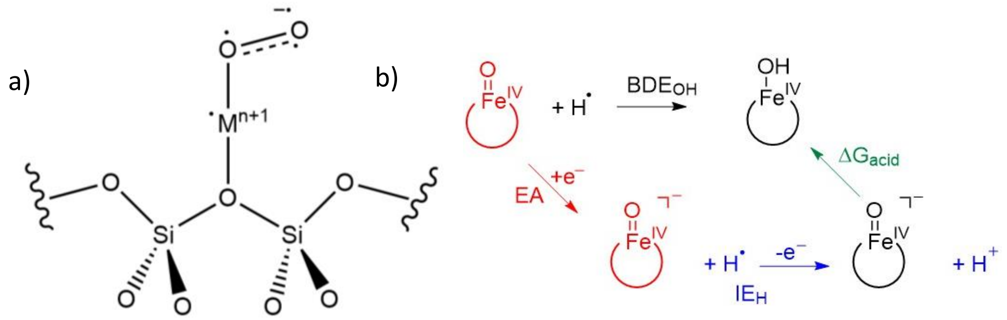

Fig. 4.6. Schematic representation of the oxo-group (a) and the thermodynamical variables within a Hess cycle (b).

	Δ$_{EA}$	**Δ$_{BDEOH}$**	**Δ$_{acid}$**
Fe(IV)O,$_{Heme}$†	389	333	1339
2Fe(IV)O,$_{Hetro}$†	269	363	1189
Au(I),$_{ZSM-5}$	503	390	1396
Na(I),$_{ZSM-5}$	443	430	1296
Cu(I),$_{ZSM-5}$	375	399	1259
Zn(I),$_{ZSM-5}$	262	370	1175
Cu(II),$_{ZSM-5}$	841	308	1816
Mn(II),$_{ZSM-5}$	738	251	1770
Co(II),$_{ZSM-5}$	725	265	1743
Fe(II),$_{ZSM-5}$	903	472	1714
Zn(II),$_{ZSM-5}$	833	436	1680
Ti(II),$_{ZSM-5}$	782	442	1623
Mg(II),$_{ZSM-5}$	807	480	1610
Mo(II),$_{ZSM-5}$	689	452	1520
Au(III),$_{ZSM-5}$	1208	334	2157
Mn(III),$_{ZSM-5}$	1428	606	2105
Fe(III),$_{ZSM-5}$	993	309	1967
Ti(III),$_{ZSM-5}$	1142	468	1957
Ti(IV),$_{ZSM-5}$	1482	438	2327
Fe(IV),$_{ZSM-5}$	1430	571	2142

Table 4.4. Calculated thermodynamical variables. All values given in kJ mol^{-1}.

(†Values taken from the work of Quesne *et al*[264])

Table 4.4. references the thermodynamic properties of the µ-nitrido-bridged diiron-oxo porphyrin catalyst as well as a model of the first coordination sphere of the heme P450 enzyme, for comparison.[252–255] Previous work has conclusively linked the activity of HAT catalysts to the acidity, **BDE_{OH},** of the active oxidant,[265,266] therefore, the more basic the metal-oxo the more of an effective methane conversion catalyst the metal exchanged zeolite will be. From the thermodynamical values given in ***Table 4.4.***, we can hypothesise that [(Zn(I)-ZSM-5]-super-oxo could be a very effective catalyst for methane activation. Indeed, the **Δ_{acid}** reported for this species is very close to the value previously reported for the µ-nitrido-bridged diiron-oxo porphyrin, the super-oxo species created with Cu(I) and Na(I) cations are approximately as basic as the natural porphyrin alternative.

4.5 Summary and Conclusions

A series of hybrid QM/MM calculations were carried out to determine the binding energies of various metal cations in different oxidation states. These optimised systems were then used to model the coordination of a diatomic oxygen molecule in two different orientations, the results of which subsequently demonstrated that the Fe(II), Mn(II), Mn(III), Cu(I), Zn(I), Ti(II), Ti(III), Mo(I) and Mo(II) systems could activate molecular oxygen and form a super-oxide species upon coordination to the metal cation, as indicated by the diatomic oxygen bond length extending from 1.2 Å for the unbound oxygen to around 1.3 Å. Both types of Au(I), Cu(I) structures along with the Na(I) and Zn(II) **b** systems yielded positive binding energies which indicate that oxygen will not bind to these cationic centres.

All metal-oxo systems were then used to model their respective hydrogen affinities, as would be the next step in this novel pathway, in which a methane C-H bond cleaves, and the hydrogen binds to the coordinated oxygen molecule. In the case of Mo(I) systems this splits the oxygen-oxygen bond of the coordinated molecule forming a hydroxyl group. From the selection of other metal cations, we see a very favourable hydrogen affinity, **BDE_{OH}**, for Mo(I) and Mn(III) systems, which were all able to form a super-oxide upon the coordination of molecular oxygen within the first set of calculations, whilst one of the Fe(IV) structures also had a similar energy, which could, however, result from the need to use a less strict convergence criterion for the calculation to complete the intended optimisation.

Using these data, a valence bond approach was employed to rationalise the oxidative power of the metal dependant oxidants. From this series of calculations, we have shown that the $\mathbf{\Delta_{acid}}$ is very low for the [Zn(I)-ZSM-5]-super-oxo complex which would suggest that it could make for a very effective catalyst for methane activation. Normally Zn(I) is a very unstable oxidation state, and so could form from a Zn(II)-ZSM-5 super-oxo precursor as a zeolite bound Zn(I) cation may not be a stable precursor. However, it has previously been reported by Qi *et al*[267] that the ZSM-5 zeolite is one of the few complexes whereby a Zn(I) cation can indeed be stabilised. The $\mathbf{BDE_{OH}}$ of this species is of a comparable energy to that of the current µ-nitrido-bridged diiron-oxo porphyrin. As was seen previously in the literature, an increase to the basicity for the active oxidant is a fundamental feature for Improving the activity of the catalyst, so it is worth noting that whilst both Cu(I) and Na(I) form super-oxo species with similar basicities to the natural porphyrin alternative, they cannot bind molecular oxygen as demonstrated by their positive binding energies. These complexes could potentially form from alternative oxidation states that undergo redox processes whilst oxygen is coordinated to the metal centres.

CHAPTER 5

Computational Modelling of Water Clusters in the Pore of H^+-ZSM-5 and Na^+-ZSM-5

5.1 Introduction

Whilst water is a relatively simple molecule it often exhibits complex behaviours which can play an important role in reactions where it can be used as a green solvent. Water can play a crucial role in zeolites and can strongly determine the catalytic and adsorption propensity of a system. As a result, there has been a great deal of research on water dynamics in zeolites and especially on how this behaviour can change within the pores of zeolites due to confinement effects; both Brønsted acid sites and defects have been shown to play a crucial role in the stability of zeolites.[91] Interaction with water can drastically alter zeolite properties, and whilst at low temperatures it has been shown to be limited to simple adsorption, higher temperatures can lead to both structural and compositional changes as detailed extensively in the introduction of this thesis (chapter 1).

From the inception of this field of study, one topic of extensive debate concerns hydroxonium ion cluster formation within the pores of zeolites. This debate has engaged many different experimental techniques[98,106,107,268] and has expanded into the realm of computational chemistry.[102,108,269] A particularly relevant study is found in the work of Bukowski *et al*,[97] who utilised *Ab-Initio* Molecular Dynamics (AIMD) to simulate different water cluster sizes within beta-zeolite with an extra-framework Sn(IV) to determine the structure and thermodynamics of water phases in defected microporous networks and detail the impact of solvents on catalytic reactions in these micropores. Sn(IV) was introduced as both Sn(IV) and Sn(IV)OH and both these extra-framework cations acted as nucleation centres for water clusters. This chapter follows a similar concept but using both H(I) and Na(I) instead of Sn as the extra-framework cation nucleation centres, to support future work at the Central Laser Facility (CLF) on the elucidation of the anharmonicity of water clusters within Na-ZSM-5.

Whilst there have been a wide range of studies debating hydroxonium ion formation many experimental works claimed formation was not favoured, such as the works of Hunger *et al*[98] and Parker *et al*[100] amongst many others. It was not until the work of Krossner and Sauer[102] as well as the works on ZSM-5 by Zygmunt *et al,*[270] that the hydroxonium ion was shown to occupy a minimum on the potential energy surface.

Subsequently, it became generally accepted that in the pore of H-ZSM-5, water clusters start to form, and hydroxonium ion formation can occur with a loading of two water molecules and reaches pore saturation with eight water molecules.[271] This dynamical behaviour occurs with several different zeolites such as FAU, and protonated zeolites have demonstrated a propensity to form stabilising hydrogen bonds. These typically occur from the water molecule's oxygen to the Brønsted acid site hydrogen, with the potential to form an additional weaker hydrogen bond from the water's hydrogen to an oxygen in the zeolite's pore wall. The addition of a second water molecule is also shown to stabilise the system to form a dimeric $H_5O_2^+$ species,[109] as determined using a combination of experimental IR studies and computational methods.[99,101] Thus, in the work of Vener *et al*[112] the protonation of water clusters was modelled in the H-SSZ-13 (Chabazite) zeolite. DFT was used to model up to four water molecules within the pore, coupled with Car-Parrinello molecular dynamics simulations, and demonstrated that the proton affinity increases with the size of the water cluster. The previously discussed water dimer was again shown to be the most stable equilibrium structure with the PBE functional,[87] but the use of the BLYP functional was found to favour a neutral complex. At loadings of three water molecules, proton transfer to the water was observed but short lived; whilst the addition of a fourth water molecule made this more thermodynamically stable.

Considering the intrinsic role water can play in the structural stability and, by extension, the important effect water has on the activity of a zeolite, we seek to model comprehensively the dynamics of low concentrations of water in ZSM-5. Specifically, this project aims to model protonated H-ZSM-5 and Na-ZSM-5, following the previous chapter, and expand on that work by demonstrating the differences between the two systems at the same concentrations of water. These differences will be characterised by simulating the IR spectrum for water clusters taken from AIMD simulations and detail how their spectroscopic shifts are affected by these changes. Furthermore, the work aspires to provide a detailed analysis that can be coupled with research in progress using novel 2D-IR methods at the Science and Technology Facilities Council (STFC) Central Laser Facility (CLF). Whilst these experimental data are not yet available, they will provide detailed information on the anharmonic behaviour of water within the pore of sodium exchanged ZSM-5 materials, including intriguing cross-coupling effects. Hence this computational research can be combined with experimental work in the future, to help elucidate the configurations of water responsible for causing this cross-coupling.

5.2.0 Methods

5.2.1 AIMD Calculations

Initial energy minimisation calculations of H(I)-ZSM-5 and Na(I)-ZSM-5 were carried out, followed by the addition of between one and three water molecules in the pore of these systems. These calculations utilised the VASP code,[74–78] discussed in Chapter 2, employing the PBE generalised-gradient-approximation (GGA)[87] to treat the valence electrons with conventional LDA reference configurations,[210] and PAW potentials[78] were utilised to treat the core electrons. A much smaller K-point mesh of 1 x 1 x 1 was applied, as we aimed only to generate reasonable initial structures and not provide an in-depth study on the energetics. As with the previous studies on lattice energies, a Gaussian smear was applied to ensure more of these K-points are on the Fermi surface, and a Grimme-D3 dispersion correction was applied.[88] The same cut-off and convergence criteria were used as previously in Chapter 3, i.e. a 520 eV planewave cut-off, and force convergence of -0.01 eV $Å^{-1}$ and an SCF cut-off of 0.00001 eV, which had been shown to yield reliable results in the work covered in Chapter 3.

These structures were then used as the initial configurations for *Ab-Initio* Molecular Dynamics (AIMD) simulations. These simulations were also run using the VASP code,[74–78] which implements a Born-Oppenheimer Molecular Dynamics (BOMD) scheme, which combines molecular dynamics and electronic structure theory to model systems at specific temperatures as discussed in the Methodology chapter of this thesis. AIMD was selected in favour of classical molecular dynamical methods as it allows the modelling of bond formation and breakage, a crucial aspect when considering the dynamical nature of hydrogen bonds in water. It is expected that water molecules form hydrogen bonds to other water molecules, the BAS and framework oxygens. Also, bond formation and breaking are key in the formation of hydroxonium ions and proton shuttling behaviours that effect the cation site.

VASP[74–78] in particular uses a Verlet algorithm,[176] as discussed in the Methodology Section (2.2.4), for the integration of Newtonian equations of motion and calculates the trajectories of particles, or in this case water molecules. The simulations were run at two temperatures: ambient room temperature (298 K) and 400 K, which encompass a range of temperatures that were used for the experimental measurements that inspired this chapter.

These AIMD calculations used an NVT ensemble (canonical ensemble) which models materials with a constant number of particles at a constant volume and allows for a fluctuating temperature around a designated equilibrium value, set at a constant 298 K and 400 K in the case of this study. Additionally, these simulations employed an unbiased approach which would allow for protons to exchange back and forth between the acid site and other water molecules in the cluster, which is particularly relevant when considering the formation and breaking of hydrogen bonds within the cluster.

All simulations were run for 20,000 steps, with each step equivalent to 0.5 fs giving an overall 10 ps snapshot of the system. These settings were used as the timestep is short enough to accurately follow the fastest atomic motions in the system, such as the O-H stretching vibration. The overall timeframe allows for the capture of events of interest such as the forming and breaking of hydrogen bonds within the water cluster, and the dynamics of the water clusters around the nucleation site.[271–273] The results of these simulations were plotted using their root mean squared deviation/displacement (RMSD), as detailed in the methodology section (2.5), from the initial structures. From these plots a selection of maxima and minima or structurally significant and distinct configurations were selected for further investigation.

5.2.2 Hybrid QM/MM Calculations

The region of interest primarily focusses on the structure and dynamics of water molecules within the pore, which interact with the wall of the pore surrounding the active site and other water molecules. As a result, it becomes appropriate to use a hybrid QM/MM methodology as the bulk of the ZSM-5 zeolite has very little bearing on the region of interest, which also has the advantage of reducing the computational requirements whilst minimising the reduction in chemical accuracy. Therefore, structures of significance were selected from the analysis of the AIMD simulations, reconstructed, and then optimised using the QM/MM methodology.

The QM/MM method used the additive approach with electrostatic coupling as implemented by the Chemshell software for modelling the zeolite.[228] This methodology is the same as that discussed in the Methodology chapter, and also employed in Chapter 4 of this thesis to model different metal centres in ZSM-5. The QM region selected was the aluminium containing ring of the pore, as this would contain the acid site interactions, and any other feasible hydrogen bonding to the walls of the pore that were observed in the AIMD simulations and is shown in ***Fig. 5.1***. The QM region was calculated with the ORCA code[182] discussed in the Metal Centres chapter, and the MM region was treated by DL-POLY implemented by the TCL Chemshell interface. As shown below, the QM region terminates at oxygen atoms and Chemshell attaches hydrogen linker atoms to maintain the corresponding valences and electrostatic embedding.

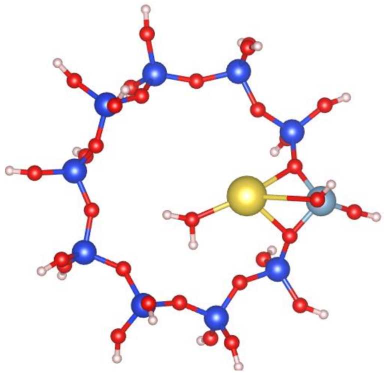

Fig. 5.1. Example QM region for Na(I)-ZSM-5 with a single water molecule coordinated to the sodium cation. Atom colours: Si: dark blue, Al: light blue, O: red, H: white and Na(I): yellow.

The QM treatment utilised the def2_TZVP basis set[229] and B3LYP functional[110,111] with a Grimme-D3 dispersion[88] and Tight SCF convergence criteria of 1.0 x10^{-8} au, whilst the sodium cation was calculated as a single gaseous cation with a Very Tight SCF criteria of 1.0 x10^{-9} au. The next step was to take these optimised structures and run vibrational frequency calculations, whereby the frequencies are calculated using the Generalised second-order Vibrational Perturbation Theory (GVPT2) function in the ORCA code,[182] as discussed in the Methodology chapter of this thesis, whilst applying the same def2_TZVP basis set[229] and B3LYP functional.[110,111] The overall workflow detailing the order of calculations is detailed below in ***Scheme 5.1.***

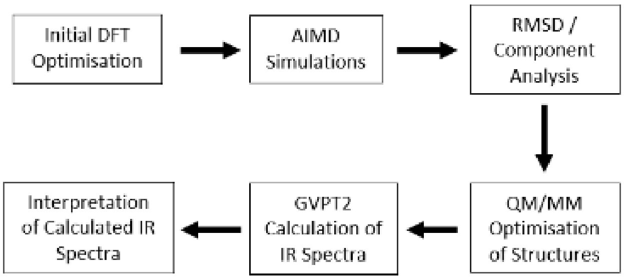

Scheme 5.1. Sequence of calculations performed in this study.

This functionality initially calculates the harmonic frequencies and normal modes with the high level DFT method outlined. Calculation of vibrations using the Born-Oppenheimer approximation[133] separates vibrations into potential energy surface terms. A double harmonic approximation is made when the potential energy surface reaches the second order calculation. The second part calculates the cubic and fourth derivatives using a lower level of DFT. To improve upon the accuracy of these calculations, a scaling method is applied to the harmonic wave numbers, which allows for the correction of the band positions within the spectrum. This approach results in a trade-off, whereby relative intensities are calculated, which can lead to low intensity contributions from common vibrations and high intensity contributions from uncommon vibrations. To correct and obtain reliable vibrational wave numbers, a time-independent method is applied, however Fermi resonances can cause errors in this anharmonic correction. In the Generalised VPT2 (GVPT2) method used in this chapter, these resonances can be removed using De-perturbed VPT2 (DVPT2) and are then reintroduced at a second stage and treated variationally. This acts as a scaling factor that transforms the harmonic results into anharmonic vibrations whilst providing highly accurate frequencies, at the cost of intensity values which are reported as relative to each other. The high accuracy of the calculated frequencies allows for a direct comparison to experimental spectra which makes it a particularly useful method for this body of work.

Whilst the vibrational modes generated via this method initially are the harmonic vibrations with a scaling factor to produce the anharmonic contributions, the cross-coupling observed in experimental data only arises from the anharmonic vibrations. Hence, whilst analysis could be made on the harmonics of the system from these initial calculations, there is a strong focus on the anharmonic contributions and specifically those that correlate with the experimental work in progress at the CLF. The experiments currently being carried out at the CLF utilise 2D-IR techniques to characterise the anharmonic cross-coupling behaviour of low water concentrations in Na-ZSM-5 across a range of temperatures.

5.3 Results and Discussion

5.3.1 H_2O Molecule

For reference a single water molecule was optimised using the same quantum mechanical criteria as used for the QM region, implemented by ORCA,[182] and the subsequent spectrum was calculated using the same GVPT2 methodology. The resultant spectrum is shown below in ***Fig. 5.2***. Here there are three distinct vibrational modes arising from the symmetric bend occurring at 1613.21 cm^{-1}, and the symmetric and asymmetric stretching modes occurring at 3782.87 cm^{-1} and 3888.23 cm^{-1} respectively.

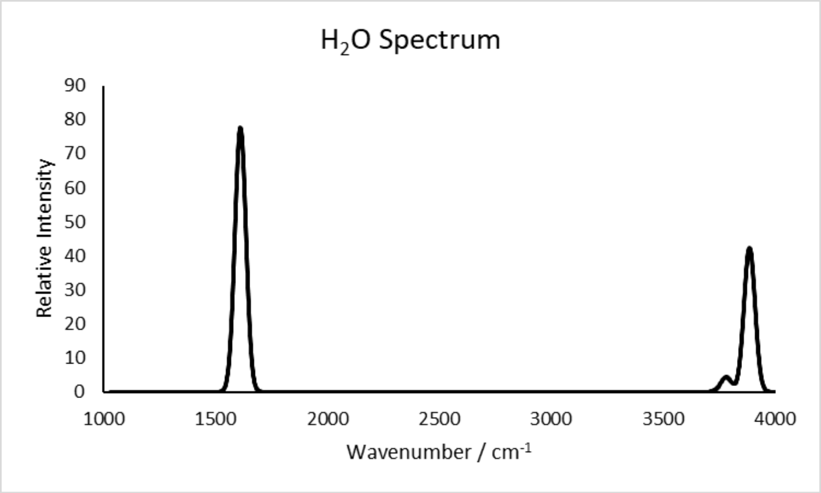

Fig. 5.2. Calculated spectrum of a single water molecule, illustrating the three peaks (from left to right) arising from the symmetric bending, symmetric stretching, and asymmetric stretching modes.

It is impossible to determine the IR spectrum for a single water molecule experimentally, as individual contributions from larger water clusters tend to overlap. However there have been studies attempting to model these larger water clusters using computational methods.[274] Water clusters of different sizes and shapes were studied by Lenz and Ojamäe[274] and demonstrated that the symmetric and asymmetric stretching modes shift between the 3000 and 4000 cm^{-1} range as a result of hydrogen bonding behaviour. When fitting a spectrum comprising of the mean calculated frequencies with an experimental liquid water spectrum conducted at -6 °C, a good agreement was observed. Thus, we can be confident that the calculated spectrum in ***Fig. 5.2.*** is accurate enough to be used for a comparison.

5.3.2 H-ZSM-5

The initial H-ZSM-5 structure was optimised using periodic DFT functionality in the VASP code,[74–78] which as noted above was used to generate the starting configurations of the systems with water molecules within the zeolite pore for the AIMD simulations. These three clusters are highlighted below in ***Fig. 5.3.*** and formed the starting point for the *ab-initio* molecular dynamics simulations. These starting structures display a propensity for hydrogen bonding to the pore wall in addition to the Brønsted acid site (BAS). As was discussed in the Introduction chapter of this thesis, Zygmunt *et al*[270] highlighted that whilst hydroxonium ion formation is possible with a single water molecule, it acts as a transition state and the addition of a second water molecule stabilises it, which is in line with the optimised structures shown in ***Fig. 5.3.***, as we see the formation of a hydroxonium ion upon the addition of the second water molecule.

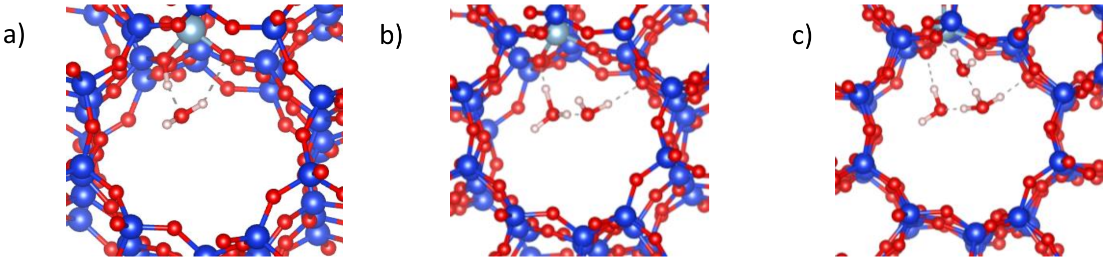

Fig. 5.3. Initial optimised geometries forming the starting structures for the *Ab-Initio* Molecular Dynamics simulations of H-ZSM-5 with 1-3 water molecules: a) A single water molecule hydrogen bonded to a proton on the framework, b) a water molecule and hydroxonium ion, c) two water molecules and a hydroxonium ion. Atom colours: Si: dark blue, Al: light blue, O: red and H: white.

As can be seen from ***Table 5.1.***, which reports the binding energies of water molecules, the addition of a single water molecule binds to the 'dry' H-ZSM-5 system by 81.7 kJ mol^{-1}. The addition of subsequent water molecules continues to lower the overall system energy with each water molecule; however, the magnitude varies. An interesting observation is that the second water molecule is 5.7 kJ mol^{-1} less strongly bound than the first at -76.0 kJ mol^{-1} compared to the initial -81.7 kJ mol^{-1}. However, the third molecule is more strongly bound than either the first or second water molecule, with an addition energy of -87.9 kJ mol^{-1} more than the two-water molecule system.

The adsorption of water in H-ZSM-5 has been investigated by Ison and Gorte *et al*[275] using a combination of temperature programmed desorption (TPD), thermogravimetric analysis and transmission infrared spectroscopy. Their study found that the adsorption of the first water molecule at the cation site had a heat of adsorption around 51 kJ mol^{-1}. Our calculations indicate a higher adsorption energy than is experimentally reported; however, when benchmarking methodologies in chapter 3 of this thesis, we noted that computational methods can overestimate binding energies and the combination of factors such as composition, defects/silanol groups and experimental conditions can influence the experimental energies. Despite this, it is also reported that the adsorption energy drops rapidly with the addition of more water molecules, whilst we report the addition of a second molecule is less favourable than the adsorption of the first water molecule; however, the adsorption of the third molecule is the most favourable and so overall replicates the reported trend. Overall, the binding energies of additional water molecules stay roughly similar within a range of 12 kJ mol^{-1}.

Structure	Energy / kJ mol^{-1}	Binding E / kJ mol^{-1}	Addition E / kJ mol^{-1}
H-ZSM-5	-221673.5	-	-
H_2O	-1371.6	-	-
H-ZSM-5 + H_2O	-223126.8	-81.7	-81.7
H-ZSM-5 + $2H_2O$	-224574.4	-157.7	-76.0
H-ZSM-5 + $3H_2O$	-226033.9	-245.5	-87.9

Table 5.1. Energies of each system, calculated using periodic DFT, detailing the overall energy, energy required to add water molecules to the acid site and the additional energy difference when increasing the number of molecules each time.

Interesting observations can be made when comparing these systems energies and their respective geometries. The single water molecule forms two hydrogen bonds; one from the BAS proton to the coordinated water and the second to the BAS oxygen. This second hydrogen bond is shifted across by one silicon tetrahedron with the addition of the second water molecule, the energetic consequence of this is unlikely to be the reason behind the lower favourability of the second water molecule. Instead, the addition of this second water molecule promotes the formation of the hydroxonium ion, as discussed previously in the work of Zygmunt *et al,*[270] by deprotonating the Brønsted acid site. Whilst this second water molecule stabilises the ion formation, it probably results in the energetic impact we observe. The addition of the third water molecule is most energetically favourable, as we observe the hydroxonium ion is now formed on the second water molecule that is not interacting with the BAS, whilst both the first and third water molecules in the chain form hydrogen bonds to the BAS oxygens. These additional hydrogen bonds, as well as the hydrogen bond formed from the hydroxonium ion to the pore wall, collectively make the cluster more energetically favourable and compensates the energetic cost of the formation of the hydroxonium ion. This behaviour drastically enhances the stability of the system, thus explaining the significantly more favourable energetics of the additional third water molecule in the system.

5.3.3 H-ZSM-5: Brønsted Acid Site Spectrum

Before a detailed analysis of how the H-ZSM-5 system interacts with water, it is useful to determine the original vibrational contribution of the Brønsted Acid Site (BAS). The calculated spectrum of H-ZSM-5 with no additional water molecules within the pore is detailed in ***Fig. 5.4.*** below.

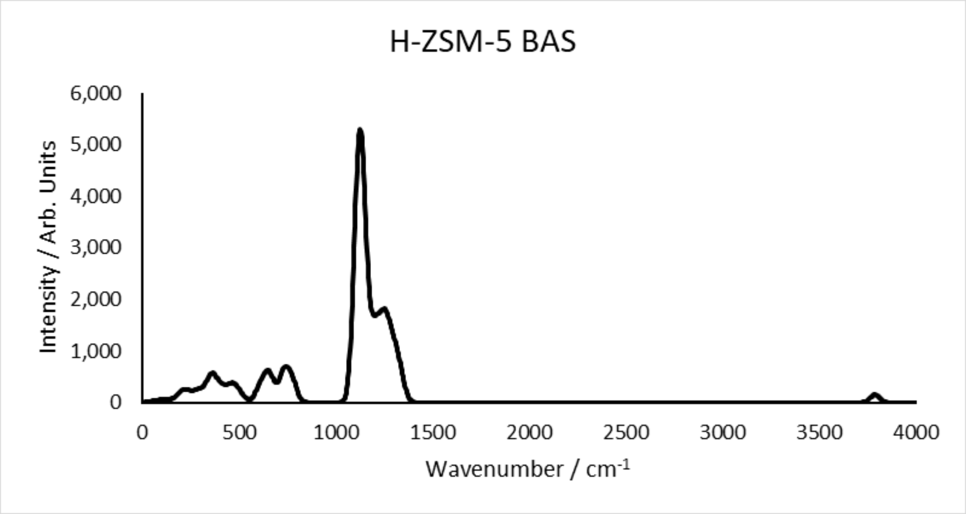

Fig. 5.4. Calculated IR spectrum for H-ZSM-5 with the characteristic peak at 3791 cm^{-1} corresponding to the BAS.

The resultant spectrum details the lattice contributions occurring within the 'fingerprint' region up to 1500 cm^{-1}. Beyond this point there is a single characteristic peak at 3791 cm^{-1} that arises from the BAS proton, bound to the oxygen atom bridging the Al and Si tetrahedra. The H-ZSM-5 zeolite has previously been characterised using FT-IR, along with HCl-ZSM-5 and HCl-OTS-ZSM-5 in the work of Tian *et al,*[276] with all three systems exhibiting absorption peaks at around 450, 550, 1095, 1220 and 1633 cm^{-1} that are characteristic of the MFI-type zeolites. This is broadly in line with our calculated spectra with peaks at 454, 655, 1107 and 1233 cm^{-1}, however we note some have been slightly shifted to higher frequencies. Furthermore, there is an omission of a peak around 1633 cm^{-1} that was reported by Tian *et al*,[276] however, the calculated spectrum is only modelling one of the pore rings of the H-ZSM-5 zeolite, so it is probable that this peak belongs to a lattice vibration outside the QM region. A terminal hydroxyl group was assigned to a peak at 3450 cm^{-1} in Tian *et al*'s[276] study, whilst our calculations produce this vibration for the BAS hydroxyl group at 3791 cm^{-1}. Whilst this is a significant shift in frequency of 341 cm^{-1}, the shift could be attributed to the difference in the location of these terminal hydroxyl groups in the experimental system when compared to our model.

5.3.4 H-ZSM-5: One Water Molecule at 298 K

As discussed earlier, the initial periodic DFT calculations were used as the starting point for the AIMD simulations. The RMSD for the entire H-ZSM-5 system with a single water molecule is shown below in ***Fig. 5.5.***, which shows a slow but steady increase in displacement over the first 4,000 fs, resulting from the temperature of the system increasing as it warms up to 298 K (also applicable for the systems at 400 K). Typically, the data from the temperature equilibration period is omitted as it is not particularly useful. Unfortunately, it becomes impossible to determine the behaviour of the water cluster from straightforward RMSD plots as the plot also includes the lattice vibrations, which obscures the specific site of interest. Instead, the same theory used to generate the RMSD was applied to the Brønsted acid site (BAS) O-H and associated water molecules rather than the whole cell.[275] The associated plot involving the O-H from the BAS and the water molecule(s) is termed a Component Analysis (CA) and details the changes in bond lengths for the cluster of interest and can be used to gather a clearer picture of the different cluster configurations.

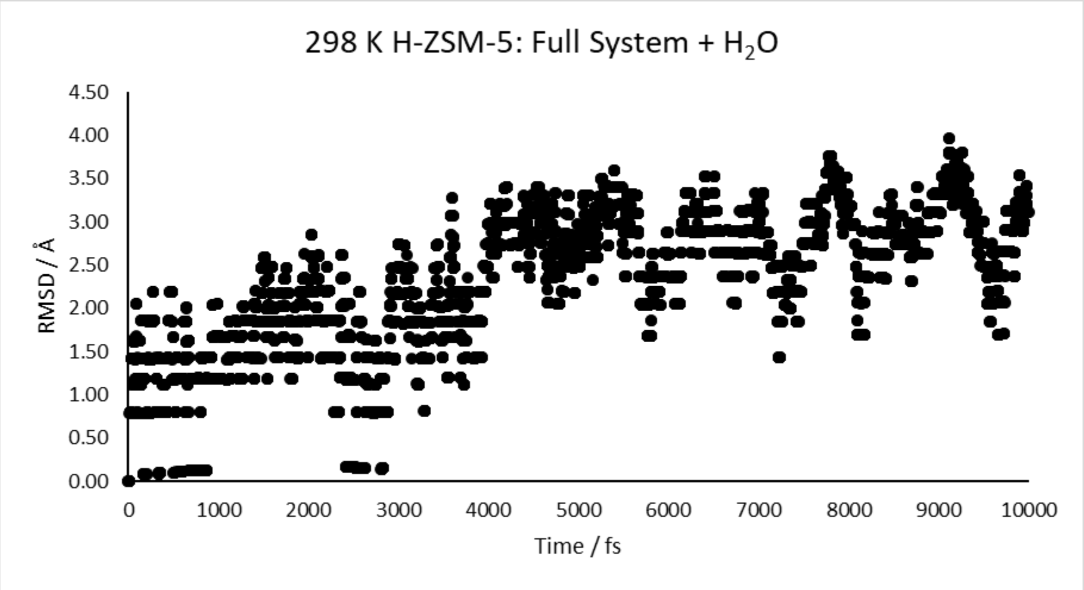

Fig. 5.5. Root Mean Squared Deviation/Displacement (RMSD) plot for a single water molecule in the pore of H-ZSM-5 at 298 K.

As can be seen from the component analysis plot, which details only the O-Na and H_2O atoms, below in ***Fig. 5.6.*** there are only two distinct cluster configurations visible at 298 K, which have displacements of below 1 Å and approximately 7 Å. Despite the temperature equilibration period forming a significant contribution in the RMSD plot, its effects are minimal in the component analysis as we are only considering the BAS and water cluster. There are less atoms in the component analysis than the RMSD plots, so displacements are more noticeable as the sum of the displacements is divided across a smaller number of atoms. In the RMSD plot the displacements of the water cluster are obscured as the displacements are mixed in with the entropic displacements of the lattice atoms resulting from temperature contributions. By removing this background contribution, the component analysis allows us to see when there is a distinctive change in the water cluster's configuration. Additionally, in the component analysis, entropic temperature effects only move the cluster atoms a tiny fraction outside of major cluster configurational changes. Since there aren't as many atoms when these displacements are summed together, they will still occupy a similar level of displacement to the cluster configuration, as a result the data points group around a similar level of displacement for a cluster until a more major conformational change occurs.

The component analysis in **Fig 5.6.** indicates a propensity towards configuration B for the duration of the simulation, deviating to system A for very brief periods of time, before returning to configuration B. The infrequency of A indicates that this would be a very minor contribution to an experimental spectrum, whilst a B type configuration would dominate at this temperature.

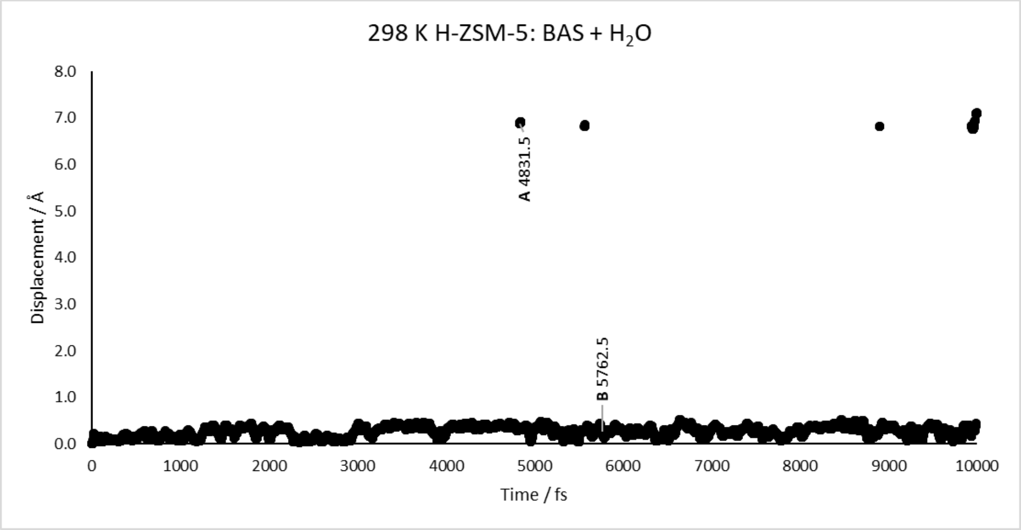

Fig. 5.6. Component Analysis for H-ZSM-5 detailing the Brønsted acid site and one water molecule at 298 K.

	Time / fs	**Energy / kJ mol^{-1}**	**ΔE from lowest / kJ mol^{-1}**
A	4831.5	-45377718.36	0.00
B	5762.5	-45377711.96	6.40

Table 5.2. Order of energies for the systems taken from the component analysis of a single water molecule in H-ZSM-5 at 298 K.

Despite the sizable differences in displacement observed in the component analysis, the data points only correlate to the single water molecule hydrogen bonding to the BAS, with corresponding energies in ***Table 5.2.*** The displacement observed throughout the simulation arises from the water molecule oscillating from one side of the pore to the other. Occasionally a second hydrogen bond is formed between the hydrogen on the water molecule and the oxygen on the nearest part of the pore wall. The two distinct structures were reconstructed and optimised using the hybrid QM/MM methodology outlined in Chapter 4, and their respective optimised QM regions are shown below in ***Fig. 5.7.*** The QM region used in this chapter consists of a single ring of the main pore of ZSM-5 and comprises of the Brønsted acid site proton, nine silicon atoms, a single aluminium atom and the corresponding oxygens associated with each tetrahedra and forms the basic QM region used for this chapter. The only changes to this QM region are the number of water molecules within the pore and the acid site counter ion, unless otherwise indicated. ***Fig. 5.6.*** also contains the linker atoms attached by the Chemshell code[228] to the terminal oxygens to maintain the correct valencies and electrostatic embedding.

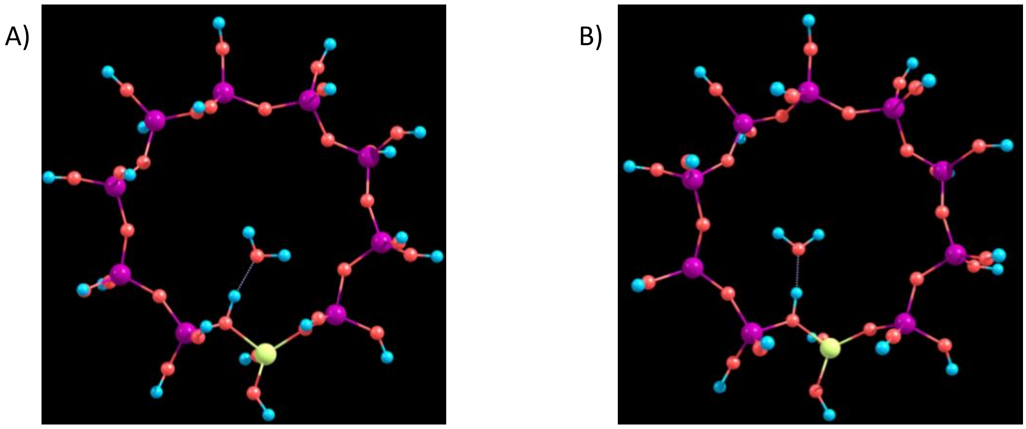

Fig. 5.7. Water clusters A and B from 298 K with the two visible configurations from the component analysis. Cluster A angles a hydrogen from the water towards the pore wall with a distance of 2.22 Å and potentially forming a hydrogen bond. Atom colours: Si: purple, O: red, H: light blue, Al: yellow.

The optimised structures displayed above were subsequently used as the structural input for calculating the IR spectrum using the GVPT2 method outlined in the Methodology section of this thesis. The code includes an initial optimisation step which is followed by the frequency calculations; however, this optimisation step was set as a single point calculation as the optimisation had been carried out separately.

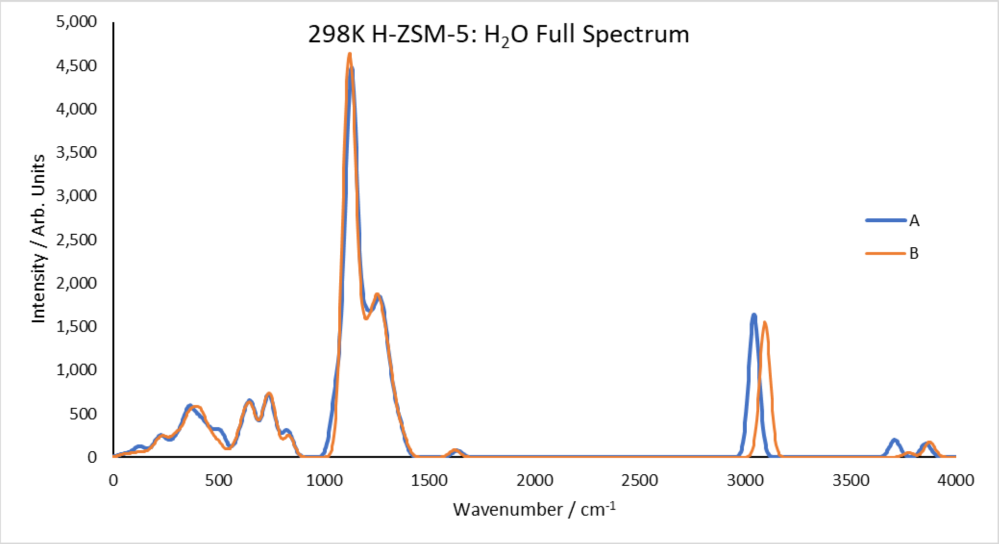

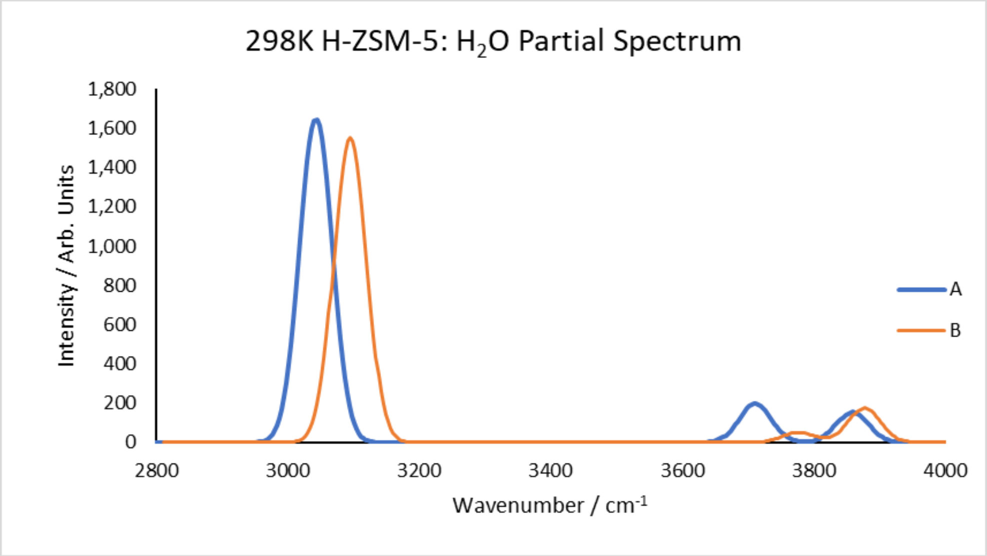

Fig. 5.8. Combined calculated spectra of the two cluster configurations for a single water molecule in the pore of H-ZSM-5 at 298 K. Line colours: Cluster A: blue, Cluster B: orange.

Whilst the spectra for a single water molecule at 298 K shown in ***Fig. 5.8.*** is understandably simple there are a few features worth addressing. It should be noted that as these spectra are calculated for a specific system, we negate the contributions that would be observed experimentally resulting from silanol groups. As reported in the FTIR experiments by Hunger *et al*,[277] silanols at the crystal surface would form a peak around 3725 cm^{-1} and silanol bands from defects at 3780 cm^{-1}. Additionally, we do not account for SiOH bands that would arise from defects in the zeolite structure at an experimentally reported 3780 cm^{-1} but note these contributions would still be shifted as a result of the adsorbed water, which is observed even at low loadings of 0.5 molecules per unit cell. When viewing the output files in Chemcraft visualisation software,[278] the individual modes can be determined allowing for the correct assignment of each specific vibration within the spectrum. This procedure enables a highly detailed analysis, as it can show which contributions overlap and if there is a significant shift changing the order of vibrational modes.

Firstly, we note that there is hardly any shifting of the symmetric bending frequency between the two systems, but they have shifted slightly up-field from the lone water molecule's 1613.21 cm^{-1} to 1622.40 cm^{-1}. However, both systems symmetric and asymmetric frequencies are shifted more down-field, with the least shifted system's (B) symmetric and asymmetric modes occurring at 3777.47 cm^{-1} and 3877.7 cm^{-1} respectively.

Secondly, there is a relatively intense peak occurring between 3000 cm^{-1} and 3200 cm^{-1} which corresponds to the Brønsted Acid Site proton vibrating to and from the coordinated water molecule. Secondly, for cluster B, which is unaffected by the pore wall, there is a greater relative intensity for the asymmetric stretching frequency than the symmetric stretching frequency. Cluster A exhibits the reverse of this characteristic, probably due to the influence of the hydrogen bond to the pore wall, which would de-shield the water oxygen and explain the down-field shift for both the symmetric and BAS vibrations. These spectra prove useful for demonstrating the effects that hydrogen bonding can have on shifting vibrational frequencies.

5.3.5 H-ZSM-5: One Water Molecule at 400 K

The same method was applied but for the 400 K simulation and the results are displayed in the component analysis plot shown below in ***Fig. 5.9.*** This gives a similar distribution to that observed at the lower temperature; however, there is another significant displacement at around 8 Å. This new configuration is mid-way between the two sides of the pore observed in the previous section, but the water molecule has been rotated approximately 90 ° so that the hydrogens are axial, pointing down the channel of the pore, rather than equatorial in the plane of the pore as shown below in ***Fig. 5.10.***

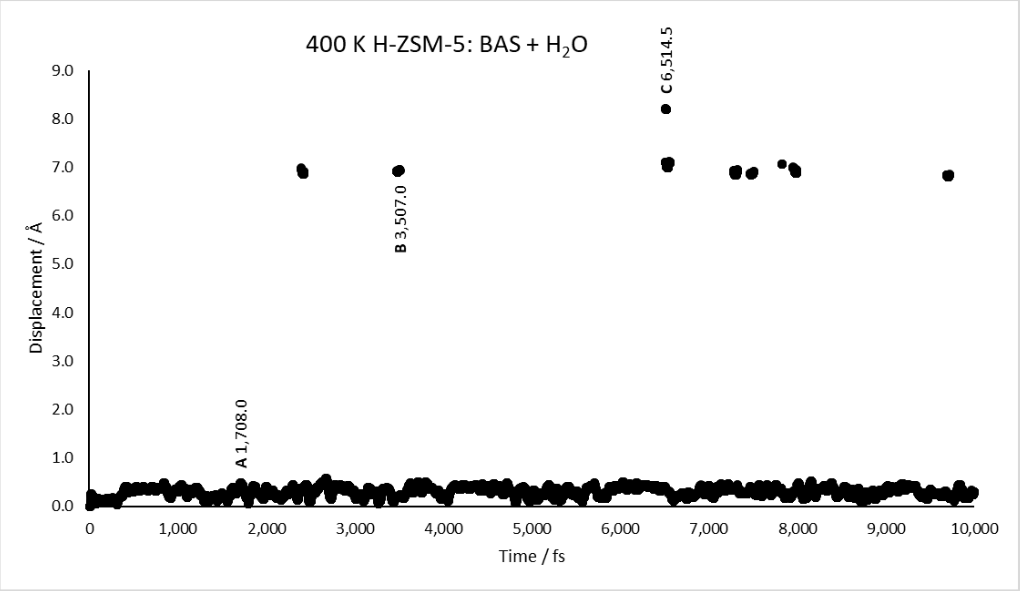

Fig. 5.9. Component Analysis for H-ZSM-5 detailing the Brønsted acid site and one water molecule at 400 K.

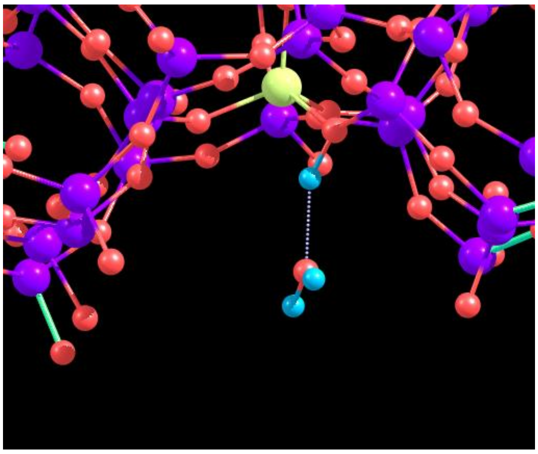

Fig. 5.10. The structure of the water molecule contribution observed at point C on the component analysis of a single water molecule in the pore of H-ZSM-5 at 400 K. Atom colours: Si: purple, O: red, H: light blue, Al: yellow.

Energy Order High to Low	**Time / fs**	**Energy / kJ mol^{-1}**	**ΔE from lowest / kJ mol^{-1}**
C	6514.5	-45377711.6	3.7
A	708	-45377713.1	2.2
B	3507	-45377715.3	0.0

Table 5.3. Order of energies for the systems taken from the component analysis of a single water molecule in H-ZSM-5 at 400 K.

The energetics of these systems are interesting when correlated with the component analysis. As can be seen in ***Table 5.3.***, this new configuration C with a displacement around 8 Å is the highest energy system; however, system B with the 7 Å displacement is lower in energy but a less populated state, whilst configuration A is the most populated but with a higher energy than that of B. Extrapolating from these datasets, we can assume that the ambient temperature of the system is enough to promote the higher energy state to be easily accessible. Since there is only one occurrence of C, which is not present in the CA at the lower temperature, coupled with its higher energy could indicate a transitional state between more accessible and energetically favourable configurations.

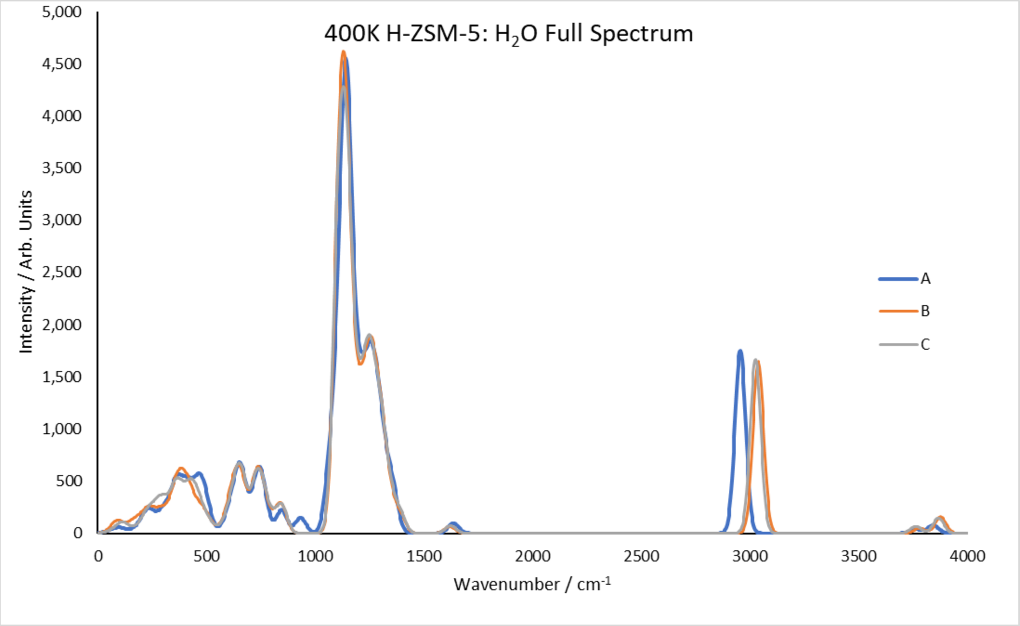

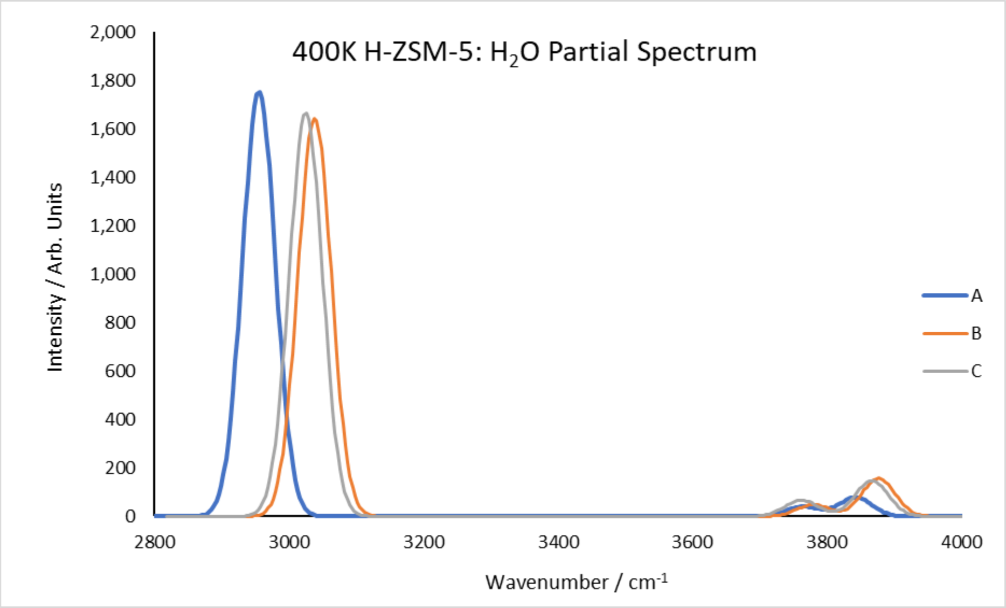

Fig. 5.11. Combined calculated spectra of the three cluster configurations for a single water molecule in the pore of H-ZSM-5 at 400 K. Line colours: Cluster A: blue, Cluster B: orange and Cluster C: grey.

At the higher temperature a similar spectrum is observed to that at the lower temperature displayed in ***Fig. 5.11.***, despite the occurrence of the new third structure. Cluster C is very similar to cluster B, but has rotated to a more horizontal geometry, which would experience similar influences; hence the spectra are very similar with only a very minor shift. The spectrum for system A has lower relative intensities for both its symmetric and asymmetric modes, but still shows a significant shift of the BAS vibration. This shift is not the result of a hydrogen bond; however, the geometry of the water effectively makes the hydrogen atoms equidistant from the BAS. As the BAS proton vibrates towards the water molecule it effectively places three protons on one side of the water molecule, which would cause the oxygen to de-shield significantly on one side, resulting in the down-field shift observed.

5.3.6 H-ZSM-5: Two Water Molecules at 298 K

Upon the addition of a second water molecule, we see the higher level of displacement from the minimised structure becoming more populated, which would be expected due to the increased levels of entropy in the system. According to the component analysis plot at this temperature, shown in ***Fig. 5.12.***, we see that the most populated displacement is around 7-8 Å with a rather thick layer on the plot, probably a result of two levels of displacement close to each other. There is also a noticeable peak between 8 and 9 Å, which could result from a higher energy transitional configuration state, correlating with the higher energy value of system E in ***Table 5.5.***

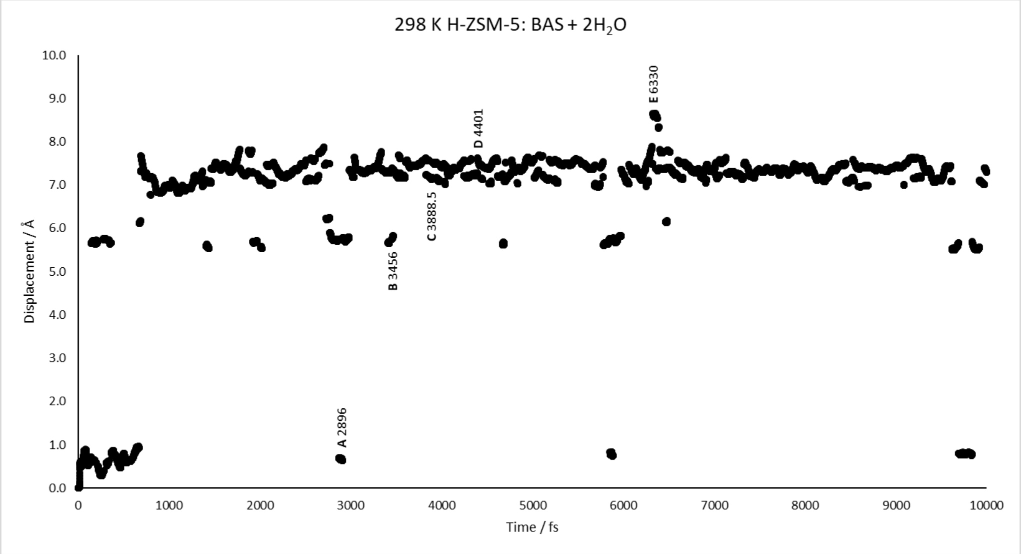

Fig. 5.12. Component Analysis for H-ZSM-5 detailing the Brønsted acid site and two water molecules at 298 K.

The optimised structure used as a starting point for the simulation exhibited the formation of a hydroxonium ion, with the water coordinating to the BAS extracting the proton from the framework to form H_3O^+, which is then stabilised by hydrogen bonds to the second water molecule. Despite this starting geometry, hydroxonium ions are not observed in the subsequent simulations for the two water molecule systems at either temperature. We note that Vener *et al,*[112] optimised H-Chabazite with a similar methodology and observed hydroxonium ion formation; however, upon raising the temperature of the system this ion formation was not observed. As is the case in our study, on raising the temperature to 298 K and 400 K, hydroxonium ion formation does not occur beyond the initial optimisation of the structure, i.e. it is not observed in the dynamical simulations.

Energy Order High to Low	**Time / fs**	**Energy / kJ mol^{-1}**	**ΔE from lowest / kJ mol^{-1}**
D	4401	-45576506.66	8.85
E	6330	-45576507.12	8.39
A	2896	-45576511.18	4.33
C	3888.5	-45576515.37	0.14
B	3456	-45576515.51	0.00

Table 5.4. Order of energies for the systems taken from the component analysis of two water molecules in H-ZSM-5 at 298 K.

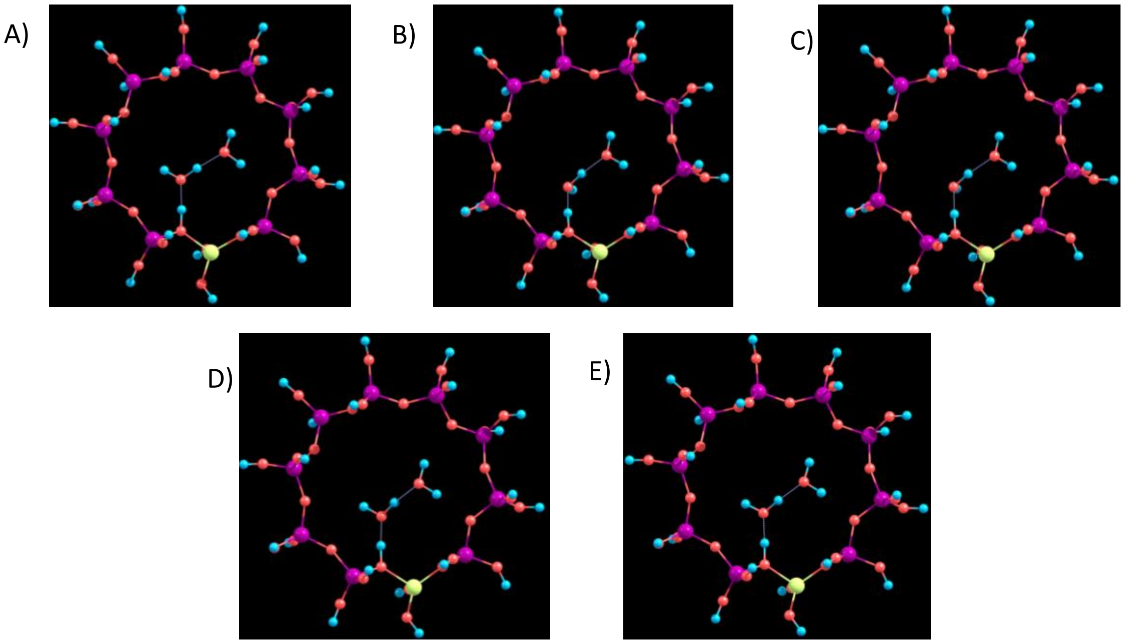

Fig. 5.13. Cluster configurations for two water molecules in the pore of H-ZSM-5, clusters A to E at 298 K. Atom colours: Si: purple, O: red, H: light blue, Al: yellow.

As can be seen from the calculated spectra shown in ***Fig. 5.14.***, there is a near uniform overlap of the third symmetric stretching mode and all three asymmetric stretching modes between 3600 cm^{-1} and 4000 cm^{-1}. Most notably with the two water molecule systems is that the vibration from the BAS proton hydrogen bonding to the water molecule has been shifted much further from 3100 cm^{-1} down to the 2200-2500 cm^{-1} range, which is a comparatively large shift, probably stemming from the peak that occurs between 3200 cm^{-1} and 3400 cm^{-1}. Using the visualisation software, this peak is identified as corresponding to the symmetric stretch of the water bound to the acid site and forming a hydrogen bond to the second water molecule, as a result this causes a noticeable de-shielding effect which shifts the vibration down-field. Additionally, this new peak has two distinct shifts: one for clusters A, D and E and another for cluster B and C. It is interesting to note that these systems group together in line with hydrogen bond lengths in a similar fashion to their spectral shifts as can be seen in ***Fig. 5.15.***

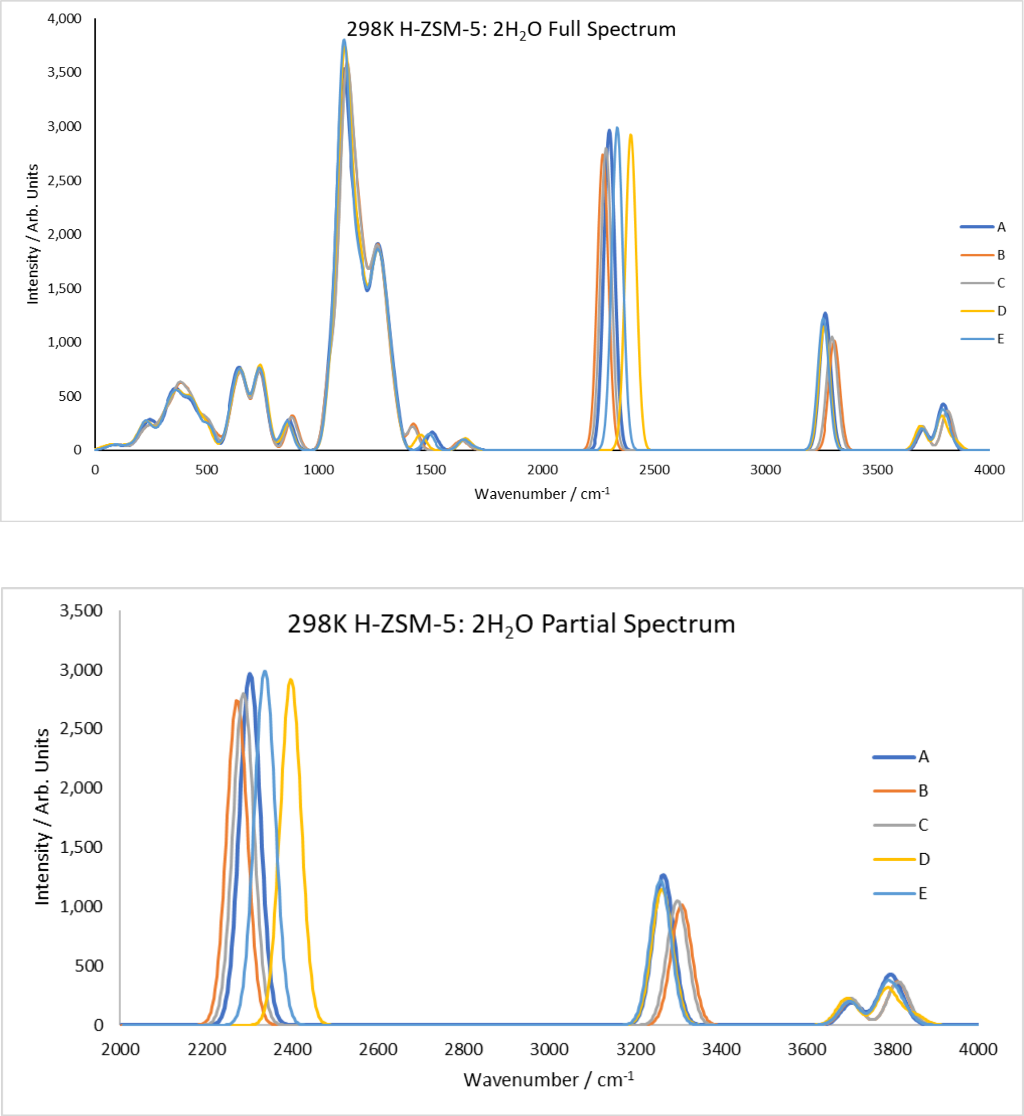

Fig. 5.14. Combined calculated spectra of $2H_2O$ molecules at 298 K. Line colours: Cluster A: blue, Cluster B: orange, Cluster C: grey, Cluster D: yellow, Cluster E: light blue.

We also note that there is an appreciable change observed in the symmetric bending frequencies (between 1300 cm^{-1} and 1700 cm^{-1}) of the acid site hydrogen, with B overlapping C and structure A overlaps with E, whilst D shifts between these two. The more down-field shift of B and C probably occurs because of the bending of the BAS proton which affects the coordinated water differently due to its rotated geometry. In clusters A, D and E, this bending frequency applies symmetrically relative to the water, whilst the rotation of the water in B and C means its effects are more asymmetrical. As a result, this probably shifts the vibration more down-field due to the de-shielding effect of the three protons, as was seen for the BAS stretching frequency. It is unclear as to why cluster D is more shifted than A and E, but it could be assumed that there is probably a smaller de-shielding effect taking place than observed for B and C. As is displayed below in ***Fig. 5.15.*** the structures group together in a similar way to their shifts based on the lengths of hydrogen bonds. Here, B and C are grouped together and A, D and E group together, as is the case with their stretching frequency for the first water molecule that forms a hydrogen bond to the second water molecule.

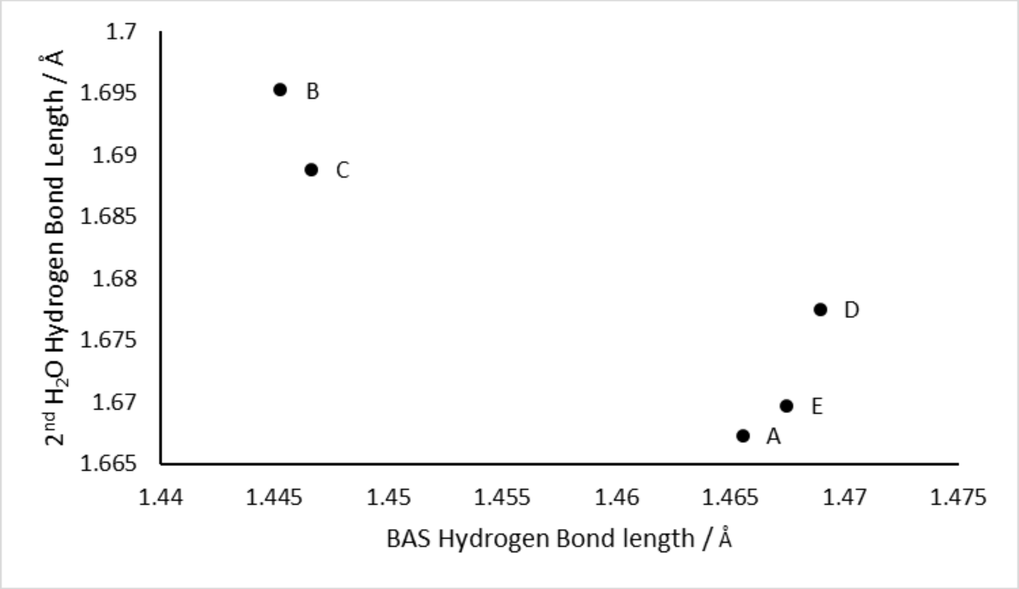

Fig. 5.15. The relationship between the two different hydrogen bond lengths and how the CA structures form two distinct groups.

The hydrogen bond lengths to the second water are largest in clusters B and C, which also have the lowest shift of this frequency, whilst the other group shift further down-field towards the shorter wavelengths. The same behaviour is observed for the hydrogen bonding from the BAS, with B and C shifting more down-field whilst having shorter hydrogen bond lengths, and the order of shifting for the other structures directly correlates with hydrogen bond length. Clearly the lengths of the hydrogen bonds formed can have a significant influence on the extent of the down-field shift of vibrations, with shorter hydrogen bonds yielding the largest shifts. This effect is in line with expectations as the stronger the hydrogen bond, the longer and therefore weaker the oxygen-hydrogen bond tends to be on the corresponding water molecule.

Anharmonic calculations often use a Morse potential to describe their frequencies, represented in this equation:

$$V(r) = D_e\left(1 - e^{-\beta(r-r_e)}\right)^2 \tag{5.1}$$

This allows for bond dissociation as governed by the dissociation energy, $\mathbf{D_e}$; the internuclear distance, **r**, whilst $\mathbf{r_e}$ is the equilibrium distance and **β** is a term that describes the bond stiffness, which is related to the force constant **k** shown in the equation below:

$$\beta = \sqrt{\frac{k}{2D_e}} \tag{5.2}$$

As the force constant **k** becomes smaller, due to weaker O-H bonds on the water molecule, **β** will also decrease the harmonic frequency and increase the anharmonic force constant corrections. Therefore, the weaker O-H bonds (or stronger hydrogen bonds from the water) the lower the **β** value, resulting in larger frequency shifts due to anharmonicity. In this thesis, the focus will be on the strength of the hydrogen bonds indicated by their respective hydrogen bond lengths, which directly correlates to the weakness of the water O-H bond, as characterised by their longer bond lengths.

5.3.7 H-ZSM-5: Two Water Molecules at 400 K

When the simulation of two water molecules is carried out at the higher temperature of 400 K, we see a similar distribution on the CA plot in ***Fig. 5.16.*** However, the denser occupation of displacements between 7 and 8 Å starts to separate out into two more distinct layers. There is also a greater population at the 1-2 Å displacement range, which could imply it is a higher energy configuration that is more accessible at 400 K than at 298 K, which is credible as configuration A is at a mid-point of the five systems energetically, with around 4 kJ mol^{-1} difference between the next highest and next lowest energy values as displayed in ***Table 5.5.***

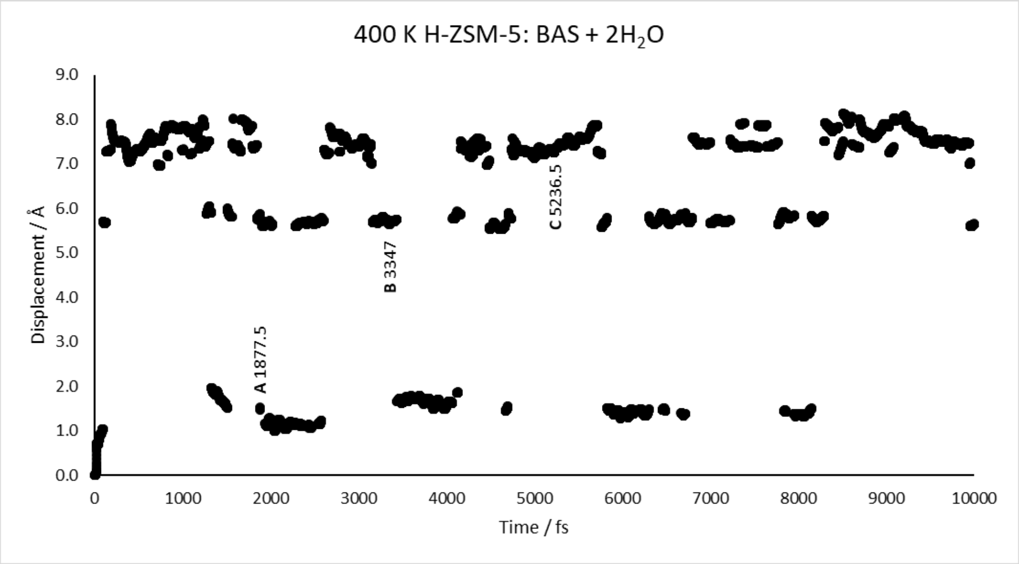

Fig. 5.16. Component Analysis for H-ZSM-5 detailing the Brønsted acid site and two water molecules at 400 K.

Energy Order High to Low	Time / fs	Energy / kJ mol^{-1}	ΔE from lowest / kJ mol^{-1}
B	3347.0	-45576489.15	15.98
A	1877.5	-45576499.41	5.72
C	5236.5	-45576505.13	0.00

Table 5.5. Order of energies for the systems taken from the component analysis of two water molecules in H-ZSM-5 at 400 K.

However, considering the broader picture, the A configuration tends to occur when water jumps to occupy the position of configuration B. Thus, the component analysis indicates that configurations occur sequentially from A to B to C and then back without skipping configuration B in the middle. When examining the structures, they are very similar as shown below in ***Fig. 5.17.***, with the main difference being the position of the second water molecule. The geometrical change results from the rotation of the first water and the associated hydrogen bond, which lends credibility to this theory. Furthermore, the lower energy of system C probably results from a more favourable influence of the second water molecule and the pore wall. The hydrogen of the second water molecule is in line with an oxygen in the pore wall, potentially resulting in an energetically favourable interaction and thus is the configuration with the highest occurrence in the simulation.

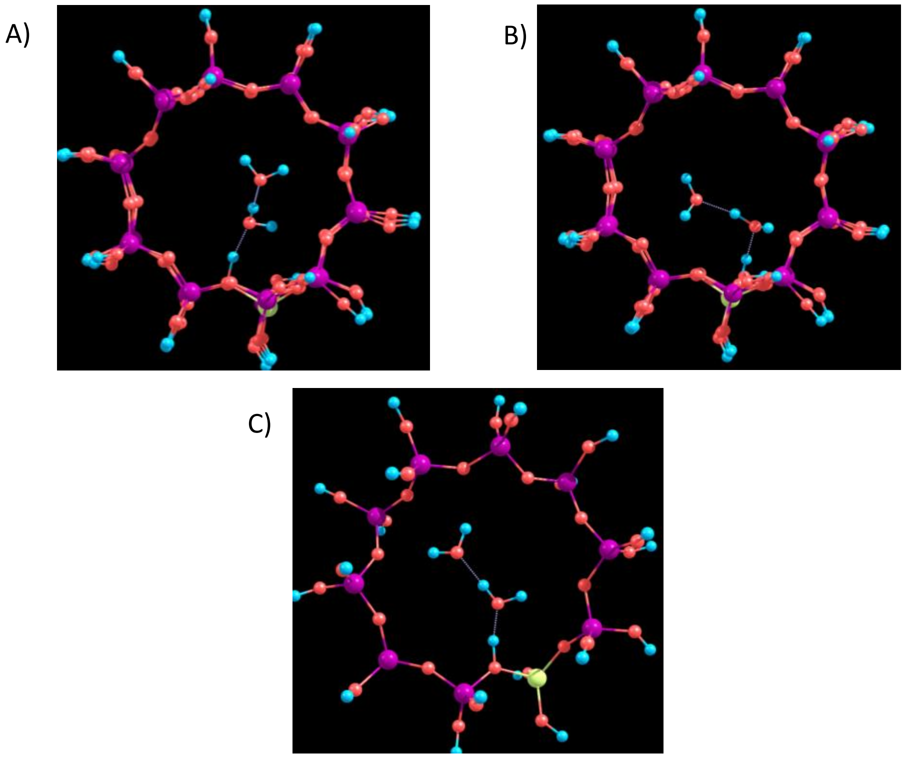

Fig. 5.17. Water clusters A to C for 2 H_2O molecules at 400 K. Atom colours: Si: purple, O: red, H: light blue, Al: yellow.

The combined spectra calculated from two water molecules at 400 K, shown below in ***Fig. 5.18.***, is noticeably different from that observed for the 298 K system. At 298 K, the vibration resulting from the BAS broadly overlaps; however, at this higher temperature there is a very significant shift of this vibration for system B in relation to the others. Clusters A and C are broadly similar with the BAS vibration occurring at 2500 cm^{-1} and 2402 cm^{-1}; this similarity correlates with the structural similarities of the two clusters, with both clusters pointing into the centre of the pore. In system B, the cluster has enabled a proton exchange from the original BAS and is now forming a hydrogen bond to the oxygen below the aluminium atom, rather than the oxygen to the side connected to the rest of the pore.

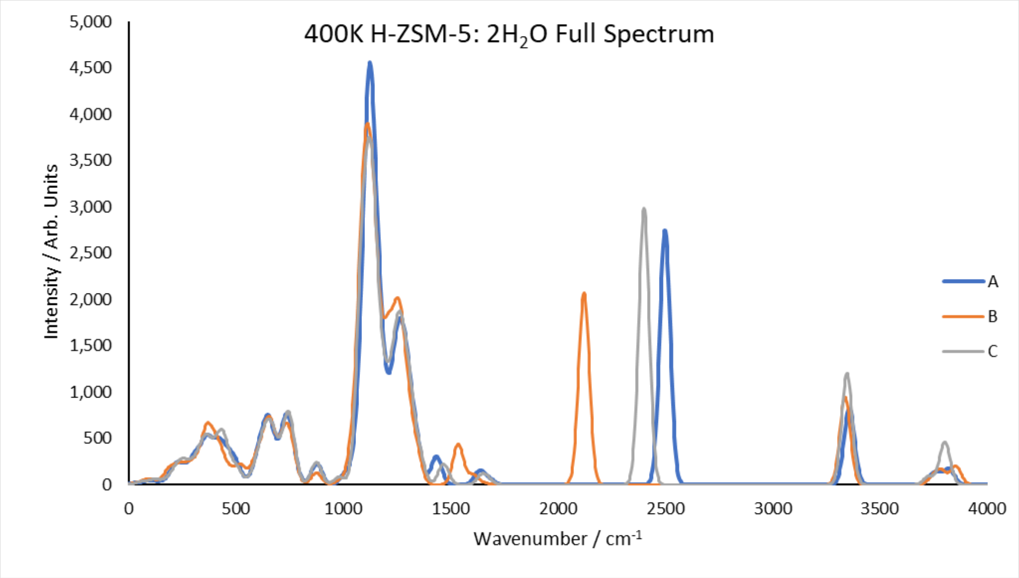

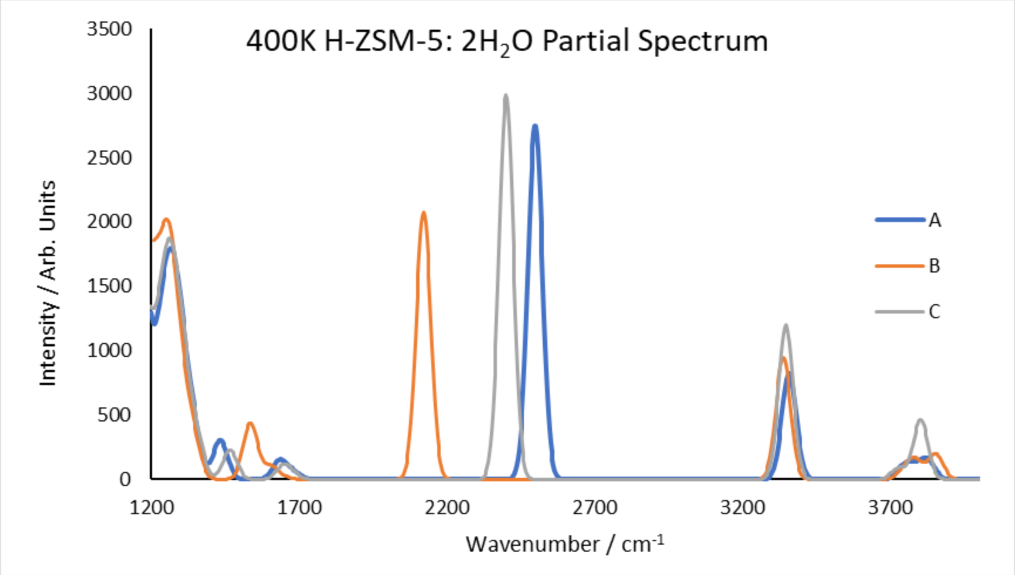

Fig. 5.18. Anharmonic spectrum of two water molecules in the pore of H-ZSM-5 at 400 K. Line colours: Cluster A: blue, Cluster B: orange and Cluster C: grey.

The relationship between the two hydrogen bond lengths is detailed in ***Fig. 5.19.*** below and shows the BAS hydrogen bond length increasing in the order B < C < A.

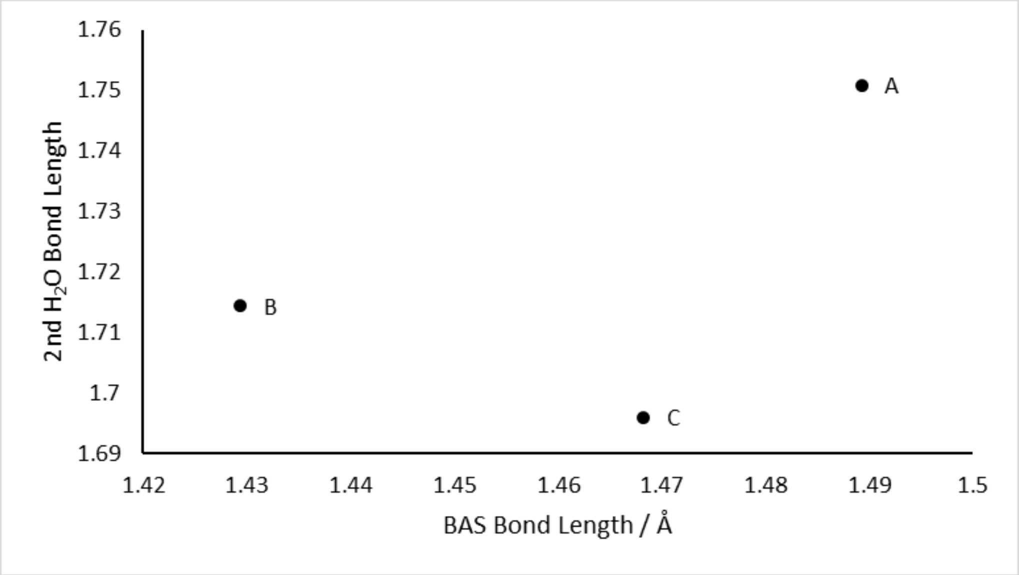

Fig. 5.19. Relationship between the two hydrogen bonds formed from the acid site and second water molecule for the two water molecule systems at 400 K.

The increase in bond length correlates with the order of shifting in the vibrational frequencies, with B shifting the most and A the least. This result shows that as the length of the hydrogen bond decreases its strength increases, which leads to an increase in the length of the hydrogen bonded water molecule's O-H bond, thus weakening it and resulting in a down-field shift. Whilst there is a similar range of bond lengths for the hydrogen bond between the first and second water molecule, there is little change as a direct result of the different bond lengths. Therefore, we can assume that the lack of change in frequencies is a result of differences in the geometries, with cluster B at an angle pointing to the left side of the pore, whilst A points into the middle and C points into the pore but slightly to the left. Since the clusters are geometrically similar, just orientated slightly differently, the second hydrogen bond is in a very similar chemical environment and so does not result in a significant shift.

5.3.8 H-ZSM-5: Three Water Molecules at 298 K

With the addition of the third water molecule, the component analysis shows four distinct levels of displacement between 1-2 Å, 5-6 Å, 6-7 Å and 7-8 Å as shown in ***Fig. 5.20.***

The increased entropy is again a factor to consider, however whilst hydroxonium ion formation can occur at a loading of two water molecules, it is typically stabilised by the third molecule in the system. This direct interaction from the third water enhances the stability of clusters and as such there would be less displacement from the starting configuration. However, the displacement is still predominantly between 7 and 8 Å, but there is now a significant population around 5 Å, which is probably a result of this stabilisation effect.

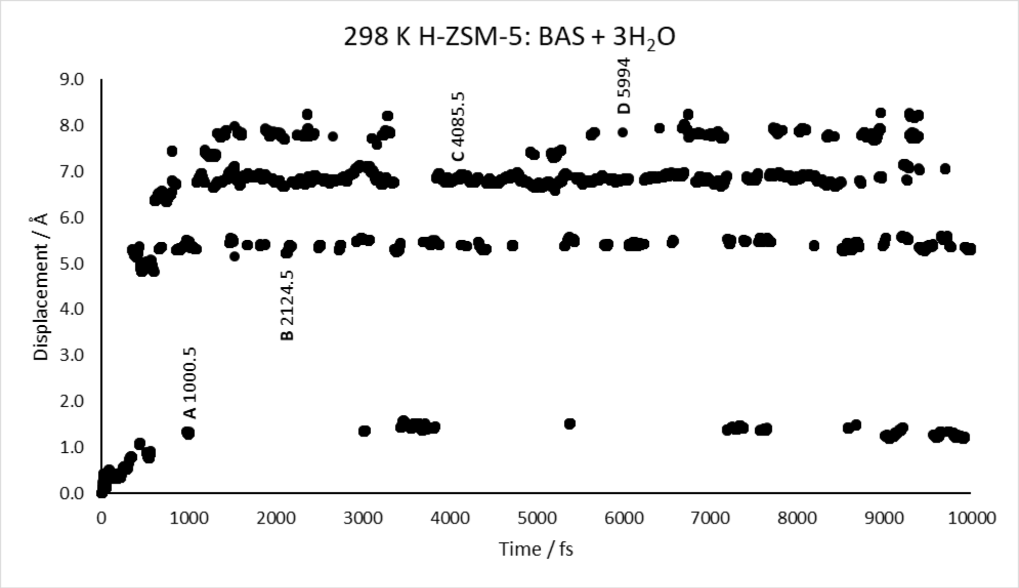

Fig. 5.20. Component Analysis for H-ZSM-5 detailing the Brønsted acid site and three water molecules at 298 K.

Energy Order High to Low	Time / fs	Energy / kJ mol^{-1}	ΔE from lowest / kJ mol^{-1}
D	5994	-45775256.92	37.25
B	2124.5	-45775272.11	22.06
A	1000.5	-45775273.42	20.75
C	4085.5	-45775294.17	0.00

Table 5.6. Order of energies for the systems taken from the component analysis of three water molecules in H-ZSM-5 at 298 K.

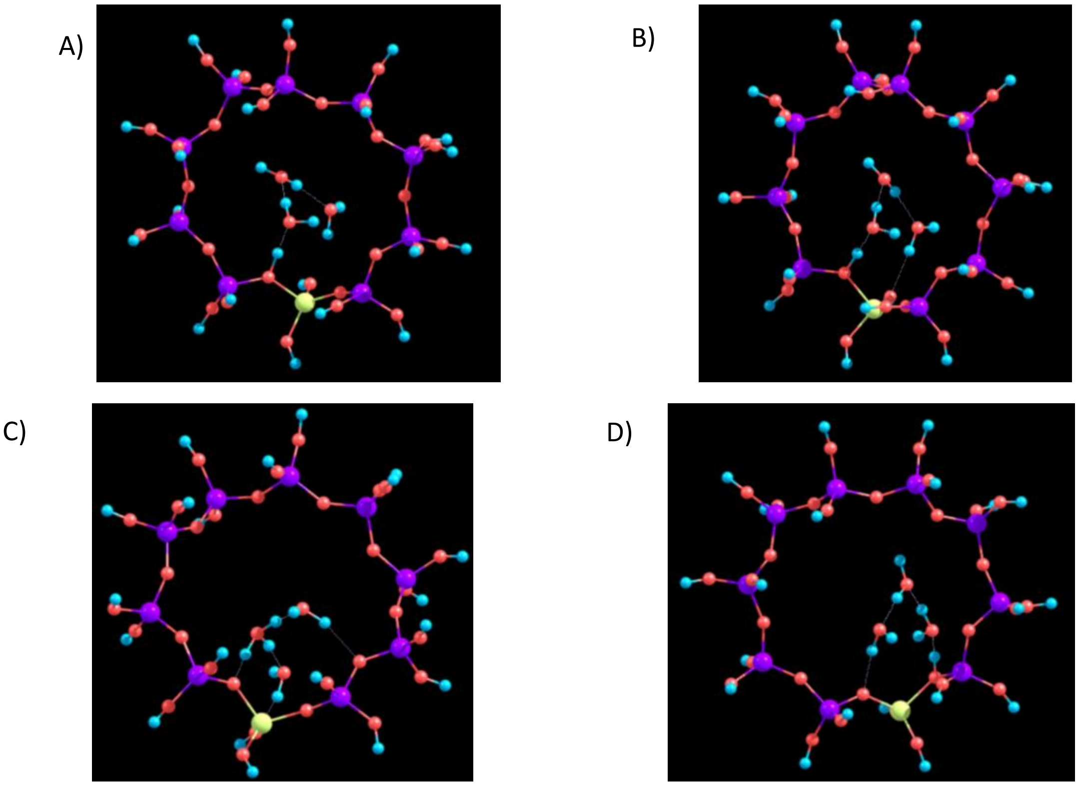

Fig. 5.21. Water clusters A to D for 3 H_2O molecules at 298 K. Atom colours: Si: purple, O: red, H: light blue, Al: yellow.

From this simulation we observe water cluster formation around the Brønsted acid site with the formation of a hydroxonium ion for system C. According to a combined experimental 2D-IR and AIMD study by Hack *et al*[279] that investigated H-ZSM-5 at high hydrations of ~13 and ~6 equivalents of water per aluminium atom, protonated water clusters are the dominant structural motif. These clusters are localised to the BAS through hydrogen bonding interactions, but extended cluster formation is hindered by the hydrophobicity of the pore. Water clusters favour Y-shaped clusters at the channel intersection, a phenomenon observed from our simulations as the BAS is placed near an intersecting channel in the extended structure (not visible in the QM region). The experimentally measured water speciation statistics in Hack's study illustrate that a large population of the water molecules in these hydrated systems donate between zero and one hydrogen bonds. Water clusters tended to form short-ranged, branched clusters that terminate after two to four molecules; and whilst we do not model up to four water molecules, we do observe this branched cluster behaviour. As shown in the correlations in 2D-IR spectra and spatial distribution function calculated from the AIMD, it was determined that the excess charge is delocalised around the water cluster, residing near the more highly coordinated water molecule.

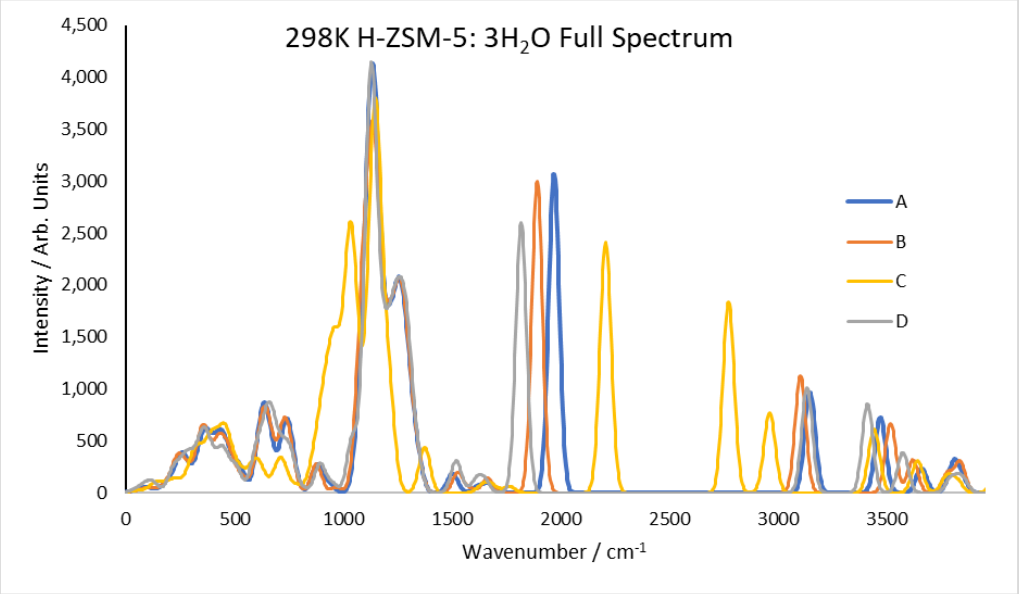

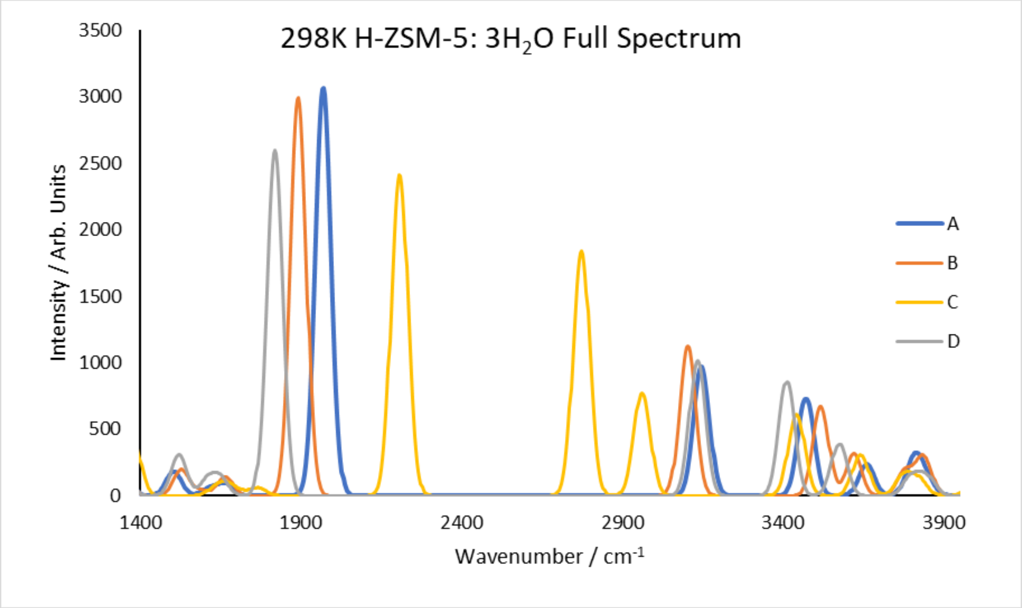

Fig. 5.22. Combined calculated spectra of three water molecules in the pore of H-ZSM-5 at 298 K. Line colours: Cluster A: blue, Cluster B: orange, Cluster C: yellow and Cluster D: grey.

When analysing the combined spectra displayed in ***Fig. 5.22.***, it is clear that there is a unique contribution arising from system C; it is therefore unsurprising that this system is the only system that formed a hydroxonium ion. First the regular system spectra will be analysed to provide context for the changes observed by the hydroxonium ion. The spectra with the most shifted vibrational mode arising from the BAS comes from system D at 1971 cm^{-1}, which is interesting as a proton exchange has occurred between the other systems and system D, whereby the original BAS proton has been abstracted from the framework to the water molecule to which it was originally forming a hydrogen bond. This water molecule loses one of its original protons to the second water, which loses its proton to the third water molecule, which in turn loses its proton to the BAS on the other side of the aluminium atom. As such, owing to these intriguing proton shuttles, the BAS vibrational mode observed with this shift is different from the others as it occurs on the opposite side of the aluminium atom. Whilst the first water molecule in this sequence still forms a hydrogen bond to the BAS, it forms from the water's hydrogen to the zeolite oxygen with a hydrogen bond length of 1.88 Å as shown below in ***Table 5.7***. This is a long bond when compared to the hydrogen bond formed from the BAS proton of 1.37 Å, which is the vibration that now corresponds to this peak.

The far shifted nature of this mode is once again probably due to the strength of this hydrogen bond which lengthens the bond of the BAS proton, resulting in a more de-shielded bond and reduces the frequency of the vibration. The symmetric stretching modes for this system form three distinct peaks, with the first peak at 3135 cm^{-1} showing very little shift relative to other systems. This peak corresponds to the first water forming a hydrogen bond to the BAS and forming a hydrogen bond of 1.62 Å to the next water molecule, which is close to the average/median hydrogen bond length for non-BAS hydrogen bonds, thus explaining its average position within the spectra. A greater than average shift is observed for the other two symmetric stretching modes, as these are the most shifted of all the systems. The peak at 3413 cm^{-1} corresponds to the middle water molecule, which has a longer hydrogen bond of 1.75 Å, which, with the exception of system C, is the shortest hydrogen bond to the third water molecule. The accompanying lengthening of the water O-H bond causes the bond to de-shield and shift the mode further down-field than the other contributions. The associated asymmetric stretching modes remain broadly constant in terms of shifting across all systems and only vary significantly in intensity.

System	BAS H-Bond / Å	BAS 2nd H-Bond / Å	H_2O from BAS H-bonds / Å		Pore Wall / Å
			1st	2nd	3rd
A	1.39	-	1.63	1.80	-
B	1.39	1.96	1.62	1.83	-
C	1.43	1.82	1.56	1.59	1.95
D	1.88	1.37	1.62	1.75	-

Table 5.7. Hydrogen bond lengths in the three-water molecule H-ZSM-5 systems at 298 K.

System B is the next most shifted in terms of its BAS vibrational mode and has its BAS on the original side. When factoring in the lengths of all BAS hydrogen bonds this is the second shortest, thus explaining why it is the second most shifted. Looking at the symmetric stretching modes, the first is the most shifted except for the hydroxonium ion system which once again correlates with the length of the hydrogen bond, whilst the second peak is one of the least shifted. The most shifted symmetric stretch arises from the water forming a hydrogen bond to the BAS proton, which again forms a hydrogen bond of length 1.62 Å, the shortest of the non-hydroxonium ion systems. The hydrogen bond formed from this middle water to the third water in the cluster is 1.83 Å, making it the longest hydrogen bond from the second water molecule in all systems, thus explaining its lack of shifting compared to others in the combined spectra. Whilst the third symmetric stretch is shifted more than other systems it is not as substantial as the shift observed in system D. It is more shifted than system C's equivalent vibration despite having a longer hydrogen bond length, which could be due to a lower de-shielding effect resulting from the hydroxonium ion in that system, or the influence of forming a hydrogen bond to the aluminium oxygen below the plane of the ring.

System A has a higher frequency for its BAS proton vibration at 1971 cm^{-1} than the previously discussed systems; however when factoring in the hydrogen bond lengths formed at both BAS (including after the proton exchange) it has the third shortest bond length at 1.39 Å, which keeps the shift in line with expectations resulting from the lengthening of the BAS O-H bond, which remains shorter than the other systems and so the force constant from a stronger bond is higher, resulting in less of a down-field shift. There are three distinct peaks arising from the symmetric stretching frequencies, with the first symmetric stretching mode resulting from the water hydrogen bonding to the BAS occurring at 3148 cm^{-1}. This is the least shifted symmetric stretch of this type which is in line with its 1.63 Å hydrogen bond length being the longest of all systems, meaning that the bond is less de-shielded with less of a shift. Such is the case for the second symmetric stretching contribution at 3473 cm^{-1}, as it is the third shortest hydrogen bond for a water molecule in the middle of the cluster. Considering the third water molecule is the only case from all four systems that does not form another hydrogen bond, it is therefore understandable as to why the symmetric stretching frequency of this mode has little to no shift.

Finally, we look at system C with the unique scenario of hydroxonium ion formation and its influence on the simulated spectra. As mentioned previously there is now an additional peak forming at 2774 cm^{-1} as a direct result of this hydroxonium ion. We note that this band is consistent with the results of experimental IR studies carried out by Jentys *et al*,[99] which showed that with three water molecules per cluster the IR spectra displayed bands at 2463 and 2885 cm^{-1} that were characteristic of hydroxonium ions. The peak generated from our spectrum is within a comparable range and is only present when forming a cluster with three water molecules, which is in line with the experimental data. Furthermore, Jentys *et al*[99] determined using thermogravimetric analysis that three water molecules per Brønsted acid site provides the threshold for hydroxonium ion formation, whilst higher loadings tended to favour hydrogen bonded clusters in lieu of ion formation, which shows that our methodology is capable of accurately reproducing experimentally observed phenomena.

Previously all water molecules forming hydrogen bonds to the BAS were at one end of the three-water molecule cluster; in this case the BAS water molecule forms the middle of the cluster. It is also worth noting that unlike the others, this system has no formally bonded proton to the acid site, as the water cluster has abstracted it from the framework to form the ion. Despite this, we still observe a corresponding vibration at a higher frequency than the other BAS O-H bond at 2209 cm^{-1}. This peak results from the hydroxonium ion O-H bond vibrating towards the BAS, where the proton was abstracted from, rather than from the BAS as in the other cases. It forms the longest hydrogen bond to the BAS which also explains why it is significantly higher-field than the other systems. The hydroxonium ion forms three O-H bonds of lengths: 1.06 Å, 1.02 Å and 1.01 Å going counter-clockwise from the abstracted proton, which are longer than the average water O-H bond length of between 0.9 Å and 1.0 Å. These longer O-H bonds play a crucial role into the down-field shifts of vibrations in this system. Most notable is the previously mentioned new peak arising at 2774 cm^{-1}, which is not a new vibration but one of the three asymmetric vibrations that typically occur between 3790 cm^{-1} and 3850 cm^{-1}. The formation of the hydroxonium ion causes this mode to shift down-field by around 1000 cm^{-1} — the greatest shift in vibrational frequency so far, which is also the most intense of the stretching frequencies and is probably the result of several factors. This large shift is corroborated by the results of the experimental 2D-IR study by Hack *et al*[279] who note that the charge tends to be localised on the highly coordinated water molecule. In our study, the most highly coordinated water molecule is the hydroxonium ion, which results in the greater de-shielding of the oxygen causing the larger downfield shift.

The relatively short hydrogen bond length of 1.56 Å and the slightly longer O-H bond of 1.02 Å, is symptomatic of the considerable amount of de-shielding observed in the spectrum. Furthermore, the hydroxonium ion forms a formal positive charge on the oxygen atom, thus creating a very polar bond, due to the asymmetric distribution of electron density with the counteracting negative charge distributed amongst the three hydrogen bonds formed by the ion. This factor, when coupled with the extension brought about by the asymmetric stretch, would increase the dipole moment of the bond further, leading to the large increase in intensity of the asymmetric stretch. The following peak is the first symmetric stretch which is understandably more down-field than observed in previous cases, as this symmetric stretch involves the ion forming three hydrogen bonds. Whilst the hydrogen bond to the BAS is a little longer than previous structures, this is off-set by the other hydrogen bonds being shorter than the equivalent hydrogen bonds of the first bound water molecule in other systems. Additionally, the role of the formal positive charge on increasing the polarity of these O-H bonds could explain why the symmetric stretch is more shifted, however, the reduced intensity indicates this is probably not the case.

The third symmetric stretch, whilst shifted falls in line with those observed in the other systems despite forming a longer hydrogen bond at 1.95 Å. Since this mode is more shifted, it is likely the hydroxonium ion that is hydrogen bonding to it is attracting electron density off the oxygen, causing an additional de-shielding effect. Thus, the resulting down-field shift is larger than expected for the hydrogen bond, which is further corroborated by the O-H bond lengths of the water molecule. The O-H that does not form a hydrogen bond has a bond length of 0.97 Å, which is similar to the hydrogen bonded O-H bond length and so there is only a small contribution to the shift. Thus, the de-shielding observed probably arises from the influence of the hydronium ion. Apart from the unusual shift for the asymmetric stretching frequency of the hydroxonium ion, the other asymmetric stretching frequencies remain within the expected range with very little shifting.

5.3.9 H-ZSM-5: Three Water Molecules at 400 K

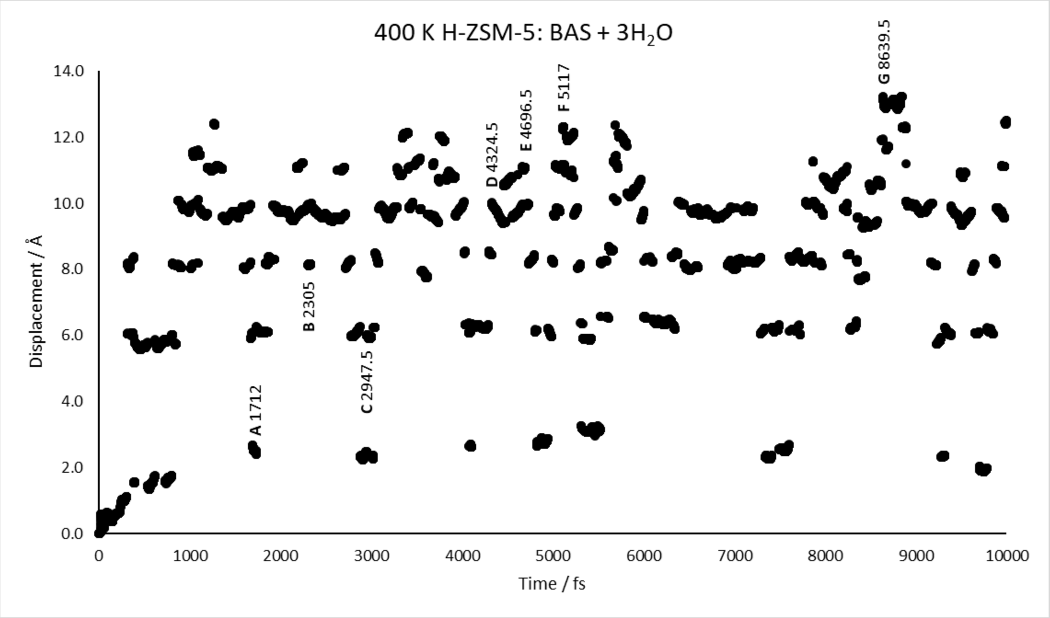

Fig. 5.23. Component Analysis for H-ZSM-5 detailing the Brønsted acid site and three water molecules at 400 K.

Energy Order High to Low	Time / fs	Energy / kJ mol^{-1}	ΔE from lowest / kJ mol^{-1}
G	8639.5	-45775255.55	45.67
C	2947.5	-45775277.90	23.32
B	2305	-45775280.92	20.30
A	1712	-45775293.75	7.47
D	4324.5	-45775299.01	2.21
F	5117	-45775300.05	1.17
E	4696.5	-45775301.22	0.00

Table 5.8. Order of energies for the systems taken from the component analysis of three water molecules in H-ZSM-5 at 400 K.

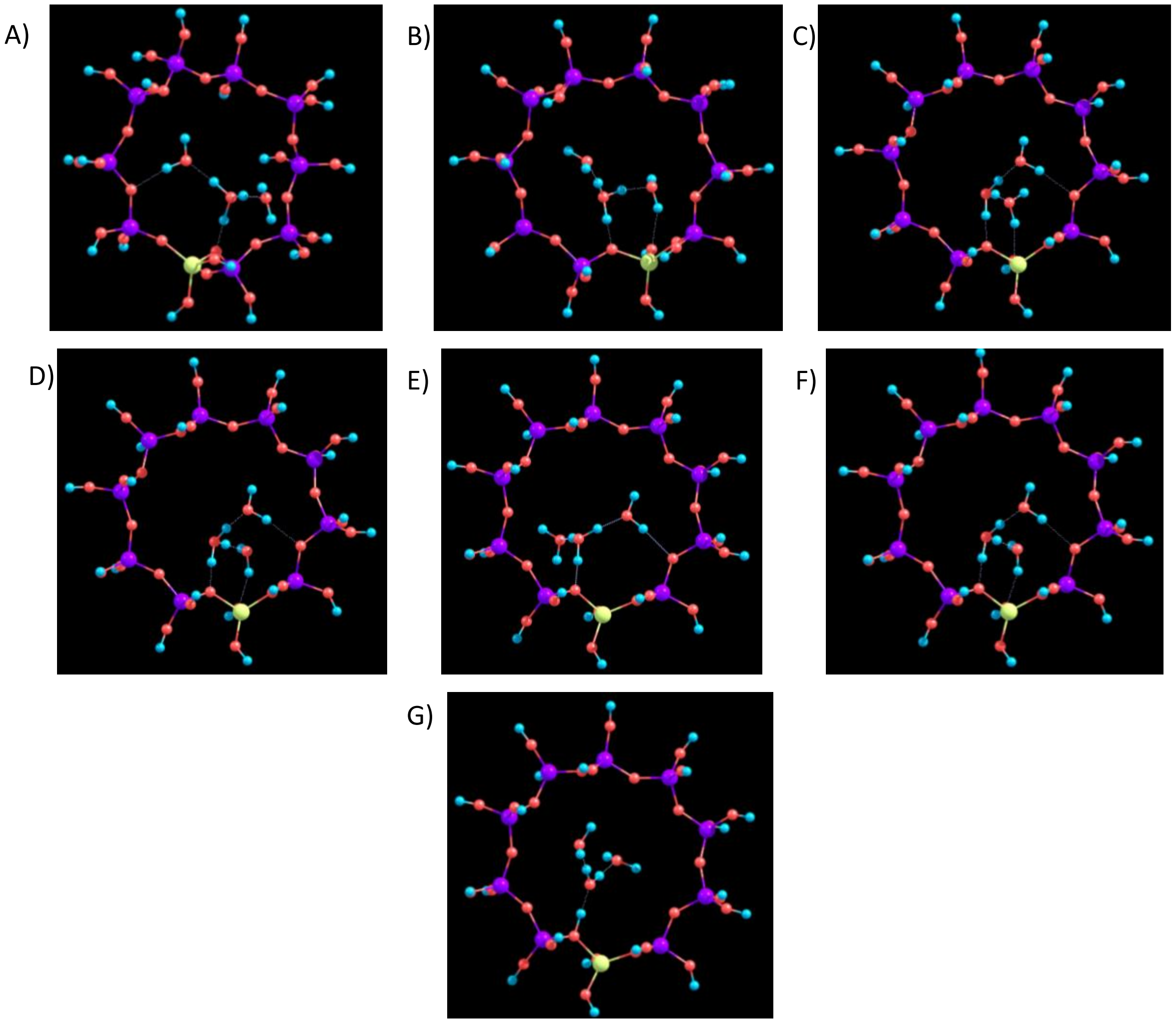

Fig. 5.24. Structures for 3 H_2O molecules at 400 K from A (top left) to G (bottom right). Atom colours: Si: purple, O: red, H: light blue, Al: yellow.

As can be seen in ***Fig. 5.24.*** there are some common traits shared between all seven clusters taken from the component analysis. Most notable is the formation of the hydroxonium ion, as predicted, at the Brønsted acid site for all clusters except for system G, as the hydrogen remains attached to the framework. The greater occurrence of these hydroxonium ions probably results from the higher temperature, as their formation was observed at 298 K, but which are now far more prominent in the simulation. As such there is a noticeably different calculated spectrum for this system when compared to the others as shown below in ***Fig. 5.25.***

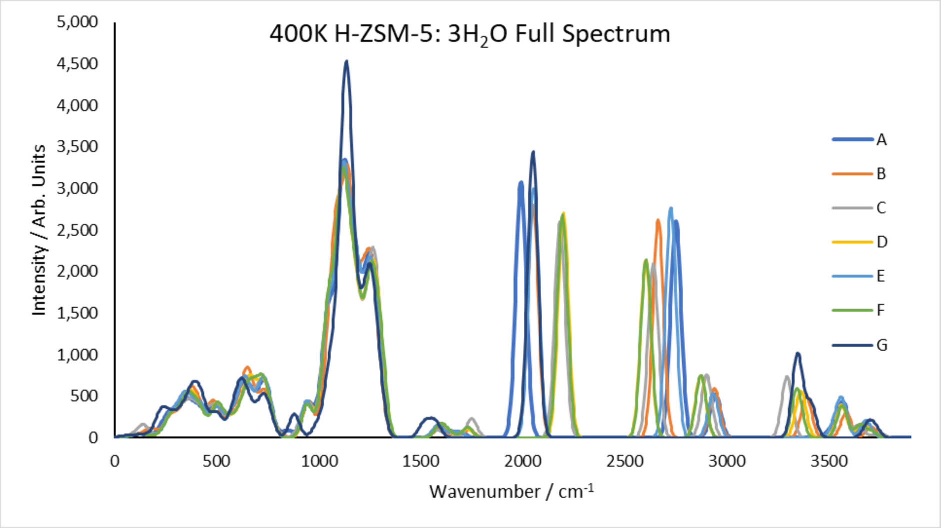

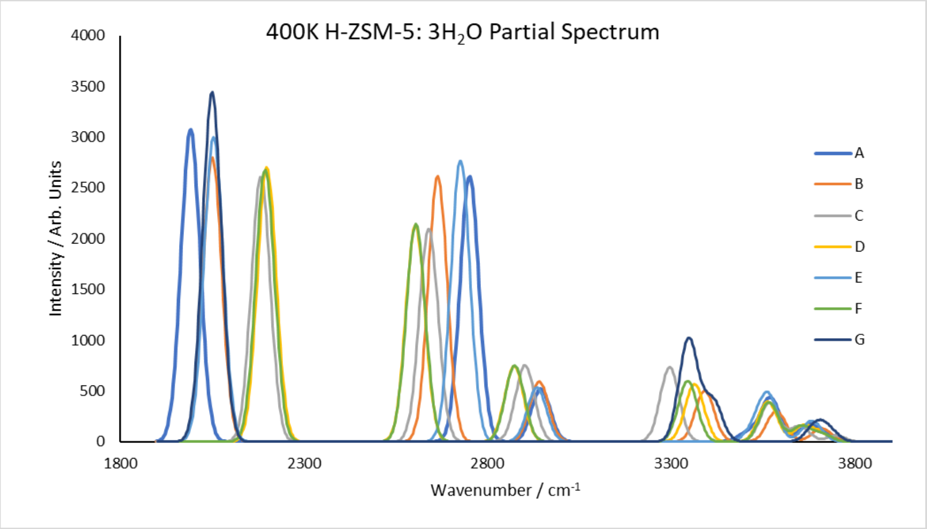

Fig. 5.25. Combined calculated spectra of three water molecules in the pore of H-ZSM-5 at 400 K. Line colours: Cluster A: blue, Cluster B: orange, Cluster C: grey, Cluster D: yellow, Cluster E: light blue, Cluster F: green and Cluster G: dark blue.

From the combined spectra displayed in ***Fig. 5.25.***, it is evident that the most down-field shift for the BAS hydrogen vibration results from system A, which occurs at 1992 cm^{-1}. Interestingly, this is not the shortest hydrogen bond as system G is shorter; however, G retains its hydrogen on the zeolite BAS whilst it has been deprotonated to form the hydroxonium. System A has the shortest hydrogen bond of all hydroxonium ion complexes, which explains the large down-field shift compared to other systems of this same chemistry. This shift is also unexpected, as despite the difference between system A and G, G has a longer O-H bond from the zeolite than the O-H bond found in the zeolite. This longer bond in G would mean the frequency would be shifted further down-field. It is therefore probable that this large shift is the result of a combination of other factors, predominantly arising from the additional hydrogen bonds this cluster forms. The asymmetric mode from the hydroxonium ion is once again shifted extensively to 2752 cm^{-1} as was observed at 298 K; however, this is the least shifted of all hydroxonium systems. Again, apart from system G, the hydroxonium ion forms the longest hydrogen bond to the next water molecule at 1.58 Å. As such the corresponding O-H bonds on the hydroxonium are longer, meaning they would vibrate at higher frequencies, which is also the case for the symmetric stretch at 2946 cm^{-1} but instead it happens to be one of the least shifted frequencies. The third symmetric stretch involves a water molecule that does not form hydrogen bonds from its hydrogen atoms, as such there is very little shift and a low intensity which overlaps with the remaining two asymmetric contributions.

System	**H-bond at BAS / Å**	**1st H_2O H-Bonds / Å**		**2nd H_2O H-bond / Å**	
A	1.41	1.58	1.56	1.96 (pore)	-
B	1.43	1.57	1.56	-	1.87 (BAS)
C	1.46	1.54	1.57	1.98 (pore)	1.76 (BAS)
D	1.47	1.56	1.55	1.98 (pore)	1.82 (BAS)
E	1.42	1.55	1.56	1.95 (pore)	-
F	1.47	1.56	1.56	1.99 (pore)	1.81 (BAS)
G	1.39	1.74	1.79	-	-

Table 5.9. Hydrogen bond lengths in the three-water molecule H-ZSM-5 systems at 400 K for each water molecule in the chain, with the 2nd water referring to water molecules on either side of the hydroxonium ion.

It is hard to distinguish which BAS is next most shifted as systems B, E and G are changed by roughly an equal amount; however, the band values are B 2051.45, E 2055.11, and G 2050.87 cm^{-1}, indicating that G is the most shifted. As mentioned previously this is probably due to the different chemistry resulting from the lack of the hydroxonium ion with a BAS O-H bond length of 1.07 Å. Since there is no hydroxonium ion formation, the corresponding asymmetric peak has not been displaced to the lower wave numbers. Instead, there is a single broad peak that encapsulates the symmetric and asymmetric stretching modes of the water molecule hydrogen bonding at the BAS. This peak has a high intensity component at 3347.68 cm^{-1} that results from the asymmetric mode and a shoulder peak at 3413.47 cm^{-1}, which is unusual behaviour as previous systems that did not form a hydroxonium ion did not shift the asymmetric contribution to a lower frequency than the symmetric stretches. This observation, combined with the short hydrogen bond from the BAS, could imply that it is at an energetic boundary just before the exchange of the proton from the BAS to the water molecule to form a hydroxonium ion, which would be further supported in the component analysis as G is a structure at the maximum of the distribution. The final symmetric stretches overlap with the asymmetric peaks of this system with very little contribution arising from both water molecules at either end of the cluster.

The third most shifted BAS contribution is for system B, which when looking at the hydrogen bonding analysis in ***Table 5.9.***, does not correspond to the next shortest BAS hydrogen bond. The next shortest BAS hydrogen bond would belong to system E and as such it is likely that there are more factors to consider. Since the hydroxonium ion that forms this bond also forms two other hydrogen bonds to two other water molecules, we can compare the extension of the relative O-H bonds on this ion. The O-H bond corresponding to the hydrogen bond at the BAS is 1.06 Å, whilst the bond length for the water molecule also attached to the BAS is 1.02 Å and the O-H bond length to the third water molecule is 1.01 Å. The BAS O-H bond is significantly longer than the other O-H bonds on the ion by almost 50 % and is only a little longer than the equivalent O-H bond in system E, which is 1.06 Å thus explaining the greater shift. Again, the asymmetric stretch of the hydroxonium ion is displaced further down-field than the three symmetric stretches and occurs at 2665 cm^{-1}, and is the fourth most displaced asymmetric stretch, but is more intense than the first three resulting from systems F, D and C.

These three systems all form an additional hydrogen bond from a terminal water molecule to the pore wall, which in turn dampens the vibrations within the system leading to a lower intensity for both the BAS mode and all asymmetric vibrations. Since this is not the case for A, B, E and G (due to lack of hydroxonium ions) it would explain why the intensity of B is higher. Despite these observations, the symmetric stretching modes are the least shifted of all systems owed to the lack of hydrogen bonds from one water and the very weak hydrogen bond to the BAS on the other at 1.87 Å, which is the weakest of this type, implying that there has been very little elongation of the O-H bond as a result.

As mentioned previously, E is the next most shifted in terms of the BAS vibrational mode, and despite having a shorter BAS hydrogen bond, its O-H bond is shorter than B resulting in a lower shifting of this peak. The asymmetric vibrational mode resulting from the hydroxonium ion is the second least shifted out of the relevant systems, as all O-H bonds on the ion are below 1.02 Å and so the shortness of the bonds results in vibrations occurring at the higher frequency. Due to the lack of hydrogen bonds on one of the terminal water molecules in the cluster, there is no reduction in intensity for the corresponding vibrational modes. A similar case is observed for the shifting of the symmetric and asymmetric vibrational modes, resulting in just two distinct peaks for both the remaining symmetric and asymmetric stretching contributions, rather than a splitting of these two types that arises from the down-field shift of some vibrations.

The last three systems (C, F and D) all have a similar frequency for the BAS vibrational mode with C's occurring at the lowest frequency of 2183.57 cm^{-1}, which also correlates to the hydrogen bond length from the BAS being the third longest at 1.46 Å. The asymmetric stretching frequency, however, is the second most displaced from all systems but also has the lowest intensity. Structurally it is very similar to system D with the key difference being a terminal water's orientation when forming a hydrogen bond to the acid site, as such the resulting spectra from both systems are similar. One of the hydrogen bonds from the hydroxonium ion has the shortest bond length at 1.54 Å when compared to equivalent systems. This hydrogen bond between the ion and BAS bound water results in O-H bond lengths on the ion of 1.02, 1.01 and 1.05 Å (BAS), which is larger compared to typical water O-H bonds causing the down-field shift. On average, the two hydrogen bonds from the ion to other waters are 1.55 Å, which is lower than the 1.56 Å average for system F; it is therefore likely that the O-H bonds are longer in F than C causing the greater shift. The most notable feature is the displacement resulting from the second symmetric vibration of the water bound to the BAS, which is the most shifted of the second symmetric stretching frequencies and can be characterised by the shortest hydrogen bond at 1.76 Å. Comparing both BAS hydrogen bonds, it is probable that it could be leading to the proton exchange witnessed at the lower temperature as the hydroxonium ion's hydrogen bond is longer, whilst those of the water molecules are shorter. The third symmetric stretch overlaps with the remaining two asymmetric stretching frequencies broadening the peak but retaining similar frequencies to the other systems.

System F is the second least shifted BAS hydrogen vibration and is structurally very similar to C and D, by forming a hydroxonium ion at the acid site in the middle of the cluster, whilst hydrogen bonded to a second water molecule that also forms a hydrogen bond to the acid site; the third water molecule also forms a hydrogen bond to the wall of the pore. Whilst structurally similar, there are some minor variations where D and F have the BAS water rotated differently from system C, which explains the similarities in the spectra across these systems, with the main variations occurring for the asymmetric stretch of the hydroxonium ion, with very similar bond lengths to system D.

As such, all arguments for D would apply to this system, except for those relating to the second symmetric stretch resulting from the BAS water molecule. The D and F systems yield the least shifted BAS vibrational mode, but also the most displaced asymmetric peak relating to the hydroxonium ion. Whilst the hydrogen bonds from the hydroxonium ion are not the shortest observed, it is likely that subtle differences in the O-H bond lengths result in this larger shift of the asymmetric stretching mode. Additionally, there is a water molecule forming a hydrogen bond of 1.81 Å to the acid site oxygen, which is very slightly shorter than in system D, yielding an O-H bond length of 0.98409 Å compared to D's 0.98319 Å (a difference of only 0.0009 Å). Considering F has a slightly longer bond length, it would only result in a minor down-field shift relative to system D as is observed. It is interesting to observe that the slight rotation of this acid site water molecule can lead to a small yet significant change in the spectroscopic outcome, due to the effect it can have over multiple bonds.

5.3.10 Na-ZSM-5

The Na-ZSM-5 structures were optimised using the same DFT method outlined in the previous section for the H-ZSM-5 systems. Similarly, one to three water molecules were then added into the pores of these structures and re-optimised using the same methodology. These optimised structures were then used as the initial structures for the *ab-initio* molecular dynamics simulations. The optimised starting structures are shown below in ***Fig. 5.26.*** and detail the probable coordination atoms to the sodium cation:

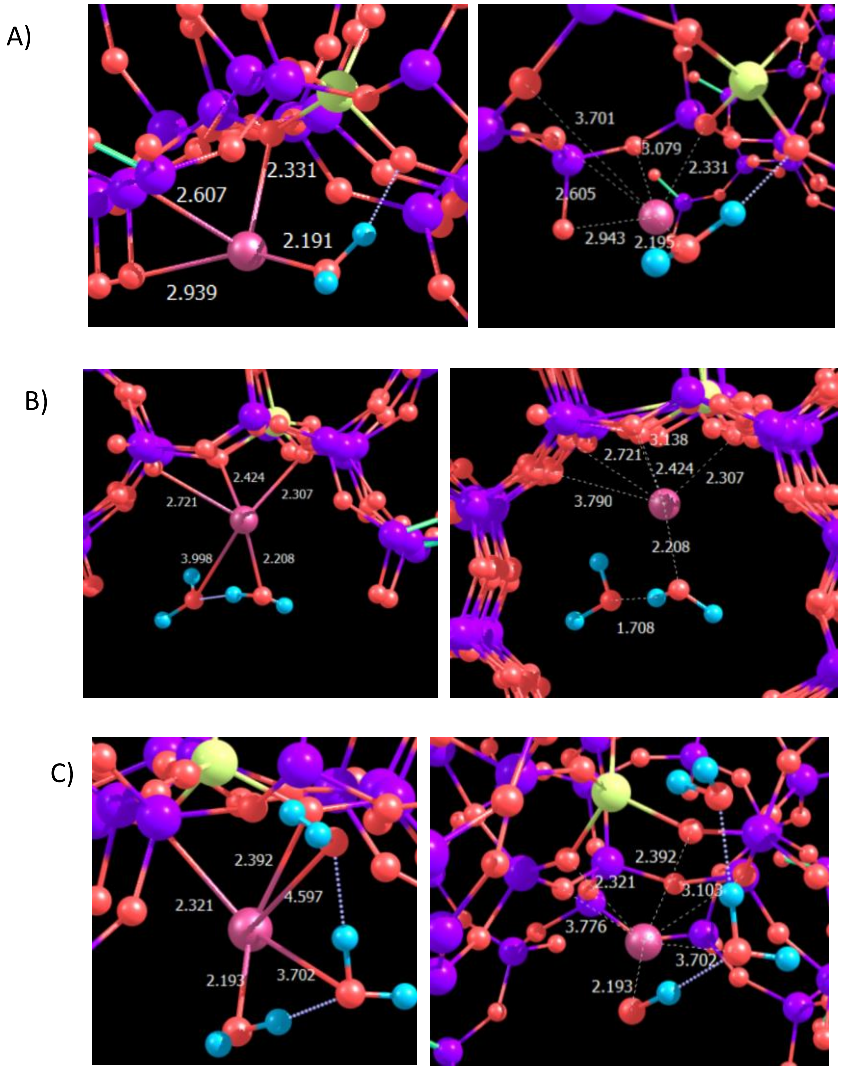

Fig. 5.26. Optimised structures for Na-ZSM-5 with water used as the starting point for the *Ab-Initio* Molecular Dynamics simulations with the distances for the sodium to the framework oxygens and surrounding water oxygen atoms: A) Starting geometry for one water molecule, B) Starting geometry for two water molecules, C) Starting geometry for three water molecules. Atom colours: Si: purple, O: red, H: light blue, Al: yellow.

We note here that the sodium cation has a propensity towards an octahedral complex, as is the case in the rock salt structure. Thus, the addition of a fourth water molecule might lead to an overall six coordinate sodium cation, with the fourth water molecule coordinating in the space left behind when coordinating three water molecules. As noted in the work of Stahl and Hanson, when sodium containing mesolite is dehydrated, the initial water loss is accompanied by an order/disorder transition in which the sodium and calcium cations in mesolite become randomly distributed.[280] Furthermore, mesolite was also shown to have one AlO_4 tetrahedron in which the oxygens coordinate to the cation, with the water molecules able to hydrogen bond to the other oxygens on the AlO_4 tetrahedra as we observe in structures A and C.

The coordination of sodium cations to both water and zeolite oxygens has been determined using XRD.[280,281] The reported sodium-oxygen distances to oxygen atoms in the dehydrated metastable form of the zeolite mesolite were 2.46, 2.57 and 2.39 Å which are broadly in line with our calculated structures in **Fig. 5.26**, as such it could be reasonable to assume that coordination distances around 3.7 Å are rather weak and indicate where a lattice distortion could arise. Additionally, the sodium-oxygen bond distances for coordinating water in metamesolite are reported to be approximately 2.23 and 2.32 Å, which is in line with our calculated geometries in **Fig. 5.26**, with the exception of a loosely bound water molecule in system C.

We also note that in the optimised structures for one and two water molecules, the sodium cation appears to coordinate strongly to three zeolite oxygens with one weak coordination to a fourth, probably resulting in the distortions reported by Stahl and Hanson.[280] These bonds would correspond to five of the vacancies for coordination with the sixth coordination being to the water molecule. The coordination to zeolite oxygens appears to drop to four with the addition of the third water molecule as it now coordinates to two of the water molecules in the cluster. It is worth noting that in **Fig 5.26**, all the bonds to framework oxygen atoms are under 4 Å, whilst the shortest bond to a water oxygen in all three structures is approximately 2.2 Å, again in agreement with the work by Stahl and Hanson.[280] According to experimental X-ray crystallography data provided in the work of Krawxczyk and Majerz on the Na-O bond distances in sodium diaquafenamate,[282] the bond distance between a sodium atom and a water molecule's oxygen atom is between 2.36 Å and 2.46 Å, with a non-water Na-O length of 2.41 Å. Thus, we could assume that for the two and three water molecule systems, the water molecules with Na-O distances exceeding 3 Å are very weakly coordinated and held in place by a slight distortion of the zeolite and their interaction with the coordinating water molecule with a small influence from the sodium cation.

Across the three structures there is some slight migration of the sodium cation, relative to the size of both the cation and bridging oxygen atoms, of 1.33 Å from one side of the aluminium to the other. Considering the size of the sodium cation relative to the distance of migration, the effect would be minor as it is still binding to a similar chemical environment. The negative charge resulting from the framework aluminium would exert a broadly consistent influence over the sodium cation across these positions. The resulting system energies, binding energies, and energy differences for the addition of each water molecule are detailed in ***Table 5.10.***, below:

Structure	**Energy / kJ mol^{-1}**	**Binding E / kJ mol^{-1}**	**Addition E / kJ mol^{-1}**
Na-ZSM-5	-221650.8	-	-
H_2O	-1371.6	-	-
Na-ZSM-5 + H_2O	-223108.5	-86	-86
Na-ZSM-5 + $2H_2O$	-224556.3	-164	-77
Na-ZSM-5 + $3H_2O$	-225990.0	-227	-63

Table 5.10. Table of energies for the initial optimised structures forming the starting structure for the *Ab-Initio* Molecular Dynamics simulations.

As is detailed in the table above, the overall system energy gets lower upon the addition of each water molecule, with the addition of three water molecules being approximately 227 kJ mol^{-1} more favourable than the base Na-ZSM-5 system. Hence why it is probably extremely difficult to remove water from the pore of zeolites completely, without leading to a decrease in the structural integrity to the point of structural collapse of the zeolite. This phenomenon is clearly demonstrated by Hunger *et al*[277] as the measurement of desorption of one water molecule per unit cell occurred between 400 and 500 K. The energy of addition for a single water molecule is similar for both H-ZSM-5 and Na-ZSM-5 systems but is approximately 4 kJ mol^{-1} more favourable for Na-ZSM-5, which is small enough to be considered insignificant.

Whilst the overall system energy continues to decrease with the addition of the second water molecule, it is significantly less favourable than for the first, which is probably due to the influence of both the charge density and the size of the sodium cation. In the Na-ZSM-5 system the second water does not form a secondary stabilising hydrogen bond to the pore wall as was observed for H-ZSM-5. Comparing the geometry of the clusters, the second water molecule protrudes further into the pore than for the H-ZSM-5, no doubt because of this increased cation size. This geometric effect is presumably what prevents the formation of a stabilising hydrogen bond from the second water molecule to the wall of the pore.

The incremental energy then drops again upon the addition of the third water molecule; however, the addition of another water molecule requires roughly 14 kJ mol^{-1} more than the addition of the second water molecule. However, the overall reduction in energy is likely a result of the formation of two additional hydrogen bonds, which stabilises the system and increases the geodesic path length. The inclusion of the third water means a chain of hydrogen bonded water molecules can form around the sodium, then back to the pore wall with a similar curvature to the cation. As a result, the third water molecule now forms a third hydrogen bond to the zeolite framework, leading to a similar stabilisation effect to that seen in the two-water molecule H-ZSM-5 system. The second water molecule now forms a hydrogen bond to the third water, which then forms an additional hydrogen bond to the framework, forming a geodesic path length of water molecules around the sodium cation. It is probable that this is the trend observed for H-ZSM-5 with two water molecules but is subdued by the Na cation’s larger size and migration effect as it binds to the framework less strongly. As was observed in the earlier chapter of this thesis on metal centres, the energy to deprotonate H-ZSM-5 was 1,098.7 kJ mol^{-1}, which is higher than the 439.2 kJ mol^{-1} needed to remove the sodium. The lower binding energy of sodium explains its mobility compared to H-ZSM-5, which would only temporarily deprotonate the original BAS, or perform an exchange that protonated the oxygen on the other side of the aluminium.

5.3.11 Na-ZSM-5: One Water Molecule at 298 K and 400 K

Results from the AIMD simulations are displayed as RMSD plots for the full Na-ZSM-5 system at 298 K with one water molecule below in ***Fig. 5.27.*** However, as with the H-ZSM-5 system, it is difficult to directly interpret the contributions of just the oxygen sodium site and water molecule, as the plot accounts for the entire displacement of the ZSM-5 lattice structure from the starting position. Despite the simulation running at a constant temperature and pressure, the initial upwards trend observed in the plot from 0 Å to around 2.5 Å corresponds to the system warming up to the designated temperature, as had been observed previously for H-ZSM-5.

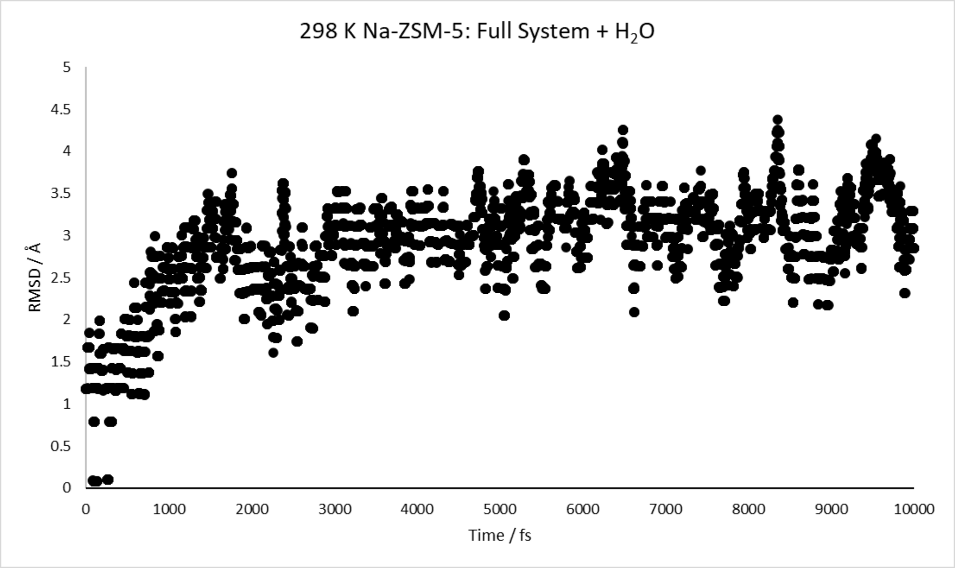

Fig. 5.27. RMSD plot of the entire Na-ZSM-5 system with one water molecule at 298 K over 10 ps.

Once again, the same theory used for the RMSD plot was modified so that it only includes the sodium atom and the oxygen that it is bonded to, as well as the additional water molecules involved in the cluster, thus forming the component analysis. This way the displacement of the water molecules from the starting position can be seen directly, but more specifically the displacements in bond length of the water cluster, which are displayed in ***Fig. 5.28.*** This figure illustrates that once reaching 298 K there are effectively three main observable configurations with very minor displacements for each of the three states.

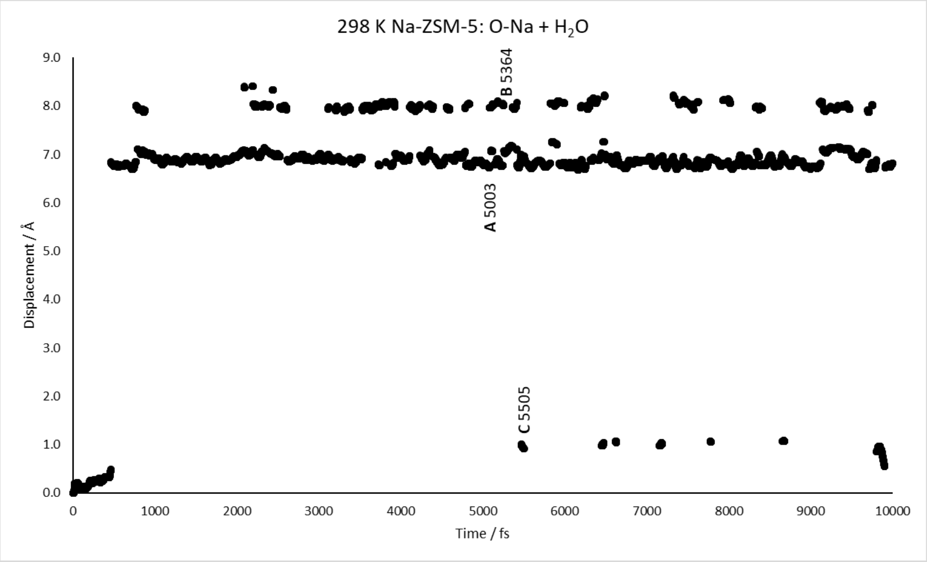

Fig. 5.28. Component Analysis of the aluminium site, Na and single water molecule at 298 K.

Energy Order High to Low	Time / fs	Energy / kJ mol^{-1}	ΔE from lowest / kJ mol^{-1}
A	5003	-14639412.9	22.03
B	5364	-14639414.0	20.92
C	5505	-14639435.0	0.00

Table 5.11. Energies of the single water configurations displayed in the CA for 298 K.

As can be seen, when comparing ***Fig. 5.28.*** and ***Fig. 5.29.*** there are effectively three main cluster configurations between the two different temperatures. When extracting a cluster configuration from each of these levels, they are essentially the same three configurations at both temperatures. There is a relatively sparse grouping of configurations for both these structures with displacements below 2 Å, whilst most configurations deviate by more than 6 Å. This finding also demonstrates that despite the higher temperature there are no further configurations made accessible, as was the case for the H-ZSM-5 systems.

The energies of these systems were determined using the QM/MM methodology previously outlined, with a base QM region size of 41 atoms including the sodium cation. The size of this QM region increases with the addition of water molecules to the system, from 44 atoms up to 50 atoms, depending on the number of water molecules inserted into the pore. When contrasting the energies of each configuration, it can be seen from ***Table 5.11.***, that the lowest energy configuration is structure C. Structure C also has the lowest amount of displacement and is the least populated state, suggesting that it could have similar behaviour to that observed for the H-ZSM-5 systems discussed previously. The infrequent occurrence of this configuration is influenced by the system temperature, whereby the water molecules have enough kinetic energy to occupy the less favourable cluster configurations at the higher levels of displacement. This reasoning can also be used to explain why most of the simulation occupies displacements of 7 Å and 8 Å in the component analysis. Whilst A is higher in energy than B, it has a higher occupation inferring that at 298 K this configuration is easily accessible for most of the simulation. With under 2 kJ mol^{-1} difference between configuration A and B it would explain why the occupation of the two states are similar, as it probably oscillates between the two similar configurations but with a propensity towards the higher energy configuration.

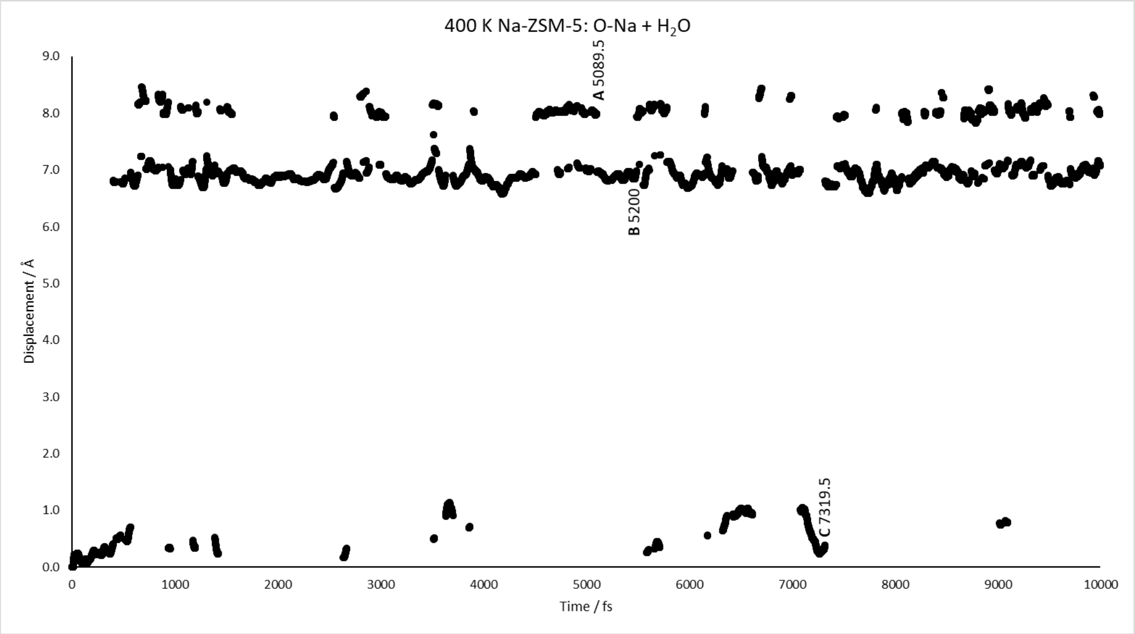

Fig. 5.29. Component Analysis of the aluminium site, Na and single water molecule at 400 K.

The CA at 400 K in ***Fig. 5.29.*** exhibits remarkably similar behaviour. Once again there are three distinct levels, with the highest population occupying the 7 Å displacement followed by the 8 Å level, with the least populated state being around 1 Å of displacement. The CA of this system at both temperatures follow very similar behaviours, and from the AIMD there are no new configurations, and as such analysis only needs to be made from one of these CAs as it will be representative of the systems across both temperatures.

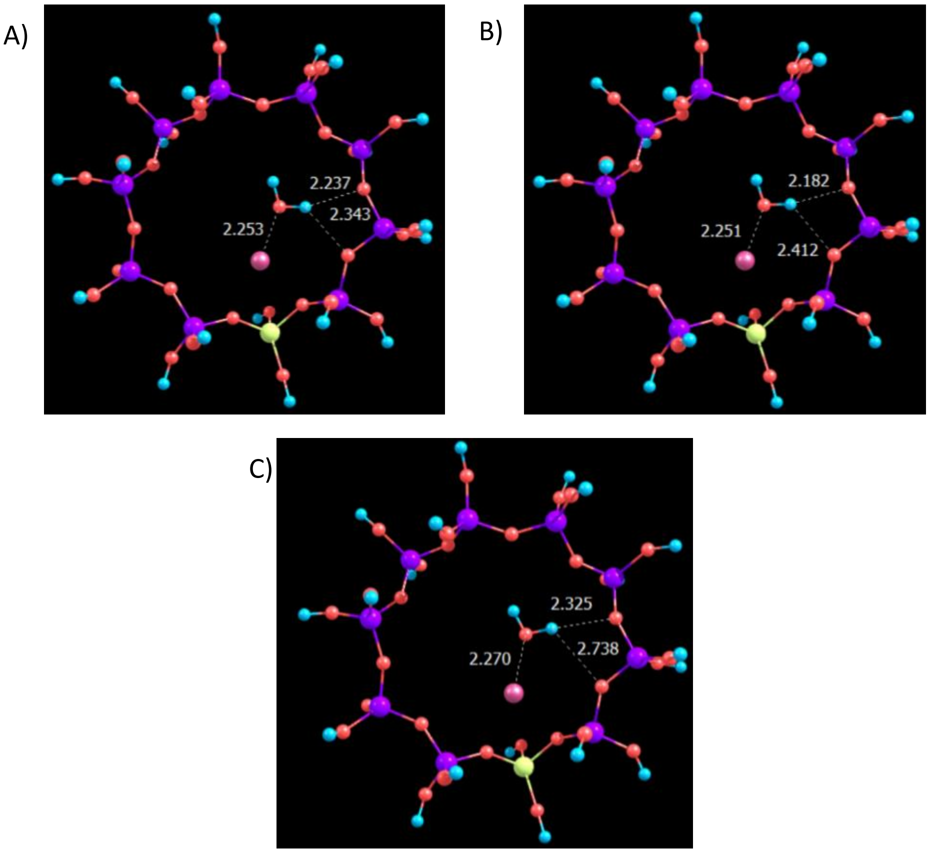

Fig. 5.30. Water molecule configurations A, B and C for 298 K systems with key distances labelled in Å. Whilst all three do look similar the third system forms a hydrogen bond from the right hydrogen atom to the nearest oxygen in the wall of the pore, whereas the first two do not. Atom colours: Si: purple, O: red, H: light blue, Al: yellow.

The three configurations from the 298 K plot were reconstructed and optimised using the hybrid QM/MM methodology used previously and are shown in ***Fig. 5.30.*** (Configurations are A 5,003 fs, B 5,364 fs and C 5,505 fs). All three clusters contain coordination distances from the sodium cation to the water molecule oxygen between 2.5 and 2.7 Å, broadly in line with the distances reported by Stahl and Hanson,[280] thus suggesting the sodium cation is coordinated to five oxygens in the zeolite wall with the water oxygen forming the sixth coordination of the octahedral geometry. The optimised QM regions look very similar but form slightly different orientations, with the final system forming a hydrogen bond to the wall of the pore. Qualitatively there is not much variation between these systems, as only a single water molecule is coordinating to the cation and remains coordinated for the duration of the simulation. The respective energies are remarkably similar with only a 22 kJ mol^{-1} difference between the highest and lowest energy systems. Whilst relatively small, this energy difference is consistent with the formation of a single hydrogen bond.

Anharmonic calculations were subsequently carried out on each of these three systems. These utilised the GVPT2 methodology outlined earlier to generate a spectrum, whereby bars represent each individual vibrational mode and their intensities relative to other vibrations within the system as shown in ***Fig. 5.31.***

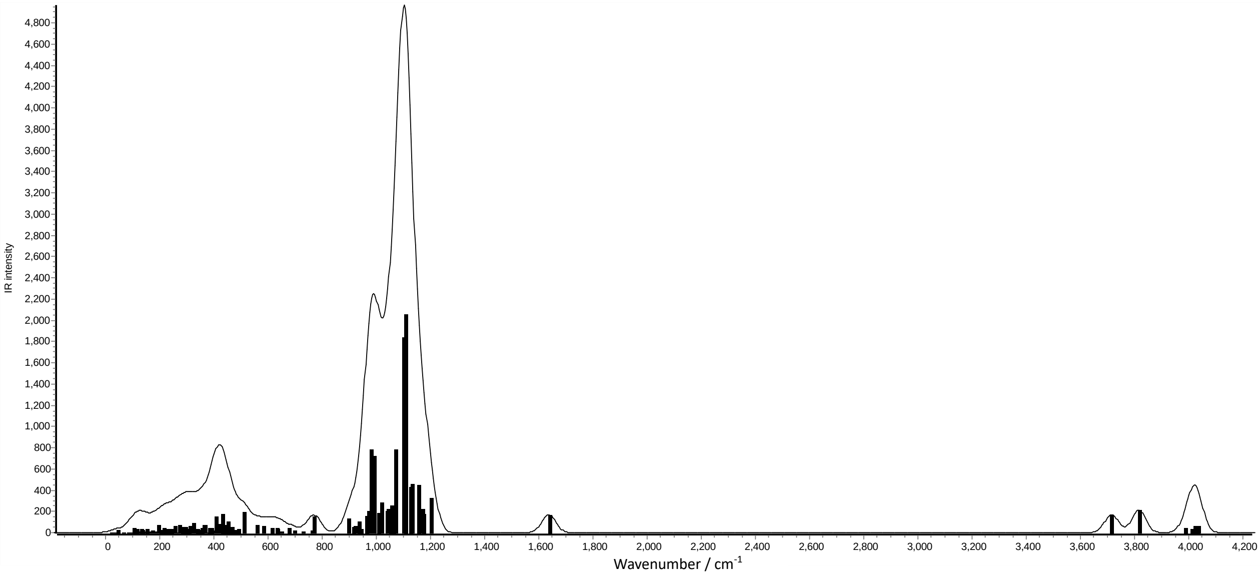

Fig. 5.31. Calculated spectrum for one water molecule at 298 K with applied Gaussian broadening from the Chemcraft software illustrating the general shape of the spectrum.

A Gaussian broadening was once again applied that transforms the bars on the graph into a continuous line, which is somewhat more representative of an experimental spectrum, allowing for values to be exported which can then be overlayed with spectra from all relevant systems at once. This allows for an easy analysis between the contributions of each of the respective systems and the corresponding shift in their frequencies as demonstrated in ***Fig. 5.32***.

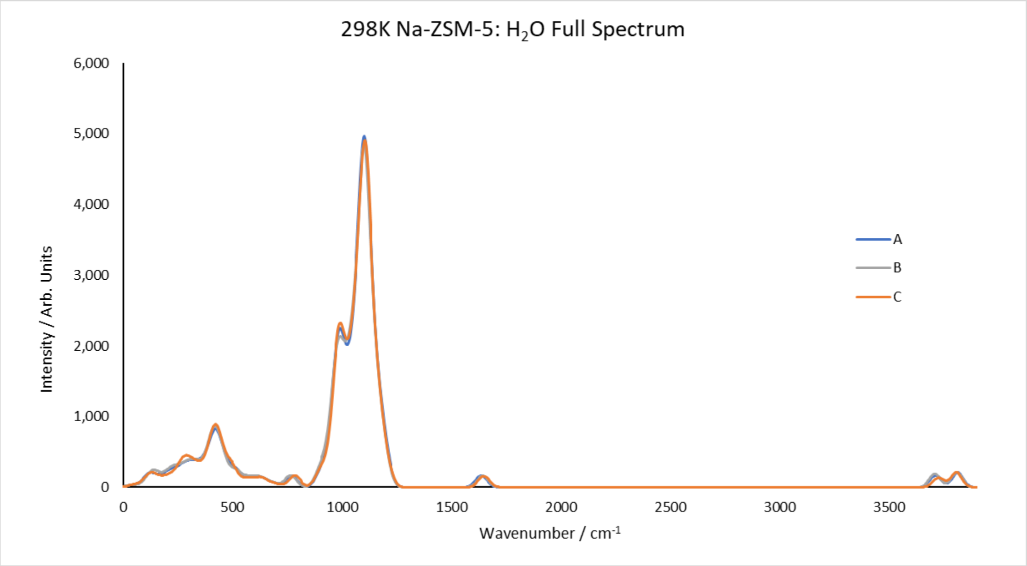

Fig. 5.32. Combined anharmonic spectra of the three cluster configurations for a single water molecule in the pore of Na-ZSM-5 at 298 K. Line colours: Cluster A: blue, Cluster B: grey and Cluster C: orange.

Three configurations were taken from 5,003 (A), 5,364 (B) and 5,505 (C) fs into the simulation and optimised using the QM/MM methodology, whilst the subsequent calculated spectra were overlayed as illustrated in ***Fig. 5.32.*** A peak would arise at approximately 4000 cm^{-1} as a result of the QM region's terminal hydrogens and has subsequently been removed from the spectrum. From these combined spectra no significant shifts for the symmetric or asymmetric modes are observed, and there is a near perfect overlap for the symmetric bending mode. Thus, it can be concluded that there were no significant shifts in the symmetric and asymmetric stretching contributions in the calculated spectra of water from either of these three systems. It is therefore likely that any cross-coupling would occur in a system containing more than a single water molecule.

Experimental FTIR carried out on Na-ZSM-5 by Hunger *et al*[277] with 1.5 and 3 water molecules per unit cell, exhibit four bands corresponding to adsorbed H_2O with two narrow bands at 3677 (±4) cm^{-1} and 3584 (±4) cm^{-1} ascribed to the 'free' antisymmetric and symmetric stretching vibrations of water O-H, with no additional intermolecular interactions as previously suggested in the work of Jentys *et al.*[268] Our results indicate these 'free' vibrations occur at around 3815 and 3715 cm^{-1} respectively, which is noticeably higher;

however, these systems have only one water molecule, and it is therefore unlikely that the discrepancy is caused by the influence of additional water molecules. It could, however, be proposed that the shift arises from the different location of the aluminium site to which the sodium is coordinating within the zeolite, thus slightly altering the electronic structure and yielding different spectroscopic shifts.

5.3.12 Na-ZSM-5: Two Water Molecules at 298 K

The same simulation process was carried out for the addition of a second water molecule to the pore of Na-ZSM-5 and the subsequent CA was plotted for the system at 298 K. The CA of this system is displayed in ***Fig. 5.33.*** and four distinct levels of water configurations are observed with an additional configuration at 3,236 fs (step 6,472) that only occurs once after the system is at temperature. This system has very little displacement from the initial structure of below 2 Å; however, since it occurs about a third of the way into the simulation it was concluded that it is a system worth modelling.

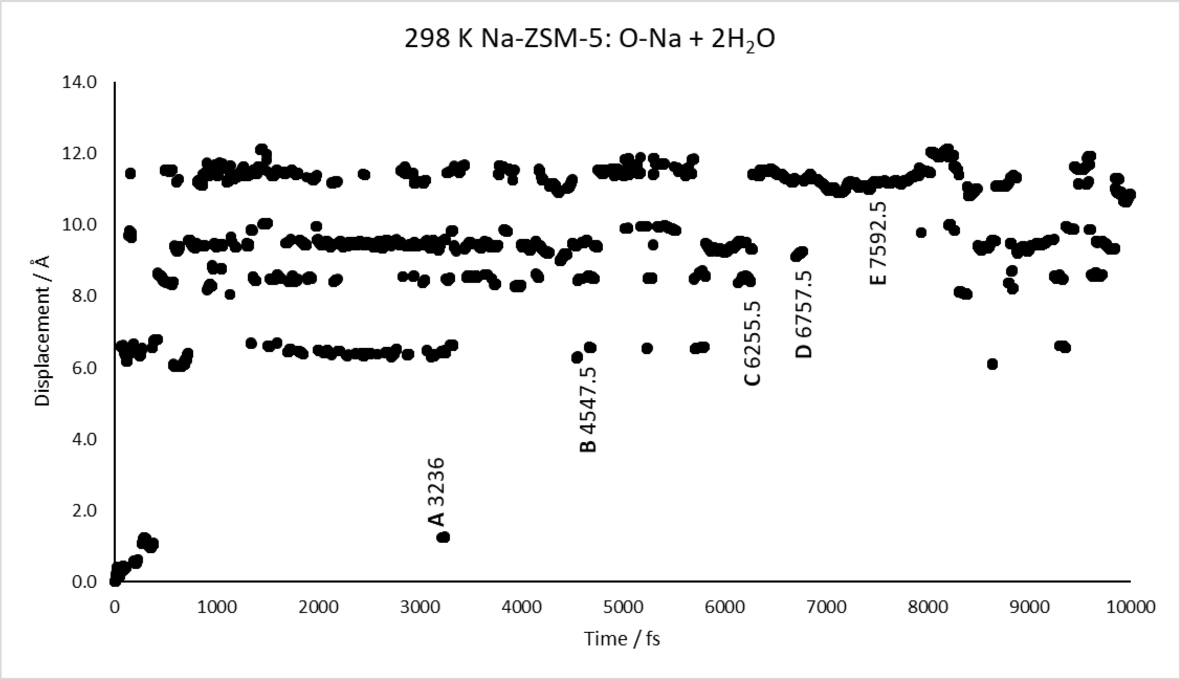

Fig. 5.33. Component Analysis of the aluminium site Na and two water molecules at 298 K.

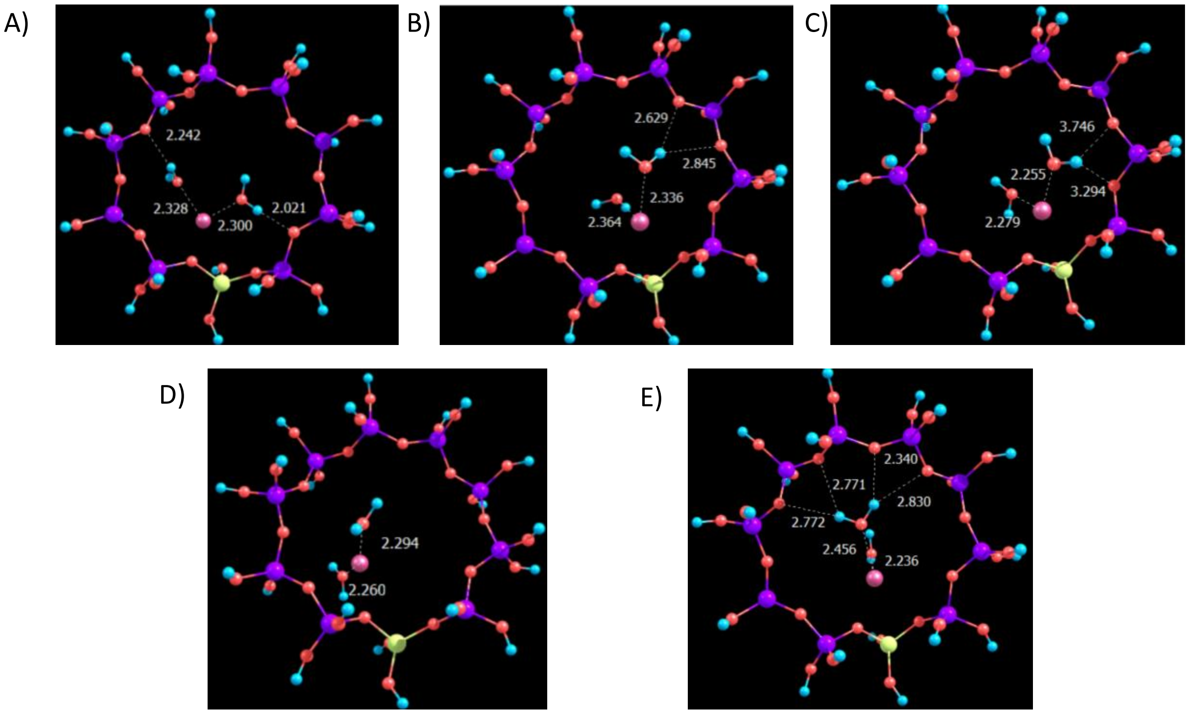

Fig. 5.34. Top left to bottom right: Structures A to E from the 298 K simulation of two water molecules. Key distances are labelled with a focus on the sodium and water oxygen distances. Atom colours: Si: purple, O: red, H: light blue, Al: yellow.

As can be seen from the optimised structures in **Fig. 5.34** the sodium cation has coordination distances of between 2.2 and 2.4 Å for the two water molecules in the cluster. These distances are comparable to those reported by Stahl and Hanson in mesolite,[280] therefore we can assume that the sodium cation is most probably coordinating to four zeolite oxygens with the two water oxygens coordination completing the expected octahedral geometry.

Energy Order High to Low	Time / fs	Energy / kJ	ΔE from lowest / kJ
B	4952.5	-45997117.7	58.2
C	6255.5	-45997120.1	55.9
E	7592.5	-45997123.4	52.5
D	6757.5	-45997165.2	10.7
A	3236	-45997175.9	0.00

Table 5.12. The energies of the optimised QM/MM configurations found in the 298 K CA for two water molecules.

When drawing a comparison between the component analysis in ***Fig. 5.33.*** and the order of energies presented in ***Table 5.12.*** the lowest energy is the outlier cluster, system A which has the lowest displacement from the optimised structure. In the previous case, the lowest displacement was also the lowest energy system, and it could be argued that this should be the most occupied state. We might expect the highest occupancy state would be the lowest energy as this would be more accessible and would occur more frequently. Additionally, since the system begins the simulation from an optimised state, this would form an energy minimum, as such a low displacement from this should be low in energy.

This argument would assume that configuration E would be higher in energy than D due to the higher level of displacement, which is the case with system E which is over 22 kJ mol^{-1} higher in energy than D. However, B has the highest energy followed by system C, despite having less displacement from the optimised structure. System C has a greater occurrence in the CA than system B, so it is probable that these occurrences are governed primarily by the effect of the systems temperature. It is interesting to note that the largest changes in energy occur between the lowest energy and second lowest energy systems, as well as the second lowest and third lowest energy system. These energy changes are approximately 10 and 42 kJ mol^{-1} respectively and contribute the most to the overall energy range of 58.2 kJ mol^{-1}. The energy range between the three highest energy systems is approximately 6 kJ mol^{-1}, which could explain why the population levels of B, C and E are broadly similar. These configurations probably interchange between each other as they are close in energy and their geometries are not dissimilar from each other.

Some of the cluster configurations from this set of data would fail to optimise to a structure similar to that observed in the AIMD simulation when using the QM region discussed above. Instead, the structure would optimise with both water molecules spread out to opposite sides of the pore rather than forming the expected cluster. Initial structure geometries retained the exact bond distances from the simulated structure to ensure the optimisation would give the desired cluster configuration. Despite this, vastly different geometries were obtained. As a result, we redesigned the QM region, increasing it from 47 atoms to 135 atoms, to accommodate more of the pore and account for any additional confinement effects that had an influence over cluster formation and is shown below in ***Fig. 5.35.***

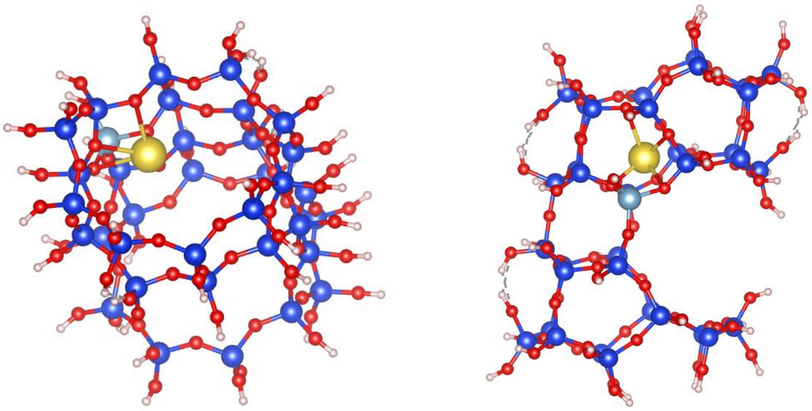

Fig. 5.35. Redesigned QM region for two water molecule systems, modelling most of the pore channel. Atom colours: Si: blue, O: red, H: white, Al: light blue, Na: yellow.

The redesign of the larger QM region accommodates the influence of the pore on different levels and its resulting confinement effects. Using this larger QM region ensured that the two water molecule systems found a minimum where the clusters very closely represented those found in the AIMD and selected from the CA.

The observed vibrations in the spectra would change slightly, but they would predominantly only affect the main lattice vibrations occurring at the lower wave numbers. The vibrational modes resulting from the water molecules occur at higher frequencies and would still be clearly defined in the spectrum. However, we note that the increased size of this region is accompanied by a much higher computational cost. Whilst the larger QM region was necessary to perform accurate optimisations of the two-water molecule systems, it was not necessary to use this larger region for the frequency calculations, as all the interactions of the water molecules occur within the smaller QM region. Despite this, a comparison could be made between the two, by using the same system to see how the spectrum is influenced by this larger region, but this is beyond the scope of this chapter.

The calculated spectrum for Na-ZSM-5 with two water molecules at 298 K is shown below in ***Fig. 5.36.*** These spectra have only a subtle amount of shifting as none of these structures are forming hydrogen bonds, however there is still important and fundamental behaviour that warrants analysis.

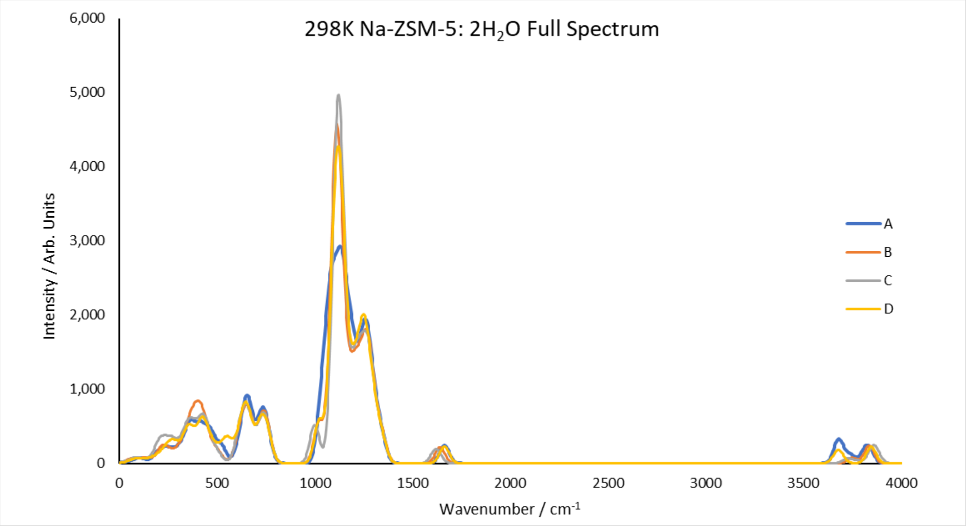

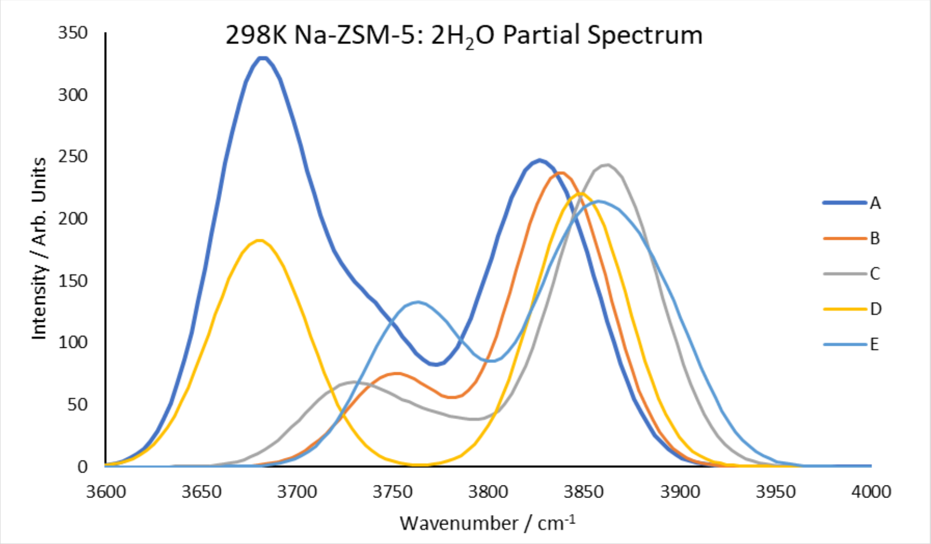

Fig. 5.36. Anharmonic spectra of two water molecules in the pore of Na-ZSM-5 at 298 K. Line colours: Cluster A: blue, Cluster B: orange, Cluster C: grey, Cluster D: yellow and Cluster E: light blue.

Overall, there is a general overlap of the asymmetric peaks with a very minor shift, but the main area of interest concerns how the symmetric stretching frequencies are affected. Systems B, C and to a lesser extent E, have similar geometries and as a result their corresponding spectra also follow similar trends. These three systems have similar shifts for their asymmetric stretching frequencies, and they also have symmetric stretching frequencies that are less intense than their symmetric frequencies. System A is the only cluster that subverts this relationship, with a more intense symmetric vibration from one water molecule with a hydrogen pointing to a framework oxygen only 2.02 Å away. It is likely that this vibration extends the hydrogen atom close enough to the oxygen to start forming a hydrogen bond, which would also explain the observed shift to the lower frequency. In the case of system D, it is unclear as to why the frequency has shifted to the lower wave numbers; however, the intensities of both the symmetric and asymmetric peaks are similar, with a slightly lower intensity for the symmetric peak. The shifting of frequencies could be a result of a de-shielding influence on the water molecules due to their proximity to the sodium cation.

5.3.13 Na-ZSM-5: Two Water Molecules at 400 K

Energy Order High to Low	**Time / fs**	**Energy / kJ mol^{-1}**	**ΔE from lowest / kJ mol^{-1}**
C	4924.5	-45997131.46	27.16
A	2670.5	-45997137.23	21.39
B	3519.5	-45997154.99	3.63
D	5425	-45997158.62	0.00

Table 5.13. Energies of the Na-ZSM-5 2 water molecule systems taken from the CA at 400 K

When comparing the data from the CA in ***Fig. 5.37.*** and the ordering of energies shown in ***Table 5.13.***, it can be seen that system D is the lowest energy with a high occupancy with displacements at approximately 12 Å. Interestingly, after around 5,000 fs, this high level of occupancy decreases significantly to the level at around 10 Å of displacement. As a result, an increase in population of the highest energy configuration (system C), which appears to be a switch of 27 kJ mol^{-1} from the lowest energy configuration to the highest energy cluster. Considering the occupancy is going from the lowest energy to highest energy configurations directly – it is probably a result of the system reaching a higher energy on average, due to the influence of the increased temperature.

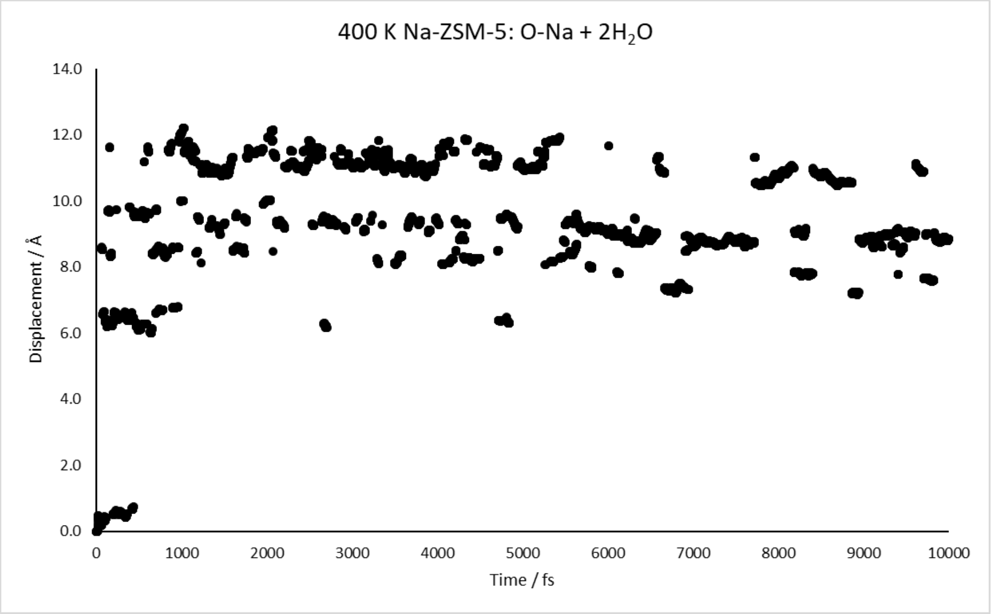

Fig. 5.37. Component analysis of the aluminium site, Na and two water molecules at 400 K.

In the first half of the simulation the lowest energy configuration is heavily occupied, however, once the system reaches the designated temperature, the water molecules have enough kinetic energy to access the highest energy configurations more frequently. Correspondingly this results in the populations of these levels inverting, so that the highest energy state is more heavily occupied for the second half of the simulation. Both configurations B and A occur far less frequently, with A not occurring again beyond this point. The low frequency of system A's occurrence, coupled with its higher energy could imply it is an early transitional geometry, which acts as a pathway to the lower energy configurations. The system subsequently stabilises into an equilibrium between configurations B, C and D. Structures B and D correlate with the gaps in the CA left between system C, suggesting that system C is the main state, that then transitions into either configuration B or configuration D, then back to C in a dynamic equilibrium.

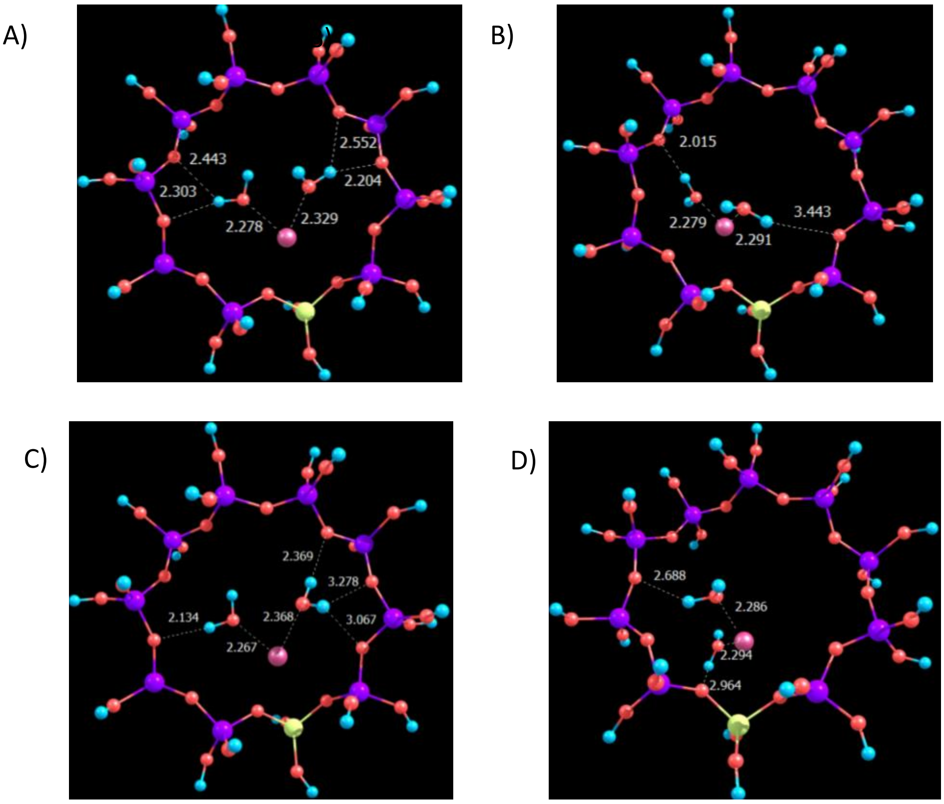

Fig. 5.38. Water cluster configurations A to D for two water molecules in Na-ZSM-5 at 400 K. Key distances are labelled with a focus on the sodium and water oxygen distances. Atom colours: Si: purple, O: red, H: light blue, Al: yellow.

Once again, the optimised structures in **Fig. 5.38** show the sodium cation with coordination distances of between 2.2 and 2.4 Å for the two water molecules in the cluster, in line with the literature.[280] It therefore follows that the sodium cation coordinates to four zeolite oxygens with the two water oxygens filling out the sodium cation's octahedral geometry.

When analysing the vibrational spectra shown below in ***Fig. 5.39.***, similar overlaps of both the intensity and frequencies are observed for the symmetric stretches in systems B and D. Likewise there is also an overlap of frequencies for the asymmetric stretching frequencies for systems A, C and D, with the symmetric bending frequencies relatively constant between all systems. Despite this overlap the relative intensity decreases from A to C to D. The far shifting of the symmetric stretches for systems B and D can be explained by their correlation to expected hydrogen bonding behaviour. These two systems are the closest to forming hydrogen bonds, with the closest hydrogen atom of B 2.01 Å from the pore wall oxygen, and the hydrogen atom from the water molecule in cluster D also being 2.01 Å from the oxygen in the pore wall. These hydrogen bond distances are slightly over 2 Å compared to the 1.66-1.70 Å range observed in the H-ZSM-5 systems. Despite which, hydrogen bond formation could still be feasible, as it would explain why there is only a minor shifting of the symmetric frequencies by 50 cm^{-1} from 3750 cm^{-1} to 3700 cm^{-1}. A and C have similar geometries, however, the rotation of one water molecule is probably the reason for the minor decrease in intensity for the symmetric stretch in A and can also be applied to the decrease in asymmetric stretching intensity in system C. There is a noticeable shift in asymmetric stretching vibrations for system B; it is however unclear as to why this occurs and is potentially a result of a more de-shielding hydrogen bonding effect from the pore on the water molecules.

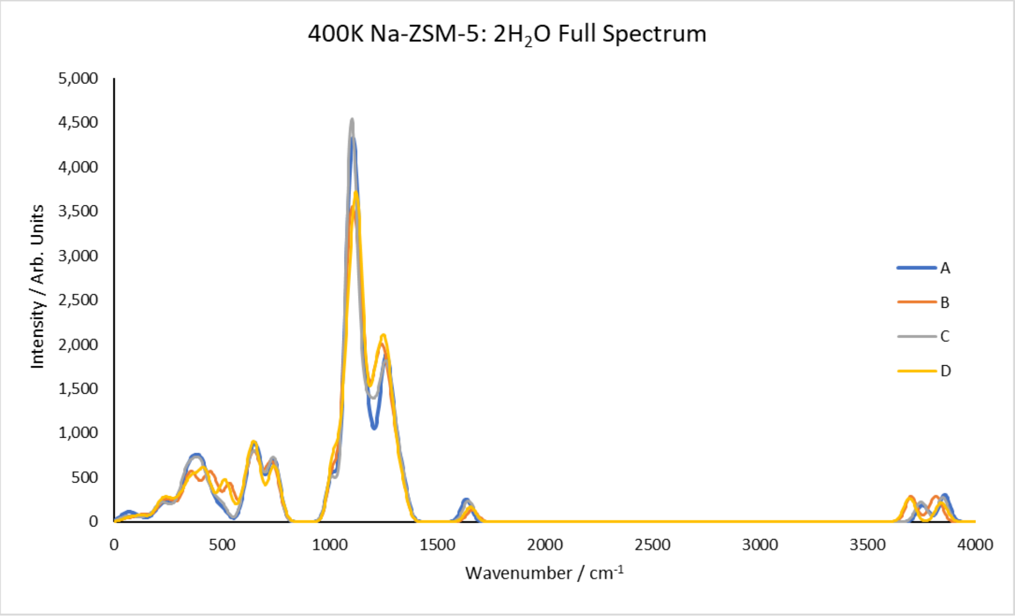

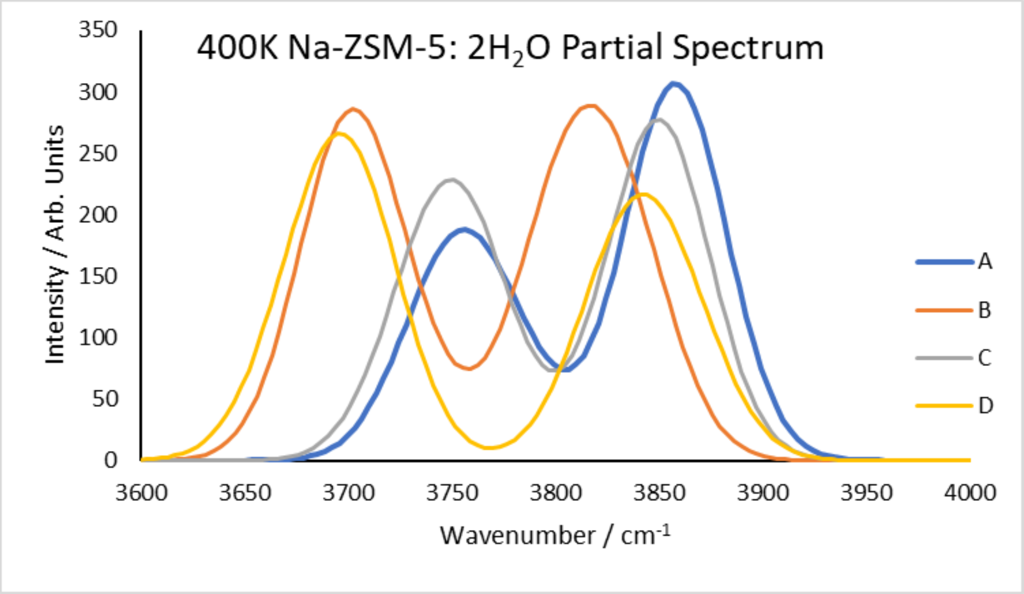

Fig. 5.39. Anharmonic spectra for two water molecules in the pore of Na-ZSM-5 at 400 K. Line colours: Cluster A: blue, Cluster B: orange, Cluster C: grey and Cluster D: yellow.

5.3.14 Na-ZSM-5: Three Water Molecules at 298 K

The next step was to simulate the three water molecule cluster systems at the two temperatures. In the case of H-ZSM-5, the addition of a second water molecule promotes the formation of hydroxonium ions, as displayed in the initial optimisation step but not in the rest of the AIMD simulations. The addition of the third water molecule was responsible for stabilising this form of clustering and further enhancing proton mobility during the AIMD simulations. This behaviour was observed in our simulations and has also been reported in studies on protonated H-ZSM-5,[107,270,271] in which the deprotonation of the acid site by one water molecule is considered a high energy transition state. The addition of a second water molecule then stabilises this structure forming a minimum and the addition of more water molecules has been shown to further enhance this stability. Much less is known about the dynamics of water in Na-ZSM-5, but it is encouraging to observe similar hydrogen bonding behaviour between water molecules and the pore wall.

Despite the encouraging similarities in hydrogen bonding behaviour between the two water molecules, hydroxonium ion formation was still not observed upon addition of the third water molecule. Considering the H-ZSM-5 system formed hydroxonium ions with a total of 5 protons (two water molecules and a BAS proton) it could have been expected that three water molecules would allow for hydroxonium ion formation. However, the lack of hydroxonium ion formation is probably due to the lack of an available proton to exchange from the aluminium site, as was the case for the BAS in H-ZSM-5.

Additionally, as was highlighted in the previous chapters, we showed the binding energy of the Na(I) cation to the aluminium site was -439.15 kJ mol^{-1} and the proton was -1,098.71 kJ mol^{-1} (in line with the literature[71,107]) indicating that the sodium binding to the aluminium site is 659.56 kJ mol^{-1} weaker than the proton. Since the binding energy of the sodium cation is weaker, it could be expected that the influence of two/three water molecules could pull it away from the aluminium site as was the case with the proton at the BAS. However, due to the greater mass and size of the sodium cation, its influence is spread over a greater area and is harder to move, resulting in the minor migration to and from each side of the aluminium site, as mentioned previously.

At a loading of three water molecules, the presence of the sodium cation continues to exert a strong influence over the water molecules, but there is an increased amount of displacement occurring throughout the 298 K simulation as displayed below in ***Fig. 5.39.*** The three water molecules now form hydrogen bonds within the clusters, but mostly between two molecules and the pore wall. The third molecule typically coordinates to the other side of the sodium cation to the two hydrogen bonded water molecules, occupying space at the entrance to the side channel. Whilst the third water molecule is mostly too far away to form hydrogen bonds to the other water molecules, there are still occasions when it can form a single cluster that involves all three molecules, but these are rare occurrences.

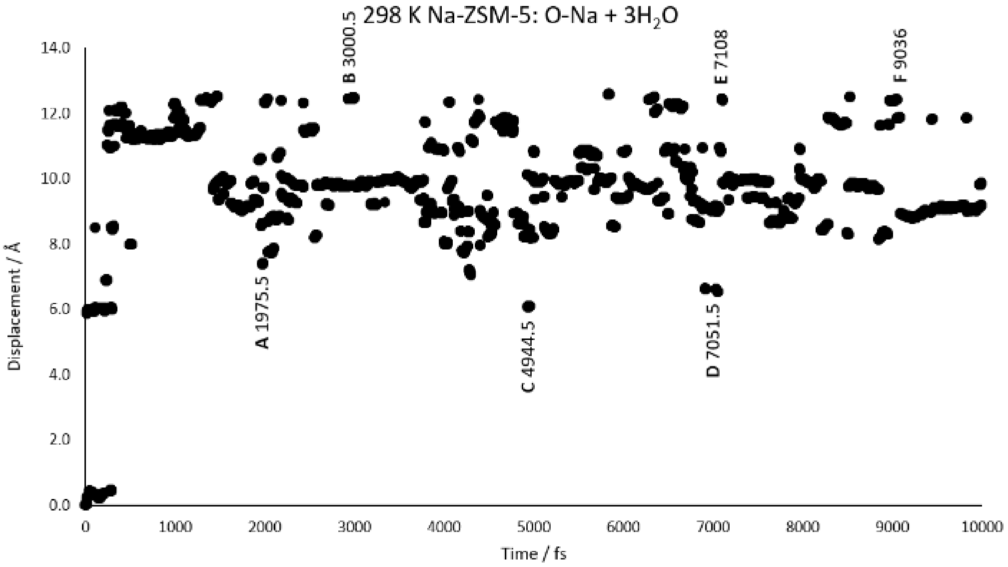

Fig. 5.40. Component analysis of the aluminium site, Na and three water molecules at 298 K.

Energy Order High to Low	Time / fs	Energy / kJ mol^{-1}	ΔE from lowest / kJ mol^{-1}
C	4944.5	-15036929.8	72.3
D	7051.5	-15036944.5	57.6
A	1975.5	-15036957.9	44.3
B	3000.5	-15036961.4	40.8
E	7108	-15036971.1	31.1
F	9036	-15037002.2	0.00

Table 5.14. Order of energies for the systems taken from the component analysis of three water molecules in Na-ZSM-5 at 298 K.

Contrasting the CA with the energies provided in ***Table 5.14.***, it is observed that systems C, D and A are the highest in energy whilst B, E and F are lower in energy, inversely correlating with displacement. At 298 K, the lowest energy structure has one of the highest displacements of around 12 Å, whilst the highest energy structure had the lowest displacement of about 6 Å. These two values form the upper and lower bounds for the sum of the bond lengths from the initial starting structure.

The selected configurations occur far less frequently than in the previous analyses as they form maxima and minima of the component analysis, however, this allows for a pragmatic approach to the sampling process as the CA is more complex. This method selects the more uncommon clusters which are more likely to be contributing to the unusual anharmonic cross-coupling that would be observed in experimental work. Configurations that occur very rarely will not contribute extensively to an experimental spectrum, as such these configurations were selected as they were frequent enough to significantly contribute to an experimental spectrum. Unlike in previous systems, there is less definition between distinct levels of configurations, which illustrates just how mobile the water molecules are in this system. The enhanced mobility has made the structures from these uncommon maxima and minima occur more frequently than previously observed. The geometries of the six structures taken from the CA are highlighted below in ***Fig. 5.41.***

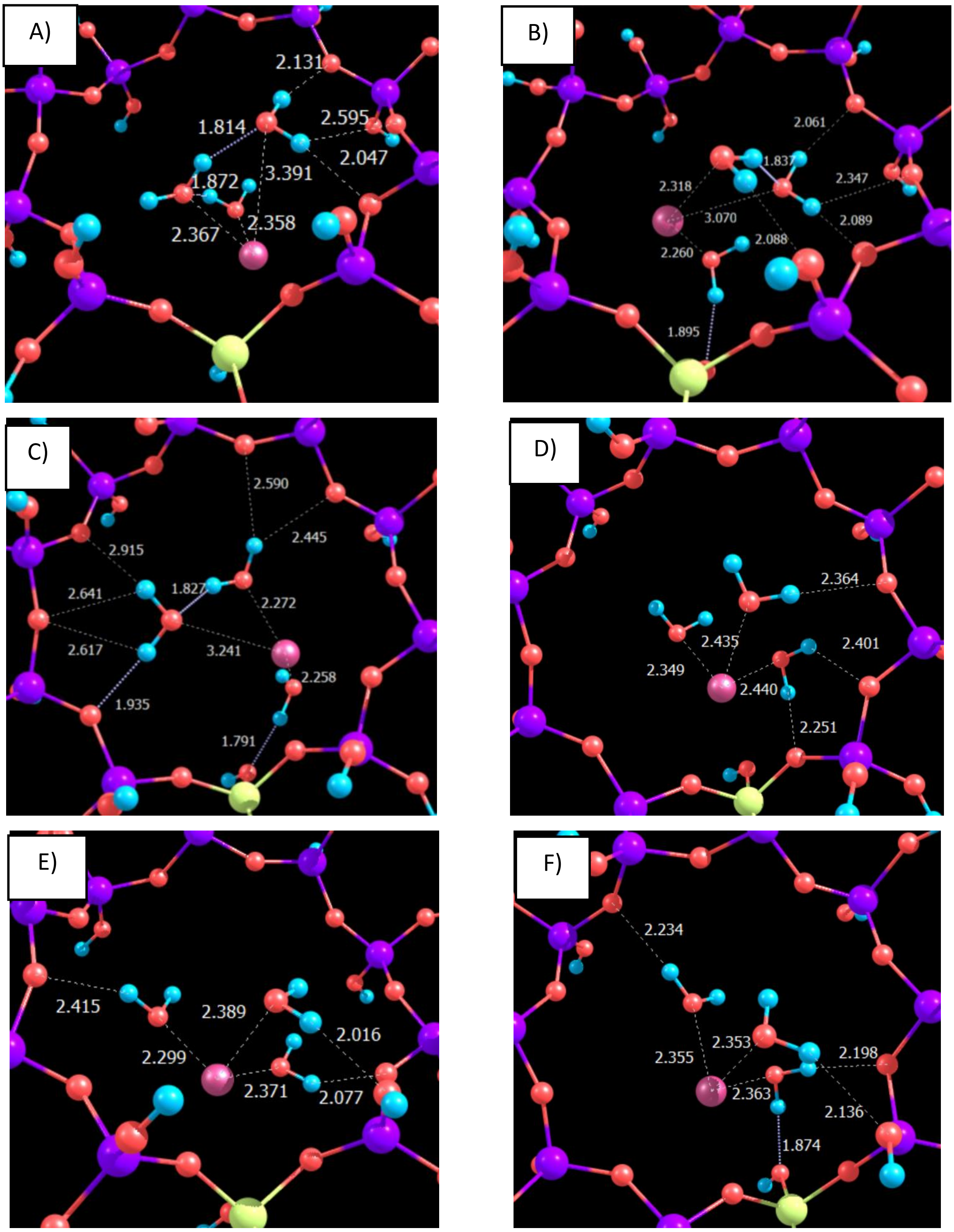

Fig. 5.41. Water cluster configurations A to F from the CA for three water molecules at 298 K. Key distances are labelled with a focus on the sodium and water oxygen distances. Atom colours: Si: purple, O: red, H: light blue, Al: yellow.

The clusters displayed in **Fig. 5.41** exhibit a range of coordination distances between water oxygen atoms and the extra-framework sodium cation. Considering the geometries of clusters A, B and C, we assume that despite the inclusion of a third water molecule only two water molecules are coordinating to the sodium cation suggesting that it is coordinating to four framework oxygens. Cluster D however only has one coordination distance to a water oxygen below 2.4 Å,[280,281] thus it is probably more highly coordinated to five zeolite oxygens as was the case in the one water molecule clusters discussed previously. Finally, clusters E and F have comparatively larger coordination distances, however the water molecules have greater distances between them which suggests that the sodium cation is coordinating to all three water molecules. Therefore, the sodium cation probably coordinates with three zeolite oxygens, which reduces the strain on the structure reducing the deformations reported by Stahl and Hanson.[280]

The highest energy structure, C, contains a two-molecule cluster that forms a hydrogen bond to the pore wall, away from the Al substitution, whilst the third water hydrogen bonds to one of the oxygens on the Al. Since this also occurs for the lower energy structures B and F, the higher energy is probably due to the hydrogen bonds further away from the Al. These systems tend to be lower in energy if the water molecules are more spaced out and not forming as many hydrogen bonds to either the pore wall or each other.

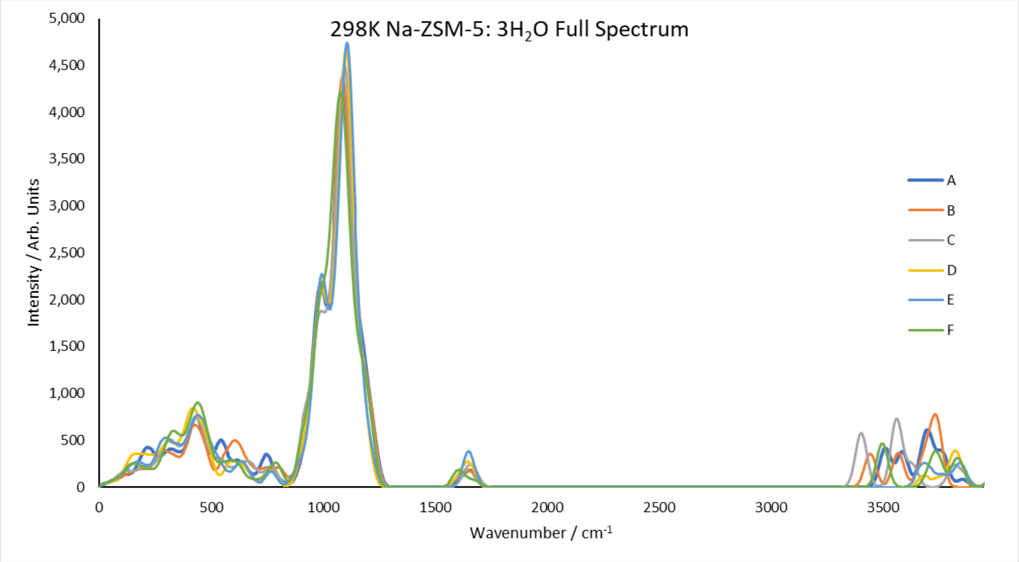

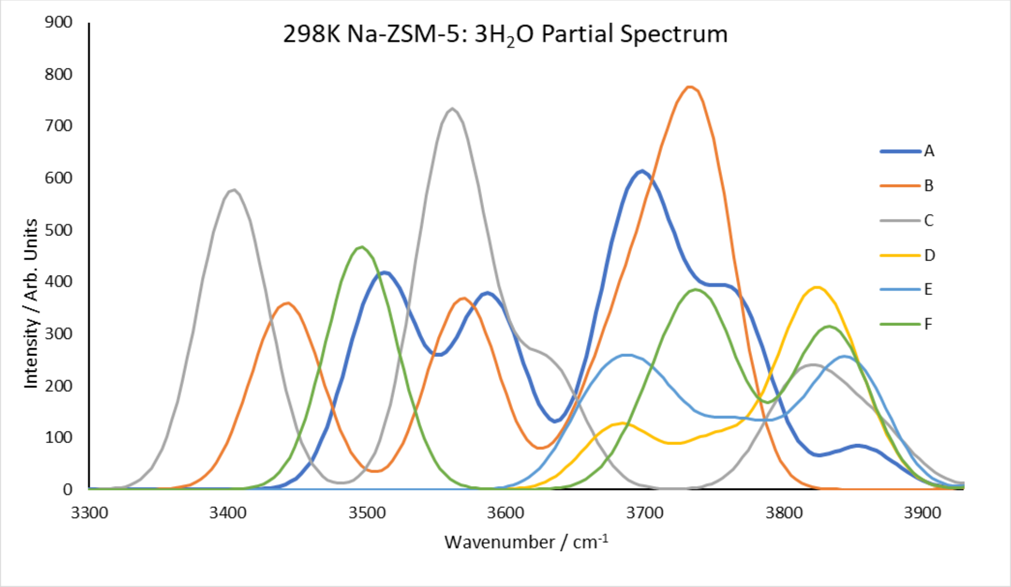

Fig. 5.42. The contributions of water's symmetric and asymmetric anharmonic vibrations in the 298 K system, with the final peak arising from the terminal hydrogens of the QM region. Line colours: Cluster A: blue, Cluster B: orange, Cluster C: grey, Cluster D: yellow, Cluster E: light blue and Cluster F: green.

The simulated spectra for three water molecules within the pore of Na-ZSM-5 at 298 K is detailed in ***Fig. 5.42.***, with the contributions of the symmetric and asymmetric vibrations highlighted. As expected, there is a very clear overlap of the peak at approximately 1000-1200 cm^{-1} corresponding to the stretching of bonds between the tetrahedral units that form the wall of the pore, as has been seen previously. There is largely a good agreement between the systems for the water symmetric bending vibration as found in the two water molecule systems, except for system **F**, which shows a slight broadening in the bending peak. There is some noticeable displacement between 0 and 1000 cm^{-1} resulting from the torsion of the pore structure as it flexes, which is however, within the expected parameters as seen in previously simulated systems. Again, there are some slight differences between the frequencies of the whole system, but they largely remain at similar intensities with minimal shifting. The focus therefore remains on the symmetric and asymmetric stretching modes which vary greatly in both their intensities and frequencies.

The highest energy cluster is system **C**, which also gave the greatest down-field shift for the symmetric stretch with a peak at 3400 cm^{-1}, corresponding to the hydrogen bond formed between the lone water molecule and one of the oxygens bound to the aluminium. The work of Schnabel *et al*[283] compares adsorption bands in NaX zeolites, and they propose that of the bands at around 3420 and 3677 cm^{-1}, the lower frequency bands correspond to an OH stretching vibration arising from the formation of hydrogen bonds between a H_2O molecule and a lattice oxygen atom. Within this system there are two symmetric stretching bands at 3404 and 3630 cm^{-1} corresponding to the hydrogen bonds formed to the aluminium site oxygen and a Si-O-Si bridging oxygen respectively, which agrees with Schnabel *et al*'s observations.[283]

System	H-bond to Al-O / Å	2nd H-Bond / Å		3rd H-bond / Å	
A	-	1.81	Cluster	1.87	Cluster
B	1.90	1.84	Separate Cluster	-	-
C	1.79	1.93	Pore wall	1.83	Cluster
D	-	-	-	-	-
E	-	-	-	-	-
F	1.87	-	-	-	-

Table 5.15. Hydrogen bond lengths in the three-water molecule Na-ZSM-5 systems at 298 K.

Additionally, looking at the hydrogen bond lengths detailed in ***Table 5.15.***, this system has the shortest hydrogen bond length. The shorter bond length has previously been shown to correlate to larger down-field shifts, as the stronger bond would cause more de-shielding of the water's oxygen. This shift is also accompanied by a broadening of the symmetric peak between 3500 and 3700 cm^{-1}; probably caused by the contribution of the two further hydrogen bonds. The third hydrogen bond is also quite short (indicating that it is relatively strong) when compared to other systems at 1.83 Å, resulting in a correspondingly longer O-H bond on the water molecule, which would shift these vibrations more down-field. Whilst there is a little shift for the hydrogen bond to the pore wall, its bond length is much larger at 1.93 Å, which results in less of a shift, causing the overlapping band to broaden. Since the water at the end of the cluster has more space to extend into, the intensity of the vibration is higher. The vibration resulting from the water in the middle is less intense as the two hydrogen bonds probably result in a dampening effect, which would explain the difference in intensity between these two contributions for the symmetric peaks. Interestingly, there is a strong overlap on the frequencies for most of the asymmetric contributions for A, C, D and F; however, they do differ in intensity.

Half of the systems (A, B & D) yield higher intensities for the asymmetric stretches than the symmetric stretches, which is, however, not a clearly defined trend based on energetics alone, as both the lowest and highest energy systems have asymmetric stretching contributions far larger than their symmetric contributions. Two of these systems have multiple hydrogen bonds which could contribute to the intensities by dampening their symmetric contributions. A and B contain multiple hydrogen bonds forming a three-water molecule cluster and a two-water molecule cluster respectively. From a geometrical perspective, system A forms hydrogen bonds from the middle water molecule to the other two molecules in the same direction, which could couple together several asymmetric vibrations and constructively interfere increasing the intensity. Such behaviour could also be the case in system B, but with the additional effect of having all water molecules oriented in the same way, leading to the highest amount of constructive interference and thus resulting in the highest intensity asymmetric peaks.

Whilst system D does not form any hydrogen bonds, two of the water molecules are oriented the same way and the orientation of the hydrogens in the third water molecule could contribute to the asymmetric vibration. As such, it could deconstructively interfere with the symmetric vibrations of the other water molecules, which would result in the lower intensity observed for the symmetric stretches. System E has approximately the same intensity for both its symmetric and asymmetric stretches and, like system D, does not form any hydrogen bonds. The hydrogens of all water molecules in the pore point roughly along the same planes and so their vibrations are likely to be evenly distributed, resulting in similar intensities.

System F has the third longest hydrogen bond of 1.87 Å and gives higher intensities for symmetric vibrations. Despite having the third longest hydrogen bond, it also has the third furthest shift of its symmetric vibration, which is probably due to clusters D and E not containing hydrogen bonds (hence their frequencies are not shifted) coupled with the fact that there is only a single hydrogen bond in the system. Structure A has two hydrogen bonds, but they do not form to an aluminium oxygen, thus the de-shielding effect is lessened. All systems where a greater shift is observed form hydrogen bonds to one of the aluminium oxygens. It is likely that the charge deficit created by the aluminium has a de-shielding effect which would shift these vibrations further down-field. A strong effect would be indicated by the extent of the shift, as the vibrations of cluster C are shifted more than system A, which has two hydrogen bonds but none to one of the aluminium site oxygens.

This effect is also present in system F, which has a strong shift compared to E and D. This shift is only observed for the symmetric stretching frequency of the water forming the hydrogen bond, resulting in the splitting of the symmetric stretching frequencies as is observed in systems A, B and C. There are two stretching modes resulting from the other two water molecules that are not forming hydrogen bonds with consequent smaller shifts. Whilst the only system with similar shifts that does not form hydrogen bonds to the aluminium oxygen is system A; it does, however, form two hydrogen bonds with one of them being the second shortest of all the clusters, which probably explains why its symmetric shift is similar to that of system F.

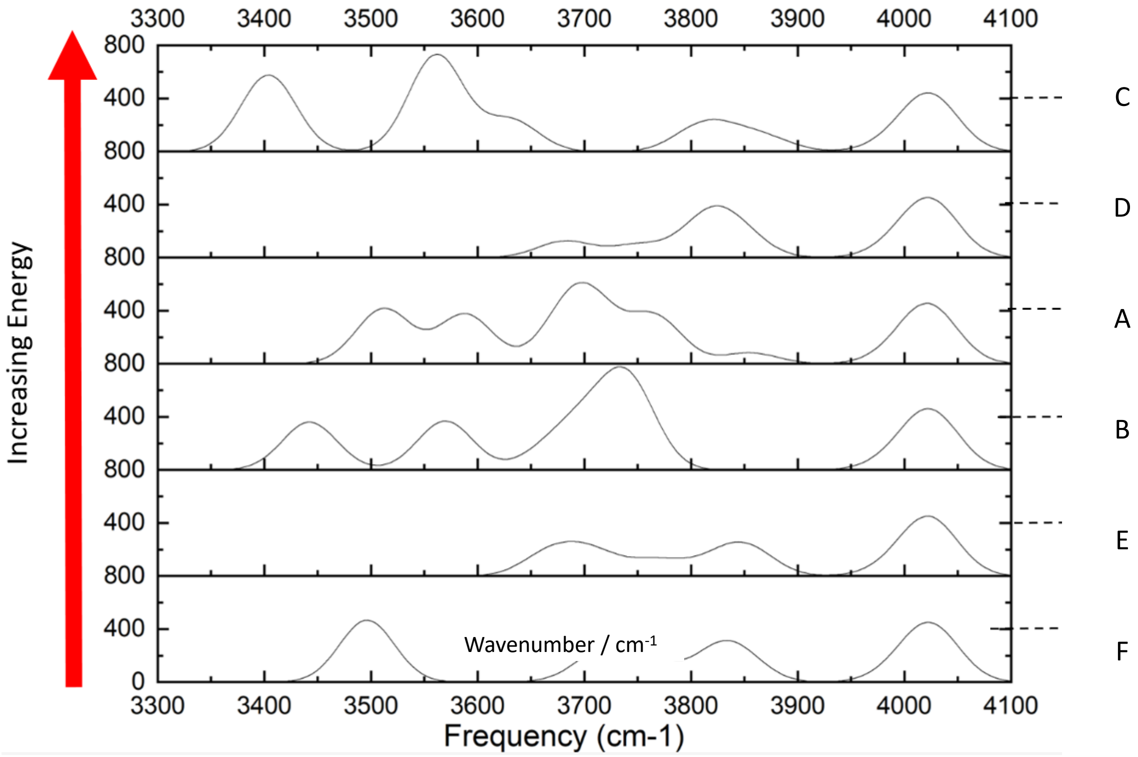

Fig. 5.43. Individual spectra of symmetric and asymmetric water vibrations at 298 K for each cluster ranked by energy with corresponding cluster configurations. Atom colours: Si: purple, O: red, H: light blue, Al: yellow.

The spectra for the three water molecule systems at 298 K are ranked by energy with the corresponding cluster configuration letter at the side are shown above in ***Fig. 5.43.*** Whilst the frequency shifts primarily depend on the hydrogen bond lengths and corresponding strengths, there is a loose generalisation that the shifting of frequencies is more probable to occur in higher energy systems.

5.3.15 Na-ZSM-5: Three Water Molecules at 400 K

The component analysis, performed for Na-ZSM-5 with three water molecules at 400 K is shown below in ***Fig. 5.44.***, with the corresponding energies of the highlighted systems displayed in ***Table 5.16.***

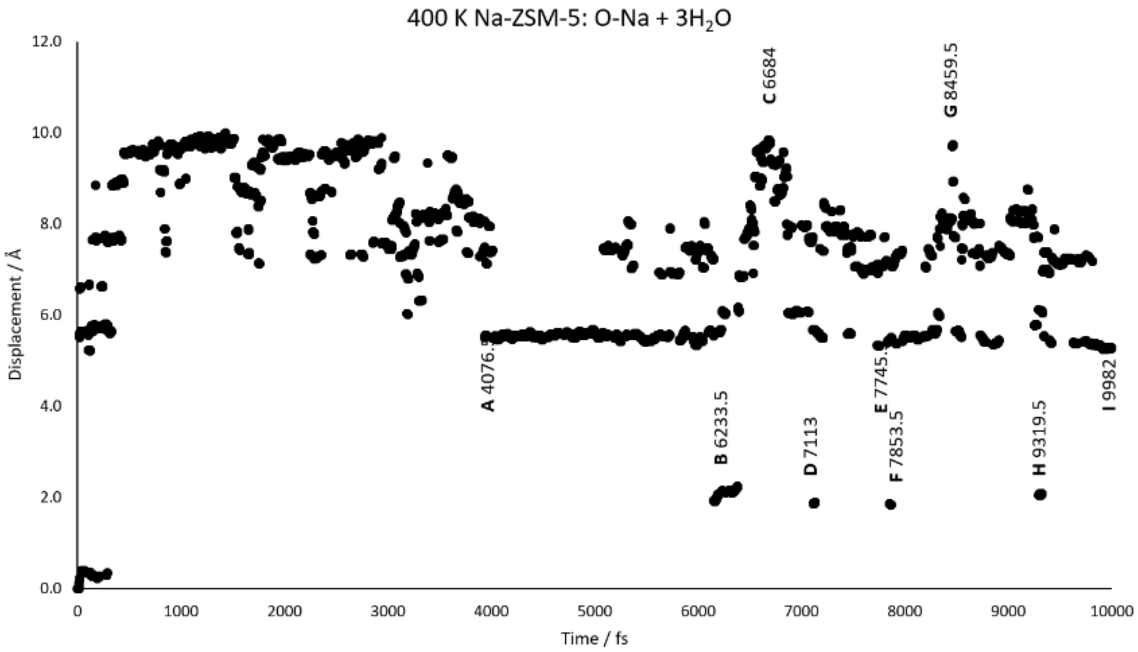

Fig. 5.44. Component analysis of the aluminium site, Na and three water molecules at 400 K.

Energy Order High to Low	**Time / fs**	**Energy / kJ mol^{-1}**	**ΔE from lowest / kJ mol^{-1}**
I	9982	-15036909.9	64.3
C	6684	-15036920.7	53.5
F	7853.5	-15036921.5	52.8
D	7113	-15036934.6	39.6
H	9319.5	-15036956.3	17.9
E	7745.5	-15036963.8	10.4
G	8459.5	-15036966.6	7.6
B	6233.5	-15036968.4	5.8
A	4076.5	-15036974.2	0.00

Table 5.16. Order of energies for the systems taken from the component analysis of three water molecules in Na-ZSM-5 at 400 K. Structure labels refer to the corresponding cluster taken from the MD trajectory in **Fig. 5.44.**

When analysing the energies of the selected structures as detailed in ***Table 5.16.***, there is a smaller variation in the energy range of 64.3 kJ mol^{-1} between the structures at 400 K than that of 72.3 kJ mol^{-1} observed at 298 K, a difference of 8 kJ mol^{-1}.

Whilst more extensive hydrogen bonded clusters form in the configurations shown in ***Fig. 5.45.***, the influence of the sodium ion (and lack of an additional proton) once again prevents water molecules from exchanging protons back and forth within these clusters to form hydroxonium ions. The large size of the sodium ion still restricts the water molecules into a curved geometry, pushed away from the sodium cation and further into the pore. This geometric influence is probably why the geodesic path length has a preference to extend only to two water molecules with a maximum of two hydrogen bonds (including to the wall of the zeolite). The coordination of three water molecules around the circumference of the sodium cation creates a geometric restriction, whereby the sodium pushes the water molecules further away from each other. This is linked to the inherent size difference between the BAS proton in H-ZSM-5 systems and the larger sodium cation in Na-ZSM-5. Since the coordinating water molecules are effectively further away, they cannot form hydrogen bonds between each other as easily, especially since this creates a larger angle between a water molecule's proton and the adjacent water molecule's oxygen atom. The resultant geometries make it less favourable to form hydrogen bonds between the water molecules, and also prevents protons from exchanging from one water molecule to another.

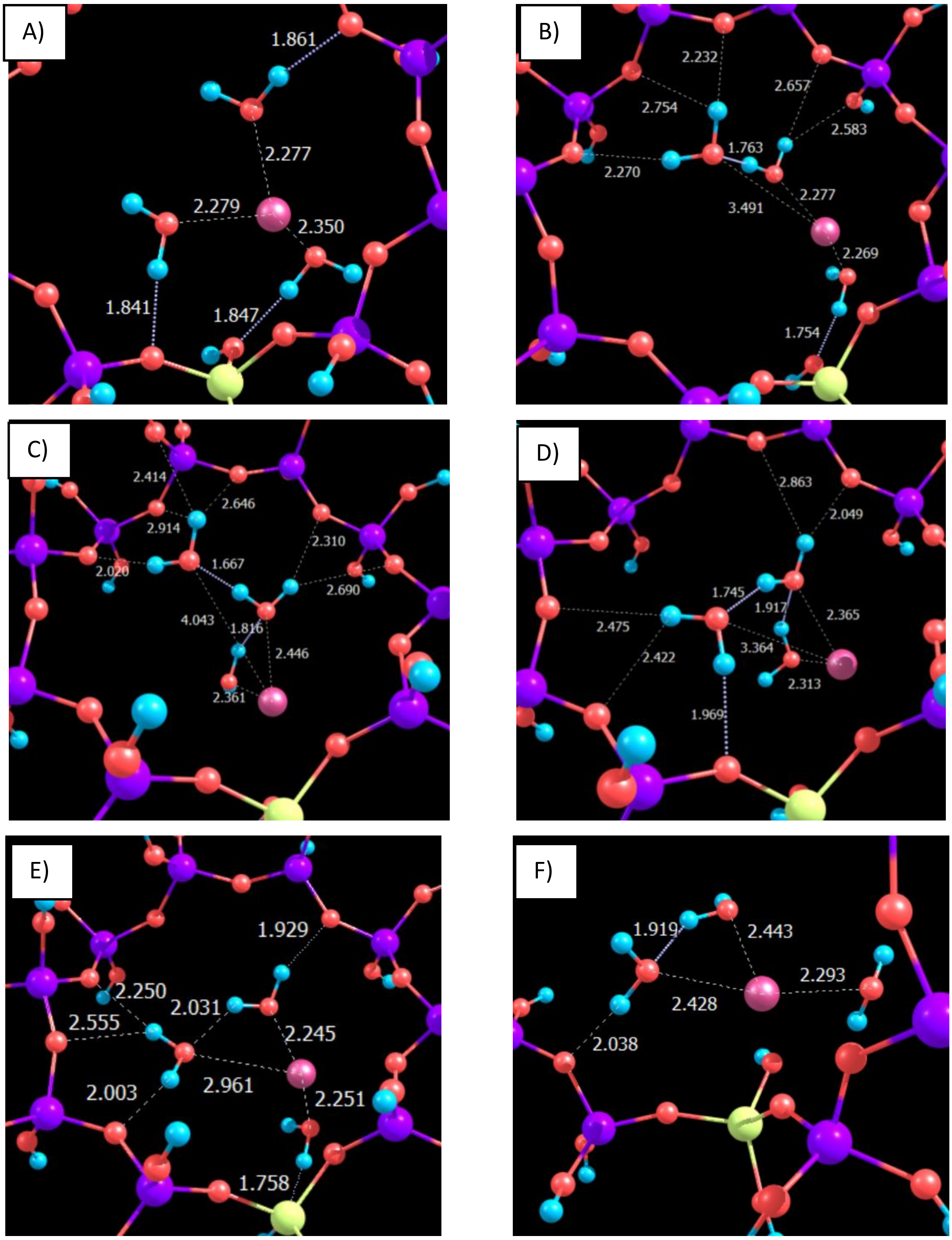

Fig. 5.45 (Part 1). Water cluster configurations A to I from the CA for three water molecules at 400 K. Key distances are labelled with a focus on the sodium and water oxygen distances. Structure labels refer to the corresponding cluster taken from the MD trajectory in **Fig. 5.44.** Atom colours: Si: purple, O: red, H: light blue, Al: yellow.

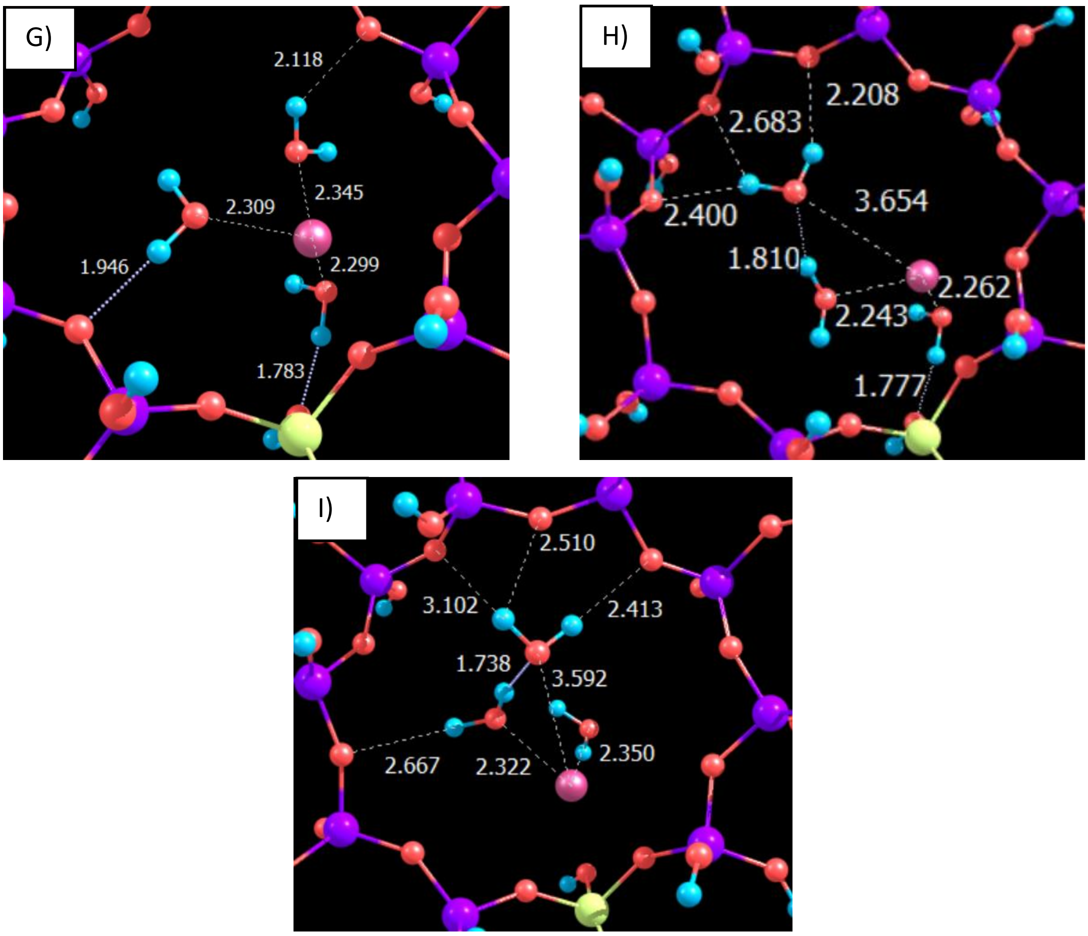

Fig. 5.45 (Part 2). Water cluster configurations A to I from the CA for three water molecules at 400 K. Key distances are labelled with a focus on the sodium and water oxygen distances. Structure labels refer to the corresponding cluster taken from the MD trajectory in **Fig. 5.44.** Atom colours: Si: purple, O: red, H: light blue, Al: yellow.

The water clusters at this higher temperature are displayed above in **Fig. 5.45** and exhibit a range of differences in the coordination of water molecules to the extra-framework sodium cation. The vast majority of clusters which includes clusters B, C, D, E, H and I appear to only coordinate two water molecule oxygens to the sodium with distances similar to those reported in the literature.[280,281] As a result, the sodium cation is predominantly coordinating to four of the zeolite oxygens across the cluster configurations however this coordination appears to change occasionally. In the case of systems A and G, the clusters appear to coordinate all three water molecules to the sodium cation, reducing its coordination to the to only three of the zeolite oxygens. In the final case of cluster F, it appears that only a single water molecule is coordinated to the sodium cation as the other two water molecules form a small hydrogen bonded cluster to an oxygen atom in the pore wall at a distance exceeding 2.4 Å.[280,281] Thus, these two water molecules can be considered as uncoordinated and the sodium cation is more highly coordinated to five of the zeolite oxygen atoms, probably resulting in a distortion of the larger unit cell.

As can be seen from the CA in ***Fig. 5.44.***, this higher temperature system has a displacement minimum around 2 Å and a maximum around 10 Å. Interestingly, this does not necessarily correspond to a higher energy term as the structure with the highest energy has a displacement of approximately 5 Å. In contrast to the lower temperature simulation, these structures are not too different in terms of displacement, as the bulk of the CA deviates within a 4 Å range between 6 Å and 10 Å. In the 298 K study the bulk of the displacement occurs within a 6 Å range of 6-12 Å giving an increase of 2 Å difference from the main system displacement. An interesting observation, as it shows that whilst the displacement from the starting structure does not directly translate into an energetic relationship, most of the higher energy systems tend to have a smaller displacement of around 4 Å. The lower displacement occurs more frequently at 400 K, probably a direct result of the effect of temperature on the system, which is further enforced by the energy values seen in ***Table 5.16.*** The structures taken from the 400 K system have a maximum about 20 kJ mol^{-1} higher than the 298 K simulation, and a minimum energy 28 kJ mol^{-1} higher than that observed at 298 K. Counter to the overall trend, the maximum at C is a rare occurrence and has the second highest energy out of all the clusters as shown in ***Table 5.16***., which could be the result of the water cluster transforming to a different configuration via a high energy transition step. Therefore, the next step is to analyse the corresponding vibrational spectra in ***Fig. 5.46.*** and their structures in ***Fig. 5.45.*** to determine specific trends.

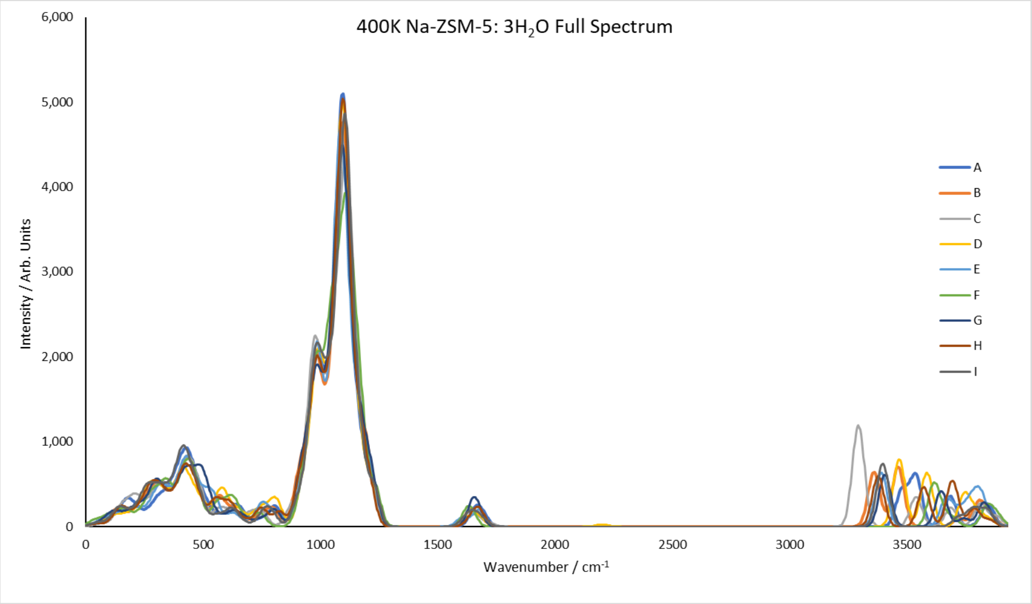

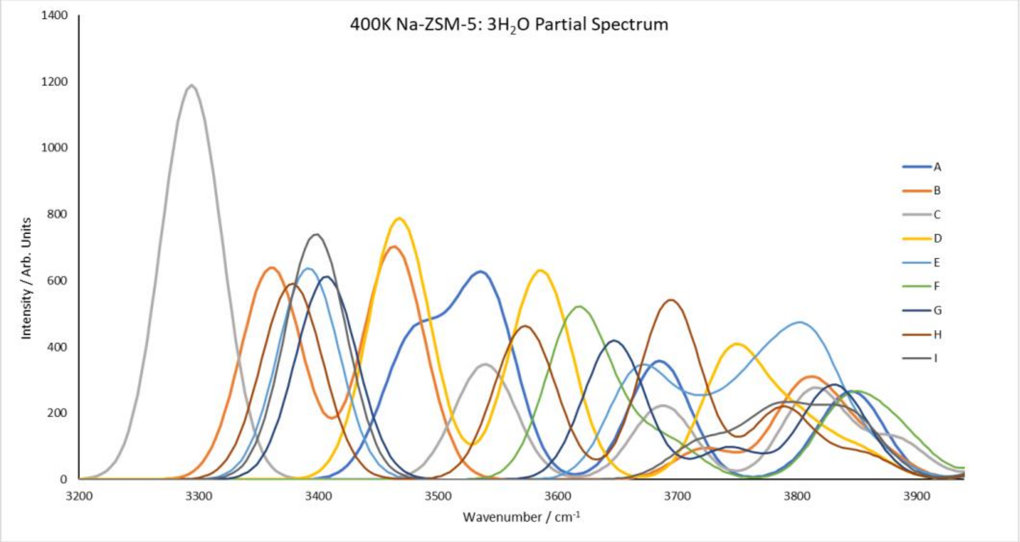

Fig. 5.46. Full vibrational spectrum for three water molecules in the pore of Na-ZSM-5 at 400 K. The contributions of water's symmetric and asymmetric anharmonic vibrations in the 400 K system, with the final peak arising from the terminal hydrogens of the QM region. Structure labels refer to the corresponding cluster taken from the MD trajectory in **Fig. 5.44.** Line colours: Cluster A: blue, Cluster B: orange, Cluster C: grey, Cluster D: yellow, Cluster E: light blue, Cluster F: green, Cluster H: brown and Cluster I: dark grey.

Once again, the terminal hydrogen contributions at around 4000 cm^{-1} have been removed from the final spectrum. Examining the full spectrum of Na-ZSM-5 with three water molecules at 400 K, there appears to be a better overlap of the symmetric bending modes than at 298 K, and so there is no need for further analysis. Additionally, the stretching frequencies arising from the zeolite tetrahedra forming the pore wall have a more consistent overlap than the 298 K system, which suggests that there is less flexing of the pore at 400 K, as is also shown by the reduced range of displacement (4 Å for 400 K instead of 6 Å for 298 K) in the CA. A small unique contribution is observed around 2200 cm^{-1} arising from system D that is not present in any of the other spectra; it arises from the torsion from the Si tetrahedral unit, adjacent to the Al, with the bulk of the zeolite.

System	**Al-O H-Bond / Å**	**Al-O 2nd H-Bond / Å**	**Other H-bonds / Å**		**Location**
A	1.85	1.84054	1.86	-	Pore Wall
B	1.75	-	1.76	-	Cluster
C	-	-	1.67	1.82	Cluster
D	1.97	-	1.74	1.92	Cluster
E	1.76	-	1.93	-	Pore Wall
F	-	-	1.92	-	Cluster
G	1.78	-	1.95	-	Pore Wall
H	1.78	-	1.81	-	Cluster
I	-	-	1.74	-	Cluster

Table 5.17. Hydrogen bond lengths in the Na-ZSM-5 systems with three water molecules at 400 K. Structure labels refer to the corresponding cluster taken from the MD trajectory in **Fig. 5.44.**

When analysing the symmetric and asymmetric shifts, the picture is once again far more complex but can largely be explained by the nature of the hydrogen bonds. System C has the greatest shift to its symmetric stretching frequencies compared to all the other spectra, forming three distinct peaks for these vibrations. Whilst this system does not form a hydrogen bond to an aluminium oxygen, it does form a hydrogen bonded cluster with all three water molecules in the pore. Furthermore, it can be seen from ***Table 5.17.***, that the shortest hydrogen bond length is 1.67 Å, corresponding to the hydrogen bond from the middle water molecule's hydrogen to the oxygen of one of the terminal water molecules. It has previously been shown that shorter, stronger hydrogen bonds cause significant down-field shifts in the spectrum, explaining why it is more shifted than the other spectra. The high relative intensity of this peak probably stems from the symmetric stretch being broadly in line with the hydrogen of the terminal water molecule, which could amplify the strength of the vibration. The third symmetric vibration remains largely unshifted and is broadly in line with that of other systems, as there is a moderate shift for the terminal water's hydrogen bond to the oxygen of the middle water molecule. Considering the average length of a hydrogen bond is 1.82 Å across these systems, this second hydrogen bond is also 1.82 Å, and so this relatively average shift is in line with expectations. The asymmetric peak broadens as a small shift is observed for the two vibrations from the waters with the shortest hydrogen bond length. Their intensity is larger, probably due to the third water being oriented at such an angle that the vibration of its hydrogen does not significantly change the hydrogen bond length. The other two water molecules are facing a similar direction and so their asymmetric vibrations can couple together, increasing the intensity of their contributions.

The second most shifted spectrum corresponds to system B, which contains two hydrogen bonds but specifically one to an aluminium oxygen. The length of this hydrogen bond is 1.75 Å making it the shortest hydrogen bond of this type. As was discussed previously, this hydrogen bond is likely to be strong, illustrated by the short hydrogen bond length, which de-shields the oxygen atom on the water molecule causing a down-field shift. This water molecule is also possibly influenced by the sodium cation with its hydrogen atoms pointing away, allowing the sodium to attract electron density off the oxygen atom, further de-shielding it. These two factors cause a greater extent of de-shielding than is observed in the other systems (excluding system C) resulting in a more extensive down-field shift, which is also the case for the shift of the second symmetric peak; however, since it lacks the strength of the hydrogen bond at the aluminium defect it is not shifted as far. The two peaks have a similar intensity as there are additional structures in line with their vibrations, which is not the case for the third symmetric stretch. As a result, the third stretch is low in intensity and the lack of hydrogen bonds prevent it from shifting; however, the hydrogen bonds broaden the asymmetric contributions which then overlap with this peak. Considering all but one of the clusters have two hydrogen bonds, the asymmetric peak is in line with these other systems.

The third most shifted is system H, which is the second most shifted spectrum for structures containing a hydrogen bond to an aluminium oxygen. Since system E has a shorter hydrogen bond of this type but is slightly less shifted, it can be deduced that the greater shift must also depend on another factor. Both water molecules bound to the aluminium oxygen are orientated in a similar way, so the effect of the sodium cation on the spectroscopic shift would be the same. Consequently, the second hydrogen bond has a length of 1.81 Å, which is more than 0.1 Å shorter than the one in system E, shifting the rest of the spectrum down-field slightly. The other two symmetric stretches have also shifted in accordance with hydrogen bond length, with the water forming the hydrogen bond to the oxygen of the second molecule being shifted more than the third molecule's vibration. The intensity of these modes is broadly similar with a slight reduction in the vibration linked to the hydrogen bond, probably resulting from the dampening effects seen previously. These two hydrogen bonds have also shifted two of the asymmetric peaks leaving a small shoulder peak broadly in line with the other systems. As is the case for all the modelled systems the asymmetric peaks are less intense than their symmetric counterparts, probably because of the orientations preventing asymmetric vibrations coupling with the hydrogen bonds and thus being amplified.

As was the case with the previous system, E forms a relatively strong hydrogen bond to the aluminium oxygen as indicated by its bond length of 1.76 Å. There is also a second hydrogen bond from the second water molecule to the pore wall, which is very weak as indicated by the long bond length of 1.93 Å, and so the resulting vibration is hardly shifted. Instead, the symmetric stretch of the unbound water molecule occurs at a lower wave number of 3667 cm^{-1} whilst the bound water vibration occurs at 3720 cm^{-1}. Hence demonstrating that whilst hydrogen bonds can form to the pore wall, away from the aluminium site, they are quite weak and cannot significantly de-shield a system to shift its vibrational frequency more than an unbound water. These peaks overlap with the asymmetric peaks and result in a lower intensity.

The next shifted spectrum results from system I, which does not form the hydrogen bond to the aluminium oxygen and instead only forms one between two water molecules. Despite which it forms the second strongest hydrogen bond out of all the systems between these two water molecules and allows for the comparison between the de-shielding effect of a strongly hydrogen bonded water cluster and a less strongly bound water to the aluminium oxygen. These hydrogen bonds may be longer to the aluminium oxygen, but the overall de-shielding effect is far greater than a strong hydrogen bond in a water cluster. Overall, this leads to a relatively broad, low intensity peak between 3700 cm^{-1} and 3850 cm^{-1} as two of the three symmetric stretching peaks overlap with the asymmetric peaks due to a lack of de-shielding. These peaks all have a similar intensity, apart from the first asymmetric stretch, which results from the terminal water molecule's unbound hydrogens. The unrestricted space allows for the vibrations to occur unimpeded, which causes an increase in the vibration's intensity.

The next system is G which forms two hydrogen bonds to the wall of the pore, with the first binding to the aluminium oxygen, and the second to the oxygen atom between the two silicon tetrahedral units adjacent to the aluminium. Again, there is the characteristic shift from the hydrogen bond to the aluminium oxygen; however, the bond length is now 1.78 Å, which whilst below 1.8 Å, is still noticeably longer than the others. There is still the concomitant shift from binding in this position, but this interaction is clearly much weaker and mitigates the extent of the shift. All other systems have chemically similar environments that bind to the same aluminium oxygen and shift further down-field. The second symmetric stretch is also shifted down-field due to its hydrogen bond; however, this is the second weakest bond of all the systems, as indicated by its bond length of 1.95 Å, despite being close to the aluminium. Thus, it can be concluded the de-shielding effect is only short ranged as the effect drops off very rapidly after one tetrahedral unit to a relatively negligible influence. There is also a steady decrease in intensity for the symmetric stretching frequencies at higher wave numbers, with the most intense contributions arising from the water molecules forming hydrogen bonds. The intensity of these peaks correlates with the strength of the hydrogen bond, with the aluminium oxygen peak having the highest intensity, followed by the second hydrogen bonded water, and finally leaving the unbound water with the lowest intensity. The asymmetric peaks overlap with the symmetric peak of the unbound water molecule but are less shifted from the hydrogen bonding; however, they follow the same trend in intensity. The asymmetric contributions share the same characteristics observed for the other systems and so the same analysis applies.

System D is the next most shifted in the combined spectra, yielding only three main peaks for all the symmetric and asymmetric contributions. Notably there is another peak occurring at around 2202 cm^{-1} that is not observed in the spectra of the other systems. This peak arises due to the vibrations resulting from torsion between one of the silica tetrahedra in the QM region and the rest of the zeolite lattice. Whilst there are three observable peaks in the spectrum, only two of them are a result of the symmetric vibrations. It could be expected that this system would yield a similar spectrum to system C, as it forms a single water cluster from all three molecules; only this time it also forms a hydrogen bond to the wall of the pore. Interestingly, the geometric similarities between these two systems do not directly translate into spectroscopic trends, as system C had the largest down-field shift, whilst system D results in one of the least shifted spectra.

As was seen in previous examples, a water molecule that has formed a hydrogen bond to the aluminium oxygen would result in a larger down-field shift. However, that is not the case for this system, probably as a result of bonding to a different aluminium oxygen, that is bound to the next silicon in the pore's ring. Moreover, the most shifted peak arises from only one symmetric stretching mode, resulting from the water in the middle of the cluster. The hydrogen bond length is the third shortest hydrogen bond overall, at only 1.74 Å, which makes this a plausible theory. Meanwhile the hydrogen bond to the aluminium oxygen is the weakest overall hydrogen bond with a length of 1.97 Å, indicating that whilst hydrogen bonds to aluminium oxygens can result in significant down-field shifts, strong hydrogen bonds elsewhere in the system can yield much greater spectroscopic shifts. If the hydrogen bond of the aluminium oxygen is especially weak, this becomes particularly notable.

The second peak arises from two symmetric stretching modes: first, the water forming a hydrogen bond to the wall, and the most up-field mode resulting from the terminal water at the other end of the cluster. There is a notable shift of this second peak when compared to other systems, which results from the hydrogen bonds that both water molecules form. The first hydrogen bond as mentioned earlier is very weak, but the hydrogen bond from the other water is also weak, as indicated by its long bond length of 1.92 Å, and so we see a very similar shifting of these frequencies, although the shorter bond's vibration is shifted less. The greater shifting of the longer bond is probably a result of the influence of a second hydrogen bond on the water molecule, which results in a slightly more de-shielded system. The intensities also decrease as symmetric contributions increase in wave number, probably a result of their geometries relative to each other; with the third water molecule only altering the length of the hydrogen bond it forms to a minor degree, resulting in less coupling and a lower intensity.

There is a noticeable shift in the asymmetric peak largely arising from the first mode, once again resulting from the middle water molecule, which happens to broaden the asymmetric peak as a result of the shorter hydrogen bond. Whilst a minor shift is observed for the other asymmetric modes, their hydrogen bonds are much weaker resulting in the smaller shift. This first asymmetric mode is noticeably more intense than the average in the spectrum. The greater intensity is probably a result of one of the hydrogens on the middle water molecule not being constrained by the hydrogen bonded cluster, and so can extend into the pore's empty space. The other hydrogen can couple with the water forming a hydrogen bond to the aluminium oxygen, further increasing the vibration's intensity.

One of the least shifted spectra results from system A, which is interesting as it contains three hydrogen bonds, including two to aluminium oxygens. The most shifted symmetric stretch of these two water molecules results from the hydrogen bond formed below the plane of the ring, which was the case observed previously, followed by the water hydrogen bonding in the plane of the ring. It is worth noting that this shift does not correspond directly to the bond length, as has largely been the case previously. The most shifted frequency arises from the longer bond length of 1.85 Å, and the less shifted mode results from the slightly shorter hydrogen bond of 1.84 Å. These two water molecules have a similar chemical environment as they both form hydrogen bonds to an aluminium oxygen; therefore, the sodium cation could play a role in this shift. However, the less shifted water is closer to the sodium cation at 2.28 Å whilst the most shifted is 2.35 Å away; thus, it can be concluded that the influence of the sodium cation is probably not the cause of this further shift. Since these proposals do not line up with observation, the alternative reason for this shift could be a result of the limitations of the QM region for this calculation. Since the aluminium below the plane of the ring does not have the influence of a SiO_4 tetrahedron, there could be a greater extent of de-shielding for this vibration than would be the case if the QM region accounted for the next tetrahedron in the lattice.

Calculations with larger QM clusters could be used for further analysis on the influence of this missing SiO_4 tetrahedron, but for the analysis discussed in this chapter, the clusters used are consistent, which allows for direct comparisons to each other. This system is also interesting as the second symmetric stretching mode is more intense than the first, which has not been observed previously. This higher intensity probably arises from the impact the vibration has on the wider structure, since it forms a hydrogen bond to an oxygen with tetrahedral units on either side, whereas the other forms a hydrogen bond to an oxygen with a linker hydrogen on it. The third water molecule forms a very weak hydrogen bond to the pore wall, as indicated by the bond length of 1.86 Å. The shift is significant when compared to systems with only two hydrogen bonds, or systems where the third water does not form a hydrogen bond. Despite this, the down-field shift is relatively minor, because of the weakness of this hydrogen bond. Once again, the asymmetric contributions have a significant overlap with those from the other spectra and so their behaviour is likely to be similar.

Finally, the least shifted spectroscopic contribution results from system F, which only forms a single hydrogen bond like system I. In this spectrum there are only two distinct peaks: one arising from solely symmetric contributions and the other from only asymmetric contributions, with no overlap between the two as was observed in previous cases. There are no hydrogen bonds to the aluminium oxygen in this system, so the most shifted symmetric stretch, which is also the most intense peak, arises from the water molecule forming a hydrogen bond with its oxygen atom. Coincidentally, this is one of the weakest hydrogen bonds as indicated by its bond length of 1.92 Å. Whilst this results in a minor de-shielding effect on the atom, it still contributes to a slight down-field shift. As a result, the symmetric peak broadens, and the increased intensity probably results from the hydrogen of this water molecule being 2.05 Å away from an oxygen in the pore wall. As the symmetric stretch occurs it reduces the distance between these two atoms, leading to a weak hydrogen bond-like influence, that would contribute towards a minor component of the shift. The other two symmetric stretches occur with similar intensities and are only shifted a small amount from each other at 3665 cm^{-1} for the second stretching frequency and 3700 cm^{-1} for the third stretch. The symmetric stretch at 3665 cm^{-1} occurs from the other water molecule in the hydrogen bonded cluster, thus explaining why it is shifted 35 cm^{-1} down-field compared to the third stretching frequency. All three of these water molecules have a similar influence from the sodium cation, with the oxygens of the water molecules in the cluster being at a distance of 2.43 Å and 2.44 Å, and the lone water molecule's oxygen being slightly closer at 2.29 Å. As a result of these weak interactions, there is very little observable shift in frequency for both the symmetric and asymmetric modes, with the asymmetric stretching modes being the least shifted of all water clusters. Despite this lack of shifting, system F is still the third highest energy system as shown below in ***Fig. 5.47.***, thus demonstrating that the extent of the shifts in the spectrum do not necessarily correspond to being a higher energy system**.**

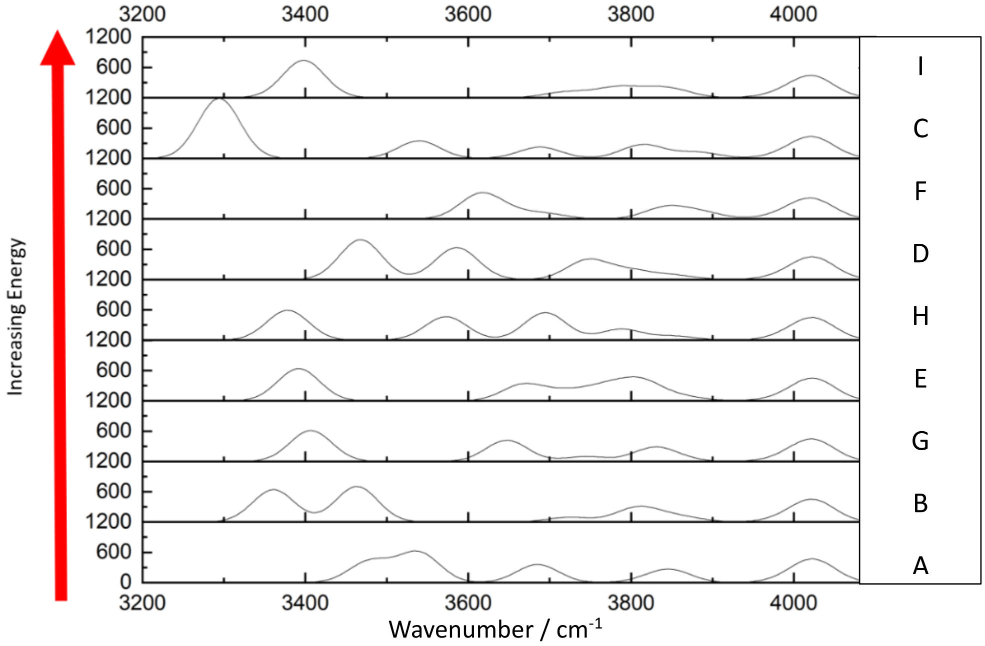

Fig. 5.47. Individual spectra of symmetric and asymmetric water vibrations at 400 K for each cluster ranked by energy with corresponding cluster configurations. Structure labels refer to the corresponding cluster taken from the MD trajectory in **Fig. 5.44.** Atom colours: Si: purple, O: red, H: light blue, Al: yellow.

This analysis has shown that there is a loose correlation between the calculated vibrational spectra and the energy of the system. However, a more accurate description of the shifting is provided when considering the strengths of hydrogen bonds (or inversely the O-H bond lengths in the water molecules) within the system as detailed by their respective bond lengths. Thus, it could be more apt to contextualise this trend as a loose correlation between geometric features and their corresponding system energies. Whilst it is useful to determine spectroscopic trends as presented within this chapter, it leaves the door open for the development of a method that weights the individual spectroscopic contributions with their occurrence within the component analysis. Weighting each spectrum this way would allow for a more realistic representation of a 'real' experimental spectrum and allow for a thorough breakdown and comparison with future experimental work.

5.4 Summary and Conclusions

Ab-Initio Molecular Dynamics simulations have successfully been performed for both the H-ZSM-5 and Na-ZSM-5 systems, containing one to three water molecules at 298 K and 400 K for 10 ps. The RMSD was deemed to obfuscate the desired data and so were subsequently replaced by component analyses on the cluster data and BAS/metal cation site. This analysis highlighted how bond lengths change through the duration of the simulation due to the formation of different clusters, and structures considered significant were taken from these plots and optimised using QM/MM techniques. Vibrational spectroscopic calculations including anharmonic effects were then run on these optimised structures and analyses of the spectra were carried out.

Both Na-ZSM-5 and H-ZSM-5 with a single water molecule have remarkably similar behaviour at both temperatures. The single water molecule either forms a hydrogen bond to the BAS or coordinates to the sodium and oscillates from one side of the pore to the other, deviating only at a higher temperature by the rotation of the water molecule, as highlighted by the CA. These similarities are reflected in the corresponding calculated spectra of these systems, in which there is a near perfect overlap with no additional anharmonic vibrations or shifts observed. The lack of shifting behaviour observed in Na-ZSM-5 leads to the conclusion that the more unusual anharmonic cross-coupling that would be observed experimentally, according to discussions with Dr. Paul Donaldson at the Central Laser Facility (CLF), would involve more than one water molecule.

The two systems deviate significantly upon the addition of a second water molecule, with H-ZSM-5 forming hydrogen bonded clusters, whilst Na-ZSM-5 spaces the water molecules far away from each other. Previous studies suggest that hydroxonium ions form at a loading of two water molecules in H-ZSM-5, forming a transition state; this hydroxonium ion formation was only observed in the optimisation of the starting structure, but not for the H-ZSM-5 system with two water molecules at either temperature. Additionally, no hydroxonium ion formation was observed with the sodium exchanged system, as the additional proton is not present. The asymmetric stretching frequencies remain constant across both temperatures for both systems, with hardly any noticeable shifting in frequencies, but deviate in intensity, whilst the symmetric stretching modes of water and the BAS (in H-ZSM-5) are shifted noticeably. The magnitudes of the shifts directly correlate with the strength of the hydrogen bonds formed by the clusters, as indicated by their shorter bond lengths. These shorter hydrogen bond lengths are accompanied by a proportional elongation of the water O-H bonds that are involved in forming these hydrogen bonds; thus, the vibrational frequencies are shifted to lower wave numbers. In the case of the H-ZSM-5 systems, the shifting of frequencies remains constant for the asymmetric modes, whilst the vibrations from the BAS hydrogen and symmetric stretching of the BAS-bound water molecule is shifted in accordance with the hydrogen bond lengths. We can infer that the stronger the hydrogen bond is (indicated by the short bond length) the longer the O-H water bond is, leading to a more de-shielded vibration, which causes a down-field shift respective to these bond lengths.

The analysis is a little more complex for the Na-ZSM-5 systems as they do not form hydrogen bonds. The exception is one specific example, in which a symmetric stretching mode can extend an O-H bond close enough to the pore wall that it could form a hydrogen bond, thus slightly de-shielding it and causing a down-field shift in its spectrum. Since Na-ZSM-5 keeps the two water molecules far apart they cannot form hydrogen bonds to each other, probably due to the size of the sodium cation. It is likely in this case that the shifting observed occurs from the proximity of the water molecules to the sodium cation. Sodium attracts the electron density towards it, slightly de-shielding the water molecule's oxygen atom, and causing a slight down-field shift.

With the addition of a third water molecule, there is a stark contrast between the H-ZSM-5 and Na-ZSM-5 systems. Notably whilst observing the AIMD, there is clear formation of hydroxonium ions in the H-ZSM-5 system at both temperatures, in line with previous work, and is accompanied by a characteristic peak in the anharmonic spectrum. This peak results from a massive down-field shift of the first asymmetric stretching mode, which shifts further down-field than any symmetric stretching mode. Due to the lack of a proton, this does not occur for the Na-ZSM-5 systems, although the water molecules in this system now form hydrogen bonds between each other, forming a weakly bound cluster. The difference in behaviour is also probably due to the influence of the sodium cation, which due to its size keeps the water molecules further apart, thus reducing the favourability of hydrogen bond formation. It also exerts a minor influence over the water molecules, occasionally resulting in a de-shielding effect that shifts some vibrational frequencies slightly more down-field.

Most of the spectra can be explained by the strength of the hydrogen bonds, whereby shorter, stronger hydrogen bonds are accompanied by an extension of the water O-H bonds. The water becomes more de-shielded as a result, shifting its symmetric stretching frequencies down-field, demonstrated by the formation of a hydrogen bond to an aluminium site oxygen. The down-field shift is probably a short-ranged effect as it is shown to have little influence on the spectroscopic shift one tetrahedral unit across. This effect also causes more de-shielding than a shorter hydrogen bond formed in a cluster not bound to the aluminium site. Once this aluminium site hydrogen bond is long enough, the de-shielding effect becomes weaker than with a conventional hydrogen bond. Typically, this is observed when a hydrogen bond is formed from the aluminium oxygen connected to a linker atom below the plane of the ring, rather than an oxygen attached to another silicon in the plane of the ring and forming the pore wall. As such it is not clear whether this large shift is a direct result of the lack of influence of the adjacent silica tetrahedron in the QM region when performing the calculation, or to this specific aluminium site oxygen.

Overall, our results show a fascinating range of behaviours, with vibrational spectroscopic properties correlating with energetic and structural characteristics of the clusters. It will be of great interest to make a detailed comparison with experiment when the new high-quality data becomes available.

Conclusions and Future Work

To conclude this thesis, we summarise the general outcomes and discoveries of each section. We first sought to benchmark different methodologies for modelling microporous materials. Two variations of interatomic potential models were successfully applied to model pure silica zeolites. In particular two distinct models were used: a partial charge model and a formal charge shell model. Energy differences (per tetrahedral unit) with respect to α-quartz were reported. The rigid ion approach generally produced energies higher than the shell model, with the latter method yielding energies closer to published experimental values. It was also shown that the lack of polarisation in the rigid ion model could lead to unphysical bond angles of 180° between Si units in some of the structures, as had been detailed for AlPOs in previous studies.

It is of note that zeolite BEA yielded a lower energy with the rigid ion model, which however, may stem from the disordered nature of the system. High level DFT was also able to reproduce similar results, but overall produces energies slightly lower than the potential based methods and closer to experimental values. In particular a significant difference between the two methodologies was observed for ITQ-39, with the DFT energy being significantly lower. This result fits the trend of normalised energy against density for the DFT study but is somewhat anomalous in the potential based study. ITQ-39 is a partially disordered material and therefore it could be concluded that potential based methods are prone to error for disordered systems. We draw a comparison between the overall trends for the shell model and DFT with experimental data reported previously, to find a very strong agreement between DFT and experimental results with near identical gradients when omitting α-quartz from the sample due to the nature of the dense phase. The shell model also shows good agreement, which becomes less accurate as the density decreases, as unlike DFT the general trendline does not run parallel to the experimental trendline but is slightly steeper. However, the potential based shell method can reproduce the general trends observed in DFT for a significantly lower cost, whilst DFT can produce cohesive energies within chemical accuracy.

The same approach was applied to modelling ALPOs; firstly, using a potential based shell model, followed by high level quantum mechanical methods. Again, energies were normalised to each tetrahedral unit, but their difference was measured against Berlinite as the alumino-phosphate equivalent to α-quartz. Both methods produced a near identical trend, scaling increasing energy with decreasing density yielding a similar distribution of the structures. For all systems, except ALPO-8, the potential based methods produced lower energies than the DFT. The potential based methods produced lattice energies that were also closer to the published experimental data, however the reason for this is unclear. When plotting both sets of calculations against experimental data, the trendlines have a greater discrepancy than observed for zeolites. In this study the gradients of the trendlines for the shell model and experimental data are almost identical, whilst that of the DFT calculations is steeper becoming less accurate when transitioning to less dense materials. We note that errors could arise as the result of calculating idealised systems compared to experimental systems, which could contain additional framework cations or even defects. For both zeolite and AlPO systems, it should be noted that composition can have a crucial influence on energetics leading to errors when comparing against the ’real’ experimental system. Owing to the overall greater energetic accuracy of the shell model, and the propensity of the rigid ion model to produce un-physical linear bond angles, the shell model was recommended for the modelling of MM environments in hybrid QM/MM calculations.

In Chapter 4 we combined both the interatomic potential shell model and quantum mechanical methods in hybrid QM/MM calculations of different metal centres in the ZSM-5 zeolite, with a focus on the catalytic aspects of microporous materials. Our aim was to utilise this hybrid method to assess the propensity of different metal ions to activate molecular oxygen and, by extension, assess the feasibility of a new catalytic pathway for methane to methanol conversion. The first aspect involved determination of the binding energies of different metal cations followed by modelling the coordination of a diatomic oxygen molecule to the metal centres.

The order of selectivity for our M(II) cations was reported as Co > Cu > Ti > Zn > Mn, which is a trend similar to that reported previously for LTA, FAU and MOR zeolites, with the placement of Mn(II) being the only consistent difference in the series. It is likely that the selectivity sequence is influenced by the structure of the zeolite, along with the location of the aluminium site within the structure and its Si:Al ratio. Furthermore, we note that the binding energies are within an expected range compared to the experimental values for LTA, FAU and MOR zeolites but are slightly more endothermic. Our calculations subsequently demonstrated that the Fe(II), Mn(II), Mn(III), Cu(I), Zn(I), Ti(II), Ti(III), Mo(I) systems were all capable of forming a super-oxo species as was indicated by the change in oxygen-oxygen bond length to a value of at least 1.3 Å. Both types of Au(I), Cu(I) structures along with the Na(I) and Zn(II) **b** systems however yielded positive binding energies indicating that oxygen would not realistically bind to these cationic centres, regardless of their ability to activate the coordinating molecule.

Finally, using the data obtained from these metal oxo systems, their respective hydrogen affinities (**BDE_{OH}**) were calculated, thus simulating the initial steps of a potential methane activation pathway. The results of these calculations suggest that the Mo(I) system readily cleaves the oxygen-oxygen bond to form a hydroxyl group. Both Mo(I) and Mn(III) systems saw very favourable hydrogen affinities (**BDE_{OH}**) and all had previously formed super-oxo species.

A valence bond approach was then employed to rationalise the oxidative power of the metal dependent oxidants, and by extension, elucidate information pertaining to the catalytic capabilities of each system. The resulting **Δ_{acid}** was shown to be very low for the [(Zn(I))-ZSM-5]-super-oxo complex suggesting that this complex could be formed, and it could make for a very effective catalyst for methane activation. Zn(I) is typically a very unstable valence state and so it could be assumed that the Zn(I) complex is formed from a Zn(II)-ZSM-5-super-oxo precursor, as it has been shown that a Zn(I) cation is not able to directly displace a proton. Qi *et al*[267] previously demonstrated that the ZSM-5 zeolite is one of the few complexes whereby a Zn(I) cation can be stabilised. The **BDE_{OH}** of this species is similar to the energy of the currently used µ-nitrido-bridged diiron-oxo porphyrin. Both Cu(I) and Na(I) cations formed super-oxo species with a similar basicity to this porphyrin alternative. Both complexes offer promise, as increasing the basicity of the active oxidant had previously proven to be a fundamental feature for improving the activity of these catalysts. However, the oxygen binding energies were endothermic which indicates that these complexes would not bind molecular oxygen, although they could be formed by reduction or oxidation from a different oxidation state.

Chapter 5 sought to utilise a variety of computational methodologies to model the behaviour of water molecules within the pore of H-ZSM-5 and Na-ZSM-5 at two different temperatures. Water plays a crucial role in the energies and activities of zeolite structures and as a result the study of water within the pores of microporous materials has become a fundamental and widely studied field. Computational methodologies allow us to improve our understanding of experimental phenomena and can aid in the process of catalyst design.

To this end, our aim was to build upon the methodologies utilised in previous chapters to model low concentrations of water molecules in the pores of H-ZSM-5 and Na-ZSM-5. Using these models, we sought to elucidate the nuanced differences in water clustering behaviours and adsorption dynamics between these two systems at two different temperatures. This study forms a foundation that can be later coupled with experimental 2D-IR work currently being undertaken at the UK Central Laser Facility, to assist in the determination of anharmonic cross-coupling phenomena observed experimentally between water and Na-ZSM-5. Unbiased a*b-initio* molecular dynamics were employed for these microporous systems, with a water-pore concentration of up to three water molecules, at temperatures similar to the experiments (298 K and 400 K) for a duration of 10 ps. Using a component analysis approach, structurally significant water clusters were selected and optimised using hybrid QM/MM methods and their subsequent vibrational spectra were calculated using a GVPT2 approach.

Both ZSM-5 systems with a single water molecule, displayed very similar behaviour at both temperatures. The water molecule either formed a hydrogen bond to the BAS proton or coordinated to the sodium cation. Neither system exhibited unusual anharmonic cross-coupling behaviour, despite the proposal that the experimental cross-coupling arose from the contribution of one water molecule at the aluminium site.

Modelling two water molecules in both of these systems leads to very different results, whereby the H-ZSM-5 systems form hydrogen bonded clusters (but not hydroxonium ions). The sodium system kept its respective water molecules apart, with Na-OH_2 distances in line with experimental crystallographic data, resulting in little to no hydrogen bonding behaviour at both temperatures. The vibrational frequency shifting observed for the H-ZSM-5 systems correlates directly with the strength of the hydrogen bonds. Shorter hydrogen bonds result in a corresponding lengthening of the O-H bonds, causing a down-field shift to occur, predominantly effecting the symmetric stretching modes. The shifting observed for Na-ZSM-5 largely occurs due to the de-shielding effect of the sodium cation on the oxygen atoms as it attracts electron density towards it, seeking to maximise the coordination of the cation.

With the addition of a third water molecule, significant differences are observed between the two systems. Hydroxonium ion formation now occurs for the H-ZSM-5 system, due to the abstraction of the proton from the BAS, which becomes more frequent at the higher temperature, but does not occur at all for Na-ZSM-5 due to the lack of this additional proton. A distinct peak is formed in the spectrum as a result of the hydroxonium ion, which is an asymmetric stretching mode that has been shifted down-field significantly. This asymmetric peak is shifted more down-field than any symmetric stretch and is characteristic of hydroxonium ion formation; thus, this peak is more common at the higher temperature.

The weaker binding energy of the sodium results in a minor migration of the cation to either side of the acid site. Hydrogen bonds do form with a loading of three water molecules in the Na-ZSM-5 system, resulting in significant spectroscopic shifts particularly for the symmetric stretching modes. Significant down-field shifts occur when water molecules form a hydrogen bond to an acid site oxygen, especially the oxygen below the plane of the QM region and attached to a linker hydrogen. As such it is not clear whether this large shift is a direct result of this particular oxygen or possibly an artefact, owed to the lack of influence of the next silicon atom arising from the boundary of the QM region.

Future work

The results obtained within this dissertation provide a wide-ranging overview of computational methodologies and their relationship to experiment. Hybrid QM/MM methods proved valuable in the determination of an alternative catalyst for the activation of oxygen within the pore of ZSM-5 using metal cations. Future work can involve modelling a greater selection of metal cations, and a comparison could be made between first and second row transition metal cations of the same oxidation state in the selectivity series. Furthermore, additional steps in the conversion of methane to methanol could be modelled as some cation systems could present a lower activation energy but not allow the desorption of products. Introduction of a second cation could also be investigated to address the issue of radical trapping, as highlighted in the literature, along with the influential effects of the second cation’s location, and the difference in selectivity on using the same and different metal cations for the second metal centre.

We present a solid foundation for further research into the dynamical behaviour of water within the pores of different ZSM-5 materials. The spectroscopic data generated for the systems within this thesis could be weighted by their energies, such as a Boltzmann distribution, to yield a more ‘realistic’ spectrum that would provide a better comparison with experimental data. An investigation could be conducted with additional defect structures, resulting from a lower Si:Al ratio with the aluminium sites in different locations such as within side channels. Additionally, there could be models using defect site hydroxyls, testing whether these interact with the adsorbed water coordinating to the cation site.

A similar approach could be utilised to model up to eight water molecules reaching the pore saturation point for a complete spectroscopic profile, with the influence of the fourth water molecule potentially providing a fully octahedrally coordinated sodium cation. Finally, this work can be coupled with the data provided by the experimental research performed with state-of-the-art 2D-IR spectroscopic techniques at the Central Laser Facility (CLF), to thoroughly analyse and compare with the simulated spectra to determine the specific spectroscopic contributions of novel anharmonic interactions.

Summary

This thesis has employed several computational methodologies to model successfully different aspects of microporous materials and systems. Our results illustrate the power and effectiveness of computational techniques in contemporary research into these materials. The techniques have proven to be an invaluable tool that can achieve accurate results complementing and comparing well to experimental data in several instances. Furthermore, these techniques have allowed for the elucidation of behaviours and energies that would either be very difficult or impossible to obtain solely by experiment.

References

1 J. Yu and R. Xu, *Chem. Soc. Rev.*, 2006, **35**, 593–604.

2 C. S. Cundy and P. A. Cox, *Chem. Rev.*, 2003, **103**, 663–701.

3 L. Sierra de Saldarriaga, C. Saldarriaga and M. E. Davis, *J. Am. Chem. Soc.*, 1987, **109**, 2686–2691.

4 B. M. Lok, C. A. Messina, R. L. Patton, R. T. Gajek, T. R. Cannan and E. M. Flanigen, *J. Am. Chem. Soc.*, 1984, **106**, 6092–6093.

5 J. M. Thomas, Y. Xu, C. R. A. Catlow and J. W. Couves, *Chem. of Mater.*, 1991, **3**, 667–672.

6 J. Yu, R. Xu and J. Li, *Solid State Sci.*, 2000, **2**, 181–192.

7 W. Yan, J. Yu, R. Xu, G. Zhu, F. Xiao, Y. Han, K. Sugiyama and O. Terasaki, *Chem. of Mater.*, 2000, **12**, 2517–2519.

8 T. F. Degnan, G. K. Chitnis and P. H. Schipper, *Microporous and Mesoporous Mater.*, 2000, **35–36**, 245–252.

9 P. H. Hoang and B. Nguyen Xuan, *RSC Adv.*, 2015, **5**, 78441–78447.

10 L. Miao, Z. Hong, G. Zhao, F. Huang and Z. Zhu, *Cat. Sci. Tech.*, 2021, **11**, 4831–4837.

11 S. H. Farahani, S. M. Alavi and C. Falamaki, *RSC Adv.*, 2017, **7**, 34012–34022.

12 D. S. Wragg, F. L. Bleken, M. G. O'Brien, M. Di Michiel, H. Fjellvåg and U. Olsbye, *Phys. Chem. Chem. Phys.*, 2013, **15**, 8662–8671.

13 S. K. Matam, A. J. O'Malley, C. R. A. Catlow, Suwardiyanto, P. Collier, A. P. Hawkins, A. Zachariou, D. Lennon, I. Silverwood, S. F. Parker and R. F. Howe, *Cat. Sci. Tech.*, 2018, **8**, 3304–3312.

14 T. Maschmeyer, F. Rey, G. Sankar and J. M. Thomas, *Nature, 1995,* **378**, 159–162.

15 Y. Hu, K. Wang, T. Wang and G. Luo, *Microporous and Mesoporous Mater.*, 2018, **270**, 149–154.

16 N. J. Azhari, N. Nurdini, S. Mardiana, T. Ilmi, A. T. N. Fajar, I. G. B. N. Makertihartha, Subagjo and G. T. M. Kadja, *J. CO2 Util.*, 2022, **59**, 101969.

17 T. Xue and L. Yang, *Front Chem*, 2021, **9**, 751581.

18 T. F. Degnan, *J. Cat.*, 2003, **216**, 32–46.

19 B. Smit and T. L. M. Maesen, *Nature, 2008*, **451**, 671–678.

20 G. Chen, G. Liu, Y. Pan, G. Liu, X. Gu, W. Jin and N. Xu, *Chem. Soc. Rev., 2023,* ***52**, 4586.*

21 K. C. Kemp, J. G. Min, H. J. Choi and S. B. Hong, *Struct. Bond*, 2020, **184**, 1–30.

22 J. Pérez-Pellitero and G. D. Pirngruber, *Struct. Bond*, 2020, **184**, 195–225.

23 L. Ćurković, Š. Cerjan-Stefanović and T. Filipan, *Water Res.*, 1997, **31**, 1379–1382.

24 R. P. Townsend, *Stud. Surf. Sci. Cat.*, 1986, **28**, 273–282.

25 O. Ursini, E. Lilla and R. Montanari, *J. Hazard Mater.*, 2006, **137**, 1079–1088.

26 C. R. A. Catlow, J. M. Thomas, S. C. Parker and D. A. Jefferson, *Nature,* 1982*,* **295**, 658–662.

27 C. R. A. Catlow, A. N. Cormack and F. Théobald, *Acta. Crystallogr.*, Sect. B, 1984, **40**, 195–200.

28 S. C. Parker, C. R. A. Catlow and A. N. Cormack, *J. Chem. Soc., Chem. Com*., 1983, **17**, 936-938.

29 R. Buckingham, *Proc. R. Soc. Lond.: A Math Phys. Sci.*, 1938, **168**, 264–283.

30 J. P. W. M. Vemparti C.S., *Radiat. Eff.*, 1983, **73**, 285.

31 M. J. Sanders, M. Leslie and C. R. A. Catlow, *J. Chem. Soc. Chem. Com.*, **1984**, 1271–1273.

32 B. W. H. Van Beest, G. J. Kramer and R. A. Van Santen, *Phys. Rev. Lett.*, 1990, **64**, 1955–1958.

33 S. Tsuneyuki, *Molec. Eng.*, 1996, **6**, 157.

34 R. A. Jackson and C. R. A. Catlow, *Mol. Simul.*, 1988, **1**, 207–224.

35 S. Girard, J. D. Gale, C. Mellot-Draznieks and G. Férey, *J. Am. Chem. Soc.*, 2002, **124**, 1040–1051.

36 S. R. Blaszkowski and R. A. Van Santen, *J. Phys.l Chem.*, 1995, **99**, 11728–11738.

37 V. Van Speybroeck, K. Hemelsoet, L. Joos, M. Waroquier, R. G. Bell and C. R. A. Catlow, *Chem. Soc. Rev.*, 2015, **44**, 7044–7111.

38 V. Van Speybroeck and R. J. Meier, *Chem. Soc. Rev.*, 2003, **32**(3), 151-157.

39 C. Lo and B. L. Trout, *J. Cat.*, 2004, **227**, 77–89.

40 H. Soscún, O. Castellano, J. Hernández and A. Hinchliffe, *Int. J. Quantum Chem.*, 2001, **82**, 143–150.

41 Y. Wang, D. Zhou, G. Yang, S. Miao, X. Liu and X. Bao, *J. Phys. Chem. A*, 2004, **108**, 6730–6734.

42 J. D. Lewis, S. Tijn Vandevyver, Y. Romμn-Leshkov and Y. Romμn-Leshkov, *Angewandte Chemie*, 2015, **127**, 9973–9976.

43 C. Perego, A. Carati, P. Ingallina, M. A. Mantegazza and G. Bellussi, *Appl. Cat. A Gen.*, 2001, **221**, 63–72.

44 M. Ravi, V. L. Sushkevich and J. A. Van Bokhoven, *J. Phys. Chem. C*, 2019, **123**, 15139-15144.

45 Y. Zhang, R. Zhao, M. Sanchez-Sanchez, G. L. Haller, J. Hu, R. Bermejo-Deval, Y. Liu and J. A. Lercher, *J. Cat.*, 2019, **370**, 424–433.

46 G. Busca, *Microporous and Mesoporous Mater.*, 2017, **254**, 3–16.

47 J. Brus, L. Kobera, W. Schoefberger, M. Urbanová, P. Klein, P. Sazama, E. Tabor, S. Sklenak, A. V. Fishchuk and J. Dědeček, *Angewandte Chemie Int. Ed.*, 2015, **54**, 541–545.

48 Z. Yu, A. Zheng, Q. Wang, L. Chen, J. Xu, J.-P. Amoureux, F. Deng, Z. W. Yu, A. M. Zheng, Q. Wang, L. Chen, J. Xu, F. Deng and J. P. Amoureux, *Angewandte Chemie*, 2010, **122**, 8839–8843.

49 J. P. Marques, I. Gener, P. Ayrault, J. C. Bordado, J. M. Lopes, F. R. Ribeiro and M. Guisnet, *Microporous and Mesoporous Mater.*, 2003, **60**, 251–262.

50 M. Bevilacqua and G. Busca, *Cat. Com.*, 2002, **3**, 497–502.

51 J. Klinowski, C. A. Fyfe and G. C. Gobbi, *J. Chem. Soc., Faraday Trans.*, 1985, **81**, 3003–3019.

52 G. Catana, D. Baetens, T. Mommaerts, R. A. Schoonheydt and B. M. Weckhuysen, *J. Phys. Chem. B*, 2002, **105**, 4904–4911.

53 K. Chen, S. Horstmeier, V. T. Nguyen, B. Wang, S. P. Crossley, T. Pham, Z. Gan, I. Hung and J. L. White, *J. Am. Chem. Soc.*, 2020, **142**, 7514–7523.

54 X. Yu, J. Mao, B. Wu, Y. Wei, Y. Sun and L. Zhong, *Chem. Cat. Chem.*, 2023, **15**, 6-17.

55 N. O. Gonzales, A. K. Chakraborty and A. T. Bell, *Cat. Lett.*, 1998, **50**, 135–139.

56 I. Pinilla-Herrero, E. Borfecchia, J. Holzinger, U. V. Mentzel, F. Joensen, K. A. Lomachenko, S. Bordiga, C. Lamberti, G. Berlier, U. Olsbye, S. Svelle, J. Skibsted and P. Beato, *J. Cat.*, 2018, **362**, 146–163.

57 Y. Ono and K. Kanae, *J. Chem. Soc., Faraday Trans.*, 1991, **87**, 669–675.

58 J. Kowalska-Kuś, A. Held and K. Nowińska, *Cat. Lett.*, 2010, **136**, 199–208.

59 L. M. Lubango and M. S. Scurrell, *Appl. Cat. A Gen.*, 2002, **235**, 265–272.

60 C. D. Keeling, T. P. Whorf, M. Wahlen and J. Van der Plichtt, *Nature*, 1995, **375**, 666–670.

61 U. Siegenthaler and H. Oeschger, *Tellus B: Chem, and Phys. Meteor.*, 1987, **39 B**, 140–154.

62 D. Bonenfant, M. Kharoune, P. Niquette, M. Mimeault and R. Hausler, *Sci. Tech. Adv. Mater.*, 2008, **9**, 013007.

63 M. R. Hudson, W. L. Queen, J. A. Mason, D. W. Fickel, R. F. Lobo and C. M. Brown, *J. Am. Chem. Soc.*, 2012, **134**, 1970–1973.

64 C. Chen and W.-S. Ahn, *Appl. Surf. Sci.*, 2014, **311**, 107–109.

65 V. R. Choudhary and S. Mayadevi, *Zeolites*, 1996, **17**, 501–507.

66 N. D. Hutson and R. T. Yang, *Adsorption*, 1997, **3**, 189–195.

67 H. M. F. Freundlich, *J. Phys. chem*, 1906, **57**, 1100–1107.

68 I. Langmuir, *J. Am. Chem. Soc.*, 1918, **40**, 1361–1403.

69 M. D. Macedonia, D. D. Moore, E. J. Maginn and M. M. Olken, *Langmuir*, 2000, **16**, 3823–3834.

70 E. García-Pérez, J. B. Parra, C. O. Ania, A. García-Sánchez, J. M. Van Baten, R. Krishna, D. Dubbeldam and S. Calero, *Adsorption*, 2007, **13**, 469–476.

71 A. J. O'Malley, A. J. Logsdail, A. A. Sokol and C. R. A. Catlow, *Faraday Discuss.*, 2016, **188**, 235–255.

72 S. A. F. Nastase, P. Cnudde, L. Vanduyfhuys, K. De Wispelaere, V. Van Speybroeck, C. Richard, A. Catlow and A. J. Logsdail, ACS Cat., 2020, **10** (15), 8904-8915.

73 M. Haris Mahyuddin, A. Staykov, Y. Shiota and K. Yoshizawa, *ACS Cat.*, 2017, **7**, 3741-3751.

74 G. Kresse and J. Furthmüller, *Phys. Rev. B*, 1996, **54**, 11169.

75 G. Kresse and J. Furthmüller, *Comp. Mater. Sci.*, 1996, **6**, 15–50.

76 G. Kresse and J. Hafner, *Phys. Rev. B*, 1994, **49**, 14251–14269.

77 G. Kresse and J. Hafner, *Phys. Rev. B*, 1993, **47**, 558–561.

78 G. Kresse and D. Joubert, *Phys. Rev. B*, 1999, **59**, 1758.

79 Y. Shiota and K. Yoshizawa, *J. Am. Chem. Soc.*, 2000, **122**, 12317–12326.

80 P. J. Smeets, J. S. Woertink, B. F. Sels, E. I. Solomon and R. A. Schoonheydt, *Inorg. Chem.*, 2010, **49**, 3573–3583.

81 M. H. Mahyuddin, Direct Hydroxylation of Methane, K. Yoshizawa, Ed., *Springer, Singapore*, **2020**, 87-100.

82 M. Ravi, V. L. Sushkevich, A. J. Knorpp, M. A. Newton, D. Palagin, A. B. Pinar, M. Ranocchiari and J. A. van Bokhoven, *Nature Cat.*, 2019, **2**, 485–494.

83 M. H. Mahyuddin, T. Tanaka, A. Staykov, Y. Shiota and K. Yoshizawa, *Inorg. Chem.*, 2018, **57**, 10146–10152.

84 J. S. Woertink, P. J. Smeets, M. H. Groothaert, M. A. Vance, B. F. Sels, R. A. Schoonheydt and E. I. Solomon, *Proc. Natl. Acad. Sci. USA*, 2009, **106**, 18908–18913.

85 R. J. Bunting, J. Thompson and P. Hu, *Phys. Chem. Chem. Phys.*, 2020, **22**, 11686–11694.

86 G. Qi, T. E. Davies, A. Nasrallah, M. A. Sainna, A. G. R. Howe, R. J. Lewis, M. Quesne, C. R. A. Catlow, D. J. Willock, Q. He, D. Bethell, M. J. Howard, B. A. Murrer, B. Harrison, C. J. Kiely, X. Zhao, F. Deng, J. Xu and G. J. Hutchings, *Nature Cat.*, 2022, **5**, 45–54.

87 J. P. Perdew, K. Burke and M. Ernzerhof, *Phys. Rev. Lett.*, 1996, **77**, 3865.

88 S. Grimme, J. Antony, S. Ehrlich and H. Krieg, *J. Chem. Phys.*, 2010, **132**, 154104.

89 E. Tabor, J. Dedecek, K. Mlekodaj, Z. Sobalik, P. C. Andrikopoulos and S. Sklenak, *Sci. Adv.*, 2020, **6**, eaaz9776.

90 B. E. R. Snyder, M. L. Bols, H. M. Rhoda, D. Plessers, R. A. Schoonheydt, B. F. Sels and E. I. Solomon, *Science*, 2021, **373**, 327–331.

90 B. E. R. Snyder, M. L. Bols, H. M. Rhoda, D. Plessers, R. A. Schoonheydt, B. F. Sels and E. I. Solomon, Science *(1979)*, 2021, **373**, 327–331.

91 G. T. Kerr, *J. Cat.*, 1982, **77**, 307–308.

92 K. C. Khulbe, T. Matsuura, C. Y. Feng and A. F. Ismail, *RSC Adv.*, 2016, **6**, 42943–42961.

93 D. E. Resasco, S. P. Crossley, B. Wang and J. L. White, *Cat. Rev. Sci. Eng.*, 2021, **63**, 302–362.

94 A. G. Pelmenschikov and R. A. Van Santen, *J. Phys. Chem.*, 1993, **97**, 10678–10680.

95 L. Márchese, J. Chen, P. A. Wright and J. M. Thomas, *J. Phys. Chem.*, 1993, **97**, 8109.

96 T. Zhou, P. Bai, J. I. Siepmann and A. E. Clark, *J. Phys. Chem. C*, 2017, **121**, 22015–22024.

97 B. C. Bukowski, J. S. Bates, R. Gounder and J. Greeley, *Angewandte Chemie Int. Ed.*, 2019, **58**, 16422–16426.

98 M. Hunger, D. Freude and H. Pfeifer, *J. Chem. Soc.*, Faraday Trans., 1991, **87**, 657–662.

99 A. Jentys, G. Warecka, M. Derewinski and J. A. Lercher, *J. Phys. Chem*, 1989, **93**, 4837–4843.

100 L. M. Parker, D. M. Bibby and G. R. Burns, *Zeolites*, 1993, **13**, 107–112.

101 J. N. Kondo, M. Iizuka, K. Domen and F. Wakabayashi, *Langmuir*, **1997**, 747–750.

102 M. Krossner and J. Sauer, *J. Phys. Chem.*, 1996, **100**, 6199–6211.

103 S. A. Zygmunt, L. A. Curtiss, L. E. Iton and M. K. Erhardt, *J. Phys. Chem.*, 1996, **100**, 6663–6671.

104 R. Shah, M. C. Payne, M. H. Lee and J. D. Gale, *Science*, 1996, **271**, 1395–1397.

105 N. Essayem, Y. Y. Tong, H. Jobic and J. C. Vedrine, *App. Cat. A. Gen.*, 2000, **194–195**, 109–122.

106 H. Jobic, M. Czjzek and R. A. van Santen, *J. Phys. Chem.*, 1992, **96**, 2758.

107 H. Jobic, A. Tuel, M. Krossner and J. Sauer, *J. Phys. Chem.*, 1996, **100**, 19545–19550.

108 J. Sauer, H. Horn, M. Häser and R. Ahlrichs, *Chem. Phys. Lett.*, 1990, **173**, 26–32.

109 S. Jungsuttiwong, J. Limtrakul and T. N. Truong, *J. Phys. Chem. B*, 2005, **109**, 13342–13351.

110 C. Lee, W. Yang and R. G. Parr, *Phys. Rev. B*, 1988, **37**, 785.

111 A. D. Becke, *Phys. Rev. A (Coll Park)*, 1988, **38**, 3098.

112 M. V. Vener, X. Rozanska and J. Sauer, *Phys. Chem. Chem. Phys.*, 2009, **11**, 1702–1712.

113 R. E. Fletcher, S. Ling and B. Slater, *Chem. Sci.*, 2017, **8**, 7483–7491.

114 C. J. Heard, L. Grajciar and P. Nachtigall, *Chem. Sci.*, 2019, **10**, 5705–5711.

115 Y. Zhang, H. Lin and D. G. Truhlar*, J. Chem. Theory Comp.*, 2007, **3**, 1378–1398.

116 A. Di Lella, N. Desbiens, A. Boutin, I. Demachy, P. Ungerer, J. P. Bellat and A. H. Fuchs, *Phys. Chem. Chem. Phys.*, 2006, **8**, 5396–5406.

117 J. Hunger, I. A. Beta, H. Böhlig, C. Ling, H. Jobic and B. Hunger, *J. Phys. Chem. B*, 2006, **110**, 342–353.

118 K. Tsutsumi, T. Kawai and T. Yanagihara, *Stud. Surf. Sci. Cat.*, 1994, **83**, 217–224.

119 D. H. Olson, W. O. Haag and W. S. Borghard, *Microporous and Mesoporous Mater.*, 2000, **35–36**, 435–446.

120 Z. Tahraoui, H. Nouali, C. Marichal, P. Forler, J. Klein and T. J. Daou, *Molecules 2020*, Vol. **25**, 2020, 25, 944.

121 S. J. Suresh, K. Kapoor, S. Talwar and A. Rastogi, *J. Mol. Liq.*, 2012, **174**, 135–142.

122 E. Moore, “Moore’s Law”, Encyclopædia Britannica, https://www.britannica.com/technology/Moores-law (accessed 9 June 2023).

123 E. Schrödinger, *Phys. Rev.*, 1926, **28**, 1049.

124 J. D. Gale and A. L. Rohl, General Utility Lattice Program (GULP), Curtin University, Perth, Australia, **2003**.

125 P. M. Morse, *Phys. Rev.*, 1929, **34**, 57.

126 S. S. I. Almishal and O. Rashwan, *RSC Adv.*, 2020, **10**, 44503–44511.

127 P. P. Ewald, *Ann. Phys.*, 1921, **369**, 253–287.

128 G. V. Lewis and C. R. A Catlow, *J. Phys. C: Solid State Phys.*, 1985, **18**, 1149–1161.

129 A. Rabdel Ruiz-Salvador, G. Sastre, D. W. Lewis, C. Richard and A. Catlow, *J. Muter. Chem*, 1996, **6**, 41.

130 J. E. Jones, *Proc. Royal Soc. Lon.: Series A, Containing Papers of a Math.l and Phys. Char.*, 1924, **106**, 441–462.

131 R. A. Buckingham, *Proc. R. Soc. A.*, RSPSA, 1938, **168**, 264–283.

132 M. Born, *Zeitschrift für Physik*, 1924, **26**, 379–395.

133 M. Born and R. Oppenheimer, *Ann. Phys.*, 1927, **389**, 457–484.

134 LibreTexts Chemistry, 2.6: Potential Energy Surfaces, University of California Davis, UCD Chem 107B: Physical Chemistry for Life Scientists, Chemistry LibreTexts, (accessed 11 August 2023).

135 D. R. Hartree, Hartree and D. R., *PCPS*, 1928, **24**, 89.

136 E. Fermi, *Zeitschrift für Physik*, 1928, **48**, 73–79.

137 L. H. Thomas, *Math. l Proc. Cambridge Phil. Soc.*, 1927, **23**, 542–548.

138 C. J. Cramer, *Essentials of Computational Chemistry: Theories and Models*, 2nd ed., Wiley, **2004**.

139 P. A. M. Dirac, *Math. Proc. Cambridge Phil. Soc.*, 1930, **26**, 376–385.

140 C. F. v. Weizsäcker, Weizsäcker and C. F. V., *Z. Phys.*, 1935, **96**, 431–458.

141 J. C. Slater, *Phys. Rev.*, 1951, **81**, 385.

142 P. Hohenberg and W. Kohn, *Phys. Rev.*, 1964, **136**, B864.

143 W. Kohn and L. J. Sham, *Phys. Rev.*, 1965, **140**, A1133.

144 J. B. Foresman, M. W. Wong, K. B. Wiberg and M. J. Frisch, *J. Am. Chem. Soc.*, 1993, **115**, 2220–2226.

145 E. Hückel, *Zeitschrift für Physik*, 1931, **72**, 310–337.

146 T. J. Zielinski, E. Harvey, R. Sweeney and D. M. Hanson, *J. Chem. Edu.*, 2005, **82**, 1880.

147 F. Jensen, Wiley Interdiscip. *Rev. Comp. Mol. Sci.*, 2013, **3**, 273–295.

148 S. Huzinaga, *Comp. Phys. Rep.*, 1985, **2**, 281–339.

149 A. Warshel and M. Levitt, *J. Mol. Biol.*, 1976, **103**, 227–249.

150 G. Groenhof, *Methods Mol. Biol.*, 2013, **924**, 43–66.

151 C. I. Bayly, P. Cieplak, W. D. Cornell and P. A. Kollman, *J. Phys. Chem*., 1993, **97**, 10269–10280.

152 B. H. Besler, K. M. Merz and P. A. Kollman, *J. Comp. Chem.*, 1990, **11**, 431-439.

153 P. Amara and M. J. Field, *Theor. Chem. Acc.*, 2003, **109**, 43–52.

154 G. Lamoureux and B. Roux, *Appl. Phys. Lett.*, 2003, **119**, 3025–3039.

155 A. Warshel, P. K. Sharma, M. Kato, Y. Xiang, H. Liu and M. H. M. Olsson, *Chem. Rev.*, 2006, **106**, 3210–3235.

156 A. K. Rappe and W. A. G. Iii, *J. Phys. Chem*., 1991, **95**, 3358–3363.

157 Y. Zhang, H. Lin and D. G. Truhlar, *J. Chem. Theor. Comp.*, 2007, **3**, 1378–1398.

158 A. Rodríguez, C. Oliva, M. González, M. Van Der Kamp and A. J. Mulholland, *J. Phys. Chem. B*, 2007, **111**, 12909–12915.

159 R. M. Nicoll, S. A. Hindle, G. MacKenzie, I. H. Hillier and N. A. Burton, *Theor. Chem. Acc.*, 2001, **106**, 105–112.

160 A. M. Khah, P. Reinholdt, J. Magnus, H. Olsen, J. Kongsted and C. Hättig, *J. Chem. Theor. Comp.*, 2020, **16**(3), 1373-1381.

161 R. Iftimie, P. Minary and M. E. Tuckerman, *Proc. Natl. Acad. Sci. USA*, 2005, **102**, 6654–6659.

162 B. J. Alder and T. E. Wainwright, *J. Chem. Phys.*, 1957, **27**, 1208–1209.

163 A. W. Lees and S. F. F. Edwards, *J. Phys. C: Solid State Phys.*, 1972, **5**, 1921-1928.

164 H. C. Andersen, *J. Chem. Phys.*, 1980, **72**, 2384–2393.

165 M. J. Gillan and M. Dixon, *J. Phys. C: Solid State Phys.*, 1983, **16**, 869.

166 S. Nosé, *J. Chem. Phys.*, 1984, **81**, 511–519.

167 R. Car and M. Parrinello, *Phys. Rev. Lett.*, 1985, **55**, 2471-2474.

168 T. Çağin and B. M. Pettitt, *Mol. Simul.*, 1991, **6**, 5–26.

169 Ch. Baerlocher and L.B. McCusker, *Database of Zeolite Structures*, http://www.iza-structure.org/databases/, (accessed 21 May 2020).

170 J. E. Lennard-Jones, *Proc. Phys. Soc.*, 1931, **43**, 461.

171 M. Born and J. E. Mayer, Gittertheorie der Ionenkristalle, *Z. Phys.*, 1932, **75**, 1-18.

172 M. S. Daw and M. I. Baskes, *Phys. Rev. Lett.*, 1983, **50**, 1285-1288.

173 J. L. Fattebert, D. F. Richards and J. N. Glosli, *Comp. Phys. Com.*, 2012, **183**, 2608–2615.

174 G. J. Bekker and N. Kamiya, *J. Phys. Chem. B*, 2021, **125**, 13376–13384.

175 L. A. Zepeda-Ruiz, A. Stukowski, T. Oppelstrup and V. V. Bulatov, *Nature*, 2017, **550**, 492–495.

176 L. Verlet, *Phys. Rev.*, 1967, **159**, 98.

177 N. Metropolis, A. W. Rosenbluth, M. N. Rosenbluth, A. H. Teller and E. Teller, *J. Chem. Phys.*, 1953, **21**, 1087–1092.

178 T. D. Kühne, Wiley, *Interdiscip. Rev. Comp. Mol. Sci.*, 2012, **4**, 391–406.

179 J. C. Grossman, E. Schwegler, E. W. Draeger, F. Gygi and G. Galli, *J. Chem. Phys*., 2004, **120**, 300–311.

180 C. Cappelli and M. Biczysko, in *Computational Strategies for Spectroscopy: from Small Molecules to Nano Systems*, ed. V. Barone, John Wiley & Sons, Inc., **2011**, pp. 309–360.

181 K. S. Yee and J. S. Chen, *IEEE Trans. Antennas Propag.*, 1997, **45**, 354–363.

182 F. Neese and J. Wiley, *Wiley Int. Rev. Comp. Mol. Sci.*, 2012, **2**, 73–78.

183 V. Barone, M. Biczysko and J. Bloino, *Phys. Chem. Chem. Phys*., 2014, **16**, 1759.

184 J. M. L. Martin, T. J. Lee, P. R. Taylor and J. P. François, *J. Chem. Phys.*, 1995, **103**, 2589–2602.

185 L. Barnes, B. Schindler, I. Compagnon and A. R. Allouche, *J. Mol. Model.*, 2016, **22**, 1–13.

186 M. A. Zwijnenburg, F. Corá and R. G. Bell, *J. Phys. Chem. B*, 2007, **111**, 6156–6160.

187 C. S. Cundy and P. A. Cox, *Chem. Rev.*, 2003, **103**, 663–701.

188 A. Navrotsky, O. Trofyrnluk and A. A. Levchenko, *Chem. Rev.*, 2009, **109**, 3885–3902.

189 D. Majda, F. A. Almeida Paz, O. Delgado Friedrichs, M. D. Foster, A. Simperler, R. G. Bell and J. Klinowski, *J. Phys. Chem. C*, 2008, **112**, 1040-1047.

190 R. Pophale, P. A. Cheeseman and M. W. Deem, *Phys. Chem. Chem. Phys.*, 2011, **13**, 12407–12412.

191 G. J. Kramer, A. J. M. De Man and R. A. Van Santen, *J. Am. Chem. Soc*., 1991, **113**, 6435–6441.

192 D. M. Dawson and S. E. Ashbrook, *J. Phys. Chem. C*, 2014, **118**, 23285–23296.

193 S. Sklenak, J. Dědeček, C. Li, B. Wichterlová, V. Gábová, M. Sierka and J. Sauer, *Phys. Chem. Chem. Phys.*, 2009, **11**, 1237–1247.

194 S. Girard, C. M. Draznieks, J. D. Gale and G. Férey, *Chem. Com.,* **2000**, 1161–1162.

195 J. G. González, J. D. L. C. Alcaz, A. R. Ruiz-Salvador, A. Gómez, A. Dago and C. de Las Pozas, *Microporous and Mesoporous Mater.*, 1999, **29**, 361–367.

196 D. Stojakovic and N. Rajic, *Computational Studies in the AlPO4-34 system*, 2001, vol. **8**.

197 A. Dorta-Urra and J. Gulín-González, *Microporous and Mesoporous Mater.*, 2006, **92**, 109–116.

198 N. J. Henson, A. K. Cheetham and J. D. Gale, *Chem. of Mater.*, 1996, **8**, 664–670.

199 A. Rabdel Ruiz-Salvador, G. Sastre, D. W. Lewis, C. Richard and A. Catlow, *J. Mater. Chem.*, 1996, **6**, 1837-1841.

200 E. R. Cope and M. T. Dove, *J. Appl. Crystall.*, 2007, **40**, 589–594.

201 J. D. Gale, J. Chem. Soc., *Faraday Trans.*, 1997, **93**, 629–637.

202 J. D. Gale, *Zeitschrift fur Kristallographie*, 2005, **220**, 552–554.

203 J. D. Gale, Phil. Mag. B: Phys. of Cond. Matter; Stat. Mechanics, Electronic, *Optical and Magnetic Properties*, 1996, **73**, 3–19.

204 J. D. Gale, P. Raiteri and A. C. T. Van Duin, *Phys. Chem. Chem. Phys.*, 2011, **13**, 16666–16679.

205 J. D. Gale and A. L. Rohl, *Mol. Simul.*, 2010, **33**, 1237-1246.

206 N. H. de Leeuw, F. M. Higgins and S. C. Parker, *J. Phys. Chem. B*, 1999, **103**, 1270–1277.

207 J. D. Gale and N. J. Henson, *J. Chem. Soc.*, Faraday Trans., 1994, **93**, 3175-3179.

208 H. Sowa, J. Macavei and H. Schultz, *Z. Kristallogr. Cryst. Mater.*, 1990, **192**, 119–136.

209 M. Fischer and R. J. Angel, *J. Chem. Phys.*, 2017, **146**, 174111.

210 J. P. Perdew, K. Burke and M. Ernzerhof, *Phys. Rev. Lett.*, 1996, **77**, 3865.

211 E. I. Román-Román and C. M. Zicovich-Wilson, *Chem. Phys. Lett.*, 2015, **619**, 109–114.

212 M. Fischer, F. O. Evers, F. Formalik and A. Olejniczak, *Theor. Chem. Acc.*, 2014, **135**, 257.

213 K. Ogata, Y. Takeuchi and Y. Kudoh, *Z. Kristallogr. Cryst. Mater.*, 1987, **179**, 403–414.

214 N. J. Henson, A. K. Cheetham and J. D. Gale, *Chem. Mater.*, 1994, **6**, 1647-1650.

215 P. M. Piccione, C. Laberty, S. Yang, M. A. Camblor, A. Navrotsky and M. E. Davis, *J. Phys. Chem. B*, 2000, **104**, 10001–10011.

216 Y. Hu, A. Navrotsky, C. Y. Chen and M. E. Davis, *Chem. of Mater.*, 1995, **7**, 1816–1823.

217 L. Wu and A. Navrotsky, *Phys. Chem. Chem. Phys.*, 2016, **18**, 10116–10122.

218 E. Stacey, M. G. Quesne and C. R. A. Catlow, *Microporous and Mesoporous Mater.*, 2023, **358**, 112382.

219 Z. Liu and J. Huang, *Chem. Synth.*, 2022, **2**, 21.

220 S. L. Scott, *Science (1979)*, 2021, **373**, 277–278.

221 R. J. Bunting, J. Thompson and P. Hu, *Phys. Chem. Chem. Phys.*, 2020, **22**, 11686–11694.

222 Home - ChemShell, https://chemshell.org/, (accessed 29 July 2023).

223 P. Sherwood, A. H. De Vries, M. F. Guest, G. Schreckenbach, C. R. A. Catlow, S. A. French, A. A. Sokol, S. T. Bromley, W. Thiel, A. J. Turner, S. Billeter, F. Terstegen, S. Thiel, J. Kendrick, S. C. Rogers, J. Casci, M. Watson, F. King, E. Karlsen, M. Sjøvoll, A. Fahmi, A. Schäfer and C. Lennartz, *J. Molec. Struc.: THEOCHEM*, 2003, **632**, 1–28.

224 J. Kästner, J. M. Carr, T. W. Keal, W. Thiel, A. Wander and P. Sherwood, *J. Phys.Chem. A*, 2009, **113**, 11856–11865.

225 W. Smith, C. W. Yong and P. M. Rodger, *Mol. Simul.*, 2002, **28**, 385–471.

226 S. A. F. Nastase, A. J. O'Malley, C. R. A. Catlow and A. J. Logsdail, *Phys. Chem. Chem. Phys.*, 2019, **21**, 2639–2650.

227 W. J. Mortier, Comp. of extra framework sites in zeolites, Butterworth Scientific Limited, **1982**.

228 S. Metz, J. Kästner, A. A. Sokol, T. W. Keal and P. Sherwood, *Wiley Int. Rev. Comp. Mol. Sci.*, 2014, **4**, 101–110.

229 F. Weigend and R. Ahlrichs, *Phys. Chem. Chem. Phys.*, 2005, **7**, 3297–3305.

230 J. R. Hill and J. Sauer, *J. Phys. Chem.*, 1995, **99**, 9536–9550.

231 U. Eichler, M. Brändle and J. Sauer, *J. Phys. Chem. B*, 1997, **101**, 10035–10050.

232 K. P. Schröder, J. Sauer, M. Leslie, C. Richard and A. Catlow, *Zeolites*, 1992, **12**, 20–23.

233 A. Delabie, K. Pierloot, M. H. Groothaert and R. A. Schoonheydt, *Eur. J. Inorg. Chem*., **2002**, 515-530.

234 A. Delabie, K. Pierloot, M. H. Groothaert, B. M. Weckhuysen and R. A. Schoonheydt, *Phys. Chem. Chem. Phys.*, 2002, **4**, 134–145.

235 K. Pierloot, A. Delabie, M. H. Groothaert and R. A. Schoonheydt, *Phys. Chem. Chem. Phys.*, 2001, **3**, 2174–2183.

236 K. Pierloot, A. Delabie, A. A. Verberckmoes, R. Schoonheydt, P. Geerlings, F. De Proft and W. Langenaeker, *Eds.; VUB Uni. Press: Brussels*, Belgium, **1999**; p 169.

237 M. H. Groothaert, K. Pierloot, A. Delabie and R. A. Schoonheydt, *Phys. Chem. Chem. Phys.*, 2003, **5**, 2135–2144.

238 M. E. Franke, M. Sierka, U. Simon and J. Sauer, *Phys. Chem. Chem. Phys.*, 2002, **4**, 5207–5216.

239 J. Sauer, C. M. Kölmel, J. R. Hill and R. Ahlrichs, *Chem. Phys. Lett.*, 1989, **164**, 193–198.

240 N. A. Ramsahye and R. G. Bell, *J. Phys. Chem. B*, 2005, **109**, 4738–4747.

241 E. Perez-Cappe, M. Aguilar-Frutis, N. Chavez, J. Ribalta and E. Reguera, *Microporous and Mesoporous Mater.*, 2012, **163**, 326–333.

242 R. M. Barrer and R. P. Townsend, *J. Chem. Soc.*, Faraday Trans., 1976, **72**, 661–673.

243 A. Maes and A. Cremers, J. Chem. Soc. Faraday Trans., 1975, **71**, 265–277.

244 D. R. Lide, *CRC Handbook of Chemistry and Physics*, **85**th ed., CRC Press, 2004.

245 A. Mukherjee, M. A. Cranswick, M. Chakrabarti, T. K. Paine, K. Fujisawa, E. Münck and L. Que, *Inorg. Chem.*, 2010, **49**, 3618–3628.

246 H. R. Pan, H. J. Chen, Z. H. Wu, P. Ge, S. Ye, G. H. Lee and H. F. Hsu, *JACS Au*, 2021, **1**, 1389–1398.

247 A. C. Rosenzweig, C. A. Frederick, S. J. Lippard and P. Nordlund, *Nature*, 1993, **366**, 537–543.

248 A. L. Feig and S. J. Lippard, *Chem. Rev*., 1994, **94**, 759–805.

249 F. E. Zilly, J. P. Acevedo, W. Augustyniak, A. Deege and M. T. Reetz, *Angewandte Chem. Int. Ed.*, 2011, **50**, 2720–2724.

250 N. Kawakami, O. Shoji and Y. Watanabe, *Angewandte Chemie Int. Ed.*, 2011, **50**, 5315–5318.

251 S. N. Kawakami, O. Shoji, Y. Watanabe, N. Kawakami, O. Shoji and Y. Watanabe, *Chem. Sci.*, 2013, **4**, 2344–2348.

252 E. V Kudrik, A. B. Sorokin, A. B. Sorokin and E. V Kudrik, *Chemistry – A European Journal*, 2008, **14**, 7123–7126.

253 Ü. Ici, P. Afanasiev, J. M. M. Millet, E. V. Kudrik, V. Ahsen and A. B. Sorokin, *Dalton Trans.*, **2009**, 7410–7420.

254 A. B. Sorokin, E. V. Kudrik and D. Bouchu, *Chem. Com.*, 2008, **0**, 2562–2564.

255 Ü. Işci, F. Dumoulin, V. Ahsen and A. B. Sorokin, *Chem. Sci.*, 2012, **14**, 324-334.

256 A. Takahashi, D. Yamaki, K. Ikemura, T. Kurahashi, T. Ogura, M. Hada and H. Fujii, *Inorg. Chem.*, 2012, **51**, 7296–7305.

256 J. S. Woon, O. R. Yon, R. Song and W. Nam, *J. Bio. Inorg. Chem.*, 2005, **10**, 294–304.

258 K. Czarnecki, S. Nimri, Z. Gross, L. M. Proniewicz and J. R. Kincaid, *J. Am. Chem. Soc.*, 1996, **118**, 2929–2935.

259 Z. Gross and S. Nimri, *Inorg. Chem.*, 1994, **33**, 1731–1732.

260 T. Yang, M. G. Quesne, H. M. Neu, F. G. C. Reinhard, D. P. Goldberg and S. P. De Visser, *J. Am. Chem. Soc.*, 2016, **138**, 12375–12386.

261 A. S. Faponle, M. G. Quesne and S. P. De Visser, *Chem. – A European Journal*, 2016, **22**, 5478–5483.

262 M. Ortmayer, F. J. Hardy, M. G. Quesne, K. Fisher, C. Levy, D. J. Heyes, C. R. A. Catlow, S. P. De Visser, S. E. J. Rigby, S. Hay and A. P. Green, *JACS Au*, 2021, **1**, 913–918.

263 B. Ruscic, *J. Phys. Chem. A*, 2015, **119**, 7810–7837.

264 M. G. Quesne, D. Senthilnathan, D. Singh, D. Kumar, P. Maldivi, A. B. Sorokin and S. P. De Visser, *ACS Cat.*, 2016, **6**, 2230–2243.

265 T. H. Parsell, M. Y. Yang and A. S. Borovlk, *J. Am. Chem. Soc.*, 2009, **131**, 2762–2763.

266 M. T. Green, J. H. Dawson and H. B. Gray, *Science*, 2004, **304**, 1653–1656.

267 G. Qi, J. Xu, J. Su, J. Chen, X. Wang and F. Deng, *J. Am. Chem. Soc.*, 2013, **135**, 6762–6765.

268 A. Jentys, G. Warecka, M. Derewinski and J. A. Lercher, *J. Phys. Chem.*, 1989, **93**, 4837–4843.

269 E. Grifoni, G. Piccini, J. A. Lercher, V.-A. Glezakou, R. Rousseau and M. Parrinello, *Nat. Com.*, 2021, **12**, 2630.

270 S. A. Zygmunt, L. A. Curtiss, L. E. Iton and M. K. Erhardt, *J. Phys. Chem.*, 1996, **100**, 6663–6671.

271 M. Wang, N. R. Jaegers, M.-S. Lee, C. Wan, J. Z. Hu, H. Shi, D. Mei, S. D. Burton, D. M. Camaioni, O. Y. Gutiérrezgutiérrez, V.-A. Glezakou, R. Rousseau, Y. Wang and J. A. Lercher, *J. Am. Chem. Soc.*, 2019, **141**, 3444–3455.

272 M. Badawi, B. Cardey, M. Grivet, J. Groetz, C. Ramseyer, F. Torrealba Anzola, C. Chambelland, D. Ducret, J. Randrianandraina, M. Badawi, B. Cardey, M. Grivet, J.-E. Groetz, C. Ramseyer, F. Torrealba Anzola, C. Chambelland and D. Ducret, *Phys. Chem. Chem. Phys.*, 2021, **23**, 264-283.

273 S. T. Roberts, K. Ramasesha and A. Tokmakoff, *Acc. Chem. Res.*, 2009, **42**, 1239–1249.

274 A. Lenz and L. Ojamäe, *J. Phys. Chem. A*, 2006, **110**, 13388–13393.

275 A. Ison and R. J. Gorte, *J. Cat.*, 1984, **89**, 150–158.

276 H. Tian, S. Liu and Q. Liu, *RSC Adv.*, 2022, **12**, 24654–24669.

277 B. Hunger, M. Heuchel, S. Matysik, K. Beck and W. D. Einicke, *Thermoch. Acta.*, 1995, **269–270**, 599–611.

278 Chemcraft - Citation, https://www.chemcraftprog.com, (accessed 2 August 2023).

279 J. H. Hack, J. P. Dombrowski, X. Ma, Y. Chen, N. H. C. Lewis, W. B. Carpenter, C. Li, G. A. Voth, H. H. Kung and A. Tokmakoff, *J. Am. Chem. Soc.*, 2021, **143**, 10203–10213.

280 K. Stahl and J. Hanson, *J. Appl. Crystallogr.*, 1994, **27**, 543–550.

281 D. L. Bish and D. W. Ming, *Natural zeolites: occurrence, properties, applications*, Mineral. Soc. of America, Washington, DC, 2001.

282 M. S. Krawczyk and I. Majerz, *Acta. Crystallogr. B Struct. Sci. Cryst. Eng. Mater.*, 2019, **75**, 766–774.

283 K. H. Schnabel, Ch. Peuker, B. Parlitz, E. Löffler, U. Kürschner and H. Kriegsmann, *Zeitschrift für Phys. Chem.*, 1987, **268O**, 225–234.